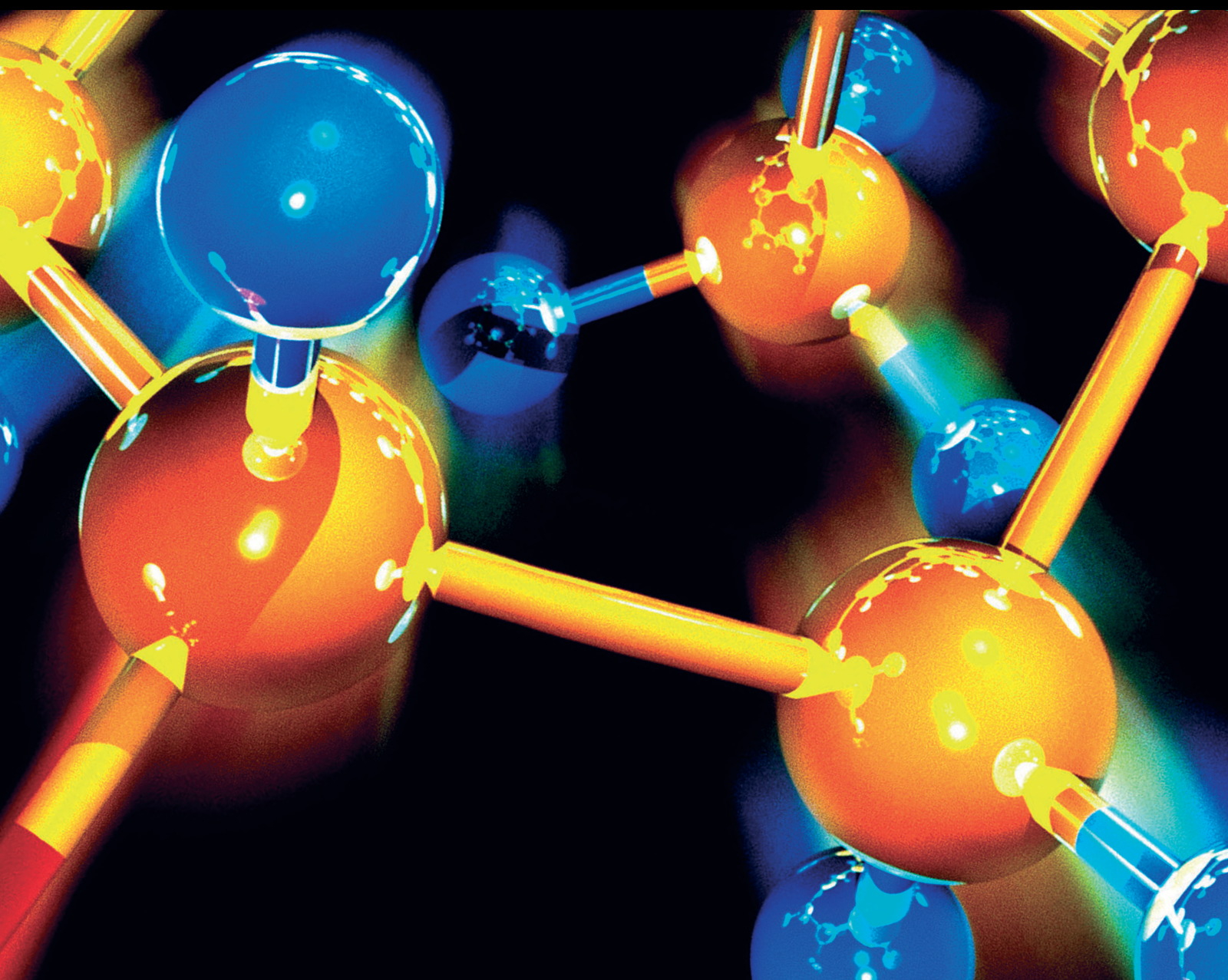


Biomass-Derived Functional Materials and their High-Efficiency Utilizations

Lead Guest Editor: Gonggang Liu

Guest Editors: Binghui Xu, Heng Jiang, and Yuanjuan Bai





Biomass-Derived Functional Materials and their High-Efficiency Utilizations

Journal of Chemistry

Biomass-Derived Functional Materials and their High-Efficiency Utilizations

Lead Guest Editor: Gonggang Liu

Guest Editors: Binghui Xu, Heng Jiang, and
Yuanjuan Bai



Copyright © 2022 Hindawi Limited. All rights reserved.


This is a special issue published in "Journal of Chemistry." All articles are open access articles distributed under the Creative Commons Attribution License, which permits unrestricted use, distribution, and reproduction in any medium, provided the original work is properly cited.

Chief Editor

Kaustubha Mohanty, India

Associate Editors

Mohammad Al-Ghouthi, Qatar


Tingyue Gu , USA

Teodorico C. Ramalho , Brazil

Artur M. S. Silva , Portugal


Academic Editors

Jinwei Duan, China

Luqman C. Abdullah , Malaysia

Dr Abhilash , India

Amitava Adhikary, USA

Amitava Adhikary , USA

Mozhgan Afshari, Iran

Daryoush Afzali , Iran

Mahmood Ahmed, Pakistan


Islam Al-Akraa , Egypt


Juan D. Alché , Spain

Gomaa A. M. Ali , Egypt

Mohd Sajid Ali , Saudi Arabia

Shafaqat Ali , Pakistan


Patricia E. Allegretti , Argentina

Marco Anni , Italy

Alessandro Arcovito, Italy

Hassan Arida , Saudi Arabia


Umair Ashraf, Pakistan


Narcis Avarvari , France

Davut Avci , Turkey


Chandra Azad , USA

Mohamed Azaroual, France

Rasha Azzam , Egypt


Hassan Azzazy , Egypt

Renal Backov, France

Suresh Kannan Balasingam , Republic of Korea

Sukanta Bar , USA

Florent Barbault , France

Maurizio Barbieri , Italy

James Barker , United Kingdom

Salvatore Barreca , Italy

Jorge Barros-Velázquez , Spain

THANGAGIRI Baskaran , India

Haci Baykara, Ecuador

Michele Benedetti, Italy

Laurent Billon, France

Marek Biziuk, Poland

Jean-Luc Blin , France

Tomislav Bolanca , Croatia


Ankur Bordoloi , India

Cato Brede , Norway


Leonid Breydo , USA


Wybren J. Buma , The Netherlands

J. O. Caceres , Spain


Patrizia Calaminici , Mexico

Claudio Cameselle , Spain

Joaquin Campos , Spain

Dapeng Cao , China

Domenica Capasso , Italy

Stefano Caporali , Italy

Zenilda Cardeal , Brazil

Angela Cardinali , Italy

Stefano Carli , Italy

Maria F. Carvalho , Portugal

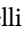
Susana Casal , Portugal


David E. Chavez, USA

Riccardo Chelli , Italy

Zhongfang Chen , Puerto Rico

Vladislav Chrastny , Czech Republic

Roberto Comparelli , Italy

Filomena Conforti , Italy

Luca Conti , Italy


Christophe Coquelet, France

Filomena Corbo , Italy

Jose Corchado , Spain

Maria N. D.S. Cordeiro , Portugal

Claudia Crestini, Italy

Gerald Culioli , France

Nguyen Duc Cuong , Vietnam

Stefano D'Errico , Italy


Matthias D'hooghe , Belgium


Samuel B. Dampare, Ghana

Umashankar Das, Canada

Victor David, Romania

Annalisa De Girolamo, Italy


Antonio De Lucas-Consuegra , Spain

Marcone A. L. De Oliveira , Brazil

Paula G. De Pinho , Portugal

Damião De Sousa , Brazil

Francisco Javier Deive , Spain

Tianlong Deng , China

Fatih Deniz , Turkey
Claudio Di Iaconi, Italy
Irene Dini , Italy
Daniele Dondi, Italy
Yingchao Dong , China
Dennis Douroumis , United Kingdom
John Drexler, USA
Qizhen Du, China
Yuanyuan Duan , China
Philippe Dugourd, France
Frederic Dumur , France
Grégory Durand , France
Mehmet E. Duru, Turkey
Takayuki Ebata , Japan
Arturo Espinosa Ferao , Spain
Valdemar Esteves , Portugal
Cristina Femoni , Italy
Gang Feng, China
Dieter Fenske, Germany
Jorge F. Fernandez-Sanchez , Spain
Alberto Figoli , Italy
Elena Forte, Italy
Sylvain Franger , France
Emiliano Fratini , Italy
Franco Frau , Italy
Bartolo Gabriele , Italy
Guillaume Galliero , France
Andrea Gambaro , Italy
Vijay Kumar Garlapati, India
James W. Gauld , Canada
Barbara Gawdzik , Poland
Pier Luigi Gentili , Italy
Beatrice Giannetta , Italy
Dimosthenis L. Giokas , Greece
Alejandro Giorgetti , Italy
Alexandre Giuliani , France
Elena Gomez , Spain
Yves Grohens, France
Katharina Grupp, Germany
Luis F. Guido , Portugal
Maolin Guo, USA
Wenshan Guo , Australia
Leena Gupta , India
Muhammad J. Habib, USA
Jae Ryang Hahn, Republic of Korea

Christopher G. Hamaker , USA
Ashanul Haque , Saudi Arabia
Yusuke Hara, Japan
Naoki Haraguchi, Japan
Serkos A. Haroutounian , Greece
Rudi Hendra , Indonesia
Javier Hernandez-Borges , Spain
Miguel Herrero, Spain
Mark Hoffmann , USA
Hanmin Huang, China
Doina Humelnicu , Romania
Charlotte Hurel, France
Nenad Ignjatović , Serbia
Ales Imramovsky , Czech Republic
Muhammad Jahangir, Pakistan
Philippe Jeandet , France
Sipak Joyasawal, USA
Sławomir M. Kaczmarek, Poland
Ewa Kaczorek, Poland
Mostafa Khajeh, Iran
Srećko I. Kirin , Croatia
Anton Kokalj , Slovenia
Sevgi Kolaylı , Turkey
Takeshi Kondo , Japan
Christos Kordulis, Greece
Ioannis D. Kostas , Greece
Yiannis Kourkoutas , Greece
Henryk Kozłowski, Poland
Yoshihiro Kudo , Japan
Avvaru Praveen Kumar , Ethiopia
Dhanaji Lade, USA
Isabel Lara , Spain
Jolanta N. Latosinska , Poland
João Paulo Leal , Portugal
Woojin Lee, Kazakhstan
Yuan-Pern Lee , Taiwan
Matthias Lein , New Zealand
Huabing Li, China
Jinan Li , USA
Kokhwa Lim , Singapore
Teik-Cheng Lim , Singapore
Jianqiang Liu , China
Xi Liu , China
Xinyong Liu , China
Zhong-Wen Liu , China





Eulogio J. Llorent-Martínez , Spain
Pasquale Longo , Italy
Pablo Lorenzo-Luis , Spain
Zhang-Hui Lu, China
Devanand Luthria, USA
Konstantin V. Luzyanin , United Kingdom
Basavarajaiah S M, India
Mari Maeda-Yamamoto , Japan
Isabel Mafra , Portugal
Dimitris P. Makris , Greece
Pedro M. Mancini, Argentina
Marcelino Maneiro , Spain
Giuseppe F. Mangiatordi , Italy
Casimiro Mantell , Spain
Carlos A Martínez-Huitle , Brazil
José M. G. Martinho , Portugal
Andrea Mastinu , Italy
Cesar Mateo , Spain
Georgios Matthaiolampakis, USA
Mehrab Mehrvar, Canada
Saurabh Mehta , India
Oinam Romesh Meitei , USA
Saima Q. Memon , Pakistan
Morena Miciaccia, Italy
Maurice Millet , France
Angelo Minucci, Italy
Liviu Mitu , Romania
Hideto Miyabe , Japan
Ahmad Mohammad Alakraa , Egypt
Kaustubha Mohanty, India
Subrata Mondal , India
José Morillo, Spain
Giovanni Morrone , Italy
Ahmed Mourran, Germany
Nagaraju Mupparapu , USA
Markus Muschen, USA
Benjamin Mwashote , USA
Mallikarjuna N. Nadagouda , USA
Lutfun Nahar , United Kingdom
Kamala Kanta Nanda , Peru
Senthilkumar Nangan, Thailand
Mu. Naushad , Saudi Arabia
Gabriel Navarrete-Vazquez , Mexico
Jean-Marie Nedelec , France
Sridhar Goud Nerella , USA
Nagatoshi Nishiwaki , Japan
Tzortzis Nomikos , Greece
Beatriz P. P. Oliveira , Portugal
Leonardo Palmisano , Italy
Mohamed Afzal Pasha , India
Dario Pasini , Italy
Angela Patti , Italy
Massimiliano F. Peana , Italy
Andrea Penoni , Italy
Franc Perdih , Slovenia
Jose A. Pereira , Portugal
Pedro Avila Pérez , Mexico
Maria Grazia Perrone , Italy
Silvia Persichilli , Italy
Thijs A. Peters , Norway
Christophe Petit , France
Marinos Pitsikalis , Greece
Rita Rosa Plá, Argentina
Fabio Polticelli , Italy
Josefina Pons, Spain
V. Prakash Reddy , USA
Thathan Premkumar, Republic of Korea
Maciej Przybyłek , Poland
María Quesada-Moreno , Germany
Maurizio Quinto , Italy
Franck Rabilloud , France
C.R. Raj, India
Sanchayita Rajkhowa , India
Manzoor Rather , India
Enrico Ravera , Italy
Julia Revuelta , Spain
Muhammad Rizwan , Pakistan
Manfredi Rizzo , Italy
Maria P. Robalo , Portugal
Maria Roca , Spain
Nicolas Roche , France
Samuel Rokhum , India
Roberto Romeo , Italy
Antonio M. Romerosa-Nievas , Spain
Arpita Roy , India
Eloy S. Sanz P rez , Spain
Nagaraju Sakkani , USA
Diego Sampedro , Spain
Shengmin Sang , USA

Vikram Sarpe , USA
Adrian Saura-Sanmartin , Spain
St phanie Sayen, France
Ewa Schab-Balcerzak , Poland
Hartwig Schulz, Germany
Gulaim A. Seisenbaeva , Sweden
Serkan Selli , Turkey
Murat Senturk , Turkey
Beatrice Severino , Italy
Sunil Shah Shah , USA
Ashutosh Sharma , USA
Hideaki Shirota , Japan
Cl udia G. Silva , Portugal
Ajaya Kumar Singh , India
Vijay Siripuram, USA
Ponnurengam Malliappan Sivakumar ,
Japan
Tom s Sobrino , Spain
Raquel G. Soengas , Spain
Yujiang Song , China
Olivier Soppera, France
Radhey Srivastava , USA
Vivek Srivastava, India
Theocharis C. Stamatatos , Greece
Athanasios Stavrakoudis , Greece
Darren Sun, Singapore
Arun Suneja , USA
Kamal Swami , USA
B.E. Kumara Swamy , India
Elad Tako , USA
Shoufeng Tang, China
Zhenwei Tang , China
Vijai Kumar Reddy Tangadanchu , USA
Franco Tassi, Italy
Alexander Tatarinov, Russia
Lorena Tavano, Italy
Tullia Tedeschi, Italy
Vinod Kumar Tiwari , India
Augusto C. Tome , Portugal
Fernanda Tonelli , Brazil
Naoki Toyooka , Japan
Andrea Trabocchi , Italy
Philippe Trens , France
Ekaterina Tsipis, Russia
Esteban P. Urriolabeitia , Spain




Toyonobu Usuki , Japan
Giuseppe Valacchi , Italy
Ganga Reddy Velma , USA
Marco Viccaro , Italy
Jaime Villaverde , Spain
Marc Visseaux , France
Balaga Viswanadham , India
Alessandro Volonterio , Italy
Zoran Vujcic , Serbia
Chun-Hua Wang , China
Leiming Wang , China
Carmen W ngler , Germany
Wieslaw Wiczkowski , Poland
Bryan M. Wong , USA
Frank Wuest, Canada
Yang Xu, USA
Dharmendra Kumar Yadav , Republic of
Korea
Maria C. Yebra-Biurrun , Spain
Dr Nagesh G Yernale, India
Tomokazu Yoshimura , Japan
Maryam Yousaf, China
Sedat Yurdakal , Turkey
Shin-ichi Yusa , Japan
Claudio Zaccone , Italy
Ronen Zangi, Spain
John CG Zhao , USA
Zhen Zhao, China
Antonio Zizzi , Italy
Mire Zloh , United Kingdom
Grigoris Zoidis , Greece
Deniz  AHİN , Turkey

Contents





Adsorption of Indigo Carmine onto Chemically Activated Carbons Derived from the Cameroonian Agricultural Waste *Garcinia cola* Nut Shells and Desorption Studies

Idris-Hermann Tiotsop Kuete , Raoul Donald Tchui fon Tchui fon , Aurelien Bopda, Christian Sadeu Ngakou, George Ndifor-Angwafor Nche , and Solomon Gabche Anagho 
Research Article (19 pages), Article ID 1236621, Volume 2022 (2022)


Flash Pyrolysis Experiment on *Albizia odoratissima* Biomass under Different Operating Conditions: A Comparative Study on Bio-Oil, Biochar, and Noncondensable Gas Products

C. Sowmya Dhanalakshmi , S. Kaliappan, H. Mohammed Ali, S. Sekar, Melvin Victor Depoures , Pravin P. Patil, Baskara Sethupathy Subbaiah, S. Socrates, and Habtewolde Ababu Birhanu 
Research Article (9 pages), Article ID 9084029, Volume 2022 (2022)



Porous Carbons Derived from Desiliconized Rice Husk Char and Their Applications as an Adsorbent in Multivalent Ions Recycling for Spent Battery

Yating Sun, Geng Su , Zhaocai He, Yuan Wei, Jinbo Hu , Huaifei Liu , and Gonggang Liu 
Research Article (12 pages), Article ID 8225088, Volume 2022 (2022)








Amino Acid-Doped Polyaniline Nanotubes as Efficient Adsorbent for Wastewater Treatment

Zhao Zhao, Yimin Yang, Longfei Xu, Zihan Qiu, Ziheng Wang, Yongfeng Luo, and Kun Du 
Research Article (12 pages), Article ID 2041512, Volume 2022 (2022)







Co-pyrolysis of Hardwood Combined with Industrial Pressed Oil Cake and Agricultural Residues for Enhanced Bio-Oil Production

P. Madhu , L. Vidhya, S. Vinodha, Shiny Wilson, S. Sekar, Pravin P. Patil, S. Kaliappan, and S. Prabhakar 
Research Article (12 pages), Article ID 9884766, Volume 2022 (2022)

Optimization by Response Surface Methodology of Biodiesel Production from *Podocarpus falcatus* Oil as a Cameroonian Novel Nonedible Feedstock

Serges Bruno Lemoupi Ngomade , Raoul Donald Tchui fon Tchui fon , Rufis Fregue Tiegam Tagne , Meme Laloi Tongnang Ngueteu , Hugues Mahouli Patai , George Ndifor-Angwafor Nche , and Solomon Gabche Anagho 
Research Article (14 pages), Article ID 3786602, Volume 2022 (2022)

Optimized Removal of Hydroquinone and Resorcinol by Activated Carbon Based on Shea Residue (*Vitellaria paradoxa*): Thermodynamics, Adsorption Mechanism, Nonlinear Kinetics, and Isotherms

Liouna Adoum Amola , Theophile Kamgaing , Rufis Fregue Tiegam Tagne , Cyrille Donlifack Atemkeng , Idris-Hermann Tiotsop Kuete , and Solomon Gabche Anagho 
Research Article (15 pages), Article ID 1125877, Volume 2022 (2022)

Research Article

Adsorption of Indigo Carmine onto Chemically Activated Carbons Derived from the Cameroonian Agricultural Waste *Garcinia cola* Nut Shells and Desorption Studies

Idris-Hermann Tiotsop Kuete ¹, Raoul Donald Tchuifon Tchuifon ^{1,2}, Aurelien Bopda,¹
Christian Sadeu Ngakou,¹ George Ndifor-Angwafor Nche ¹ and
Solomon Gabche Anagho ¹

¹Materials and Process Engineering Team (MPET),

Research Unit of Noxious Chemistry and Environmental Engineering (RUNOCHEE), Department of Chemistry,
Faculty of Science, University of Dschang, P.O. Box 67, Dschang, Cameroon

²Laboratory of Energy Materials Modeling and Method, Department of Process Engineering,
National Higher Polytechnic School of Douala, University of Douala, Douala, Cameroon

Correspondence should be addressed to Solomon Gabche Anagho; sg_anagho@yahoo.com

Received 11 May 2022; Revised 25 June 2022; Accepted 5 July 2022; Published 31 August 2022

Academic Editor: Gonggang Liu

Copyright © 2022 Idris-Hermann Tiotsop Kuete et al. This is an open access article distributed under the Creative Commons Attribution License, which permits unrestricted use, distribution, and reproduction in any medium, provided the original work is properly cited.

In the quest for a sustainable environment and clean water resources, the efficacy of activated carbons synthesized from *Garcinia cola* nut shells impregnated with KOH (CBK_{1/1}) and ZnCl₂ (CBZ_{1/1}) for the adsorption of indigo carmine (IC) dye was studied using the batch technique. The prepared activated carbons were characterized using iodine number, elemental analysis, scanning electron microscopy (SEM), FTIR spectroscopy, powder X-ray diffraction (XRD), TGA/DTA, Boehm titration, and pH at point of zero charge. The elemental analysis showed a high percentage of carbon in both activated carbons (ACs). FTIR and Boehm titration analysis indicated the presence of several functional groups on the surfaces of both ACs which could influence the adsorption of IC. The primary adsorption mechanisms involved electrostatic interaction, hydrogen bonds formation, and π - π interactions. Maximum adsorption capacity values obtained using the Fritz-Schlunder III three-parameter model were 19.019 mg·g⁻¹ and 18.299 mg·g⁻¹ for CBK_{1/1} and CBZ_{1/1}, respectively. The Fritz-Schlunder model exponent m_{FS} of value less than 1 showed that the adsorption of IC by the ACs occurred on heterogeneous surfaces. Positive values of ΔQ obtained by the linear and nonlinear forms of the Temkin model indicate the exothermic character of the adsorption process.

1. Introduction

Nowadays, several industries discharge their colored effluents containing synthetic dyes into aquatic environments [1]. These dyes are considered as chief contaminants in water since they pose serious threats to human beings and aquatic organisms [2]. Wastewater is often discharged into rivers and lakes or infiltrates into aquifers, where it can affect the quality of freshwater supplies. Globally, over 80% of the wastewater sent into the environment without treatment causes negative consequences for the marine environment

[3]. Water pollution by dyes is becoming a major environmental problem since colouring agents cause significant environmental damage to both human health and aquatic organisms. These dyes are highly toxic, carcinogenic, mutagenic, teratogenic, and stable during aerobic degradation [4]. The discharges of industrial wastewater containing very low concentrations of dyes reduce light penetration through the water surface, precluding photosynthesis of the aqueous flora.

Indigo carmine dye is used in the textile industry for dyeing clothes and in cosmetics, plastics, and paper mills, while in medicine, it is used as an aid to diagnosis [5]. Indigo

carmines is considered in the class of the highly toxic indigoid dyes. Its contact with the skin can cause irritation, while with the eye, it can cause both irritation and permanent injury to the cornea and conjunctiva [6].

Consumption of this dye at high concentration has also been shown to be fatal, as it is carcinogenic by nature and can cause reproductive, developmental, neurological, and acute toxicity [6]. It has also been reported to cause mild-to-severe hypertension and cardiovascular and respiratory effects [6]. According to the World Health Organization standards, the limit concentration of indigo carmine is $0.005 \text{ mg}\cdot\text{L}^{-1}$ [7]. Thus, indigo carmine is not only a noxious substance to aquatic life but also to us humans. Therefore, the elimination of this type of dye in wastewater or at the exit of industries becomes a major concern.

Several techniques have been discussed in the literature for the removal of dyes from water and wastewater. Among these techniques, adsorption is considered the most economically favorable among those available, such as membrane separation, oxidation, and irradiation, because of its high removal efficiency, low operation cost, and its ability to separate a wide range of contaminants from industrial effluents [8].

Amongst the adsorbents used in the adsorption processes, one of the most widespread for the removal of contaminants from water is activated carbon (AC) [9,10] which, due to its pore structure and various functional groups on its surface, provides exceptional adsorption capacity. Different activating carbons can be manufactured by exploiting a wide variety of carbonaceous precursors such as coal, petroleum, peat, wood, and agricultural wastes [11], resulting in the production of a variety of adsorbents with different characteristics and qualities.

The use of biomass waste for the preparation of porous activated carbon has increased considerably in recent years. Some of the residual biomasses used for the manufacture of activated carbons are coffee waste [9], tucumã seeds [10], Ayous sawdust and Cucurbitaceae peelings [12], rice and coffee husks [13], olives stones and cotton cake [14], *Vitellaria paradoxa* [15], and rice hull and tamarind (*T. indica*) seeds [16].

This work had a double interest: valorizing the residues coming from a Cameroonian biomass to prepare activated carbons using chemical treatment techniques and testing their performance in the water treatment. In this work, the residual biomass, *Garcinia cola* nut shells from Cameroon, was proposed as a raw material for the development of activated carbons by chemical activation using KOH and ZnCl_2 , in order to recycle these wastes that are currently generated in large quantities and are of little use in Cameroon [17].

In this research, the feasibility of producing activated carbons suitable for the efficient removal of indigo carmine was demonstrated.

Specifically, this research was subdivided into three parts:

- (i) Production of activated carbons from *Garcinia cola* nut shells by chemical activation with KOH and ZnCl_2

- (ii) Application of the activated carbons as adsorbents for the removal of indigo carmine in aqueous solution and evaluation of their efficacy
- (iii) Demonstration of the reusability of each adsorbent by studying desorption

2. Materials and Methods

2.1. Preparation of Activated Carbons. ACs were produced by the following procedure: first, 200 g of particles of dried *Garcinia cola* nut shell (CB) with diameters varying between 250 and 1000 μm was blended in a 1 : 1 weight ratio with the activating agent KOH or ZnCl_2 . Each resulting paste was dried and placed in a porcelain crucible with lid and introduced into an electric furnace of mark ISUNU and heated from the ambient temperature up to 400°C , using a heating rate of $5^\circ\text{C}\cdot\text{min}^{-1}$ in absence of CO_2 , H_2O , O_2 , and N_2 gases. The temperature of the furnace was kept fixed at the maximum temperature of 400°C for 1 hour. It was then allowed to cool to room temperature, and the activated carbon obtained was washed with distilled water until the excess activating agent was removed. The samples were coded as $\text{CBK}_{1/1}$ and $\text{CBZ}_{1/1}$, respectively, according to KOH and ZnCl_2 used as the activating agent.

2.2. Characterization. Activated carbons were characterized to determine the surface functional groups by Fourier-transform infrared (FTIR) spectroscopy using a Nicolet iS5 FTIR Spectrometer. The physical and chemical characteristics of both activated carbons were found out by ASTM methods. Thermogravimetric analysis of both activated carbons was performed on STA 409 CD thermos-balance with a heating rate of $10^\circ\text{C}\cdot\text{min}^{-1}$ in a nitrogen flow and temperature range of $50\text{--}1500^\circ\text{C}$. Elemental analysis of both activated carbons was determined using CHNS elemental analyses from the HEKAtech CHNS Analyzer. Scanning electron images of the two activated carbons were obtained using a scanning electron microscope, furnished by sputter coater analysis. Crystalline structure of the activated carbons was analyzed by X-ray diffraction (XRD) analysis using a STOE Stadi-p X-ray powder diffractometer (STOE & Cie GmbH, Darmstadt, Germany). Figure 1 shows the preparation and characterization steps for the different activated carbons.

2.3. Adsorbate. Stock solution of indigo carmine at $500 \text{ mg}\cdot\text{L}^{-1}$ was prepared by dissolving a previously calculated mass of 123.75 mg of the latter in a 250 mL volumetric flask containing 100 mL of distilled water, homogenize until the pollutant is completely dissolved, and then make up to the mark and store in a dark place. The working indigo carmine solution was prepared by diluting the stock solution with distilled water. Figure 2 shows the 3D structure of indigo carmine.

2.4. Adsorption and Desorption Studies. Batch adsorption studies were carried out at room temperature by mechanical agitation at a constant speed of 200 rpm to deduce the

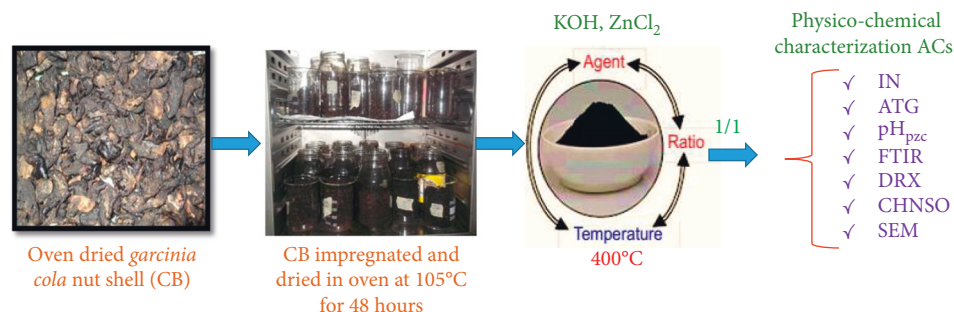


FIGURE 1: Preparation and characterization of activated carbons.

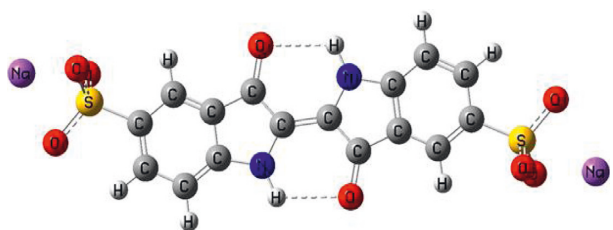


FIGURE 2: 3D structure of indigo carmine ($C_{16}H_8N_2Na_2O_8S_2$).

optimum pH, contact time, adsorbent mass, initial indigo carmine concentration, and the effect of ionic strength. For each run, 20 mL of indigo carmine dye solution of known initial concentration varying between 30 and 100 mg L⁻¹ was treated with 100 mg each of the activated carbons, CBK_{1/1} and CBZ_{1/1}, at optimum pH. The pH value of each solution was adjusted by addition of 0.1 M solution of HCl or NaOH. After agitation, the solution was filtered using the Whatman no.1 filter paper, and the filtrate was analyzed to obtain the residual concentration of indigo carmine using a UV/Vis spectrophotometer (Jenway, model 6715) at a wavelength (λ) of 610 nm. Similar measurements were carried out by varying the pH of the solution (2–8), contact time (5–120 min), adsorbent mass (50–400 mg), and ionic strength varying NaCl concentration (0.01–0.06 mol·L⁻¹). The amount of dye adsorbed (Q_e) and the percentage removal (%ads) of dye were calculated using the following expressions:

$$Q_e = \frac{(C_0 - C_e)}{m} \cdot V, \quad (1)$$

$$\%ads = \frac{(C_0 - C_e)}{C_0} \cdot 100,$$

where C_0 is the initial concentration of the dye, C_e is the concentration of the dye at the equilibrium time, V is the volume of the adsorbate solution, and m is the mass of the adsorbent.

For the desorption studies, 400 mg of each adsorbent was mixed in a flask with 100 mL of indigo carmine dye solution at an initial concentration of 50 mg·L⁻¹. Mixtures were stirred at a constant speed of 200 rpm for 80 min. After stirring, suspensions were filtered and filtrates were analyzed by measuring absorbance using a UV-Visible spectrophotometer. Indigo carmine loaded with each adsorbent was collected after filtration and was dried in an oven at 105°C, and 50 mg of each of these materials was contacted with

10 mL of desorption solutions of 4×10^{-2} mol·L⁻¹ of NaOH or H₂SO₄ and 10 mL of H₂O. The mixtures were stirred at a constant speed of 200 rpm for 80 min. After stirring, suspensions were filtered and filtrates were analyzed by measuring absorbance using a UV-Visible spectrophotometer. Desorption percentages (%des) were calculated by the following equation [18, 19]:

$$\%des = \frac{C_f - C_r}{C_f} \cdot 100, \quad (2)$$

where C_f (mg·L⁻¹) is the initial concentration of dyes loaded with each adsorbent and C_r (mg·L⁻¹) is the final concentration of dyes loaded with each adsorbent.

2.5. Equilibrium and Kinetic Studies. In this work, four two-parameter adsorption isotherm models (Langmuir, Freundlich, Temkin, and Halsey), one three-parameter model (Fritz–Schlunder III), and five kinetic models (pseudo-first order, pseudo-second order, Avrami kinetics, intraparticle diffusion, and Boyd) were tested. In the aim to study the mechanisms of adsorption process and the equilibrium relationship between adsorbents and adsorbate, linear and nonlinear models were modelled using Microsoft Excel 2013 and plotted using OriginPro 9, 64 bit.

2.6. Error Functions. In order to determine the best fitting of nonlinear models, four different error functions were examined by minimizing the respective error functions across the concentration and time range studied. “SOLVER ADD-IN” of Microsoft’s spread sheet was used. Expressions of the error functions are given as follows [20]:

$$\chi^2 = \sum_{i=1}^N \frac{(Q_{e, \text{exp}} - Q_{e, \text{cal}})^2}{Q_{e, \text{cal}}^2},$$

$$RMSE = \sqrt{\frac{1}{n-2} \sum_{i=1}^N (Q_{e, \text{exp}} - Q_{e, \text{cal}})^2}, \quad (3)$$

$$SCE = \sum_{i=1}^N (Q_{e, \text{exp}} - Q_{e, \text{cal}})_i^2,$$

$$r^2 = \frac{\sum_{i=1}^N (Q_{e, \text{cal}} - Q_{m \text{ exp}})^2}{\sum_{i=1}^N (Q_{e, \text{cal}} - Q_{m \text{ exp}})^2 + (Q_{e, \text{cal}} - Q_{m \text{ exp}})^2},$$

where $Q_{e,exp}$ and $Q_{e,cal}$ ($\text{mg}\cdot\text{g}^{-1}$) are the equilibrium capacity of adsorption obtained from the experiment and by calculating from the model, respectively, and N is the number of data points.

3. Results and Discussion

3.1. Characterization of Adsorbent

3.1.1. Physical and Chemical Characteristics of ACs and Elemental Analysis. Physical and chemical properties of ACs CBK_{1/1} and CBZ_{1/1} activating are reported in Table 1. pH_{pzc} values show that surfaces of the different ACs are dominated by the basic functional group. Bulk densities of the different ACs shown in Table 1 are higher than the limit of $0.25\text{ g}\cdot\text{cm}^{-3}$ according to American Water Works Association. Higher density gives a higher volume activity and normally indicates a better AC quality. Bulk densities of different ACs provide information on the microcrystalline structure and strong interlinking bonds. Moisture content values of different ACs obtained as presented in Table 1 are within the norm, since the traditional value for moisture content ranges from 1 to 5% by mass. Iodine number of the ACs obtained in this work is higher than limit ($500\text{ mg}\cdot\text{g}^{-1}$), thus showing the good quality of the ACs obtained, reflecting the presence of micropores. Methylene blue number obtained and presented in Table 1 reflects the presence of mesopores on the surface of the ACs.

In Table 1, the quantity of basic groups is higher than the acidic groups on the surface of CBK_{1/1} and CBZ_{1/1} activated carbons, indicating that KOH and ZnCl_2 as activating agents for production of activated carbons by *Garcinia cola* nut shells generate carbons with higher amount of basic functional groups on their surface. The ratios of the sum of the basic groups divided by the sum of the acid groups are 1.269 (for CBK_{1/1}) and 1.253 (for CBZ_{1/1}), indicating that CBK_{1/1} would be more basic than CBZ_{1/1}, as confirmed by the total basicity of CBK_{1/1} ($3.08\text{ meq}\cdot\text{g}^{-1}$) and CBZ_{1/1} ($3.045\text{ meq}\cdot\text{g}^{-1}$). These results follow the pH_{pzc} values, which imply that, in AC, having a higher ratio of total basic groups divided by total acid group leads to higher pH_{pzc} values. Taking into account the results of the Boehm titration and the pH_{pzc} , it can be stated that these results are in total agreement.

Elemental analyses of CBK_{1/1} and CBZ_{1/1} are presented in Table 1. The prepared ACs have high percentages of carbon, which in itself is a fact that justifies the use of *Garcinia cola* nut shells as a carbon source. The percentages of nitrogen and oxygen are consistent with the amount of functional groups present on activated carbons CBK_{1/1} and CBZ_{1/1}.

3.1.2. Fourier-Transform Infrared (FTIR) Spectroscopy.

Figure 3 shows that the FTIR spectra of CBK_{1/1} and CBZ_{1/1} are very similar to each other and different from that of the raw material, indicating that the activating agent did not influence the surface chemical group of the AC. The FTIR identified chemical groups on the surface of both ACs such as the broad peak around 3349 cm^{-1} for CBK_{1/1} and CBZ_{1/1} which are related to OH group stretching [9]. The band obtained approximately at 1587 cm^{-1} in both ACs indicates

the presence of C=O stretching vibration of lactone and carbonyl groups [17]. This band can also be attributed to the C=C stretching vibration of alkene or aromatic ring [17]. The band around 1374 cm^{-1} corresponds to the C-H bending vibration or C-N stretching vibration of amines or amides of nitroaromatic compounds ($-\text{NO}_2$).

3.1.3. X-Ray Diffraction Analysis (XRD). Figure 4 shows the XRD of ACs. In this figure, the absence of a sharp peak reveals that both ACs prepared from *Garcinia cola* nut shells are mainly amorphous structure, which is an advantageous property for well-defined porous adsorbents. However, the small sharp peak presented by the X-ray graph of CBZ_{1/1} ($2\theta = 28^\circ$) indicates very low crystallinity may be due to the presence of zinc oxide and zinc carbide [17].

3.1.4. Thermogravimetric Analysis (TGA/DTA). TGA is performed to investigate the thermal stability of AC. The weight loss curves for CBK_{1/1} and CBZ_{1/1} as can be seen on the TG curves for both ACs are very similar (Figure 5).

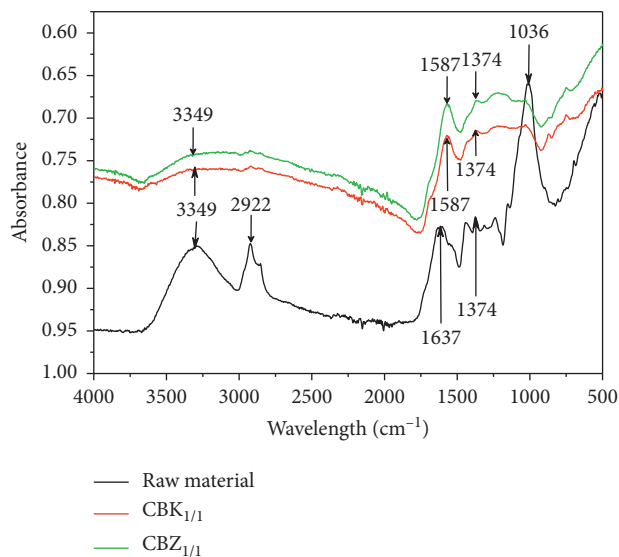
In Figure 5, the TGA/DTA curves of both ACs suggest three typical distinct weight losses. The first weight loss of 2.016% for CBK_{1/1} and 4.314% for CBZ_{1/1} at temperature below 200°C corresponds to the elimination of the water content (physisorption phenomenon) in the ACs, which means that there is still physisorbed water remaining in the micropores and mesopores of the various activated carbons. The second weight loss of 20.413% for CBK_{1/1} and 26.712% for CBZ_{1/1} within the temperature range of 200°C – 900°C may be due to the predominant decomposition of the surface chemical groups of the different ACs and the formation of H_2O , CO, and CO_2 during the calcination/activation process. In this temperature range, the decomposition of the lactone functions usually takes place between 350 and 600°C .

The third weight loss is secondary degassing which is observed above 900°C , and the resulting intermediate product linked to the carbon skeleton of the ACs involves further decomposition through the formation of residual products such as tar and oxides which are subsequently removed. Of the two ACs, the less thermally stable is CBZ_{1/1}, as its total mass loss is higher (37.04%), and the more thermally stable is CBK_{1/1} with a lower total mass loss of 30.546%. According to the DTA curve, the thermal decomposition of the two activated carbons is dominated by an endothermic process (0°C – 1250°C).

3.1.5. Scanning Electron Microscopic Images. The textural surface properties of CBK_{1/1} and CBZ_{1/1} were investigated by SEM (Figure 6). According to this figure, SEM images showing the prepared ACs CBK_{1/1} and CBZ_{1/1}, respectively, illustrate an irregular and heterogeneous surface morphology with a porous structure developed and fragmented in different sizes [17]. However, it can be seen on the micrographs that the external surface of the ACs shows cracks and crevices [17]. These pores result not only from the evaporation of the chemical reagents (KOH and ZnCl_2) during carbonization, leaving empty spaces, but also from the

TABLE 1: Elemental analysis, total acidity and basicity, and physical and chemical properties.

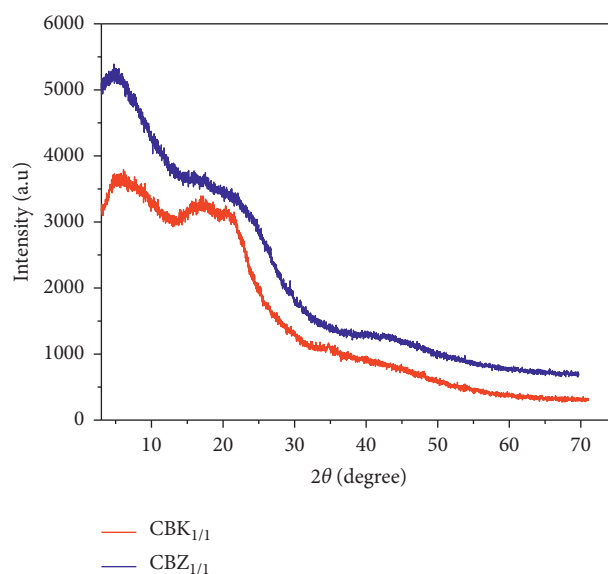
AC	C%	H%	N%	S%	O% _(diff)	Others (%)	Moisture content (%)	Bulk density (g·cm ⁻³)	I_I (mg·g ⁻¹)	I_{MB} (mg·g ⁻¹)	Total acidity (meq·g ⁻¹)	Total basicity (meq·g ⁻¹)	pH _{pzc}
CBK _{1/1}	71.877	3.874	2.133	0	19.348	2.768	2.8	0.750	1065	73.177	2.428	3.08	8.324
CBZ _{1/1}	67.807	3.693	2.082	0	24.206	2.212	3.2	0.825	970.82	72.590	2.43	3.045	7.589

FIGURE 3: FTIR spectra of activated carbon (CBK_{1/1} and CBZ_{1/1}) and raw material.

degradation of the lignocellulosic material during carbonization and subsequent removal of volatile materials leaving samples with pores [17].

3.2. Batch Studies

3.2.1. Effect of pH. From Figure 7, the results show that maximum adsorption capacity is obtained for pH 2 and adsorption is favoured for pH < pH_{pzc}. We observe that the adsorption capacity decreases with increasing pH from 8.354 to 3.159 mg·g⁻¹ and from 7.960 to 2.876 mg·g⁻¹ for ACs CBK_{1/1} and CBZ_{1/1}, respectively. It is generally known that due to the abundant presence of H⁺ ions, the anionic dyes such as IC are preferentially adsorbed by the adsorbent at lower pH [21]. At that particular pH (=2) (pH < pH_{pzc}), protons are advantageously available for protonation of the AC surface, which increases the electrostatic interaction between the now positively charged adsorbent sites and the negatively charged sites or nucleophilic sites (-SO₃⁻) of indigo carmine. Similar results have also been observed by several authors for the adsorption of IC [22, 23]. At the same time, IC is an anionic dye with two sulphonic acid groups and two aromatic rings; this is probably the other reason for its high removal efficiency at the low pH. A similar trend was

FIGURE 4: XRD of activated carbons: CBK_{1/1} and CBZ_{1/1}.

reported by Zhao et al. [24] where they use amino acid-doped polyaniline nanotubes as adsorbent for wastewater treatment. However, increased pH (pH > pH_{pzc}) of the adsorbate makes it more soluble and the negative charges on the surface of the ACs increase the electrostatic repulsion force between the adsorbates (sulphonic functional group of the pollutants) and the -OH groups on the surface of the ACs due to the increase in hydroxyd ions. The electrostatic repulsion force between indigo carmine and the adsorbent promotes the decrease in adsorption capacity. A similar result was obtained from the adsorption of thymol blue onto powdered activated carbons from *Garcinia cola* nut shells impregnated with H₃PO₄ and KOH [25].

3.2.2. Effect of Contact Time. Figure 8 shows the evolution of adsorption capacity of indigo carmine as a function of the contact time at room temperature. Rapid adsorption of IC takes place in the first 5 minutes for the two ACs; this rapid phase may be attributed to rapid dye attachment on the ACs surface due to either the large amount of surface area available or to the availability of more adsorption vacant sites at the initial stage. Thereafter, the rate of adsorption decreased gradually with the progress of adsorption within 5–80 minutes for the two ACs and reached equilibrium in about 80 minutes. The adsorption capacities at these

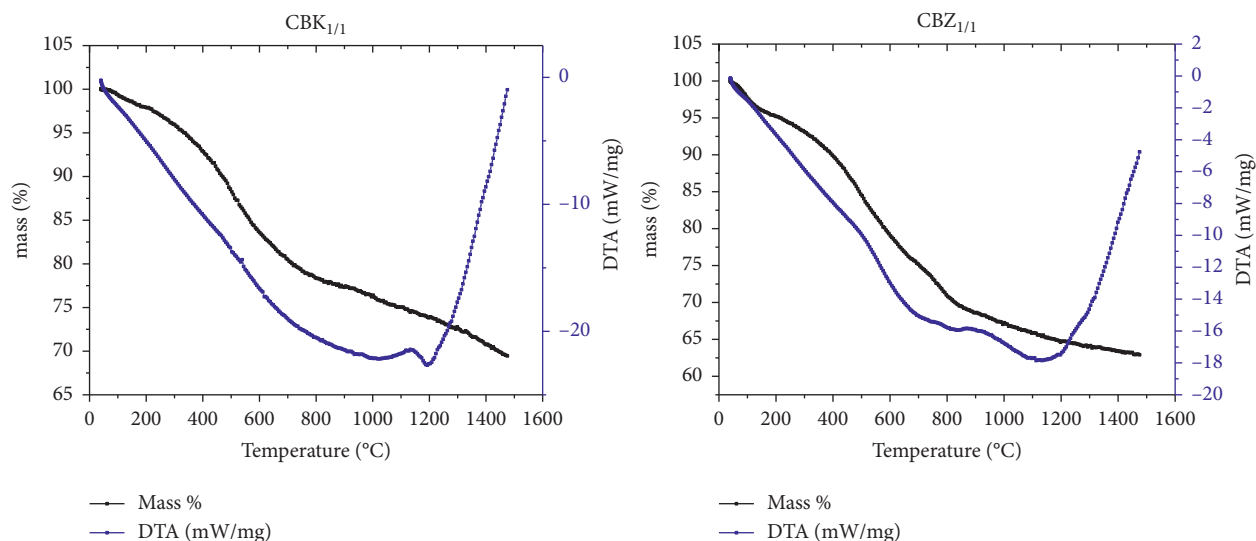
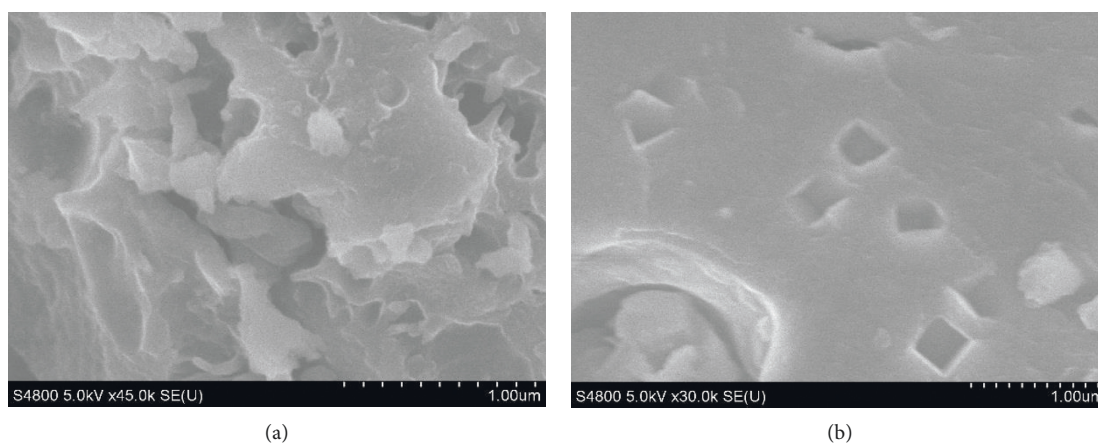


FIGURE 5: Thermogravimetric analysis (TGA) and differential thermogravimetric curves (DTA) of $CBK_{1/1}$ and $CBZ_{1/1}$.



(a) (b)

FIGURE 6: SEM images of $CBK_{1/1}$ (a) and $CBZ_{1/1}$ (b).

equilibrium points are $8.60593 \text{ mg}\cdot\text{g}^{-1}$ $CBK_{1/1}$ and $8.03346 \text{ mg}\cdot\text{g}^{-1}$ $CBZ_{1/1}$. This can be explained by the fact that the available sites for adsorption have been greatly reduced by the indigo carmine molecules already attached there and decrease in the total adsorbent surface area and less available binding sites. The quantities adsorbed can be attributed to the π - π interactions, electrostatic attractions, and formation of hydrogen bonding. In the third phase, there is no significant change in the quantity of dye adsorbed after the equilibrium time due to the saturation of the adsorption active sites by the dye molecules [26].

3.2.3. Effect of Adsorbent Mass. Effect of adsorbent mass on the removal of indigo carmine was studied, and the results of this study are shown in Figure 9. In this figure, the percentage removal of indigo carmine by $CBK_{1/1}$ and $CBZ_{1/1}$ increased as the adsorbent dosage increased. The removal percentage of indigo carmine increased from 76.8 to 97.7% and 75.1 to 92.7% for $CBK_{1/1}$ and $CBZ_{1/1}$, respectively. This

is because the increase in the mass of the adsorbent leads to the increase in the adsorption sites and the contact area of each adsorbent becomes free and available for indigo carmine fixation during the adsorption process. This increase in the mass of each adsorbent further promotes the increase in their adsorption percentage. A similar trend was reported in Hameed et al. [27] for the adsorption of chromotrope dye onto activated carbons obtained from the seeds of various plants.

3.2.4. Effect of Initial Indigo Carmine Concentration. The effect of initial concentration on the adsorption of indigo carmine was investigated of 30 – $100 \text{ mg}\cdot\text{L}^{-1}$. Figure 10 shows the quantity of indigo carmine adsorbed at equilibrium increases with the concentration from 5.814 to $11.349 \text{ mg}\cdot\text{g}^{-1}$ and 5.756 to $10.823 \text{ mg}\cdot\text{g}^{-1}$, respectively, from $CBK_{1/1}$ and $CBZ_{1/1}$. This result can be explained by the π - π interactions, electrostatic attraction, and formation of hydrogen bonding between the dyes and the surface functional groups of

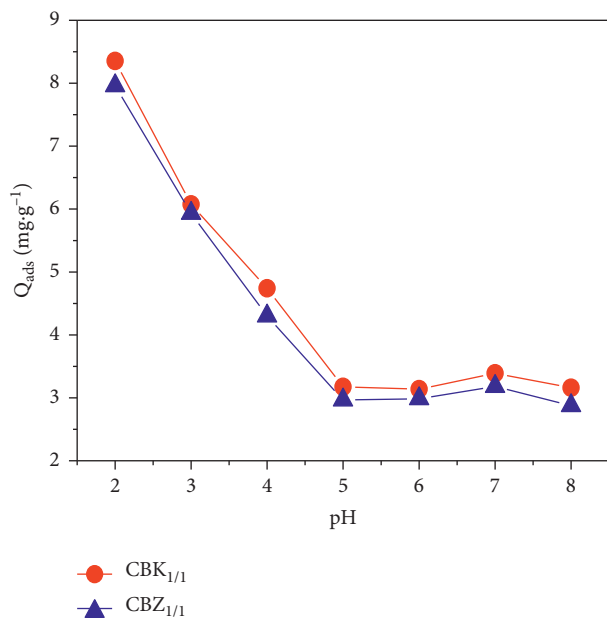


FIGURE 7: Effect of pH solution on the adsorption of indigo carmine. Experimental conditions: $C_0 = 50 \text{ mg}\cdot\text{L}^{-1}$; $m = 100 \text{ mg}$; $V = 20 \text{ mL}$; $t = 80 \text{ min}$; speed = 200 rpm at room temperature.

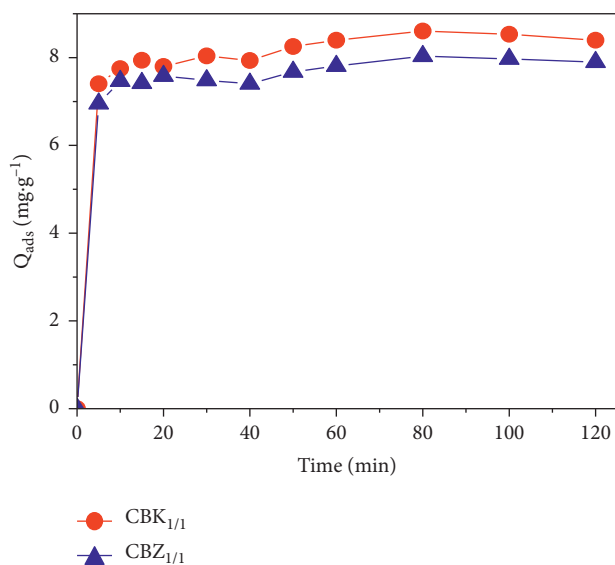


FIGURE 8: Effect of contact time on the adsorption of indigo carmine. Experimental conditions: $C_0 = 50 \text{ mg}\cdot\text{L}^{-1}$; $m = 100 \text{ mg}$; $V = 20 \text{ mL}$; $\text{pH} = 2$; speed = 200 rpm at room temperature.

activated carbons on the one hand and the difference in the pore size of these carbons on the other hand. This can also be explained by the fact that increasing the initial concentration of indigo carmine would increase the driving force of mass transfer and, consequently, the speed at which indigo carmine molecules pass from the solution to the surface of the ACs [28]. In this figure, we observe a saturation of the adsorption sites which is progressively increasing until reaching a plateau caused by the formation of monolayers on the surface of each adsorbent. The isotherm forms of CBK_{1/1}

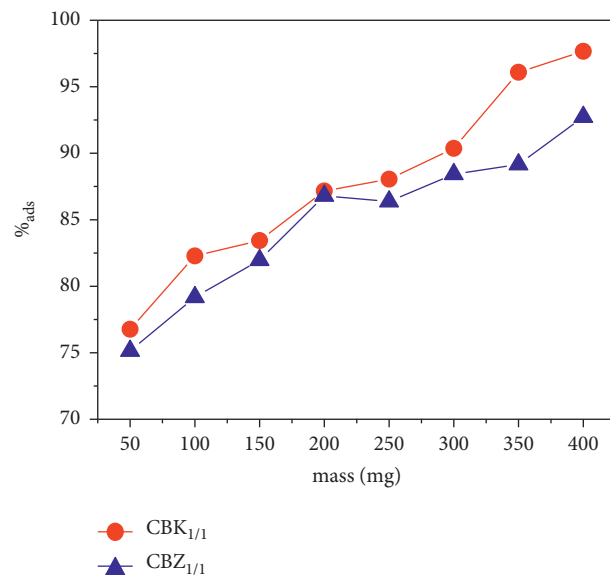


FIGURE 9: Effect of adsorbent dosage on the adsorption of indigo carmine. Experimental conditions: $C_0 = 50 \text{ mg}\cdot\text{L}^{-1}$; $V = 20 \text{ mL}$; $\text{pH} = 2$; $t = 80 \text{ min}$; speed = 200 rpm at room temperature.

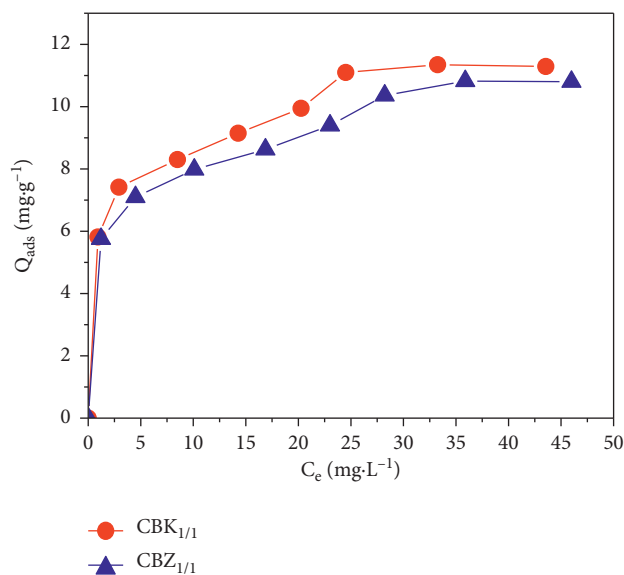


FIGURE 10: Effect of initial concentration on the adsorption of indigo carmine. Experimental conditions: $m = 100 \text{ mg}$; $V = 20 \text{ mL}$; $\text{pH} = 2$; $t = 80 \text{ min}$; speed = 200 rpm at room temperature.

and CBZ_{1/1} have been classified as type L which can be better explained by the Langmuir, Freundlich, and Temkin models that show a relatively high affinity between the adsorbate and adsorbent.

3.2.5. Effect of Ionic Strength. The effect of ionic strength on adsorption of indigo carmine onto CBK_{1/1} and CBZ_{1/1} was studied in the NaCl solutions with concentrations ranging from 0.01 to 0.06 mol.L⁻¹, and the results are illustrated in Figure 11. When the ionic strength increased, the adsorption

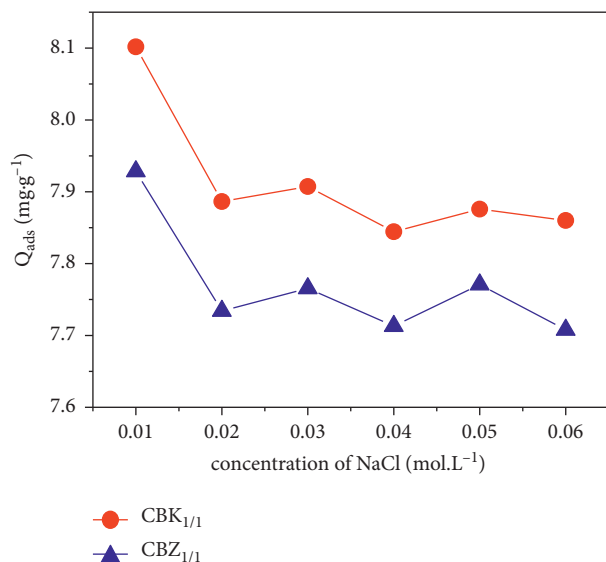


FIGURE 11: Effect of ionic strength on the adsorption of indigo carmine. Experimental conditions: $C_0 = 50 \text{ mg}\cdot\text{L}^{-1}$; $m = 100 \text{ mg}$; $V = 20 \text{ mL}$; $\text{pH} = 2$; $t = 80 \text{ min}$; speed = 200 rpm at room temperature.

TABLE 2: Linear and nonlinear kinetic models.

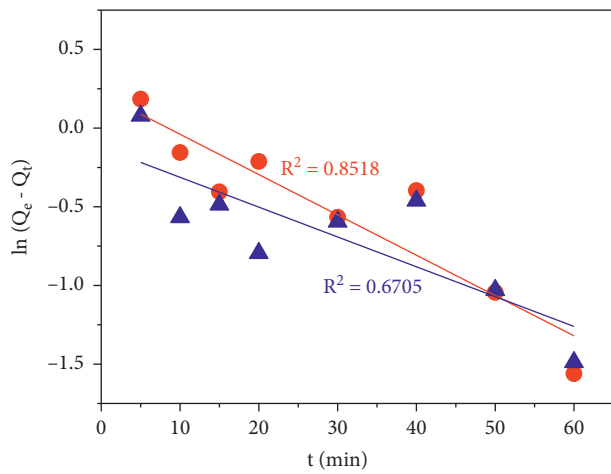
Kinetic models	Linear and nonlinear forms	Equation number	References
Pseudofirst order	$dQ_t/dt = K_1(Q_e - Q_t)$	(4)	[30]
	$\ln(Q_e - Q_t) = \ln Q_e - K_1 t$	(5)	
	$Q_t = Q_e(1 - e^{-K_1 t})$	(6)	
Pseudosecond order	$dQ_t/dt = K_2(Q_e - Q_t)^2$	(7)	[31]
	$t/Q_t = (1/K_2 Q_e^2) + (t/Q_e)$	(8)	
	$Q_t = K_2 Q_e^2 t / (1 + K_2 Q_e t)$ and $h = K_2 Q_e^2$	(9)	
Avrami	$\ln(\ln(Q_{\text{exp}}/Q_{\text{exp}} - Q_t)) = n_{AV} \ln K_{AV} - n_{AV} \ln t$	(10)	[32]
	$Q_t = Q_e \{1 - \exp[-(K_{AV} t)^{n_{AV}}]\}$	(11)	
Intraparticle diffusion	$Q_t = K_{\text{int}} t^{1/2} + C$	(12)	[33]
Boyd	$B_t = -0.4977 - \ln(1 - F)$	(13)	[18]
	$F = (Q_t/Q_e)$	(14)	
	$B = \pi^2 D_i / r^2$	(15)	

capacity of indigo carmine decreased (from 8.102 to 7.860 $\text{mg}\cdot\text{g}^{-1}$ and 7.928 to 7.708 $\text{mg}\cdot\text{g}^{-1}$) for CBK_{1/1} and CBZ_{1/1}, respectively. This result can be explained by the fact that the surface of the ACs becomes difficult to access by indigo carmine when the amount of NaCl salt in solution increases. Consequently, the adsorption capacity of indigo carmine decreases. This result is in agreement with the literature, which reports that when the electrostatic attraction forces between the surface of an adsorbent and the ions of an adsorbate are attractive, the increase in ionic strength thus decreases the adsorption capacity [29].

3.3. Adsorption Kinetics. In this work, the data from the kinetic experiments were analyzed using the different linear and nonlinear kinetic models presented in Table 2.

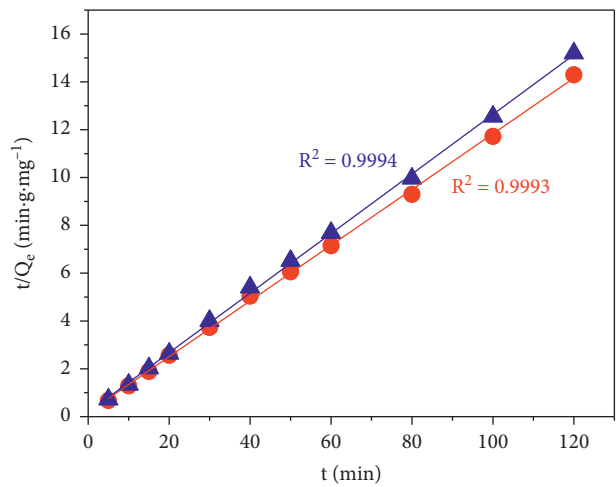
The linear and nonlinear regression graphs of adsorption kinetics for indigo carmine adsorption onto both ACs are shown in Figures 12 and 13, respectively, and the corresponding constants are summarized in Tables 3 and 4.

According to Table 3, the data linear kinetic model indicates that the pseudo-second order model is perfectly appropriate to describe the adsorption kinetics of indigo carmine and on both ACs with a high correlation coefficient ($R^2 \geq 0.9993$). Moreover, it can be observed that the experimental $Q_{e,\text{exp}}$ values obtained during the equilibrium adsorption process are close to the $Q_{e,\text{cal}}$ values calculated from the pseudo-second order model, which indicates that the adsorption of indigo carmine on both ACs is a process dominated by the interaction $\pi-\pi$ [33]. The values of the initial rate of reaction and the reaction half time determined from pseudo-second order model confirm that the accumulation kinetics of indigo carmine is faster at the surface of AC CBK_{1/1} than at the surface of CBZ_{1/1}. Figure 12(d) shows that the plot of $Q_t = f(t^{1/2})$ is not a straight line through the origin of the marker. This indicates that the intraparticle diffusion is not the limiting step or the only rate control step in the adsorption process of indigo carmine on ACs. In this case, other kinetic models can also control the adsorption rate to describe other adsorption mechanisms.



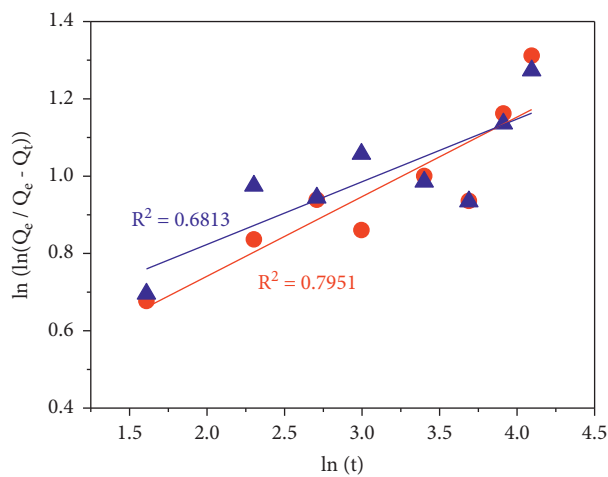
- Experimental CBK_{1/1}
- ▲ Experimental CBZ_{1/1}
- Linear CBK_{1/1} Pseudo first-order
- Linear CBZ_{1/1} Pseudo first-order

(a)



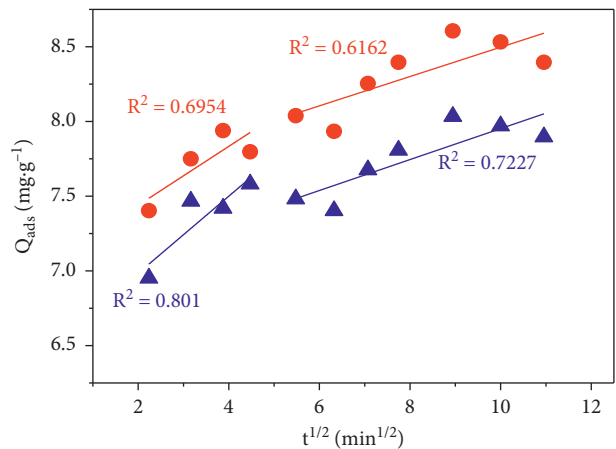
- Experimental CBK_{1/1}
- ▲ Experimental CBZ_{1/1}
- Linear CBK_{1/1} Pseudo second-order
- Linear CBZ_{1/1} Pseudo second-order

(b)



- Experimental CBK_{1/1}
- ▲ Experimental CBZ_{1/1}
- Linear CBK_{1/1} Avrami
- Linear CBZ_{1/1} Avrami

(c)



- Experimental CBK_{1/1}
- ▲ Experimental CBZ_{1/1}
- Linear (CBK_{1/1})₁ Diffusion Intra
- Linear (CBZ_{1/1})₁ Diffusion Intra
- Linear (CBK_{1/1})₂ Diffusion Intra
- Linear (CBZ_{1/1})₂ Diffusion Intra

(d)

FIGURE 12: Continued.

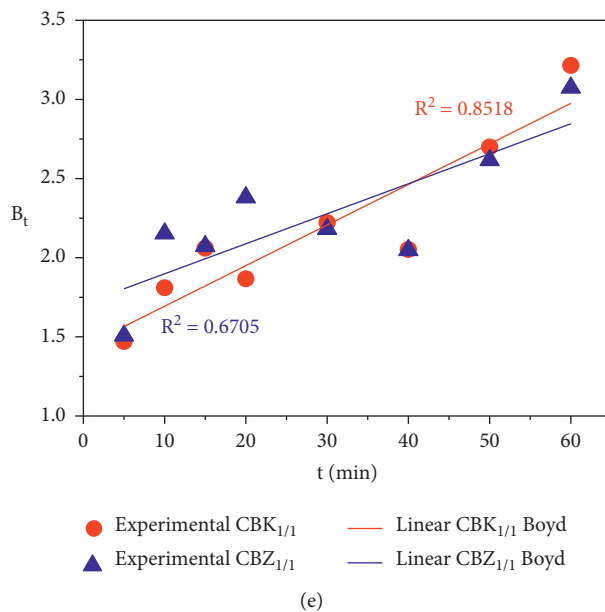


FIGURE 12: Linear regression of adsorption kinetics of (a) pseudofirst order, (b) pseudosecond order, (c) Avrami, (d) intraparticle diffusion, and (e) Boyd.

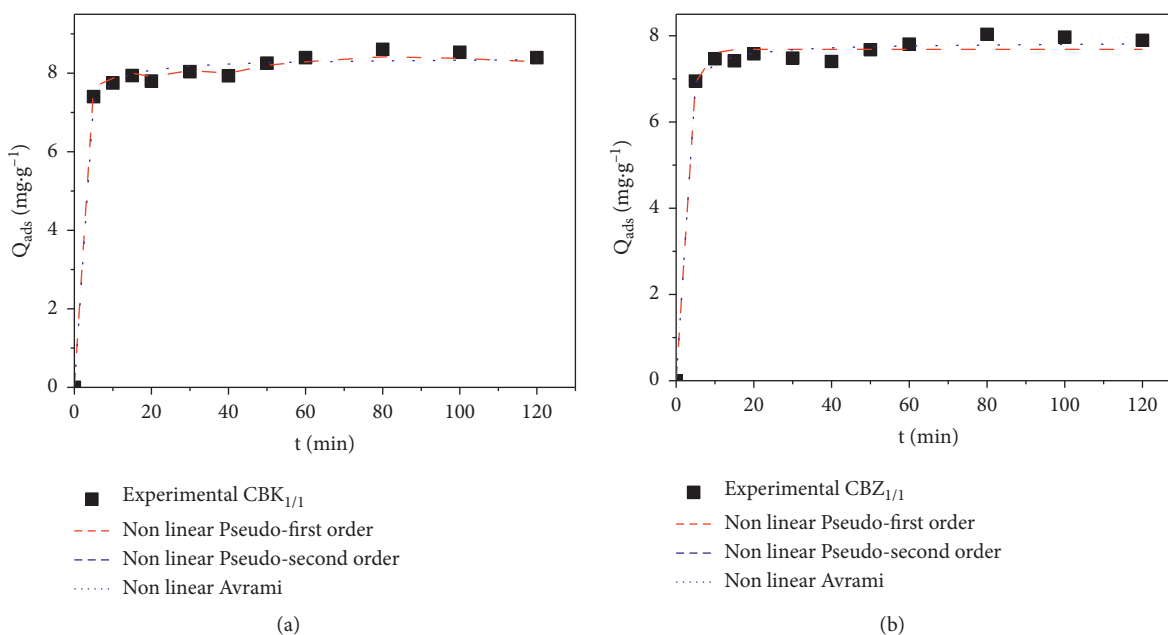


FIGURE 13: Nonlinear regression of adsorption kinetics.

As shown in Figure 12(d), the adsorption of indigo carmine on ACs forms two straight line segments over the entire time interval, meaning that this adsorption process can be controlled by at least two mechanisms occurring simultaneously [33]. This can be attributed to the difference in mass transfer rate between the initial stage and the final stage in ACs. It can be said that at least two types of pores, namely, micropores and mesopores, are involved in the adsorption of indigo carmine. The analysis of Table 4 shows

that the first step is faster than the second since $K_{id1} > K_{id2}$. However, the values of boundary layer thickness C for each linear portion not approaching zero ($C_2 > C_1$) corresponding to the increase in boundary layer thickness indicate that intraparticle diffusion is not the only step in controlling the adsorption rate in all stages [34].

Figure 12(e) shows that the Boyd model lines do not pass through the origin of the graph, meaning that external mass transfer primarily governs the rate controlling step at the

TABLE 3: Linear and nonlinear parameters of kinetic models for adsorption of IC onto ACs.

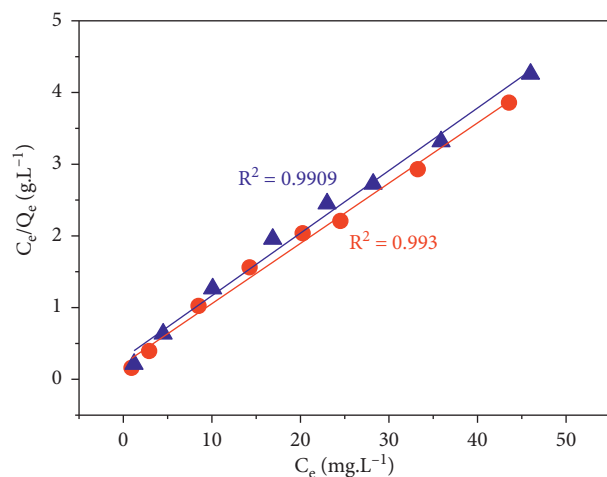
Models	Linear pseudofirst order	Linear pseudosecond order	Linear Avrami	Nonlinear pseudofirst order	Nonlinear pseudosecond order	Nonlinear Avrami
<i>CBK1/1</i>						
Parameter	$Q_{e, cal} = 1.243$ ($\text{mg}\cdot\text{g}^{-1}$)	$Q_{e, cal} = 8.584$ ($\text{mg}\cdot\text{g}^{-1}$)	—	$Q_{e, cal} = 14.243$ ($\text{mg}\cdot\text{g}^{-1}$)	$Q_{e, cal} = 8.396$ ($\text{mg}\cdot\text{g}^{-1}$)	$Q_{e, cal} = 12.121$ ($\text{mg}\cdot\text{g}^{-1}$)
$Q_{e, exp} = 8.605$ ($\text{mg}\cdot\text{g}^{-1}$)	$K_1 = 0.0256$ (min^{-1})	$K_2 = 0.07615$ ($\text{g}\cdot\text{mg}^{-1}\cdot\text{min}^{-1}$)	$K_{Av} = 0.20202$ (min^{-1})	$K_1 = 0.104$ (min^{-1})	$K_2 = 0.151$ ($\text{g}\cdot\text{mg}^{-1}\cdot\text{min}^{-1}$)=	$K_{Av} = 0.104$ (min^{-1})
		$h = 5.6107$ ($\text{mg}\cdot\text{g}^{-1}\cdot\text{min}^{-1}$)	$n_{Av} = -0.20591$		$h = 10,644$ ($\text{mg}\cdot\text{g}^{-1}\cdot\text{min}^{-1}$)	$n_{Av} = 0.079$
r2				0.762	0.752	0.884
χ^2				0.022	0.043	0.020
RMSE				0.141	0.199	0.134
SCE				0.179	0.355	0.163
<i>CBZ1/1</i>						
Parameter	$Q_{e, cal} = 0.8843$ ($\text{mg}\cdot\text{g}^{-1}$)	$Q_{e, cal} = 8.0282$ ($\text{mg}\cdot\text{g}^{-1}$)	—	$Q_{e, cal} = 7.686$ ($\text{mg}\cdot\text{g}^{-1}$)	$Q_{e, cal} = 7.853$ ($\text{mg}\cdot\text{g}^{-1}$)	$Q_{e, cal} = 11.485$ ($\text{mg}\cdot\text{g}^{-1}$)
$Q_{e, exp} = 8.034$ ($\text{mg}\cdot\text{g}^{-1}$)	$K_1 = 0.01896$ (min^{-1})	$K_2 = 0.0847$ ($\text{g}\cdot\text{mg}^{-1}\cdot\text{min}^{-1}$)	$K_{Av} = 0.46717$ (min^{-1})	$K_1 = 0.460$ (min^{-1})	$K_2 = 0.187$ ($\text{g}\cdot\text{mg}^{-1}\cdot\text{min}^{-1}$)	$K_{Av} = 0.104$ (min^{-1})
		$h = 5.4591$ ($\text{mg}\cdot\text{g}^{-1}\cdot\text{min}^{-1}$)	$n_{Av} = -0.82541$		$h = 11.532$ ($\text{mg}\cdot\text{g}^{-1}\cdot\text{min}^{-1}$)	$n_{Av} = 0.067$
r2				0.525	0.731	0.810
χ^2				0.063	0.035	0.025
RMSE				0.231	0.173	0.144
SCE				0.482	0.268	0.187

TABLE 4: Intraparticle diffusion and Boyd parameters for adsorption of IC onto ACs.

Models	Constants	Values
<i>CBK1/1</i>		
Linear intraparticle diffusion	K_{id1} ($\text{mg}\cdot\text{g}^{-1}\cdot\text{min}^{-1/2}$)	0.197
	K_{id2} ($\text{mg}\cdot\text{g}^{-1}\cdot\text{min}^{-1/2}$)	0.09814
	C_1	7.0454
Linear Boyd	C_2	7.5157
	B (min^{-1})	0.02563
	$Di \times 10^{-9}$ ($\text{cm}^2\cdot\text{s}^{-1}$)	1.083
<i>CBZ1/1</i>		
Linear intraparticle diffusion	K_{id1} ($\text{mg}\cdot\text{g}^{-1}\cdot\text{min}^{-1/2}$)	0.2578
	K_{id2} ($\text{mg}\cdot\text{g}^{-1}\cdot\text{min}^{-1/2}$)	0.1035
	C_1	6.4687
Linear Boyd	C_2	6.9168
	B (min^{-1})	0.01896
	$Di \times 10^{-9}$ ($\text{cm}^2\cdot\text{s}^{-1}$)	0.8012

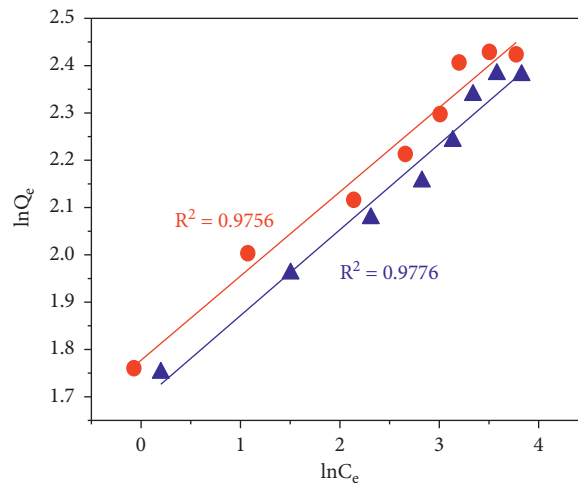
TABLE 5: Isotherm models.

Parameters	Isotherms	Nonlinear forms	Equation number	References
Two	Langmuir	$Q_e = Q_m K_L C_e / (1 + K_L C_e)$	(16)	[36]
		And $R_L = 1 / (1 + K_L C_0)$	(17)	
	Freundlich	$Q_e = K_f C_e^{1/n}$	(18)	[37]
	Temkin	$Q_e = (RT/\Delta Q) \ln(AC_e)$	(19)	[38]
	Halsey	$Q_e = \exp((\ln K_H - \ln C_e) / n_H)$	(20)	[39]
	Fritz-Schlunder III	$Q_e = Q_{mFS} K_{FS} C_e / (1 + Q_{mFS} C_e^{mFS})$	(21)	[40]



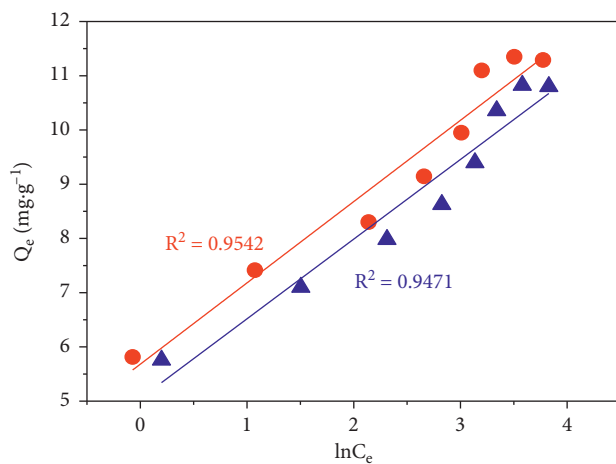
- Experimental CBK_{1/1} 400°C
- ▲ Experimental CBZ_{1/1} 400°C
- Linear Langmuir CBK_{1/1}
- Linear Langmuir CBZ_{1/1}

(a)



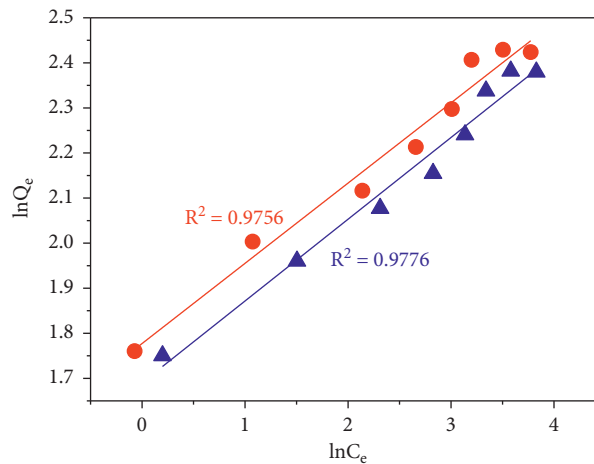
- Experimental CBK_{1/1} 400°C
- ▲ Experimental CBZ_{1/1} 400°C
- Linear Freundlich CBK_{1/1}
- Linear Freundlich CBZ_{1/1}

(b)



- Experimental CBK_{1/1} 400°C
- ▲ Experimental CBZ_{1/1} 400°C
- Linear Temkin CBK_{1/1}
- Linear Temkin CBZ_{1/1}

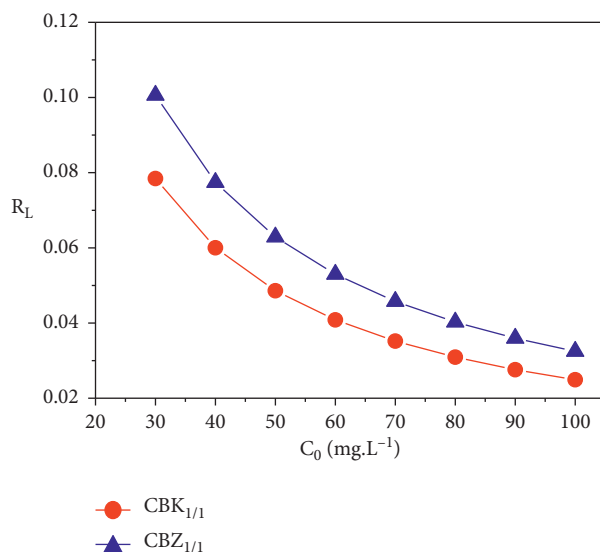
(c)



- Experimental CBK_{1/1} 400°C
- ▲ Experimental CBZ_{1/1} 400°C
- Linear Halsey CBK_{1/1}
- Linear Halsey CBZ_{1/1}

(d)

FIGURE 14: Continued.



(e)

FIGURE 14: Linear regression of isotherm models of (a) Langmuir, (b) Freundlich, (c) Temkin, (d) Halsey, and (e) separation factor graphs.

initial stages [18, 35]. In Table 4, the low values of the correlation coefficient obtained do not make it possible in this case to validate Boyd's model.

Based on the nonlinear regression data of the different models shown in Table 3 and on the low values obtained from SCE and other error functions, it can be concluded that the retention kinetics of indigo carmine are best described by the nonlinear Avrami model. The values of the Avrami exponent $n_{AV} < 1$ show that the adsorption mechanism follows a multiple kinetic order during the adsorption process of indigo carmine on the two ACs. Thus, in this work, the pseudo-first order shows a multilayer adsorption on the surface of the adsorbent based on a weak interaction between the adsorbate and the adsorbent like the Van der Waals forces and the pseudo-second order model allows us to say that the interaction $\pi-\pi$ [33] also intervenes in this adsorption process of indigo carmine on the two ACs, thus showing an adsorption of chemical nature.

3.4. Adsorption Isotherms. Adsorption isotherms can contribute to elucidating adsorption mechanisms. In this work, data from the isotherm experiments were analyzed using the different linear and nonlinear kinetic models presented in Table 5.

The linear and nonlinear regression graphs of adsorption isotherms for indigo carmine adsorption onto both ACs are shown in Figures 14 and 15, respectively, and the corresponding constants are summarized in Tables 6 and 7.

The linear regression and separation factor graphs of adsorption isotherms obtained for indigo carmine adsorption onto both ACs are shown in Figure 14. The corresponding constants obtained from the linear regressions are presented in Table 6. According to this figure, the values of correlation coefficient (R^2) in the Langmuir model were

closer to unity showing fitness of model on the adsorption experiment. This result indicates that adsorption of indigo carmine could take place at homogeneous adsorption sites and that monolayer adsorption occurs on the surface of the adsorbent [41]. The values of the separation factor falling between 0 and 1 (Figure 14(e)) show a favorable adsorption of IC by the two ACs.

Parameters calculated for Freundlich and Halsey isotherms by employing their linear and nonlinear forms are given in Tables 6 and 7. The results show that the Freundlich and Halsey isotherms have a very good coefficient of determination ($r^2 > 0.96$) and very low values of the error functions (χ^2 , RMSE, and SCE), thus better describing the phenomenon of indigo carmine adsorption. This assumes that the adsorbent surface is heterogeneous with a non-uniform distribution of the heat of adsorption over this surface showing multilayer adsorption [42]. The values of $1/n$ evaluated from the Freundlich model are less than unity, meaning that adsorption is favorable for dye [43] and physical process is favorable [44]. This confirms the heterogeneity of the adsorbents as found by the SEM.

Maximum adsorption capacities were obtained by the nonlinear Fritz-Schlunder III model and are $19.019 \text{ mg}\cdot\text{g}^{-1}$ and $18.299 \text{ mg}\cdot\text{g}^{-1}$ for CBK_{1/1} and CBZ_{1/1}, respectively. The Fritz-Schlunder model exponent m_{FS} value obtained by the nonlinear Fritz-Schlunder III isotherm of less than 1 means that the adsorption of indigo carmine by the two ACs cannot be reduced to the Langmuir isotherm showing that adsorption takes place on heterogeneous surfaces.

3.5. Possible Adsorption Mechanisms. Surface characteristics of adsorbents play an important role in adsorption processes [49]. Thus, the interaction of any molecule in the adsorption process is strongly influenced by the presence of functional

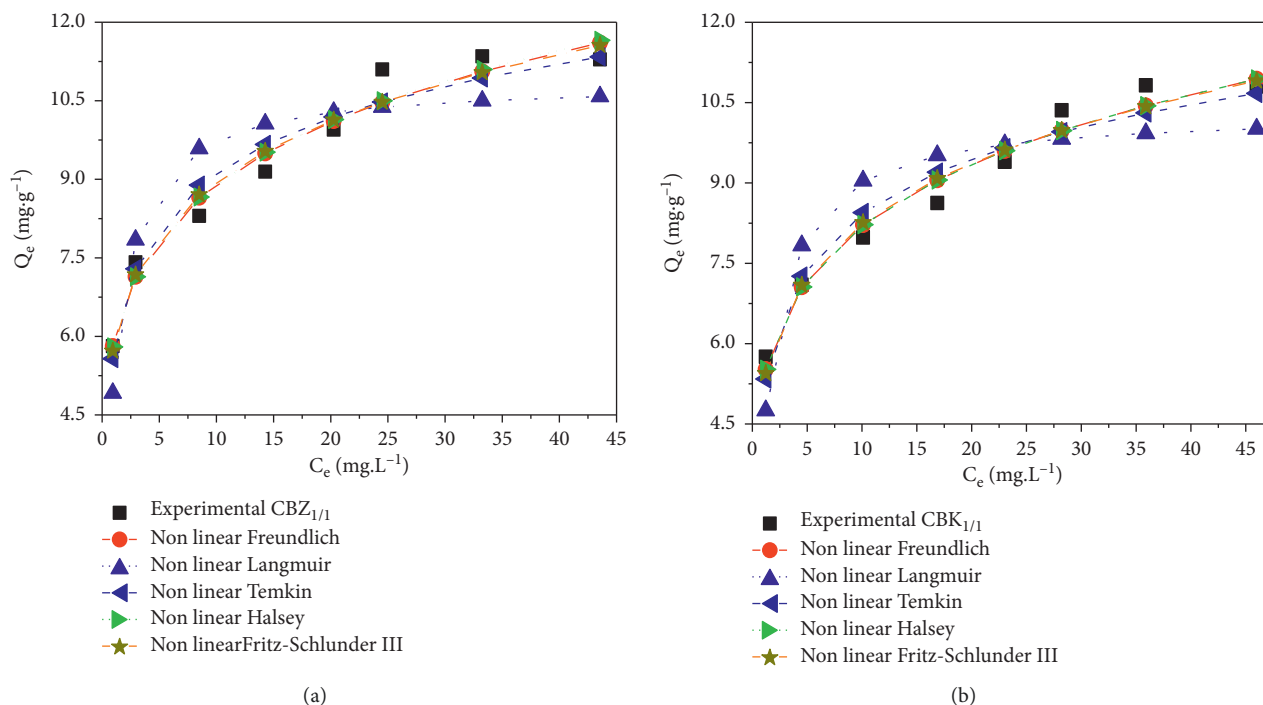


FIGURE 15: Nonlinear regression of adsorption isotherm models.

TABLE 6: Linear parameters of isotherm models for adsorption of IC onto ACs.

Isotherms	Constants	Values	r^2	χ^2	RMSE	SCE
<i>CBK_{1/1}</i>						
Langmuir	Q_m (mg·g ⁻¹)	11.905	0.8484	2.582	1.30822	10.2687
	K_L (L·mg ⁻¹)	0.3916				
Freundlich	K_F (L·g ⁻¹)	5.9133	0.9657	0.095	0.39434	0.93302
	1/n	0.178				
Temkin	ΔQ (J·mol ⁻¹)	1653.04	0.9542	0.138	0.46666	1.3064
	A (L·g ⁻¹)	44.2992				
Halsey	K_H	4.6×10^5	0.9668	0.095	0.39434	0.93304
	n_H	-5.618				
<i>CBZ_{1/1}</i>						
Langmuir	Q_m (mg·g ⁻¹)	11.455	0.8387	2.6225	1.2483	9.3496
	K_L (L·mg ⁻¹)	0.298				
Freundlich	K_F (L·g ⁻¹)	5.4211	0.9699	0.0724	0.3366	0.679903
	1/n	0.1814				
Temkin	ΔQ (J·mol ⁻¹)	1686.5	0.9471	0.1477	0.45710	1.2537
	A (L·g ⁻¹)	31.094				
Halsey	K_H	9×10^5	0.9699	0.0724	0.3366	0.67992
	n_H	-5.513				

groups on the surface of the adsorbent and also by the pH of the adsorbate solution [50]. The probable mechanism of adsorption of the dye on carbon is presented in Figure 16.

The equilibrium study showed the possibility of multilayer adsorption, in which the adsorbate-adsorbent interactions are carried out up to the saturation of the monolayer. Furthermore, based on the chemical structure of the adsorbent surface, the dyes, and considering the condition of the pH of the medium below the pH of zero charge point, which leads to

a positively charged adsorbent surface, we can say that, in the adsorption process, there occurs the electrostatic interaction (attraction) between the protonated groups under acidic conditions (e.g., $-\text{OH}_2^+$ and $-\text{COOH}_2^+$) and anionic sulphonate groups ($-\text{SO}_3^-$) of the dye on the one hand. If electrostatic interaction dominates the adsorption process of IC in aqueous solution, the ACs will exhibit lower adsorption capacity due to electrostatic repulsion between the adsorbent and the adsorbate at pH 2 because the functional groups

TABLE 7: Nonlinear parameters of isotherm models for adsorption of IC onto ACs.

	Isotherms	Constants	Values	r^2	χ^2	RMSE	SCE		
Nonlinear methods	Langmuir	Q_m (mg·g ⁻¹)	CBK _{1/1}	10.853	0.836	0.619	0.9426	5.3307	
			K_L (L·mg ⁻¹)	0.8901					
	Freundlich	K_F (L·g ⁻¹)	5.8875	0.966	0.094	0.3937	0.9299		
			$1/n$	0.1799					
	Temkin	ΔQ (J·mol ⁻¹)	1652.9	0.954	0.138	0.4666	1.3064		
			A (L·g ⁻¹)	44.293					
	Halsey	K_H	5×10^{-5}	0.968	0.094	0.3937	0.9299		
			n_H	-5.5593					
	Fritz-Schlunder III	Q_{mFS} (mg·g ⁻¹)	19.019	0.966	0.0998	0.4031	0.9753		
			K_{FS} (L·mg ⁻¹)	6.113					
			m_{FS}	0.831					
	Nonlinear methods	Langmuir	Q_m (mg·g ⁻¹)	CBZ _{1/1}	10.320	0.810	0.672	0.9383	5.2825
				K_L (L·mg ⁻¹)	0.6993				
		Freundlich	K_F (L·g ⁻¹)	5.3160	0.973	0.072	0.3297	0.6521	
				$1/n$	0.1885	0.947	0.148	0.4571	1.2537
		Temkin	ΔQ (J·mol ⁻¹)	1686.5					
A (L·g ⁻¹)				31.095	0.973	0.072	0.3297	0.6521	
Halsey		K_H	0.0001						
			n_H	-5.3076					
Fritz-Schlunder III		Q_{mFS} (mg·g ⁻¹)	18.299	0.970	0.0856	0.3517	0.7423		
			K_{FS} (L·mg ⁻¹)	5.4982					
	m_{FS}		0.8204						

TABLE 8: Comparison of adsorption capacity of indigo carmine with other adsorbents.

Adsorbents	Quantity adsorbed (mg·g ⁻¹)	Reference
Crab shell chitosan	96.15	[45]
Peanut shell activated carbon	82.64	[45]
LDH nanoparticles	55.5	[46]
AC (KOH)	13.405	[7]
AC (H ₃ PO ₄)	5.089	[7]
Chitin	5.78	[47]
Brazil nut shell	1.09	[48]
PKSAC	11.025	[21]
PKSAC/BVA	12.642	[21]
CBK _{1/1}	19.019	Present study
CBZ _{1/1}	18.299	Present study

(-OH₂⁺ and -COOH₂⁺) of the ACs (pHpzc = 8.324 for CBK_{1/1}; 7.589 for CBZ_{1/1}) and indigo carmine (pKa = 12.2) are positively charged in such an acidic environment. This does not correspond to the experimental results obtained at pH = 2; we have a high adsorption capacity. On the other hand, intermolecular hydrogen bonding of dye molecules generally leads to multilayer adsorption [24]. Adsorption of indigo carmine follows the multilayer adsorption pattern heterogeneous surfaces until saturation of the monolayer. This indicates that hydrogen bonding could be the dominant force for adsorption accompanied by the π - π interaction between the aromatic rings of the dye and the ACs, which is also considered responsible for the adsorption process [51]. Electrostatic attraction also plays an important role in indigo carmine adsorption.

3.6. Desorption. In this study, the desorbing agents such as H₂O, NaOH, and H₂SO₄ 4×10^{-2} mol·L⁻¹ were used to regenerate both ACs. The results presented in Figure 17 show that the higher desorption percentage, 61.259% for IC CBK_{1/1} and 55.08% for IC CBZ_{1/1}, is obtained in NaOH solution. This result can be explained by the phenomenon of anionic exchange between OH⁻ of NaOH solution and the activated carbons charged by indigo carmine. However, the low percentage of desorption obtained with CBZ_{1/1} compared to CBK_{1/1} is due to the strong bond formed between the IC and the surface of activated carbon CBZ_{1/1} [18, 52]. A similar result was obtained by Ngaha et al. [19] in the indigo carmine and 2,6-dichlorophenolindophenol removal using cetyltrimethylammonium bromide-modified palm oil fiber.

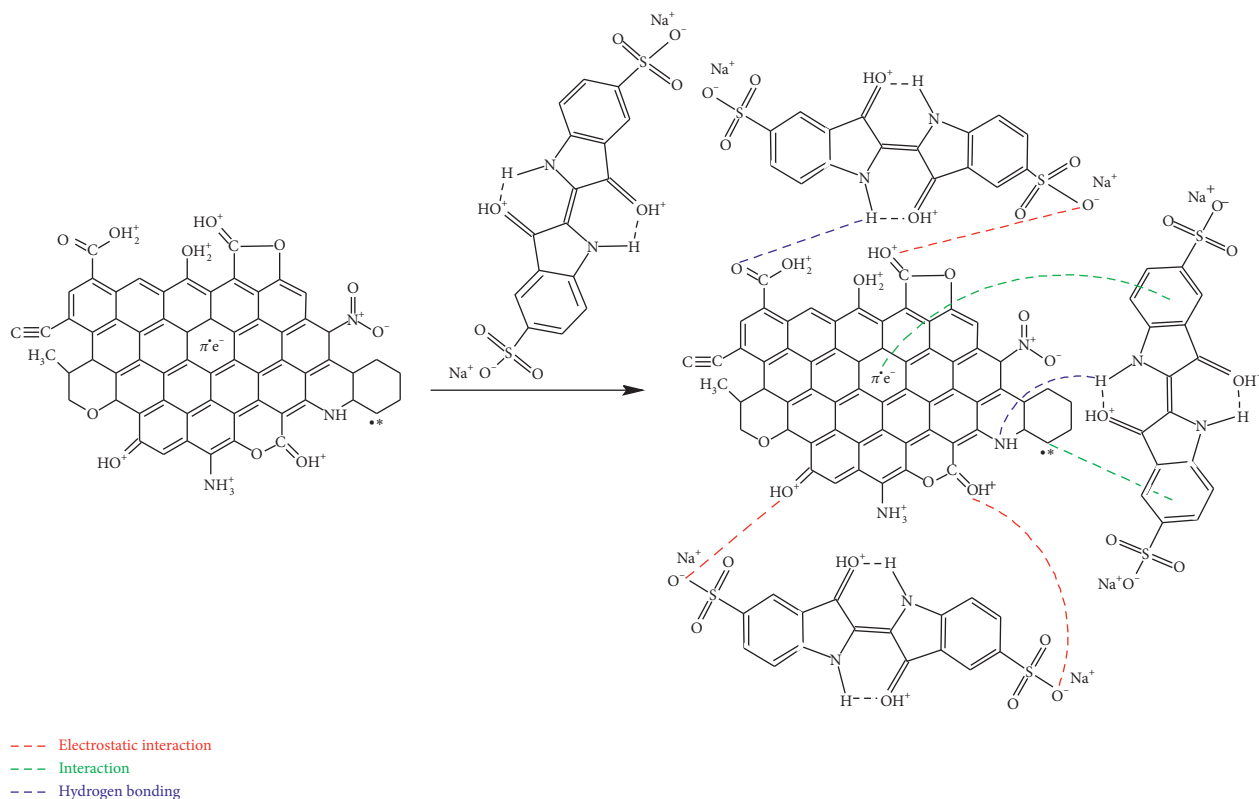


FIGURE 16: Probable mechanism involved during adsorption of IC by activated carbons.

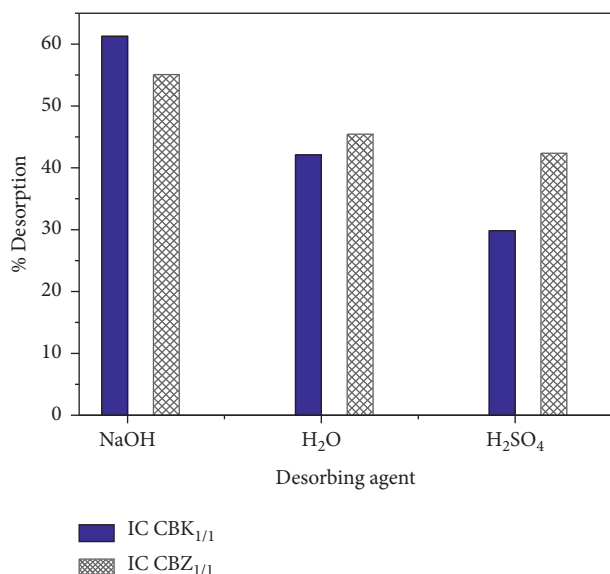


FIGURE 17: Percentage of desorption obtained onto different ACs after adsorption of IC. Experimental conditions: 50 mg; $t = 80$ min; $\nu = 200$ rpm; $V = 10$ mL, at room temperature.

4. Conclusion

In this study, activated carbons were prepared from *Garcinia cola* nut shell by chemical activation using KOH and $ZnCl_2$. They were used for removal of indigo carmine from aqueous solution by the batch process. SEM and N_2 adsorption-

desorption analysis showed that the surfaces of the ACs were heterogeneous and contained with micropores and mesopores. The adsorption process of IC onto the adsorbents was strongly dependent on the pH of the dye solution, contact time, adsorbent dosage, initial concentration of IC, and the presence of ionic strength. Linear and nonlinear kinetic and equilibrium isotherm models were applied to the adsorption of IC onto activated carbons obtained. Nonlinear kinetic models better describe the mechanism of adsorption process than linear kinetic models which show that the adsorption mechanism follows a multiple kinetic order during the adsorption process of indigo carmine on the ACs according to Avrami exponent n_{Av} lower than 1. Nature and the mechanism of the adsorption processes were studied by employing the intraparticle diffusion model and Boyd plot. External mass transfer primarily governs the rate controlling step at the initial stages for the adsorption of the IC. Linear and nonlinear equilibrium isotherm models show that IC adsorption is done on heterogeneous surface and forms nonideal monolayer. This heterogeneity was also confirmed by the constants of Fritz-Schlunder III. Comparison between linear and nonlinear isotherm models with two parameters shows that transformations of nonlinear isotherm equations to linear forms implicitly alter their error structure. Nonlinear forms better describe adsorption process than linear forms. Desorption using NaOH solution as the desorbing agent recovers a maximum quantity of IC and considers the reuse of activated carbons. In future work, we plan to study the life cycle of the biomass used, to use these activated carbons for biogas purification, and finally to study

the influence of the NaOH concentration on the desorption percentage and the desorption kinetics of the two activated carbons.

Data Availability

The data used to support the findings of this study are available from the corresponding author upon request and have been deposited in the Mendeley repository (<https://www.mendeley.com/reference-manager/library/all-references/>).

Conflicts of Interest

The authors declare that they have no conflicts of interest.

Acknowledgments

This work was funded by the Government of Cameroon by Research Modernization grants to researchers of higher education. The authors are grateful for technical assistance rendered by the researchers of Materials and Process Engineering Team/RU-NOGEE of the Department of Chemistry, Faculty of Science, University of Dschang, Cameroon. They are also grateful to Kamdem Tamo Arnaud of the Freiburg Materials Research Center (FMF), University of Freiburg, Stefan Meier Strasse 21, 79104, Freiburg, Germany, and Doungmo Giscard of the Institute of Inorganic Chemistry, Christian-Albrechts-Universität zu Kiel, Max-Eyth-Straße 2, 24118 Kiel, Germany.

References




- [1] R. D. C. Soltani, A. Khataee, M. Safari, and S. Joo, "Preparation of bio-silica/chitosan nanocomposite for adsorption of a textile dye in aqueous solutions," *International Biodeterioration & Biodegradation*, vol. 85, pp. 383–391, 2013.
- [2] J. Shen, X.-L. Wang, Y.-X. Niu, Y.-G. Wang, G. Liu, and Q.-T. Sheng, "Removal of phenol by powdered activated carbon prepared by residue extracted from coal gasification tar residue," *Environmental Technology*, vol. 10, pp. 1–8, 2017.
- [3] R. Connor, A. Renata, C. Ortigara et al., "The united nations world water development report 2017," 2017, <https://wedocs.unep.org/20.500.11822/20448>.
- [4] V. K. Gupta and I. Ali, "Environmental water," *Advances in Treatment, Remediation and Recycling*, Elsevier, Oxford, UK, 2013.
- [5] J.-C. Saurin, "Role of chromoendoscopy for the management of colorectal neoplasia," *Gastroentérologie Clinique et Biologique*, vol. 33, no. 10-11, pp. 1–6, 2009.
- [6] P. Himanshu and R. Vashi, "Decolonization of Dyeing Mill waste water by adsorption and coagulation," *E-Journal of chemistry*, vol. 7, pp. 1468–1476, 2010.
- [7] A. N. Odogu, K. Daouda, B. B. P. Desiré, N. J. Nsami, and K. J. Mbadcam, "Removal of indigo carmine dye (IC) by batch adsorption method onto dried cola nut shells and its active carbon from aqueous medium," *International Journal of Engineering Sciences & Research Technology*, vol. 5, pp. 874–887, 2016.
- [8] H. N. Tran, S.-J. You, T. V. Nguyen, and H.-P. Chao, "Insight into the adsorption mechanism of cationic dye onto biosorbents derived from agricultural wastes," *Chemical Engineering Communications*, vol. 204, no. 9, pp. 1020–1036, 2017.
- [9] S. Rovani, M. T. Censi, S. L. Pedrotti, E. C. Lima, R. Cataluña, and A. N. Fernandes, "Development of a new adsorbent from agro-industrial waste and its potential use in endocrine disruptor compound removal," *Journal of Hazardous Materials*, vol. 271, pp. 311–320, 2014.
- [10] C. S. Umpierres, P. S. Thue, E. C. Lima et al., "Microwave-activated carbons from tucumã (*Astrocaryum aculeatum*) seed for efficient removal of 2-nitrophenol from aqueous solutions," *Environmental Technology*, vol. 39, no. 9, pp. 1173–1187, 2018.
- [11] J. Yener, T. Kopac, G. Dogu, and T. Dogu, "Dynamic analysis of sorption of Methylene Blue dye on granular and powdered activated carbon," *Chemical Engineering Journal*, vol. 144, no. 3, pp. 400–406, 2008.
- [12] C. S. Ngakou, H. M. Ngomo, and S. G. Anagho, "Batch equilibrium and effects of ionic strength on kinetic study of adsorption of phenacetin from aqueous solution using activated carbon derived from a mixture of ayous sawdust and Cucurbitaceae peelings," *Current Journal Applied Science and Technology*, vol. 26, no. 2, pp. 1–24, 2018.
- [13] D. R. T. Tchuifon, S. G. Anagho, G. N. Nche, and J. M. Ketcha, "Adsorption of salicylic and sulfosalicylic acid onto powdered activated carbon prepared from rice and coffee husks," *International Journal of Current Engineering and Technology*, vol. 5, pp. 1641–1652, 2015.
- [14] B. Aurelien, R. T. T. Donald, G. N. A. Nche, D. Giscard, and S. G. Anagho, "Non-linear equilibrium and kinetic study of the adsorption of 2, 4-dinitrophenol from aqueous solution using activated carbon derived from olives stones and cotton cake," *African Journal of Environmental Science and Technology*, vol. 13, no. 9, pp. 365–380, 2019.
- [15] L. A. Amola, T. Kamgaing, R. F. Tiegam Tagne, C. D. Atemkeng, I.-H. T. Kuete, and S. G. Anagho, "Optimized removal of hydroquinone and resorcinol by activated carbon based on shea residue (*Vitellaria paradoxa*): thermodynamics, adsorption mechanism, nonlinear kinetics, and isotherms," *Journal of Chemistry*, vol. 2022, Article ID 1125877, 15 pages, 2022.
- [16] T. Kopac, "Hydrogen storage characteristics of bio-based porous carbons of different origin: a comparative review," *International Journal of Energy Research*, vol. 45, no. 15, pp. 20497–20523, 2021.
- [17] K. T. Idris-Hermann, T. T. D. Raoul, D. Giscard, and A. S. Gabche, "Preparation and characterization of activated carbons from bitter kola (*Garcinia kola*) nut shells by chemical activation method using H_3PO_4 , KOH and $ZnCl_2$," *Chemical Science International Journal*, vol. 23, no. 4, pp. 1–15, 2018.
- [18] M. C. D. Ngaha, L. G. Djemmoe, E. Njanja, and I. T. Kenfack, "Biosorption isotherms and kinetics studies for the removal of 2, 6-dichlorophenolindophenol using Palm tree trunk (*Elaeis guineensis*)," *Journal of Encapsulation and Adsorption Sciences*, vol. 08, no. 03, pp. 156–177, 2018.
- [19] M. C. D. Ngaha, E. Njanja, G. Doungmo, A. Tamo Kamdem, and I. K. Tonle, "Indigo carmine and 2, 6-dichlorophenolindophenol removal using Cetyltrimethylammonium bromide-modified Palm Oil fiber: adsorption isotherms and mass transfer kinetics," *International Journal of Biomaterials*, vol. 2019, Article ID 6862825, 18 pages, 2019.

- [20] M. Hadi, M. R. Samarghandi, G. McKay, and G. McKay, "Equilibrium two-parameter isotherms of acid dyes sorption by activated carbons: study of residual errors," *Chemical Engineering Journal*, vol. 160, no. 2, pp. 408–416, 2010.
- [21] G. Agbor Tabi, L. Ngouateu Rene Blaise, K. Daouda et al., "Non-linear modelling of the adsorption of Indigo Carmine dye from wastewater onto characterized activated carbon/volcanic ash composite," *Arabian Journal of Chemistry*, vol. 15, pp. 103515–103612, 2022.
- [22] T. B. Gupta and D. H. Lataye, "Adsorption of indigo carmine dye onto acacia nilotica (babool) sawdust activated carbon," *Journal of Hazardous, Toxic, and Radioactive Waste*, vol. 21, no. 4, pp. 1–11, 2017.
- [23] T. Oymak and E. Bagda, "Crosslinked egg white as eco-friendly, reusable and cost-effective biosorbent for rapid removal of indigo carmine," *Clean: Soil, Air, Water*, vol. 46, no. 6, Article ID 1700186, 2018.
- [24] Z. Zhao, Y. Yang, L. Xu et al., "Amino acid-doped polyaniline nanotubes as efficient adsorbent for wastewater treatment," *Journal of Chemistry*, vol. 2022, Article ID 2041512, 12 pages, 2022.
- [25] I.-H. T. Kuete, D. R. T. Tchui fon, G. N. Ndifor-Angwafor, A. T. Kamdem, and S. G. Anagho, "Kinetic, isotherm and thermodynamic studies of the adsorption of thymol blue onto powdered activated carbons from garcinia cola nut shells impregnated with H_3PO_4 and KOH: non-Linear regression analysis," *Journal of Encapsulation and Adsorption Sciences*, vol. 10, no. 01, pp. 1–27, 2020.
- [26] P. Saha, S. Chowdhury, S. Gupta, and I. Kumar, "Insight into adsorption equilibrium, kinetics and thermodynamics of Malachite Green onto clayey soil of Indian origin," *Chemical Engineering Journal*, vol. 165, no. 3, pp. 874–882, 2010.
- [27] K. Shahul Hameed, P. Muthirulan, and M. Meenakshi Sundaram, "Adsorption of Chromotrope dye onto activated carbons obtained from the seeds of various plants: equilibrium and kinetics studies," *Arabian Journal of Chemistry*, vol. 10, pp. S2225–S2233, 2017.
- [28] S. Chowdhury and P. Saha, "Sea shell powder as a new adsorbent to remove basic green 4 (malachite green) from aqueous solutions: equilibrium, kinetic and thermodynamic studies," *Chemical Engineering Journal*, vol. 164, no. 1, pp. 168–177, 2010.
- [29] G. Alberghina, R. Bianchini, M. Fichera, and S. Fisichella, "Dimerization of Cibacron Blue F3GA and other dyes: influence of salts and temperature," *Dyes and Pigments*, vol. 46, no. 3, pp. 129–137, 2000.
- [30] S. G. Anagho, J. M. Ketcha, D. R. T. Tchui fon, and J. N. Ndi, "Kinetic and equilibrium studies of the adsorption of mercury (II) ions from aqueous solution using kaolinite and meta-kaolinite clays from Southern Cameroon," *International Journal of Research in Chemistry and Environment*, vol. 3, pp. 1–11, 2013.
- [31] Y. S. Ho and G. McKay, "Pseudo-second order model for sorption processes," *Process Biochemistry (Oxford, United Kingdom)*, vol. 34, no. 5, pp. 451–465, 1999.
- [32] A. A. Inyinbor, F. A. Adekola, and G. A. Olatunji, "Kinetics, isotherms and thermodynamic modeling of liquid phase adsorption of Rhodamine B dye onto Raphia hookerie fruit epicarp," *Water Resources and Industry*, vol. 15, pp. 14–27, 2016.
- [33] H. N. Tran, S.-J. You, and H.-P. Chao, "Fast and efficient adsorption of methylene green 5 on activated carbon prepared from new chemical activation method," *Journal of Environmental Management*, vol. 188, pp. 322–336, 2017d.
- [34] A. Gundogdu, C. Duran, H. B. Senturk et al., "Adsorption of phenol from aqueous solution on a low-cost activated carbon produced from tea industry waste: equilibrium, kinetic, and thermodynamic study," *Journal of Chemical & Engineering Data*, vol. 57, no. 10, pp. 2733–2743, 2012.
- [35] N. Sharma and B. K. Nandi, "Utilization of sugarcane bagasse, an agricultural waste to remove malachite green dye from aqueous solutions," *Journal of Materials and Environmental Science*, vol. 4, no. 6, pp. 1052–1065, 2013.
- [36] I. Langmuir, "The constitution and fundamental properties of solids and liquids. Part I. Solids," *Journal of the American Chemical Society*, vol. 38, no. 11, pp. 2221–2295, 1916.
- [37] H. M. F. Freundlich, "Over the adsorption in solution," *Journal of Physical Chemistry*, vol. 57, pp. 385–471, 1906.
- [38] M. I. Tempkin and V. Pyzhev, "Kinetics of ammonia synthesis on promoted iron catalyst," *Acta Physicochimica U.R.S.S.* vol. 12, pp. 327–356, 1940.
- [39] S. Rangabhashiyam, N. Anu, M. S. Giri Nandagopal, and N. Selvaraju, "Relevance of isotherm models in biosorption of pollutants by agricultural byproducts," *Journal of Environmental Chemical Engineering*, vol. 2, no. 1, pp. 398–414, 2014.
- [40] A. M. Aljeboree, A. N. Alshirifi, and A. F. Alkaim, "Kinetics and equilibrium study for the adsorption of textile dyes on coconut shell activated carbon," *Arabian Journal of Chemistry*, vol. 10, pp. 3381–3393, 2017.
- [41] G. Moussavi, A. Alahabadi, and K. Yaghmaeian, "Investigating the potential of carbon activated with NH_4Cl for catalyzing the degradation and mineralization of antibiotics in ozonation process," *Chemical Engineering Research and Design*, vol. 97, pp. 91–99, 2015.
- [42] A. B. Albadarin and C. Mangwandi, "Mechanisms of Alizarin Red S and Methylene blue biosorption onto olive stone byproduct: isotherm study in single and binary systems," *Journal of Environmental Management*, vol. 164, pp. 86–93, 2015.
- [43] Z. Wu, H. Zhong, X. Yuan et al., "Adsorptive removal of methylene blue by rhamnolipid-functionalized graphene oxide from wastewater," *Water Research*, vol. 67, pp. 330–344, 2014.
- [44] M. Saleh Bashanaini, M. H. Al-Douh, and H. S. Al-Ameri, "Removal of malachite green dye from aqueous solution by adsorption using modified and unmodified local agriculture waste," *Science Journal of Analytical Chemistry*, vol. 7, no. 2, pp. 42–56, 2019.
- [45] J. K. Fatombi, E. A. Idohou, S. A. Osseni et al., "Adsorption of indigo carmine from aqueous solution by chitosan and chitosan/activated carbon composite: kinetics, isotherms and thermodynamics studies," *Fibers and Polymers*, vol. 20, no. 9, pp. 1820–1832, 2019.
- [46] M. A. Ahmed, A. A. brick, and A. A. Mohamed, "An efficient adsorption of indigo carmine dye from aqueous solution on mesoporous Mg/Fe layered double hydroxide nanoparticles prepared by controlled sol-gel route," *Chemosphere*, vol. 174, pp. 280–288, 2017.
- [47] A. G. S. Prado, J. D. Torres, E. A. Faria, and S. C. L. Dias, "Comparative adsorption studies of indigo carmine dye on chitin and chitosan," *Journal of Colloid and Interface Science/Colloid and Interface Science*, vol. 277, no. 1, pp. 43–47, 2004.
- [48] S. M. de Oliveira Brito, H. M. C. Andrade, L. F. Soares, and R. P. de Azevedo, "Brazil nut shells as a new biosorbent to remove methylene blue and indigo carmine from aqueous solutions," *Journal of Hazardous Materials*, vol. 174, no. 1–3, pp. 84–92, 2010.

- [49] R. Ahmad and R. Kumar, "Adsorptive removal of Congo red dye from aqueous solution using bael shell carbon," *Applied Surface Science*, vol. 257, no. 5, pp. 1628–1633, 2010.
- [50] P. C. Bhomick, A. Supong, M. Baruah, C. Pongener, C. Gogoi, and D. Sinha, "Alizarin Red S adsorption onto biomass-based activated carbon: optimization of adsorption process parameters using Taguchi experimental design," *International journal of Environmental Science and Technology*, vol. 17, no. 2, pp. 1137–1148, 2019.
- [51] C. Moreno-Castilla, "Adsorption of organic molecules from aqueous solutions on carbon materials," *Carbon*, vol. 42, no. 1, pp. 83–94, 2004.
- [52] W. Wan Maznah, A. T. Al-Fawwaz, and M. Surif, "Biosorption of copper and zinc by immobilised and free algal biomass, and the effects of metal biosorption on the growth and cellular structure of chlorella sp. and chlamydomonas sp. isolated from rivers in penang, Malaysia," *Journal of Environmental Sciences*, vol. 24, no. 8, pp. 1386–1393, 2012.

Research Article

Flash Pyrolysis Experiment on *Albizia odoratissima* Biomass under Different Operating Conditions: A Comparative Study on Bio-Oil, Biochar, and Noncondensable Gas Products

C. Sowmya Dhanalakshmi ¹, S. Kaliappan,² H. Mohammed Ali,³ S. Sekar,⁴ Melvin Victor Depoures ⁵, Pravin P. Patil,⁶ Baskara Sethupathy Subbaiah,⁷ S. Socrates,² and Habtewolde Ababu Birhanu ⁸

¹Department of Mechanical Engineering, SNS College of Technology, Coimbatore 641035, Tamil Nadu, India

²Department of Mechanical Engineering, Velammal Institute of Technology, Chennai 601204, Tamil Nadu, India

³Department of Mechanical Engineering, SRM Institute of Science and Technology-Ramapuram Campus, Chennai 600089, Tamil Nadu, India

⁴Department of Mechanical Engineering, Rajalakshmi Engineering College, Chennai 602105, Tamil Nadu, India

⁵Department of Thermal Engineering, Saveetha School of Engineering, Saveetha Institute of Medical and Technical Sciences, Chennai 600124, Tamil Nadu, India

⁶Department of Mechanical Engineering, Graphic Era Deemed to be University, Clement Town, Dehradun 248002, Uttarakhand, India

⁷Department of Automobile Engineering, Velammal Engineering College, Chennai 600066, Tamil Nadu, India

⁸Faculty of Mechanical Engineering, Arba Minch Institute of Technology, Arba Minch University, PO Box 21, Arba Minch, Ethiopia

Correspondence should be addressed to Habtewolde Ababu Birhanu; habtewold.ababu@amu.edu.et

Received 18 May 2022; Revised 20 June 2022; Accepted 24 June 2022; Published 8 July 2022

Academic Editor: Binghui Xu

Copyright © 2022 C. Sowmya Dhanalakshmi et al. This is an open access article distributed under the Creative Commons Attribution License, which permits unrestricted use, distribution, and reproduction in any medium, provided the original work is properly cited.

This study deals with the flash pyrolysis of *Albizia odoratissima* biomass wastes at different temperature, sweep gas flow rate, and heating rate in a fluidized bed reactor. In the first phase of the experimental work, the effect of temperature (350–550°C) on product yield was analyzed, the second and third phases of the work were to analyze the effect of sweeping gas (N₂), flow rate (1.25–2.25 m³/hr), and heating rate (20–40°C/min). The experimental works were carried out to get maximum bio-oil production. The experimental results demonstrated that the maximum yield of bio-oil was obtained at a temperature of 450°C, N₂ flow rate of 1.75 m³/hr, and heating rate of 30°C/min. Temperature was found to be the crucial factor rather than sweep gas flow rate in the product distribution. Fourier transform infrared spectroscopy (FT-IR), gas chromatography mass spectroscopy (GC-MS), and elemental analysis were done on the obtained bio-oil, biochar, and noncondensable gas products. The heating value of the bio-oil and biochar was identified as 18.15 and 23.47 MJ/kg, respectively. The chemical analysis of the bio-oil showed that the oil is a mixture of phenol and oxygenated elements. The gas analyses showed that hydrogen and carbon dioxide were dominant, followed by carbon monoxide and methane.

1. Introduction

Finding alternative and sustainable energy to replace fossil fuels has been prompted for the past three decades by rising fossil fuel prices and resource depletion. Biomass is a

renewable carbonaceous material that has received widespread attention. It is available in a variety of forms and is used for power and chemical production [1]. Currently, the availability of biomass accounts for about 10% of the total global energy production [2], and its annual availability are

estimated at 100 billion tonnes per year. According to the IEA, biomass can replace 27% of the global transportation energy needs by 2050 [3]. Biochemical and thermochemical are the two efficient approaches for the production of biofuels. Methane and alcohol are the two main products of biochemical conversion techniques, whereas pyrolysis, gasification, combustion, hydrothermal liquefaction, and carbonization are the different types of thermochemical conversion methods [4, 5]. Among the various thermochemical conversion techniques, pyrolysis is considered as a most attractive method [6].

Slow and fast pyrolysis is the two different types of pyrolysis. Slow pyrolysis is a very old technique that has been used for millennia for the production of char for firing purposes [7]. Fast or flash pyrolysis is the most efficient technique which produces energy-rich bio-oil rather than the production of char and gaseous fuel. The yields of pyrolysis are strongly influenced by the reaction conditions. In fast pyrolysis, biomass decomposes fastly to release most of condensable vapours with a lower yield of char and gaseous components. The condensable vapours can be cooled to get dark brown liquid oil called pyrolysis oil [8]. Wood chips or agricultural leftovers from lignocellulosic biomass are commonly used feedstocks for biomass pyrolysis. Several studies have focused on the pyrolysis characteristics of various materials and their product characterization at the laboratory and industrial scale, including their reaction kinetics and modeling. However, the yield of biofuel and its quality basically depends upon the quality of feedstock and various operating parameters [9, 10]. For the past three decades, many articles have been published related to the pyrolysis of various biomass materials by using different types of reactors. Zhang et al. [11] reviewed various physicochemical characteristics of pyrolysis oil. The study identified the problems that must be addressed to improve the reaction. Isahak et al. [12] revised their findings on bio-oil by focusing on biomass characterization and the design of the reactor. Ahmed et al. [13] studied pyrolysis and thermal stability analysis of *Acacia auriculiformis* biomass to produce biofuels. Khuenkao and Tippayawong [14] conducted pyrolysis experiments on corncobs, coconut shells, and bamboo residue using an ablative reactor. The study investigated the production of pyrolysis oil and char by changing inert gas flow rate (nitrogen), rotating frequency, and reaction temperature. The study showed a higher bio-oil yield of 72 wt% with the corncob under the N₂ flow rate of 5 L/min and 6 Hz rotation frequency compared to the coconut shell and bamboo residues. Next to the corncob bio-oil, the coconut shell yielded 50 wt% of bio-oil under varying flow rate and frequency.

Fluidized bed technology is a good platform for pyrolysis of wood-based biomass due to its simple design, higher efficiency, higher contact surface, and shorter residence time [15]. Fluidized bed reactors are particularly designed for maximum oil production [16]. Many studies previously yielded more bio-oil when the mallee wood [17], beech wood [18], pine [19], and bamboo [20] biomass was pyrolyzed using fluidized bed reactors. From these literatures, it can be

understood that the pyrolysis reactor is the significant one to control product yields. Pattiya [21] conducted pyrolysis experiment on cassava residues using a fluidized bed reactor and produced 65 wt% bio-oil. Kim et al. [22] pyrolyzed *Jatropha* wastes and produced maximum oil fractions of 48 wt%. Park et al. [23] conducted fast pyrolysis of carbonaceous materials by utilizing sawdust and empty fruit bunches. The study reported that 60 wt% of oil was obtained at 500°C. In this series, Griffin et al. [24] discussed the uses of Australian acacias for biofuel production, and Madhu et al. [25] concentrated on production of pyrolysis oil from the cotton shell and empty fruit bunches. Wood and wood bark pyrolysis of *Albizia amara* conducted by Sowmya Dhanalakshmi and Madhu [26] showed maximum production of bio-oil of 48.5 wt%. The produced bio-oil was acetic in nature and they suggested the liquid oil as a feedstock for industrial chemicals. From the above said literatures, the fluidized bed pyrolysis of biomass produced maximum oil products compared to other pyrolysis reactors.

Albizia odoratissima is a tree that belongs to Fabaceae family. It is the fastest growing tree native to India, China, Bangladesh, and Sri Lanka. The wood of the tree is dark brown in colour, typically striped, sturdy, and dense. The wood can be used for making furniture and agricultural equipment. It grows up to 35 metres height with a short trunk. The bark of the tree is identified in dark grey with horizontal lenticels. The wood generally has 12 wt% moisture content, and it is 20–40% stronger than teak [27]. The trees have been widely planted as shade trees in tea and coffee estates. The physicochemical analysis of the biofuel obtained from various biomass materials is an important study to find its suitability and applications. Sahoo et al. [28] carried out a deep characterization study on biofuels obtained from rice straw, wheat straw, and sugarcane bagasse. The oil products obtained from these biomasses were acidic, with an overall calorific value of 10 MJ/kg. The authors suggested using this oil as a fuel due to its lower ash content and lower viscosity compared to commercial fuel. The SEM and CHNS analysis of the biochar showed it to be used as a fertilizer for soil to restore its nutrients. According to Charusiri and Vitidsant [29], the bio-oil produced from sugarcane leaves, cannot be utilized as a fuel for direct burning due to lower calorific value. But the cocatalytic pyrolysis process was recommended by the authors to produce potential biofuel and chemicals. *Azadirachta indica* was transformed into noncondensable gases using pyrolysis by Sowmya Dhanalakshmi and Madhu et al. [30]. The obtained gas was reported to have a higher amount of methane and carbon monoxide.

Accordingly to these findings, the authors of this paper decided to conduct pyrolysis experiments on *Albizia odoratissima* as, a potential candidate for renewable energy generation, since the feedstock is widely available and very cheap. This study presents the production of bio-oil, char, and noncondensable biogas through flash pyrolysis by changing its process parameters. The biofuels were also examined to analyze their physical and chemical characteristics through various chromatographic techniques.

2. Materials and Methods

2.1. Materials. Wood and wood barks of *Albizia odoratissima* were collected in the city of west Coimbatore, India. The collected materials were initially tested to find their moisture level. The higher moisture content in the biomass was eliminated by pulverizing. The material was crushed to an average size of 0.5–0.75 mm. The sample was then dried under sunlight for three days. The dried samples were further kept in the furnace at 100°C. The samples were then tested for their moisture content and found to be less than 5%.

2.2. Experimental Set-Up. The experiments were conducted on a lab scale fluidized bed reactor that consists of a cylindrical tube of 50 mm ID and 100 cm long [31]. The reactor is heated externally with the help of an electrical heater. The heat input is controlled by the PID controller. The outlet pipe is connected to a cyclone separator where the escaped char content is collected. The evolved gas after char separation was allowed to condense into the condenser. The condenser is distributed with surplus water kept at 5°C. Five K type thermocouples have been attached at five different points. The feedstock to the reactor is permitted over the screw feeder. A sand particle of 0.5 mm in diameter is used for fluidization inside the reactor. The distributor plate, which is placed at the bottom, allows pressurized gas into the reactor bed. Initially, compressed air is admitted, and once the reactor has reached a desired temperature, the nitrogen gas is admitted more than minimum fluidization velocity.

2.3. Pyrolysis Experiment. Initially, the reactor was heated to reach the preferred temperature at the heating rate of 30°C/min. After that, the supply of air was cut and the N₂ was allowed to fluidize. The minimum fluidization velocity of the particle was estimated as 0.11 m/s. The experiments were conducted at different temperatures of 350–550°C at 50°C intervals. The experiments were further conducted by changing sweep gas flow rate and heating rate. For the analysis of sweep gas flow rate, the N₂ gas was supplied at 1.25, 1.75, 2.00, and 2.25 m³/hr by keeping the reactor at 450°C. The effect of heating rate was analyzed by changing heating rate as 20, 30, and 40°C/min. The biomass samples were supplied continuously at 25 g/min. In order to analyze the product distributions, the experiments were conducted at two different phases. The first phase deals with the effect of temperature, and the second phase deals with the effect of sweep gas flow rate. Each run was conducted till no vapour was physically identified from the reactor. The condensed bio-oil and char particles were collected and stored. For yield analysis, the obtained oil and char particles were weighed with the help of a digital weighing machine. The noncondensable gas fractions were found by remaining material balance [32].

2.4. Pyrolysis Reaction Mechanism. The following governing equations (1) to (3) represent the transformation of woody biomass into volatiles obtained from literature [33]

$$\frac{d\alpha}{dt} = f(T)f(\alpha), \quad (1)$$

$$f(T) = Ae^{-(Ea/RT)}, \quad (2)$$

where A is pre-exponential factor, R is universal gas constant (J/mol K), Ea is activation energy (kJ/mol), and T is absolute temperature

$$\alpha = \frac{m_i - m_a}{m_i - m_f}, \quad (3)$$

where α is mass fraction of conversion, m_i is initial mass, m_a is actual mass, and m_f is final mass. Under constant temperature the equations (1) and (2) can be rewritten as [34].

$$\frac{d\alpha}{dt} = \frac{A}{\beta} e^{-(Ea/RT)} f(\alpha), \quad (4)$$

where β is heating rate.

2.5. Characterization Study. The proximate analysis of the feedstock was done by the proximate analyzer. The amount of fixed carbon in the material was found by difference. The ultimate analysis of the biomass and char elements was found directly using a CHNS analyzer, while the amount of oxygen was found by difference. All the analyses were performed by following ASTM standards. The degradation study of the biomass was analyzed using the TGA701 analyzer (LECO Corporation, Michigan). The TGA was performed under an N₂ atmosphere by heating the samples to 700°C. FT-IR and GC-MS (THERMO GC, VER: 5.0, MS DSQ-II) spectroscopy were employed for chemical analysis of the bio-oil and gas. The physical analysis of oil was done by the standard Pensky Martein closed cup apparatus, Parr-6772 calorimetric thermometer, digital pH meter, and redwood viscometer.

3. Results and Discussion

3.1. Biomass Characterization. The results of the analysis of the biomass material are revealed in Table 1. It is understood that the material has higher volatile matter (61.3%). Bio-oil and biogas are produced in large amounts from biomass with increased volatile matter [35]. The presence of more fixed carbon (25.36%) yields more biochar and boosts the carbon conversion rate, resulting in the highest heating value. The elemental analysis of the biomass reveals that the material has higher carbon and hydrogen. The lower amount of nitrogen and sulphur is recommended to produce biofuel with low environmental effects.

3.2. Thermogravimetric Analysis. Differential thermogravimetric (DTG) and TGA were done to analyze the pyrolysis behaviour under the nitrogen environment. The analysis was carried out by heating 5 mg of powdered sample kept on an aluminium pan to 700°C at the rate of 20°C/min. According to the TG curve (Figure 1), the first thermal event occurred at 54°C resulting in the weight loss of 6.95%. This

TABLE 1: Characterization of biomass.

Parameter	Proximate analysis (wt%)			Ultimate analysis (wt%)								
	Volatile matter	Fixed carbon ^s	Moisture content	Ash	C	H	N	S	O ^s	H/C	O/C	Heating value
<i>Albizia odoratissima</i>	61.3	25.36	6.40	6.94	51.04	6.28	1.20	0.01	50.47	1.779	0.901	19.21

^sBy difference.

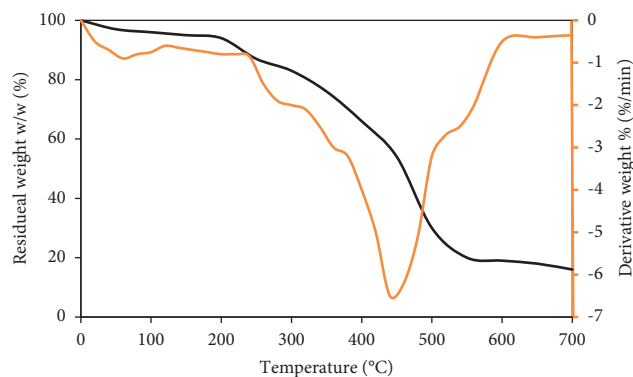


FIGURE 1: TG and DTG curve of the biomass material.

phenomenon is representing the evaporation of water molecules from the material [36]. The second peak appeared at 235°C attributed to the breakdown of lignocellulosic content. After 500°C, the samples were converted into carbon residues representing the breakdown of lignin [37]. After this stage, the passive pyrolysis occurs with leaving 18% of solid residues.

3.3. Pyrolysis Experiment

3.3.1. Impact of Temperature. Figure 2 represents the impact of process temperature on pyrolysis of biomass. Increasing temperature resulted in the maximization of bio-oil. It can be understood that the higher reactor temperature direct to maximum bio-oil production, while lower temperatures result in higher char production. Therefore, optimal bio-oil can be reached at 450°C (43.2 wt%). Increased temperature permits heavy hydrocarbon compounds to break, resulting in increased oil and gaseous content and lower char yield [38]. While increasing temperature from 450 to 550°C, the oil output was decreased by 9.72%. Horne and Williams [39] and Varma et al. [40] also reported a same trend related to pyrolysis temperature. The char produced during initial pyrolysis reactions underwent secondary reactions at elevated temperatures that resulted in increased gas products with reduced char. At elevated temperatures, more heat energy supplied to the material may surpass the bond cessation energy, releasing more volatiles. These volatile biomass elements are released as gases, leading to minimize the char and oil production. The gas yield at 350°C was 27.6 wt% and it reached to 40.2 wt% at 550°C. Due to a considerable loss of volatiles or secondary decomposition reaction at elevated temperatures, the production of char decreases. This may also result in the production of certain

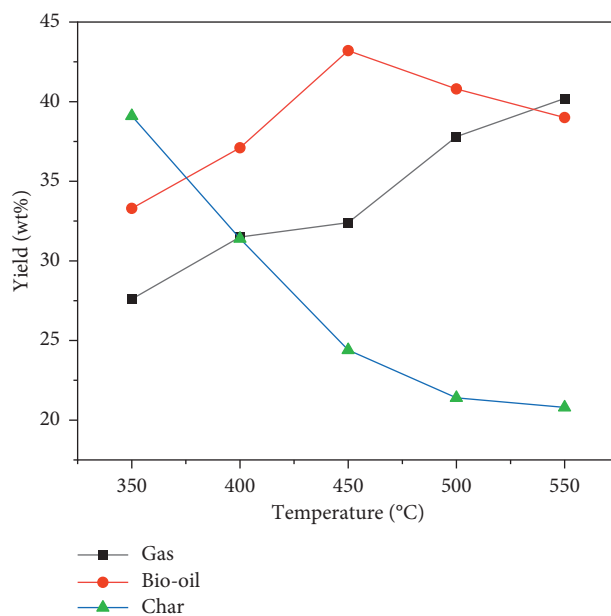


FIGURE 2: Effect of temperature on product distribution.

gases [41]. The yield of char in this study decreased from 39.1 to 20.8 wt% as the temperature was changed from 350°C to 550°C.

3.3.2. Effect of Nitrogen Gas Flow Rate. Nitrogen is generally used as a carrier gas for fluidized purpose and its flow rate is considerably affecting the yield of products [42–44]. The experiments for this phase were carried out at 450°C by varying the sweep gas flow rate. The vapours generated from the reactor at different N₂ flow rates were condensed into bio-oil, which is reported in Figure 3. From the figure, it is understood that the oil yield was increased up to 47.4 wt% when the flow rate is changed from 1.25 m³/hr to 1.75 m³/hr. At 1.75 m³/hr, the optimum oil output achieved a maximum of 47.4 wt%. The inadequate quenching of pyrolysis vapours in this phase increases the gas flow in this case. According to Uzun et al. [45], eliminating the developed pyrolysis vapours quickly with surplus N₂ and adequate quenching should result in higher bio-oil yields. With a continuous increase in sweep gas flow rate, the production of char is steadily increased from 24.4 wt% to 33.4 wt%. The higher flow rate of N₂ accelerated the movement of particles, resulting in good mixing of sand and biomass. The proper mixing of biomass and sand boosted heat transfer and resulted in increased condensable volatiles.

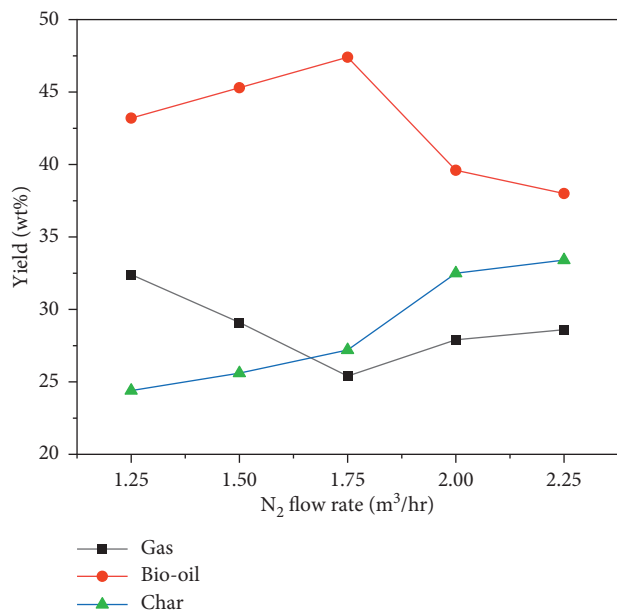


FIGURE 3: Effect of sweep gas flow rate on product distribution.

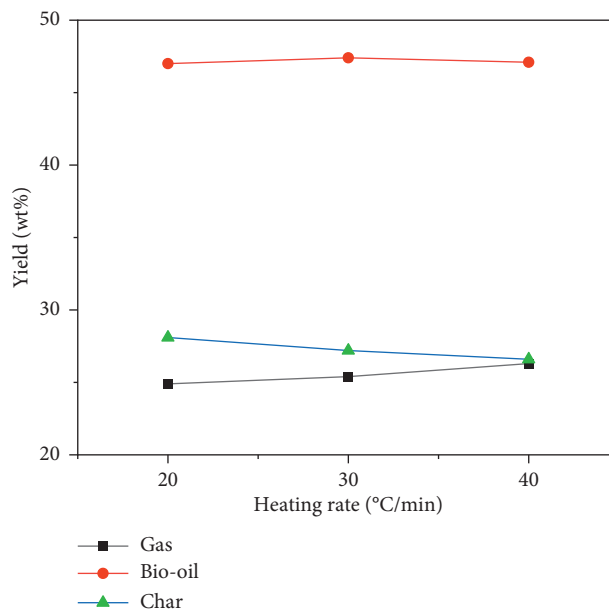


FIGURE 4: Effect of heating rate on product distribution.

3.3.3. Effect of Heating Rate. Heating rate is also an important factor that determines the product distribution. Many studies have conducted the effect of heating rate on biomass pyrolysis [46, 47]. Generally, the higher heating rate breakdowns the heat transfer restrictions and increases the release of volatiles. In this study, in comparison to the heating rate, temperature has a greater impact on pyrolysis yields [48]. There were no significant changes in pyrolysis product yields. With an increasing heating rate, the gas product is increased. At 20°C/min, the yield of gas was 24.9 wt% which is increased to 26.3 wt% at 40°C/min. The yield of char was reduced by 5.34% when the heating rate was increased. The yield of oil was increased at 30°C/min. At the point, the yield of oil was 47.4 wt% and the yield was decreased to 47.1 wt% at 40°C/min. The heat transfer limitations at higher heating rates increase the production of gas fractions [49]. Figure 4 represents the effect of heating rate on product distributions.

3.4. Product Characterization

3.4.1. Analysis of Bio-Oil. The basic characteristics of the bio-oil are displayed in Table 2. The physical analysis is a crucial one since the quality of the oil is determined by its physical characteristics. The application and suitability of the bio-oil are also identified based on its physical nature. The higher density and viscosity compared to petrodiesel shows that the oil affects the operation of the fuel atomizer during firing. The higher flash point represents safety during storage. The heating value is a vital one for any oil, which represents the burning efficiency which is found to be 18.15 MJ/kg. The bio-oil can be further processed using various chemical treatments to improve the heating value.

The functional group composition identified through FT-IR is shown in Figure 5. The large absorbance peak of

TABLE 2: Physical characteristics of the bio-oil.

Unit	Density kg/m ³	Viscosity cSt	pH —	Flash point °C	Heating value MJ/kg	Reference
Bio-oil	1020	7.2	3.6	145	18.15	This study
Diesel	850	3.9	—	57	43.6	[50]

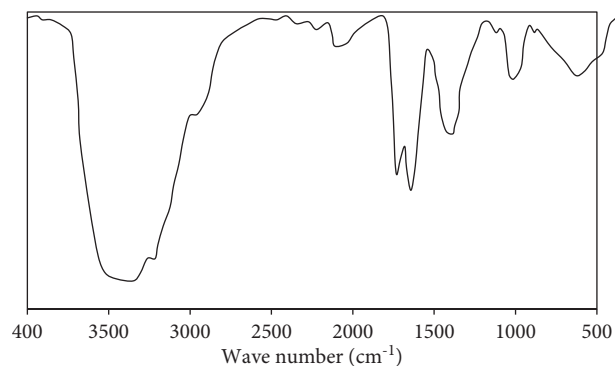


FIGURE 5: FT-IR analysis of the bio-oil.

O-H stretching vibration at 3450 cm⁻¹ suggested the presence of water, alcohols, phenols, and other hydroxyl compounds [51, 52]. Alkanes are identified by the absorbance peak of C-H vibration at 2950 cm⁻¹. The occurrence of ketones and aldehydes in the oil is pointed out by the C=O stretching vibrations at 1720 and 1680 cm⁻¹. The availability of alkane group components is identified by the CH bending at 1385 cm⁻¹ [53]. The presence of alcohols is further identified by the C-O stretching vibration at 1030 cm⁻¹ [54].

The chemical composition of the pyrolysis oil changes significantly depending on the nature of raw material and

TABLE 3: GC-MS analysis of the bio-oil.

Retention time (min)	Compound name	Formula	Area (%)
7.62	2-Isopropyl-2,5-dihydrofuran	C ₇ H ₁₂ O	3.72
7.56	2-Acetyl furan	C ₆ H ₆ O ₂	7.94
9.04	5-Hydroxymethylfurfural4	C ₆ H ₆ O ₃	1.78
12.36	Pyrogallol 1,3-dimethyl ether	C ₈ H ₁₀ O ₃	3.04
13.44	2,6-Dimethylphenol	C ₈ H ₁₀ O	4.07
17.99	2,3,5-Trimethoxytoluene	C ₁₀ H ₁₄ O ₃	3.14
18.42	2,5-Dimethoxytoluene	C ₉ H ₁₂ O ₂	2.11
18.56	3-Methylphenol	C ₇ H ₈ O	4.94
20.04	Tetradecane	C ₁₄ H ₃₀	2.65
20.55	Phenol	C ₆ H ₆ O	19.26
21.27	Di-(2-ethylhexyl) phthalate	C ₂₄ H ₃₈ O ₄	3.44
21.46	Phenol, 2,6-dimethoxy	C ₈ H ₁₀ O ₃	3.48
22.04	Eugenol	C ₁₀ H ₁₂ O ₂	1.50
22.38	Ethanol	C ₁₃ H ₂₂ O ₃	0.99
22.71	Phenol, 2-methoxy	C ₇ H ₈ O ₂	4.67
23.45	2-Isopropyl-2,5-dihydrofuran	C ₇ H ₁₂ O	6.41
24.11	2-Methoxy-3-methylhydroquinone	C ₈ H ₁₀ O ₃	2.97
24.87	Cyclopentanol	C ₅ H ₁₀ O	1.46
25.22	2,3,5-Trimethoxytoluene	C ₁₀ H ₁₄ O ₃	3.38
26.45	1,2-Benzendiol	C ₆ H ₆ O ₂	4.50
27.08	Nonane, 5-methyl-5-propyl-	C ₁₃ H ₂₈	3.28
28.50	1,2-Bis (2'-quinolylmethyl) ethylene	C ₂₀ H ₁₄ N ₂	1.86
29.41	Octacosane	C ₂₈ H ₅₈	2.93
29.49	Campesterol	C ₂₈ H ₄₈ O	3.83
29.78	Pregnenolone	C ₂₁ H ₃₂ O ₂	1.81

TABLE 4: Component analysis of char.

Proximate analysis (wt%)			Ultimate analysis (wt%)						H/C	O/C	Heating value (MJ/kg)
Volatile matter	Fixed carbon ^s	Moisture content	Ash	C	H	N	S	O ^s			
24.52	68.31	2.12	5.05	52.41	7.54	3.22	0.21	36.62	1.714	0.524	23.47

^sBy difference.

pyrolysis conditions [55]. During thermal breakdown, the primary components of feedstock, such as hemicelluloses, cellulose, and lignin are usually transformed into different hydrocarbons, phenols, and acids. Table 3 displays the outcome of the GC-MS analysis. The oil was verified to be a combination of various chemicals. The analysis showed a higher amount of phenols and their derivatives. The total area percentage of these compounds are 36.42. Phenol is an aromatic organic compound that is primarily used for various chemical processes. This is a very important chemical used for the production of nylon and other synthetic fibers. From this analysis, we can know that the chemical components identified in this study can be used for various chemical and pharmaceutical industries.

3.4.2. Analysis of Char. The characteristics of char components were determined and listed in Table 4. The heating value of the char is found as 23.47 MJ/kg. The percentage of carbon in the char is 52.41 wt%. On the other hand, the percentage of oxygen is identified as 36.62 wt%. The value of the carbon can be increased by increasing carbonization temperature. The higher carbon with lower oxygen can be recommended for use as a fuel. The lower amount of

nitrogen and sulphur in char is shown to be good for environmental sustainability during burning. For household cooking, the volatile matter should be between 20 and 40%. The volatile matter of the char is found to be within the range. The higher volatile content makes it easy to ignite although it can produce a smoky flame [56]. The fixed carbon is 68.31 wt%, which is in the range between 65 and 90% as recommended by Mythili and Venkatachalam [57]. The moisture level is identified as 2.12 wt%, which is much lower than the acceptable level of the charcoal (7%). The lower ash level of 5.05 wt% in the char implies that using it as a fuel may result in the production of lower clinkers.

3.4.3. Analysis of Noncondensable Gas. The noncondensable gases fractions are shown in Figure 6. Hydrogen is identified as a major one with 8.04%. Carbon dioxide and carbon monoxide are also detected at 6.47% and 2.14%, respectively, in the pyrolysis gas. The greater carbon monoxide than carbon dioxide is due to the reverse Boudouard reaction [58]. It is an important reaction inside the reactor, whereas the drop of iron oxides is not attained directly by carbon but by carbon monoxide. The produced carbon dioxide endures a Boudouard reaction with char. Generally, the variation in

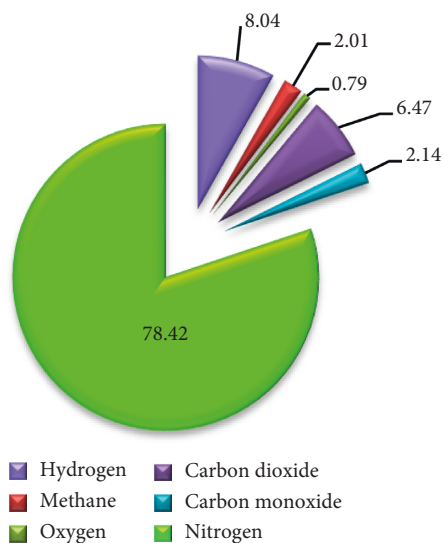


FIGURE 6: Noncondensable gas fractions.

hydrogen and carbon monoxide is a function of heat which is applied during pyrolysis [59]. The amount of methane in the gas is 2.01%.

4. Conclusion

Flash pyrolysis experiment on *Albizia odoratissima* has been performed at various pyrolysis temperatures and sweeping gas flow rates on a fluidized bed reactor. The selected wood sample yielded the maximum bio-oil of 47.4 wt% at optimized conditions of reactor temperature of 450°C sweeping gas flow rate of 1.75 m³/hr and heating rate of 30°C/min. The sample yielded maximum char and noncondensable gas of 39.1 and 40.2 wt%, respectively. The bio-oil produced in this study has a medium heating value, which can be further processed to be used as a fuel for industrial applications. The char has higher volatiles and fixed carbons with lesser ash and moisture, which makes it fit to utilize as a fuel for heating boilers and furnaces. The analyses of noncondensable gases showed that hydrogen and carbon dioxide were dominant, followed by carbon monoxide and methane.

Data Availability

The data used to support the findings of this study are included within the article.

Conflicts of Interest

The authors declare that there are no conflicts of interest regarding the publication of this article.

References

- [1] K. N. Yogalakshmi, P. Sivashanmugam, S. Kavitha et al., "Lignocellulosic biomass-based pyrolysis: a comprehensive review," *Chemosphere*, vol. 286, no. Pt 2, Article ID 131824, 2022.
- [2] A. A. Khan, W. de Jong, P. J. Jansens, and H. Spliethoff, "Biomass combustion in fluidized bed boilers: potential problems and remedies," *Fuel Processing Technology*, vol. 90, no. 1, pp. 21–50, 2009.
- [3] S. Wang, G. Dai, H. Yang, and Z. Luo, "Lignocellulosic biomass pyrolysis mechanism: a state-of-the-art review," *Progress in Energy and Combustion Science*, vol. 62, pp. 33–86, 2017.
- [4] E. Kwietniewska and J. Tys, "Process characteristics, inhibition factors and methane yields of anaerobic digestion process, with particular focus on microalgal biomass fermentation," *Renewable and Sustainable Energy Reviews*, vol. 34, pp. 491–500, 2014.
- [5] G. Wang, Y. Dai, H. Yang et al., "A review of recent advances in biomass pyrolysis," *Energy & Fuels*, vol. 34, no. 12, pp. 15557–15578, 2020.
- [6] A. V. Bridgwater, "Review of fast pyrolysis of biomass and product upgrading," *Biomass and Bioenergy*, vol. 38, pp. 68–94, 2012.
- [7] S. H. Beis, Ö. Onay, and Ö. M. Koçkar, "Fixed-bed pyrolysis of safflower seed: influence of pyrolysis parameters on product yields and compositions," *Renewable Energy*, vol. 26, no. 1, pp. 21–32, 2002.
- [8] K. B. Ansari, B. Kamal, S. Beg et al., "Recent developments in investigating reaction chemistry and transport effects in biomass fast pyrolysis: a review," *Renewable and Sustainable Energy Reviews*, vol. 150, Article ID 111454, 2021.
- [9] I. Y. Mohammed, Y. A. Abakr, F. K. Kazi, S. Yusuf, I. Alshareef, and S. A. Chin, "Pyrolysis of Napier grass in a fixed bed reactor: effect of operating conditions on product yields and characteristics," *Bioresources*, vol. 10, no. 4, pp. 6457–6478, 2015.
- [10] A. T. Hoang, H. C. Ong, I. M. R. Fattah et al., "Progress on the lignocellulosic biomass pyrolysis for biofuel production toward environmental sustainability," *Fuel Processing Technology*, vol. 223, Article ID 106997, 2021.
- [11] Q. Zhang, J. Chang, T. Wang, and Y. Xu, "Review of biomass pyrolysis oil properties and upgrading research," *Energy Conversion and Management*, vol. 48, no. 1, pp. 87–92, 2007.
- [12] W. N. R. W. Isahak, M. W. Hisham, M. A. Yarmo, and T. y. Yun Hin, "A review on bio-oil production from biomass by using pyrolysis method," *Renewable and Sustainable Energy Reviews*, vol. 16, no. 8, pp. 5910–5923, 2012.
- [13] A. Ahmed, S. Hidayat, M. S. Abu Bakar, A. K. Azad, R. S. Sukri, and N. Phusunti, "Thermochemical characterisation of *Acacia auriculiformis* tree parts via proximate, ultimate, TGA, DTG, calorific value and FTIR spectroscopy analyses to evaluate their potential as a biofuel resource," *Biofuels*, vol. 12, no. 1, pp. 9–20, 2021.
- [14] N. Khuenkaeo and N. Tippayawong, "Production and characterization of bio-oil and biochar from ablative pyrolysis of lignocellulosic biomass residues," *Chemical Engineering Communications*, vol. 207, no. 2, pp. 153–160, 2020.
- [15] I. Barbarias, G. Lopez, M. Artetxe, A. Arregi, J. Bilbao, and M. Olazar, "Valorisation of different waste plastics by pyrolysis and in-line catalytic steam reforming for hydrogen production," *Energy Conversion and Management*, vol. 156, pp. 575–584, 2018.
- [16] J. A. Garcia-Nunez, M. R. Pelaez-Samaniego, M. E. Garcia-Perez et al., "Historical developments of pyrolysis reactors: a review," *Energy & Fuels*, vol. 31, no. 6, pp. 5751–5775, 2017.
- [17] J. Shen, X. S. Wang, M. Garcia-Perez, D. Maurant, M. J. Rhodes, and C. Z. Li, "Effects of particle size on the fast

- pyrolysis of oil mallee woody biomass," *Fuel*, vol. 88, no. 10, pp. 1810–1817, 2009.
- [18] R. J. M. Westerhof, H. S. Nygard, W. P. M. van Swaaij, S. R. A. Kersten, and D. W. F. Brillman, "Effect of particle geometry and microstructure on fast pyrolysis of beech wood," *Energy & Fuels*, vol. 26, no. 4, pp. 2274–2280, 2012.
- [19] H. Zhang, S. Shao, Y. Jiang, T. Vitidsant, P. Reubroycharoen, and R. Xiao, "Improving hydrocarbon yield by two-step pyrolysis of pinewood in a fluidized-bed reactor," *Fuel Processing Technology*, vol. 159, pp. 19–26, 2017.
- [20] G. Xiao, M. J. Ni, H. Huang et al., "Fluidized-bed pyrolysis of waste bamboo," *Journal of Zhejiang University–Science*, vol. 8, no. 9, pp. 1495–1499, 2007.
- [21] A. Pattiya, "Bio-oil production via fast pyrolysis of biomass residues from cassava plants in a fluidised-bed reactor," *Bioresource Technology*, vol. 102, no. 2, pp. 1959–1967, 2011.
- [22] S. W. Kim, B. S. Koo, J. W. Ryu et al., "Bio-oil from the pyrolysis of palm and Jatropha wastes in a fluidized bed," *Fuel Processing Technology*, vol. 108, pp. 118–124, 2013.
- [23] J. Y. Park, J. K. Kim, C. H. Oh, J. W. Park, and E. E. Kwon, "Production of bio-oil from fast pyrolysis of biomass using a pilot-scale circulating fluidized bed reactor and its characterization," *Journal of Environmental Management*, vol. 234, pp. 138–144, 2019.
- [24] A. R. Griffin, S. J. Midgley, D. Bush, P. J. Cunningham, and A. T. Rinaudo, "Global uses of Australian acacias—recent trends and future prospects," *Diversity and Distributions*, vol. 17, no. 5, pp. 837–847, 2011.
- [25] P. Madhu, M. I. Neethi, and H. Kanagasabapathy, "Parametric analysis of cotton shell and palmyra palm fruit bunch for bio oil in fixed bed pyrolysis system," *International Journal of Applied Environmental Sciences*, vol. 9, no. 5, pp. 2427–2436, 2014.
- [26] C. Sowmya Dhanalakshmi and P. Madhu, "Utilization possibilities of Albiziaamarara as a source of biomass energy for bio-oil in pyrolysis process," *Energy Sources, Part A: Recovery, Utilization, and Environmental Effects*, vol. 41, no. 15, pp. 1908–1919, 2019.
- [27] C. Orwa, A. Mutua, R. Kindt, R. Jamnadass, and A. Simons, *Agroforestry Database: A Tree Reference and Selection Guide*, World Agroforestry Centre, Nairobi, Kenya, 2009.
- [28] K. Sahoo, A. Kumar, and J. P. Chakraborty, "A comparative study on valuable products: bio-oil, biochar, non-condensable gases from pyrolysis of agricultural residues," *Journal of Material Cycles and Waste Management*, vol. 23, no. 1, pp. 186–204, 2021.
- [29] W. Charusiri and T. Vitidsant, "Biofuel production via the pyrolysis of sugarcane (*Saccharumofficinarium* L.) leaves: characterization of the optimal conditions," *Sustainable Chemistry and Pharmacy*, vol. 10, pp. 71–78, 2018.
- [30] C. Sowmya Dhanalakshmi and P. Madhu, "Biofuel production of neem wood bark (*Azadirachta indica*) through flash pyrolysis in a fluidized bed reactor and its chromatographic characterization," *Energy Sources, Part A: Recovery, Utilization, and Environmental Effects*, vol. 43, no. 4, pp. 428–443, 2021.
- [31] Y. K. S. S. Rao, C. S. Dhanalakshmi, D. K. Vairavel et al., "Investigation on forestry wood wastes: pyrolysis and thermal characteristics of ficus religiosa for energy recovery system," *Advances in Materials Science and Engineering*, vol. 2022, pp. 1–9, 2022.
- [32] S. Thirugnanam, R. Srinivasan, K. Anand et al., "Utilisation possibilities of waste medium-density fiberboard: a material recycling process," *Materials Today Proceedings*, vol. 59, pp. 1362–1366, 2022.
- [33] L. Hu, X. Y. Wei, X. H. Guo, H. P. Lv, and G. H. Wang, "Investigation on the kinetic behavior, thermodynamic and volatile products analysis of chili straw waste pyrolysis," *Journal of Environmental Chemical Engineering*, vol. 9, no. 5, Article ID 105859, 2021.
- [34] T. Rasool, I. Najar, V. C. Srivastava, and A. Pandey, "Pyrolysis of almond (*Prunus amygdalus*) shells: kinetic analysis, modelling, energy assessment and technical feasibility studies," *Bioresource Technology*, vol. 337, Article ID 125466, 2021.
- [35] P. Madhu, C. Sowmya Dhanalakshmi, and M. Mathew, "Multi-criteria decision-making in the selection of a suitable biomass material for maximum bio-oil yield during pyrolysis," *Fuel*, vol. 277, Article ID 118109, 2020.
- [36] K. Thanzami, C. Malsawmtluangi, H. Lalhlenmawia et al., "Characterization and in vitro antioxidant activity of *Albizia stipulata* Boiv. gum exudates," *International Journal of Biological Macromolecules*, vol. 80, pp. 231–239, 2015.
- [37] P. Madhu, M. Sasireka, R. Samikannu et al., "Production and characterization of maximum liquid oil products through individual and copyrolysis of pressed neem oil cake and waste thermocol mixture," *Advances in Polymer Technology*, vol. 2022, pp. 1–11, 2022.
- [38] M. Tripathi, J. N. Sahu, and P. Ganesan, "Effect of process parameters on production of biochar from biomass waste through pyrolysis: a review," *Renewable and Sustainable Energy Reviews*, vol. 55, pp. 467–481, 2016.
- [39] P. A. Horne and P. T. Williams, "Influence of temperature on the products from the flash pyrolysis of biomass," *Fuel*, vol. 75, no. 9, pp. 1051–1059, 1996.
- [40] A. K. Varma, L. S. Thakur, R. Shankar, and P. Mondal, "Pyrolysis of wood sawdust: effects of process parameters on products yield and characterization of products," *Waste Management*, vol. 89, pp. 224–235, 2019.
- [41] R. S. Chutia, R. Katak, and T. Bhaskar, "Characterization of liquid and solid product from pyrolysis of *Pongamia glabra* deoiled cake," *Bioresource Technology*, vol. 165, pp. 336–342, 2014.
- [42] R. Pan, Y. Zan, and G. Debenest, "Oil production from waste polyethylene and polystyrene co-pyrolysis: interactions of temperature and carrier gas flow rate," *Journal of Environmental Chemical Engineering*, vol. 10, no. 3, Article ID 107555, 2022.
- [43] C. Wang, R. Diao, Z. Luo, and X. Zhu, "Study on the influence of residence time on the componential evolution of biomass pyrolysis vapors during indirect heat exchange process through a combining method of bio-oil composition inversion and function fitting," *Applications in Energy and Combustion Science*, vol. 9, Article ID 100047, 2022.
- [44] P. Kim, S. Weaver, and N. Labbé, "Effect of sweeping gas flow rates on temperature-controlled multistage condensation of pyrolysis vapors in an auger intermediate pyrolysis system," *Journal of Analytical and Applied Pyrolysis*, vol. 118, pp. 325–334, 2016.
- [45] B. B. Uzun, A. E. Pütün, and E. Pütün, "Rapid pyrolysis of olive residue. 1. Effect of heat and mass transfer limitations on product yields and bio-oil compositions," *Energy & Fuels*, vol. 21, no. 3, pp. 1768–1776, 2007.
- [46] T. Iwasaki, S. Suzuki, and T. Kojima, "Influence of biomass pyrolysis temperature, heating rate and type of biomass on produced char in a fluidized bed reactor," *Energy and Environment Research*, vol. 4, no. 2, pp. 64–72, 2014.

- [47] K. M. Qureshi, A. N. Kay Lup, S. Khan, F. Abnisa, and W. M. A. W. Daud, "Pyrolysis of palm kernel shell using screw-assisted fluidization: effect of heating rate," *Brazilian Journal of Chemical Engineering*, pp. 1–11, 2021.
- [48] D. Chen, Y. Li, K. Cen, M. Luo, H. Li, and B. Lu, "Pyrolysis polygeneration of poplar wood: effect of heating rate and pyrolysis temperature," *Bioresource Technology*, vol. 218, pp. 780–788, 2016.
- [49] D. Chen, D. Liu, H. Zhang, Y. Chen, and Q. Li, "Bamboo pyrolysis using TG-FTIR and a lab-scale reactor: analysis of pyrolysis behavior, product properties, and carbon and energy yields," *Fuel*, vol. 148, pp. 79–86, 2015.
- [50] D. Raguraman, A. Kumar, S. Prasanna Raj Yadav et al., "Performance and emission characteristics of pyrolysis oil obtained from neem de Oiled cake and waste polystyrene in a compression ignition engine," *Advances in Materials Science and Engineering*, vol. 2021, pp. 1–10, Article ID 3728852, 2021.
- [51] F. Abnisa, W. W. Daud, W. N. W. Husin, and J. N. Sahu, "Utilization possibilities of palm shell as a source of biomass energy in Malaysia by producing bio-oil in pyrolysis process," *Biomass and Bioenergy*, vol. 35, no. 5, pp. 1863–1872, 2011.
- [52] A. B. Fadhil, M. A. Alhayali, and L. I. Saeed, "Date (Phoenix dactylifera L.) palm stones as a potential new feedstock for liquid bio-fuels production," *Fuel*, vol. 210, pp. 165–176, 2017.
- [53] M. Nurul Islam, R. Zailani, and F. Nasir Ani, "Pyrolytic oil from fluidised bed pyrolysis of oil palm shell and its characterisation," *Renewable Energy*, vol. 17, no. 1, pp. 73–84, 1999.
- [54] P. Madhu, T. S. Livingston, and H. Kanagasabapathy, "Flash pyrolysis of lemon grass (*Cymbopogon flexuosus*) for bio-oil production in an electrically heated fluidized bed reactor," *Waste and Biomass Valorization*, vol. 9, no. 6, pp. 1037–1046, 2018.
- [55] K. P. Shadangi and K. Mohanty, "Production and characterization of pyrolytic oil by catalytic pyrolysis of Niger seed," *Fuel*, vol. 126, pp. 109–115, 2014.
- [56] M. T. Misginna and H. M. Rajabu, "The Potential of charcoal making stove to enhance energy efficiency," *International Journal of Innovation and Applied Studies*, vol. 5, no. 3, p. 206, 2014.
- [57] R. Mythili and P. Venkatachalam, "Product yield and characteristics of char," *Energy Sources, Part A: Recovery, Utilization, and Environmental Effects*, vol. 37, no. 24, pp. 2632–2638, 2015.
- [58] J. A. Menéndez, A. Domínguez, Y. Fernández, and J. J. Pis, "Evidence of self-gasification during the microwave-induced pyrolysis of coffee hulls," *Energy & Fuels*, vol. 21, no. 1, pp. 373–378, 2007.
- [59] A. Kaupp, *Gasification of Rice Hulls: Theory and Practices*, Eschborn: Deutsches Zentrum Fuer Entwicklungs Technolgie, Eschborn, Germany, 1984.

Research Article

Porous Carbons Derived from Desiliconized Rice Husk Char and Their Applications as an Adsorbent in Multivalent Ions Recycling for Spent Battery

Yating Sun, Geng Su , Zhaocai He, Yuan Wei, Jinbo Hu , Huaifei Liu , and Gonggang Liu 

Hunan Province Key Laboratory of Materials Surface & Interface Science and Technology,
College of Materials Science and Engineering, Central South University of Forestry and Technology, Changsha 410004, China

Correspondence should be addressed to Geng Su; sugeng199@163.com and Huaifei Liu; huaifei011@126.com

Received 17 February 2022; Revised 10 May 2022; Accepted 11 May 2022; Published 27 May 2022

Academic Editor: Jianqiang Liu

Copyright © 2022 Yating Sun et al. This is an open access article distributed under the Creative Commons Attribution License, which permits unrestricted use, distribution, and reproduction in any medium, provided the original work is properly cited.

Recycling of spent lithium-ion batteries (LIBs) has attracted increasing attentions recently on account of continuous growth demand for corresponding critical metals/materials and environmental requirement of solid waste disposal. In this work, rice husk as one of the most abundant renewable fuel materials in the world was used to prepare rice husk char (RC) and applied to recycle multivalent ions in waste water from hydrometallurgical technology dispose of spent LIBs. Rice husk char with specific surface area and abundant pores was obtained via pickling and desilication process (DPRC). The structural characterization of the obtained rice husk char and its adsorption capacity for multivalent ions in recycled batteries were studied. XRD, TEM, SEM, Raman, and BET were used for the characterization of the raw and the modified samples. The results show rice husk chars after desilication has more flourishing pore structure and larger pore size about 50–60 nm. Meanwhile, after desilication, the particle size of rice husk char decreased to 31.392 μm , and the specific surface area is about 402.10 m^2/g . Its nitrogen adsorption desorption curve (BET) conforms to the type IV adsorption isotherm with H_3 hysteresis ring, indicating that the prepared rice husk char is a mesoporous material. And the adsorption capacity of optimized DPRC for Ni, Co, and Mn ions is 7.00 mg/g, 4.84 mg/g, and 2.67 mg/g, respectively. It also demonstrated a good fit in the Freundlich model for DPRC-600°C, and a possible adsorption mechanism is proposed. The study indicates biochar materials have great potential as an adsorbent to recover multivalent ions from spent batteries.

1. Introduction

With the development of social economy, the demand for lithium-ion and nickel metal hydride batteries in portable electronic equipment and electric vehicles is increasing, which brings more and more pressure to the environmental impact of solid waste treatment. The total global Li consumption amount for LIBs is estimated to 0.265 million tons by the year 2025 and will continue to amplify to 511 million tons by 2050 [1]. With the current growth rate, significant pressure is imposed on the supply side of cobalt and lithium. It is predicted that Co and Li will face a serious shortage in the foreseeable future [2]. More seriously, a large number of spent LIBs will be produced in the future. These spent batteries contain harmful electrolytes, such as organic

solvents and lithium fluoride salts, which may contaminate soil and groundwater, seriously endangering human health and the ecological environment [3, 4]. In addition, high-priced metals contained in lithium ion batteries, such as lithium, cobalt, nickel, copper, and aluminum, also have good resource values [5]. Therefore, considering environmental and resource issues, effective recycling of spent lithium-ion batteries is crucial to ensure the sustainable development of the field [6–12]. Hydrometallurgy with high metal recovery, high product purity, low energy consumption, and minimal gas emissions is considered to be the most suitable technology for recovering spent LIBs [13]. The widely used hydrometallurgical methods include acid leaching, alkali leaching, solvent extraction [14], chemical precipitation [15], and adsorption [16]. Adsorbents include

activated carbon [17–19], metal-organic framework [20–26], and zeolite adsorbents [27–31]. Among them, carbon adsorption is considered as an ideal battery wastewater treatment technology due to its simple operation and low cost [32]. Besides, during hydrometallurgical technologies, low content of multivalent ions in waste water is urgent to be treated. Porous carbon with developed pore structure, large specific surface area, and rich surface functional groups has strong adsorption and removal of multivalent ions in battery wastewater [18].

Compared with coal resources, biomass resources have the advantages of large resources, wide sources, less pollution, and renewable resources [33]. Agricultural solid waste is a cheap biomass resource, which is common in all countries in the world. It can be transformed into porous carbon with excellent performance, including peanut shell [34], tea [35], cotton [36], and coconut shell [37]. Rice is the third largest food in the world after wheat and corn. The world produces 571 million tons of rice every year and 140 million tons of rice husk waste [38]. Rice husk is one of the cheapest and abundantly available biomass in which the constituents of rice husk are silica (20%), cellulose (40%), hemicellulose (20%), and lignin (20%) used for the preparation of carbon [39–44]. In recent years, surface-modified activated carbon was prepared to improve the adsorption capacity and removal efficiency of multivalent ions [45–47]. Under low temperature conditions, the chemical activation method can prepare activated carbon with abundant pore structure and low energy consumption. For example, potassium hydroxide as an activator can fully exploit the micropores of biochar [48]. Sanka et al. [49] studied the removal effect of RC on multivalent ions in industrial wastewater by carbonizing rice husk directly at different temperatures (500, 600, and 700°C). The results showed that the removal effect of Cr (65%), Fe (90%), and Pb (>90%) was the best when rice husk was carbonized at 600°C. Some studies have used hot alkali leaching to desilicize rice husks. Studies have shown that alkali pretreatment of RC with sodium hydroxide (NaOH) with a mass ratio of 2–4% can reduce the ash content to 74–93% [50]. In addition, metal impurities in rice husks can also hinder the pore development of activated carbon. Ma et al. [51] treated rice husk with 2 mol/L hydrochloric acid for 1 h at 60°C, and more than 90% of the metal impurities could be extracted. Pickling of rice husks can also promote the dissolution of silica, increase the content of volatile matter and fixed carbon, and affect the pore structure and specific surface area of the material.

The performance of rice husk char for wastewater treatment mainly depends on the pore structure and pore size distribution of the carbon material. In addition, the high silica content in rice husk ash can also hinder the pore development of activated carbon. Therefore, the removal of silica from rice husk is an important key to the formation of porous structure. Vunain et al. [52] used rice husk as raw material and reacted potassium hydroxide with silica in rice husk to generate soluble sodium silicate for desilication, which was then activated by phosphoric acid and pyrolyzed at 600°C. By adjusting pH value, it is found that when pH

value is 2.0, the adsorption capacity of Cr (VI) is the largest, and the removal rate of Cr is up to 99.88%.

In this paper, rice husk as one of the most abundant renewable fuel materials in the world was used to prepare rice husk char (RC) and applied to recycle multivalent ions in wastewater from hydrometallurgical technology dispose of spent LIBs. The pickling activated carbonized rice husk char (PRC) was desilicated by NaOH solution, which provided a new carbon material in multivalent ions recycling for spent battery and opened up a new field for the application of rice husk. The comprehensive diagram of specific routes is shown in Figure 1. The surface morphology of untreated rice husk char (RC), pickling rice husk char (PRC), and desilicated pickling rice husk char (DPRC) is analyzed, and the adsorption capacities of Co, Ni and Mn ions in spent battery wastewater by DPRC-600°C are investigated.

2. Materials and Methods

2.1. Materials. The rice husks come from Changsha suburb, the chemical reagent sodium hydroxide (NaOH, AR) comes from Shanghai Sinopharm (China), and the hydrochloric acid (HCl, 37%, AR) was purchased from Chengdu Kelong Chemical Co. (China).

2.2. Preparation of PRC and DPRC. The rice husks used in the research were taken from the suburbs of Changsha. 50-g rice husk was taken and soaked in 200 ml of 0.1 mol/L (1 : 4 solid–liquid ratio in hydrochloric acid) for 12 hours [51], then washed, dried and crushed, and passed through a gauze mesh of 100 mesh. This was then followed by the pyrolysis treatment (activation) step in which pickled rice husk powder was placed into a quartz boat for carbonization. In a nitrogen atmosphere, the temperature was increased at a rate of 10°C/min, kept at 300°C for 15 min, and then heated to 500°C and 600°C for carbonization for 3 h to prepare 500°C carbonized rice husks and 600°C carbonized rice husks, which denoted as pickled rice husk char (PRC). 10 g of PRC was weighed and mixed with 96 mL of 1 mol/L NaOH solution in a mass ratio of 1 : 10 and stirred in a constant temperature magnetic stirrer at 60°C for 6 hours [50]. The desilication solution was then vacuum filtered, while it was hot, and the precipitate was filtered, washed to nitrite at pH 7, and dried in an oven at 45°C to obtain desilication pickling rice husk char (DPRC). After adding the excess acid solution for 24 hours, the change of filtrate was observed.

2.3. Characterization of PRC and DPRC. The physico-chemical characterizations of porous carbons including the morphologies, carbon structural properties, and pore structure were analyzed. The morphologies of porous carbons were characterized by scanning electron microscope (SEM, TESCAN MIRA3, Czech Republic). The carbon structural properties of porous carbons were analyzed by X-ray diffraction (XRD, Bruker D8 Advance, Germany) via Cu K α radiation. The Raman analysis was performed in a laser Raman spectrometer (Raman, Horiba LabRAM HR Evolution, Japan). The TEM analysis was performed by a



FIGURE 1: Synthesis and application of DPRC.

transmission electron microscope (TEM, FEI Tecnai F20, TF30, Holland). The pore structure and the specific surface areas of porous carbons were analyzed by the nitrogen adsorption and desorption isotherm at 77 K, 1.33 Pa (BET, ASAP2010, USA). The particle size parameters of the materials were determined by Laser particle sizer (Hydro 2000Mu England). The contents of metals in the solution before and after adsorption treatment were determined by ICP-AES with inductively coupled plasma emission spectrometer (ICP, PQ9000, Germany).

2.4. Adsorption Experiments. The battery waste solution was diluted in 100 times to get solution A, and the concentrations of Ni, Co, and Mn ions in battery waste solution A are 464 g/L, 408 g/L, and 248 g/L, respectively. The battery waste solution was diluted in 2 times to get solution B.

In adsorption process, 50 mL of solution A and B was, respectively, put into two beakers, and 0.3-g rice husk activated carbon was added to each, kept at 30°C in a constant temperature magnetic stirrer, pH was adjusted to 5, stirred for 2 h, the adsorption solution was removed and filtered, and the change of adsorption solution content was analyzed. The content of multivalent ions in rice husk solution before and after porous carbon adsorption treatment was determined by ICP-AES.

3. Results and Discussion

3.1. Characterization of Samples. Figure 2 shows the typical SEM images of obtained porous carbons. It can be seen from the Figures 2(a) and 2(b) that both the pickled rice husk chars (PRC) and unpickled rice husk chars (RC) have pores, and the pore structure of the RC is not obvious. Figure 2(c) shows the diagram of rice husk carbon without acid pickling and direct desilication (DRC). The comparison result between Figures 2(c) and 2(d) shows that the pore structure distribution of DPRC is more closely distributed. Therefore, pickling treatment promotes the development of pores in rice husk char. After desilication treatment process, the Si-rich protective layer structure on the outer surfaces of PRC disappeared. The outer surface of DPRC showed a rough morphology, and part of the pore structure was exposed.

In order to investigate the effect of temperature on porous carbon, DPRC-500°C and DPRC-600°C were prepared. Figure 3 shows clearly that the surface of the PRC is relatively smooth without a large number of pores, while the surface roughness of the DPRC increases. Besides, as can be seen from the comparison between Figures 3(c) and 3(d), when the carbonization temperature was 600°C, most of the rice husk shell is peeled off, showing the internal network porous structure, and the pore size distribution is more uniform. Therefore, the carbonization temperature has a certain influence on the structure of porous carbon.

TEM characterization was conducted to further characterize the morphology of rice husk chars before and after desilication. Figure 4 shows the TEM images of PRC-600°C (Figures 4(a), 4(b)) and DPRC-600°C (Figures 4(c), 4(d)). It can be seen from Figures 4(a), 4(b), PRC-600°C has typical porous structure, and its surface pore size is about 25–30 nm. As shown in Figures 4(c), 4(d), DPRC-600°C has a looser porous structure, and the pores of the rice husk carbon material after desilication are more flourishing and obviously enlarged. The pore size is about 50–60 nm. The results indicate rice husk chars after desilication has more flourishing pore structure and larger pore size.

The colors of the desilication filtrate at different carbonization temperatures are shown in Figures 5(a) and 5(b). Its color changes with the increase of carbonization temperature. The 500°C desilication filtrate is light yellow, and the 600°C desilication filtrate is colorless and transparent. When the carbonization temperature is low, part of the tar produced during rice husk carbonization will adhere to the surface, and the viscosity of tar is high. When dissolved in sodium hydroxide solution, the solution changes from colorless to pale yellow. The adhesion of tar will reduce the specific surface area of the obtained rice husk char; that is, the effective contact area during the desilication reaction will decrease, thus reducing the reaction efficiency. Therefore, when the carbonization temperature is raised to 600°C, it is conducive to the further volatilization of organic matter, the pyrolysis of tar into small molecules, and the improvement of desilication efficiency.

Figures 5(c) and 5(d) is the solution diagram of the desilication filtrate treated with acid at 600°C. Some white floccules can be seen in the Figure 4(a). After standing

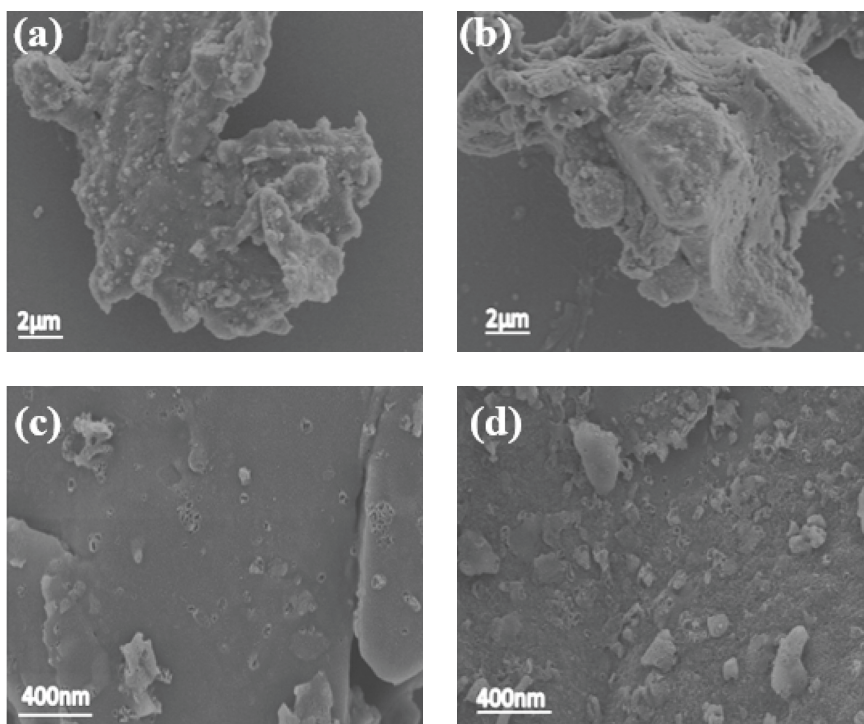


FIGURE 2: SEM images of RC (a) and PRC (b); SEM images of DRC (c) and DPRC (d).

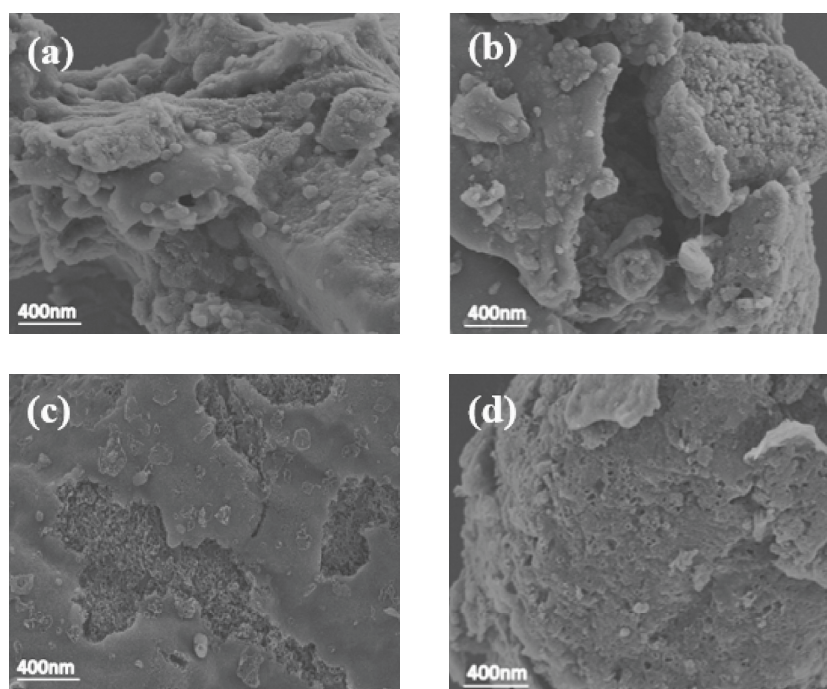


FIGURE 3: SEM of PRC-500°C (a) and PRC-600°C (b); SEM images of DPRC-500°C (c) and DPRC-600°C (d).

for a period of time, hydrochloric acid reacts with sodium silicate in the filtrate to form a gel, indicating that silicon dioxide dissolves from PRC during hot-base desilication. Therefore, combined with the SEM analysis, the optimum carbonization temperature of the rice husk char is 600°C.

The XRD patterns of PRC-600°C, DPRC-600°C, and DPRC-500°C are shown in Figure 6(a). All samples exhibited two typical diffraction peaks at around 22° and 45° corresponding to the diffuse reflection of amorphous nature and low graphitization degree of carbon framework. The existence of the amorphous structure may be due to the

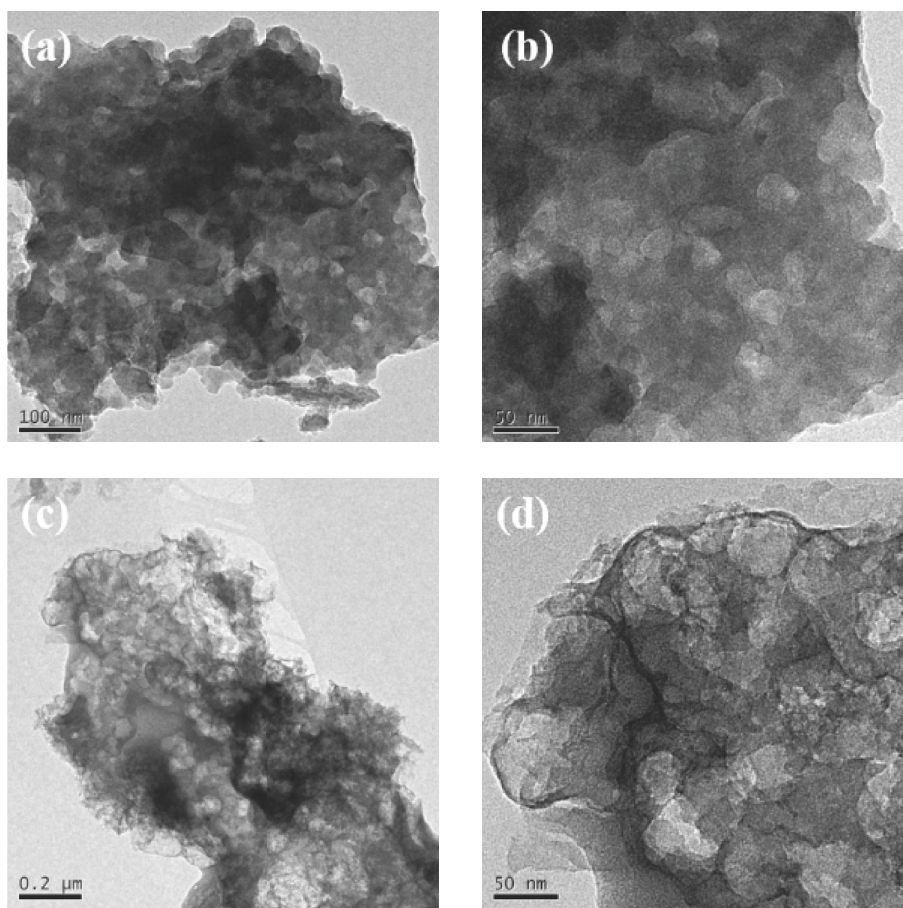


FIGURE 4: TEM of PRC-600°C (a), (b) and DPRC-600°C (c), (d).

diffraction overlap between the silica crystal plane and the carbon (002) crystal plane in rice husk [53].

XRD patterns also show that the DPRC-500°C and DPRC-600°C phase structures are similar. Compared with the other two curves, the diffraction peak shape of DPRC-600°C in the range of 15~30° becomes wider. This may be caused by the further decomposition of organic matter during high temperature pyrolysis, which increases the carbon disorder degree. In the process of hot NaOH treatment, the dissolution of silica will also reduce the intensity and shape of the diffraction peaks of DPRC, but the decrease is relatively low, indicating that the desilicization is not complete. At 2θ of 45°, the intensity of the diffraction peak increases, and the peak shape becomes sharp, which indicates that the rice husk char after hot alkali treatment becomes more ordered and regular, and the degree of graphitization increases, which will lead to a decrease in the interlayer spacing of the pore structure and the decrease in the adsorption properties of the material.

The carbon crystallinity of rice husk-derived PRC and DPRC has been presented by Raman spectra as shown in Figure 6(b). The spectra of both PRC and DPRC presented two peaks at 1358 and 1591 cm^{-1} , corresponding to the characteristic *D* (structural defects associated with disordered carbon structure) band and *G* (graphite crystals associated with sp^2 -ordered carbon structure) band,

respectively [54]. The ratio of relative intensity of the two peaks (I_D/I_G) for PRC and DPRC was found to be 2.94 and 2.73, respectively. It indicated that the carbon composite obtained from pyrolysis of rice husk sample after NaOH desilication treatment had a higher graphitization degree. Raman results are consistent with XRD results. After desilication, rice husk carbon will form original defects and form porous structure, resulting in a large specific surface area, which is conducive to ion adsorption.

Particle size parameters of PRC and DPRC are shown in Table 1. The particle size of PRC is less than 5.965 μm ; accounting for 10%, the average particle size is 45.184 μm , and 90% of the particles are less than 111.909 μm in size. The average particle size of the DPRC was 31.392 μm , and 90% of the particles were smaller than 89.619 μm . Comparing the two, it can be seen that the particle size of the DPRC has decreased. After carbonization, the epidermal cells where silica is mainly distributed in rice husk were destroyed, and the volatilization of organic matter reduced the connection degree between lignin and silica. In the process of thermo-alkali treatment, silica in rice husk is easy to react with sodium hydroxide and dissolve out, and certain pores are developed. In addition, the dissolution of silica as skeleton will lead to loose material structure, and DPRC will be more easily broken in subsequent grinding. These are the main reasons for the smaller particle size of DPRC.

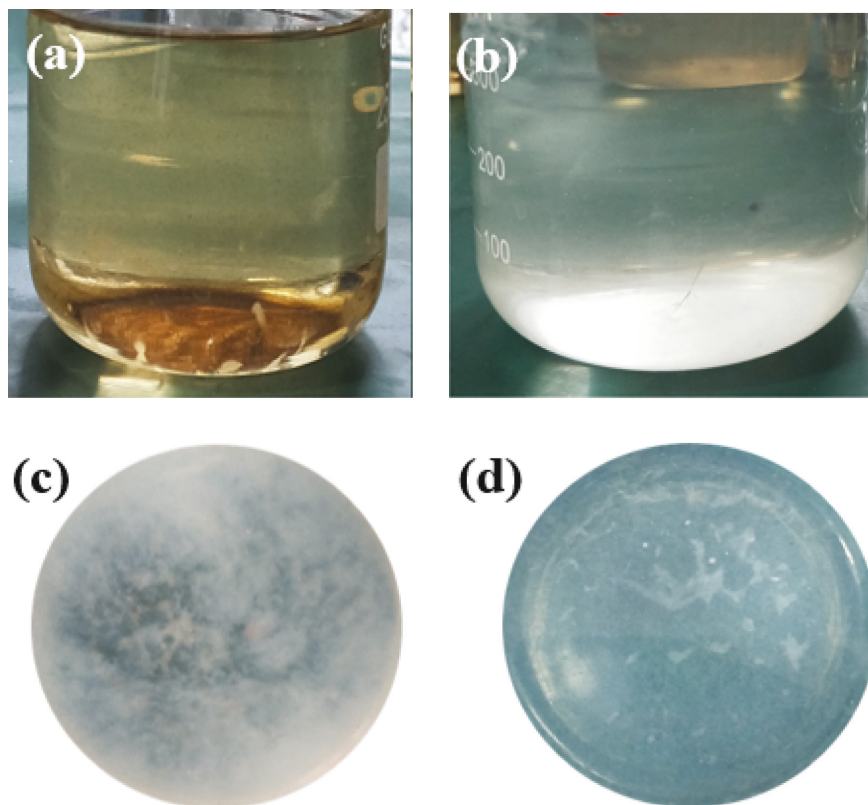


FIGURE 5: 500°C desilicization filtrate (a), 600°C desilicization filtrate (b); solution after acid treatment of desilicization filtrate at 600°C (c) and solution after standing for 24 h (d).

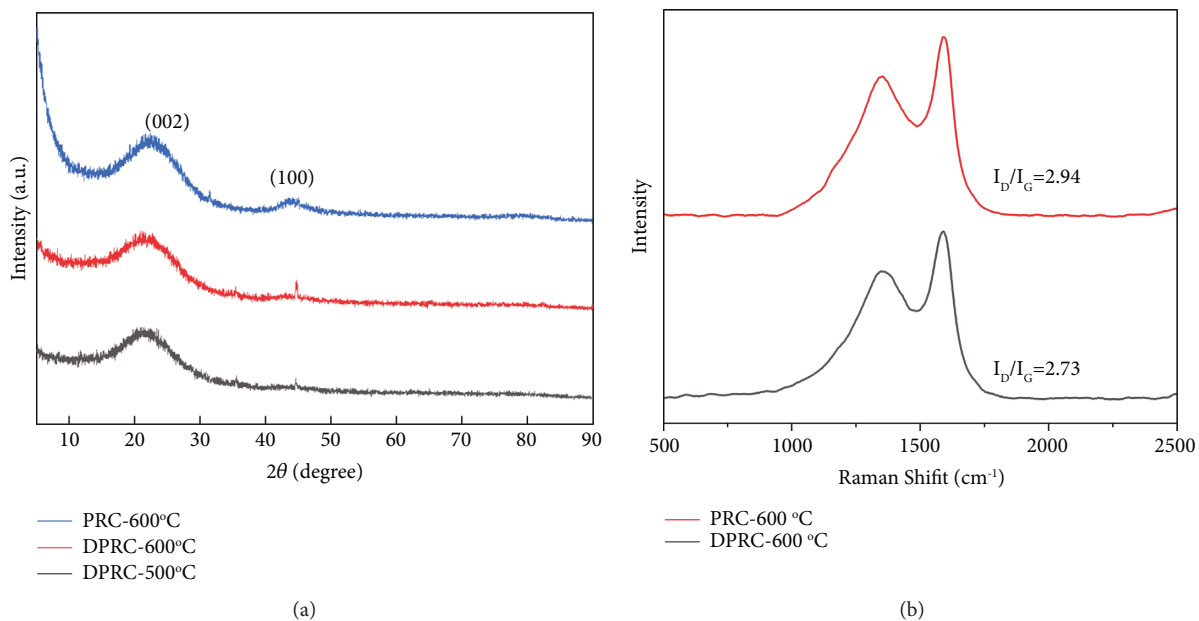


FIGURE 6: (a) XRD patterns of PRC-600°C, DPRC-600°C, and DPRC-500°C. (b) Raman spectra of PRC-600°C and DPRC-600°C.

Silica is mainly concentrated in the striated outer skin of rice husk, especially the raised part. After carbonization, the epidermal cells of rice husk were destroyed, and organic matter was volatilized at high temperature, which reduced the binding degree of lignin and silica. In the process of thermo-alkali treatment, silica in rice husk is easy to react

with sodium hydroxide to precipitate and form certain pores. At the same time, silica acts as a skeleton, and its dissolution leads to loose structure, which explain why DPRC is more easily broken and has smaller particle size.

The pore structure and the pore size distribution of porous carbons are investigated via the N_2 adsorption/desorption

TABLE 1: Particle size analysis of PRC and DPRC.

Samples	PRC	DPRC
Surface area average particle size (μm)	14.447	11.840
Volume average particle size (μm)	51.993	39.919
D (0.1) (μm)	5.965	5.010
D (0.5) (μm)	45.184	31.392
D (0.9) (μm)	111.909	89.619

isotherms as illustrated in Figure 7. As seen from the Figure 7(a), the N_2 adsorbed increases sharply when the value of P/P_0 is under 0.1 and it indicates the existence of micropores. Then, with the increase of relative pressure, the adsorption capacity increases gradually. When $P/P_0 > 0.5$, there is a hysteresis loop, and the adsorption capacity of the material continues to increase with the increase of the relative pressure. When the relative pressure is 1.0, the adsorption value reaches the maximum, indicating that there is a certain amount of mesopores in the sample. The initial part of the isotherm is due to the volume filling effect of the micropores, which can complete the adsorption equilibrium in a relatively short time. However, with the increasing relative pressure, the microporous adsorption gradually transformed into mesoporous adsorption, and capillary condensation occurred in the mesopores, which increased the adsorption amount of N_2 . It can be seen from the Figure 7(a) that N_2 adsorption-desorption isotherms of the two rice husk char conform to typical type IV adsorption isotherms. And PRC has H_4 hysteresis ring, while DPRC has H_3 hysteresis ring. The results show that the desilication process of rice husk char enlarged some micropores into mesopores. With the increase of mesoporous structures and mesoporous pores in the appearance, the isotherms changed accordingly [55]. Therefore, N_2 adsorption capacity of DPRC at $P/P_0 < 0.1$ microporous adsorption stage is less than that of rice husk char. As the number of mesopores increased, the maximum N_2 adsorption of DPRC was higher than that of PRC and the hysteresis ring of desilicated rice husk char appeared earlier. As it can be seen from Figure 7(b), the difference in pore structure between PRC and DPRC is mainly in the mesoporous region of 2–50 nm. DPRC has a larger internal pore size, with fewer mesopores in the range of 2–17 nm than PRC, and more pore sizes in the range of 17–50 nm. This indicates that desilication sample is a kind of mesoporous material with less micropore number, more mesoporous number, and larger mesoporous aperture than PRC, which is consistent with the isotherm analysis of nitrogen adsorption and desorption shown in Figure 7(a). The BET results are consistent with TEM observation results.

To further evaluate the impact of desilication treatment, the pore structure characteristics of PRC and DPRC are summarized in Table 2. It was found that desilication treatment increased the values of average pore size and pore volume, especially the mesoporosity. However, DPRC has a BET surface area of $402.10 \text{ m}^2/\text{g}$, which is slightly lower than that of PRC ($470.67 \text{ m}^2/\text{g}$). Combined with the pore size distribution diagrams in Figure 7(b), it can be seen that the number of micropores in the DPRC decreases and the number of mesopores increases, thereby reducing the specific

surface area. This phenomenon is attributable to the removal and destruction of SiO_2 protective layer of PRC, promoting the development and transformation of some micropores to mesopores [56]. In addition, most of the grain size of silica in rice husk is between 8 and 22 nm, while only a small part is between 1 and 7 nm.

3.2. Multivalent Ions Recycling for Spent Battery. SEM images show that DPRC has abundant and uniform pores. BET results show that the specific surface area is $402.10 \text{ m}^2/\text{g}$. As a result, DPRC is easy to form physical and chemical adsorption with multivalent ions in wastewater, which has certain adsorption and purification effects. Figure 8 show the comparison of the adsorption capacity of 0.30 g of rice husk char to treat 50 mL of high and low concentration battery wastewater. The adsorption capacity of Ni, Co, and Mn ions by DPRC in high-concentration A solution is 7.00 mg/g, 4.84 mg/g, and 2.67 mg/g, respectively. While in the low-concentration B solution, the adsorption capacity is 5.00 mg/g, 2.34 mg/g, and 1.84 mg/g, respectively. The results show that DPRC has a large adsorption capacity for A solution. This may be because the increase of metal ion concentration increases the probability of ion contact collision with DPRC adsorption site of rice husk. Therefore, the filling rate of DPRC adsorption site by ion adsorption material is increased, and the adsorption capacity of the material is increased. At the same time, the adsorption capacity of Ni on the DPRC is the largest, followed by Co and Mn. The reason for this phenomenon may be that the competitive adsorption of multivalent ions and the adsorption of Co and Mn on DPRC are affected by the saturated adsorption of Ni. On the other hand, the maximum adsorption capacity of different types of biochar for various multivalent metals in water is compared and shown in Table 3. From the results of reference [54–59], as-prepared DPRC has a satisfying multivalent metals adsorption capacity.

3.3. Adsorption Isotherms. The adsorption isotherms were performed with different initial concentrations ranging from 40 to 900 mg/L, at optimized pH of 5. The adsorbent dose is 300 mg with constant agitation at a fixed duration of 120 min. Different initial concentrations of wastewater were prepared by proper dilution of 105.92 g/L battery wastewater with distilled water, and the results are presented in Figure 9. With an increase of total concentration of Ni, Co, and Mn ions from 40 to 900 mg/L, the equilibrium adsorption capacity of Ni, Co, and Mn ions has increased from 2.96 to 14.5 mg/g. It has been established that as the initial concentration of Ni, Co, and Mn ion solution increased, the amount of these ions adsorbed per unit mass of the adsorbents has a substantial increase. It may be because the rate of adsorption occurred at reduced pace but increasing the concentration resulting in the competition of binding sites on the adsorbents by ions, thereby increasing adsorption capacity at lower initial metal ion concentration [63]. Then, it has a smaller increase at higher concentration, which is due to the saturation of binding sites. This occurs due to an

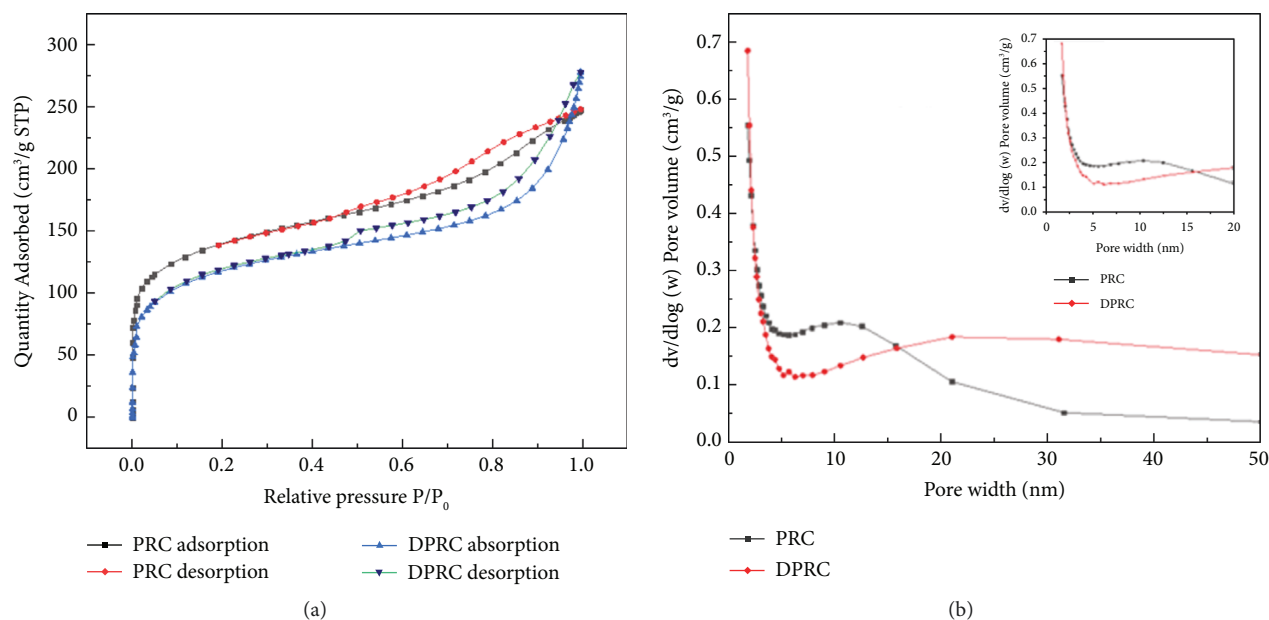


FIGURE 7: Nitrogen adsorption-desorption isotherms of PRC and DPRC (a); BJH pore size distribution of PRC and DPRC (b).

TABLE 2: Void correlation coefficient of PRC and DPRC.

Parameters	PRC	DPRC
BET specific surface area (m ² /g)	470.669	402.092
Pore volume (cm ³ /g)	0.381	0.410
Average pore size (nm)	3.240	4.077
Mesopore average pore size (nm)	4.077	5.168
Average pore size of micropores (nm)	1.018	1.019

TABLE 3: Maximum adsorption capacities of different types of biochar to different multivalent metal ions according to references [54–59].

Material type	Adsorption capacity (mg/g) to multivalent metal ions		
Hardwood	6.79 Cu (II)	4.54 Zn (II)	[57]
Corn cob	17.21 Cd (II)		[58]
Mushroom-stick biochar	21.0 Pb (II)	9.80 Ni (II)	[59]
Rice straw	10.10 Cr (VI)		[60]
Sawdust biochar	15.10 Cu (II)		[61]
Peanut shells biochar	4.00 Cd (II)	22.82 Pb (II)	[62]

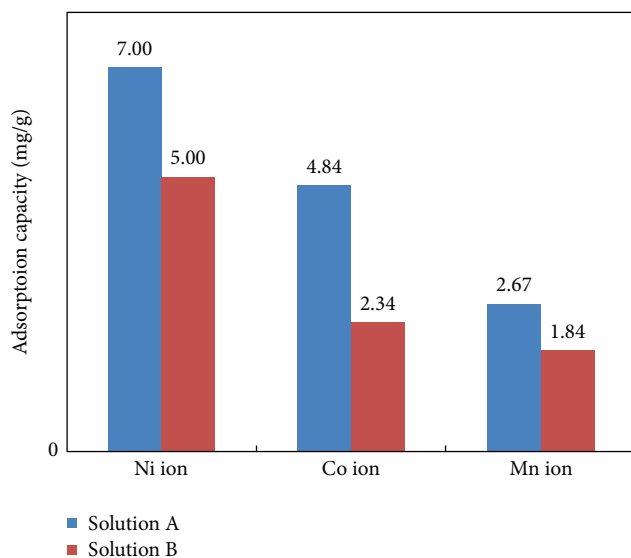


FIGURE 8: Ions adsorption capacity of DPRC.

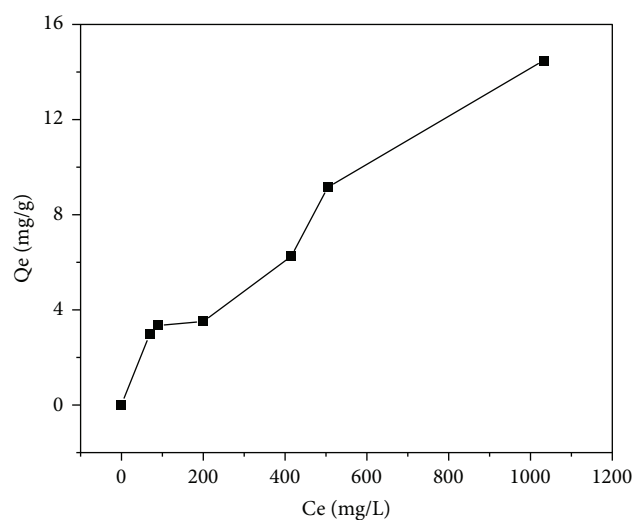


FIGURE 9: Adsorption capacity of concentration of different initial Ni, Co, and Mn ions by DPRC-600°C.

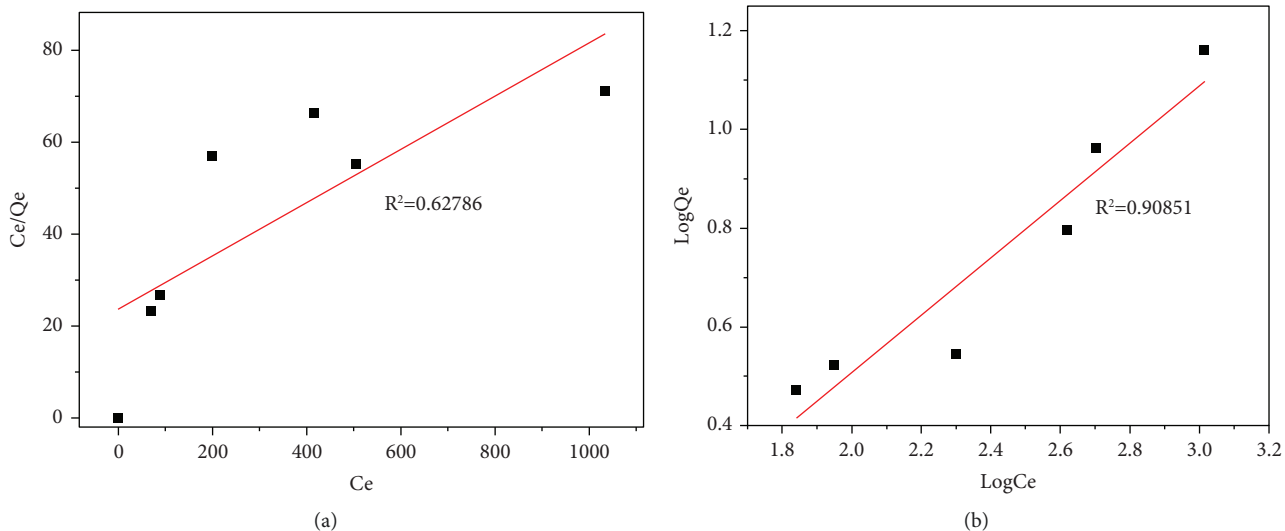


FIGURE 10: Langmuir plot (a) and Freundlich plot (b) for Ni, Co, and Mn adsorption on DPRC-600°C.

TABLE 4: Isotherm constant for the adsorption of Ni, Co, and Mn ions by DPRC-600°C.

	Langmuir			Freundlich		
	q_m	K_L	R^2	K_f	n	R^2
DPRC-600°C	17.2592	0.0245	0.6279	0.2230	1.7235	0.9085

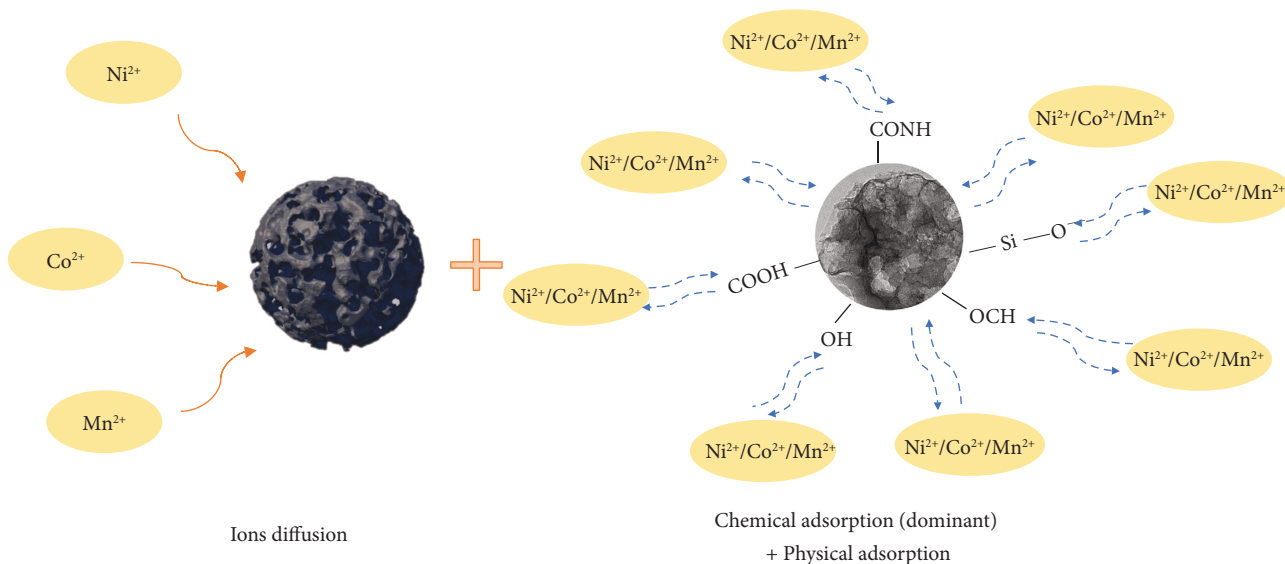


FIGURE 11: Possible adsorption mechanism of Ni, Co, and Mn ions on the DPRC surface.

increase in a number of ions competing for existing binding sites in the adsorbents [64].

In order to study the adsorption mechanism of DPRC for Ni, Co, and Mn ions, the adsorption isotherms were fitted with Langmuir and Freundlich models, respectively.

3.4. Langmuir Isotherm. The linearized form of this isotherm model can be represented as follows:

$$\frac{C_e}{q_e} = \frac{1}{KLq_m} + \frac{C_e}{qm} \tag{1}$$

3.5. Freundlich Isotherm. The heterogeneous sorption linear model of Freundlich isotherm is expressed by the following relationship:

$$\log q_e = \log K_f + \frac{1}{n} \log C_e. \quad (2)$$

The correlation coefficient (R^2) obtained from the linear plot of Langmuir isotherm model (Figure 10(a)) for the study is 0.62786. And the correlation coefficient (R^2) obtained from the linear plot of Freundlich isotherm model (Figure 10(b)) for the study is 0.90851. It demonstrated a good fit in the Freundlich model for DPRC-600°C rather than the Langmuir isotherm model. As shown in Table 4, according to literature reports for Freundlich model [65], when the value of $1/n = 1$, the adsorption is linear. When the value of $1/n < 1$, it indicates that chemical action exists in the adsorption process. When the value is close to 0, the adsorbent is heterogeneous surface. Because the value of n is greater than 1, that is, $1/n$ is less than 1 (0.5802), the adsorption of the three multivalent ions on DPRC-600°C is heterogeneous and there is a chemical mechanism in the adsorption process [31, 65].

Based on analysis above and references [63–65], a possible adsorption mechanism of Ni, Co, and Mn ions on the DPRC surface is proposed and shown in Figure 11. After desilication treatment, the pore of rice husk carbon becomes larger, which is conducive to the diffusion of ions and subsequent adsorption. In addition to physical adsorption from these pores, there is chemical adsorption according to the model fitting results, which play an important role in adsorption process. The oxygen-containing functional groups such as hydroxyl, carbonyl, and carboxyl on the surface of DPRC-600°C can be used as adsorption sites for multivalent ions. The isolated pairs of electrons on oxygen atoms in these oxygen-containing functional groups cobond with the external orbitals of multivalent metal ions to form stable complexes to fix multivalent ions [66]. According to metal ion classification, hard metal ions (Co^{2+} , Ni^{2+} , and Mn^{2+}) are adsorbed to the surface of the oxygen-containing functional group (carboxyl and hydroxyl) [67]. In addition, a small amount of silicon-oxygen bonds may exist on the surface of DPRC-600°C though desilication process has been completed, which is also contributed to the adsorption of positive metal ions [68]. Therefore, DPRC has decent adsorption ability for Co^{2+} , Ni^{2+} , and Mn^{2+} , which may be used as an adsorbent to recover multivalent ions from spent batteries.

4. Conclusion

In this study, the facile desilication and activation route showed great ease in raise the porosity of porous carbons derived from a green and sustainable feedstock of rice husk char for recycling multivalent ions in spent battery. Rice husk biochars are prepared at different pyrolysis temperatures, that is, 500 and 600. The effects of different carbonization temperatures and desiliconization processes on the development of material pores are investigated through experiments, and their treatment effects in batteries wastewater are studied. The results show that rice husk char at the carbonization temperature of 600°C after pickling and desilication has abundant pores and uniform pore size distribution. The silica in rice husk char is dissolved after

thermal alkali treatment, and the greatly increased porosity leads to a large increase in the adsorption rate of multivalent ions. Desilicated pickling rice husk char as adsorbent has potential application prospect in multivalent ions recovery of spent batteries.

Data Availability

Data sharing is not applicable to this article as no new data were created or analyzed in this study.

Conflicts of Interest

The authors declare that they have no conflicts of interest.

Acknowledgments

This work was supported by the Scientific Research Project of Hunan Education Department (21B0242), Hunan Provincial Natural Science Foundation of China (2020JJ5962, 2020JJ2058, and 2019JJ40535), and Hunan high-level talent gathering project-innovative talents (No. 2019RS1061).

References

- [1] S. Yang, F. Zhang, H. Ding, P. He, and H. Zhou, "Lithium metal extraction from seawater," *Joule*, vol. 2, no. 9, pp. 1648–1651, 2018.
- [2] W. Lv, Z. Wang, H. Cao, Y. Sun, Y. Zhang, and Z. Sun, "A critical review and analysis on the recycling of spent lithium-ion batteries," *ACS Sustainable Chemistry & Engineering*, vol. 6, no. 2, pp. 1504–1521, 2018.
- [3] J. B. Goodenough and K.-S. Park, "The Li-ion rechargeable battery: a perspective," *Journal of the American Chemical Society*, vol. 135, no. 4, pp. 1167–1176, 2013.
- [4] M. Chen, X. Ma, B. Chen et al., "Recycling end-of-life electric vehicle lithium-ion batteries," *Joule*, vol. 3, no. 11, pp. 2622–2646, 2019.
- [5] L.-F. Zhou, D. Yang, T. Du, H. Gong, and W. B. Luo, "The current process for the recycling of spent lithium ion batteries," *Frontiers of Chemistry*, vol. 8, 2020.
- [6] R. E. Ciez and J. F. Whitacre, "Examining different recycling processes for lithium-ion batteries," *Nature Sustainability*, vol. 2, no. 2, pp. 148–156, 2019.
- [7] Y. Zhao, X. Yuan, L. Jiang et al., "Regeneration and reutilization of cathode materials from spent lithium-ion batteries," *Chemical Engineering Journal*, vol. 383, Article ID 123089, 2020.
- [8] J. Xiao, J. Li, and Z. Xu, "Challenges to future development of spent lithium ion batteries recovery from environmental and technological perspectives," *Environmental Science & Technology*, vol. 54, no. 1, pp. 9–25, 2019.
- [9] F. Arshad, L. Li, K. Amin et al., "A comprehensive review of the advancement in recycling the anode and electrolyte from spent lithium ion batteries," *ACS Sustainable Chemistry & Engineering*, vol. 8, no. 36, pp. 13527–13554, 2020.
- [10] S. A. El-Safty, M. Awual, M. Shenashen, and A. Shahat, "Simultaneous optical detection and extraction of cobalt (II) from lithium ion batteries using nanocollector monoliths," *Sensors and Actuators B: Chemical*, vol. 176, pp. 1015–1025, 2013.
- [11] D. J. Garole, R. Hossain, V. J. Garole, V. Sahajwalla, J. Nerkar, and D. P. Dubal, "Recycle, recover and repurpose strategy of

- spent li-ion Batteries and catalysts: current status and future opportunities,” *ChemSusChem*, vol. 13, no. 12, pp. 3079–3100, 2020.
- [12] D. L. Thompson, J. M. Hartley, S. M. Lambert et al., “The importance of design in lithium ion battery recycling—a critical review,” *Green Chemistry*, vol. 22, no. 22, pp. 7585–7603, 2020.
- [13] Y. Yao, M. Zhu, Z. Zhao, B. Tong, Y. Fan, and Z. Hua, “Hydrometallurgical processes for recycling spent lithium-ion batteries: a critical review,” *ACS Sustainable Chemistry & Engineering*, vol. 6, no. 11, pp. 13611–13627, 2018.
- [14] G. Hu, J. Li, and H. Hou, “A combination of solvent extraction and freeze thaw for oil recovery from petroleum refinery wastewater treatment pond sludge,” *Journal of Hazardous Materials*, vol. 283, pp. 832–840, 2015.
- [15] B. P. Espósito, S. Epsztejn, W. Breuer, and Z. Cabantchik, “A review of fluorescence methods for assessing labile iron in cells and biological fluids,” *Analytical Biochemistry*, vol. 304, no. 1, pp. 1–18, 2002.
- [16] J. Dasgupta, D. Mondal, S. Chakraborty, J. Sikder, S. Curcio, and H. Arafat, “Nanofiltration based water reclamation from tannery effluent following coagulation pretreatment,” *Ecotoxicology and Environmental Safety*, vol. 121, pp. 22–30, 2015.
- [17] R. Shahrokhi-Shahraki, C. Benally, M. G. El-Din, and J. Park, “High efficiency removal of heavy metals using tire-derived activated carbon vs. commercial activated carbon: insights into the adsorption mechanisms,” *Chemosphere*, vol. 264, Article ID 128455, 2021.
- [18] D. Kołodnyńska, J. Krukowska, and P. Thomas, “Comparison of sorption and desorption studies of heavy metal ions from biochar and commercial active carbon,” *Chemical Engineering Journal*, vol. 307, pp. 353–363, 2017.
- [19] M. Safa Gamal, N. Asikin-Mijan, M. Arumugam, U. Rashid, and Y. Taufiq-Yap, “Solvent-free catalytic deoxygenation of palm fatty acid distillate over cobalt and manganese supported on activated carbon originating from waste coconut shell,” *Journal of Analytical and Applied Pyrolysis*, vol. 144, Article ID 104690, 2019.
- [20] L. Esrafil, F. D. Firuzabadi, A. Morsali, and M. L. Hu, “Reuse of pre-designed dual-functional metal organic frameworks (DF-MOFs) after heavy metal removal,” *Journal of Hazardous Materials*, vol. 403, Article ID 123696, 2021.
- [21] N. Abdollahi, S. A. Akbar Razavi, A. Morsali, and M. L. Hu, “High capacity Hg (II) and Pb (II) removal using MOF-based nanocomposite: cooperative effects of pore functionalization and surface-charge modulation,” *Journal of Hazardous Materials*, vol. 387, Article ID 121667, 2020.
- [22] L. Esrafil, A. Morsali, M. L. Hu et al., “Size-selective urea-containing metal-organic frameworks as receptors for anions,” *Inorganic Chemistry*, vol. 59, no. 22, pp. 16421–16429, 2020.
- [23] J. Q. Liu, G. P. Li, W. C. Liu et al., “Two unusual nanocage-based In-MOFs with triazole sites: highly fluorescent sensing for Fe^{3+} and $\text{Cr}_2\text{O}_7^{2-}$, and selective CO_2 capture,” *Chem-PlusChem*, vol. 81, no. 12, pp. 1299–1304, 2016.
- [24] H.-R. Fu, Y. Zhao, Z. Zhou, X. G. Yang, and L. F. Ma, “Neutral ligand TIPA-based two 2D metal-organic frameworks: ultra-high selectivity of $\text{C}_2\text{H}_2/\text{CH}_4$ and efficient sensing and sorption of Cr (VI),” *Dalton Transactions*, vol. 47, no. 11, pp. 3725–3732, 2018.
- [25] G.-X. Wen, M. L. Han, X. Q. Wu et al., “A multi-responsive luminescent sensor based on a super-stable sandwich-type terbium (III)-organic framework,” *Dalton Transactions*, vol. 45, no. 39, pp. 15492–15499, 2016.
- [26] H.-R. Fu, N. Wang, J. H. Qin, M. L. Han, L. F. Ma, and F. Wang, “Spatial confinement of a cationic MOF: a SC-SC approach for high capacity Cr (VI)-oxyanion capture in aqueous solution,” *Chemical Communications*, vol. 54, no. 82, pp. 11645–11648, 2018.
- [27] T. Tamiji and A. Nezamzadeh-Ejehieh, “Sensitive voltammetric determination of bromate by using ion-exchange property of a Sn (II)-clinoptilolite-modified carbon paste electrode,” *Journal of Solid State Electrochemistry*, vol. 23, no. 1, pp. 143–157, 2019.
- [28] M. Nosuhi and A. Nezamzadeh-Ejehieh, “An indirect application aspect of zeolite modified electrodes for voltammetric determination of iodate,” *Journal of Electroanalytical Chemistry*, vol. 810, pp. 119–128, 2018.
- [29] M. Borandegi and A. Nezamzadeh-Ejehieh, “Enhanced removal efficiency of clinoptilolite nano-particles toward Co (II) from aqueous solution by modification with glutamic acid,” *Colloids and Surfaces A: Physicochemical and Engineering Aspects*, vol. 479, pp. 35–45, 2015.
- [30] S. Haghshenas and A. Nezamzadeh-Ejehieh, “Clinoptilolite nanoparticles modified with dimethyl glyoxime as a sensitive modifier for a carbon paste electrode in the voltammetric determination of Ni (II): experimental design by response surface methodology,” *New Journal of Chemistry*, vol. 41, no. 22, pp. 13355–13364, 2017.
- [31] A. Nezamzadeh-Ejehieh and M. Kabiri-Samani, “Effective removal of Ni (II) from aqueous solutions by modification of nano particles of clinoptilolite with dimethylglyoxime,” *Journal of Hazardous Materials*, vol. 260, pp. 339–349, 2013.
- [32] A. Mullick, S. Moullick, and S. Bhattacharjee, “Removal of hexavalent chromium from aqueous solutions by low-cost rice husk-based activated carbon: kinetic and thermodynamic studies,” *Indian Chemical Engineer*, vol. 60, no. 1, pp. 58–71, 2018.
- [33] S. De, A. M. Balu, J. C. van der Waal, and R. Luque, “Biomass-derived porous carbon materials: synthesis and catalytic applications,” *ChemCatChem*, vol. 7, no. 11, pp. 1608–1629, 2015.
- [34] L. A. d. Silva, S. M. S. Borges, P. N. Paulino et al., “Methylene blue oxidation over iron oxide supported on activated carbon derived from peanut hulls,” *Catalysis Today*, vol. 289, pp. 237–248, 2017.
- [35] Z. Guo, Z. Xiao, G. Ren et al., “Natural tea-leaf-derived, ternary-doped 3D porous carbon as a high-performance electrocatalyst for the oxygen reduction reaction,” *Nano Research*, vol. 9, no. 5, pp. 1244–1255, 2016.
- [36] X. Duan, C. Srinivasakannan, X. Wang, F. Wang, and X. Liu, “Synthesis of activated carbon fibers from cotton by microwave induced H_3PO_4 activation,” *Journal of the Taiwan Institute of Chemical Engineers*, vol. 70, pp. 374–381, 2017.
- [37] Q. Liang, Y. Liu, M. Chen et al., “Optimized preparation of activated carbon from coconut shell and municipal sludge,” *Materials Chemistry and Physics*, vol. 241, Article ID 122327, 2020.
- [38] M. M. Alam, M. A. Hossain, M. D. Hossain et al., “The potentiality of rice husk-derived activated carbon: from synthesis to application,” *Processes*, vol. 8, no. 2, p. 203, 2020.
- [39] E. I. El-Shafey, “Behaviour of reduction-sorption of chromium (VI) from an aqueous solution on a modified sorbent from rice husk,” *Water, Air, and Soil Pollution*, vol. 163, no. 1–4, pp. 81–102, 2005.
- [40] H. Jaman, D. Chakraborty, and P. Saha, “A study of the thermodynamics and kinetics of copper adsorption using chemically modified rice husk,” *Clean—Soil, Air, Water*, vol. 37, no. 9, pp. 704–711, 2009.

- [41] N. Yalçın and V. Sevinç, "Studies of the surface area and porosity of activated carbons prepared from rice husks," *Carbon*, vol. 38, no. 14, pp. 1943–1945, 2000.
- [42] Y. Guo, S. Yang, K. Yu, J. Zhao, Z. Wang, and H. Xu, "The preparation and mechanism studies of rice husk based porous carbon," *Materials Chemistry and Physics*, vol. 74, no. 3, pp. 320–323, 2002.
- [43] Y. Guo, K. Yu, Z. Wang, and H. Xu, "Effects of activation conditions on preparation of porous carbon from rice husk," *Carbon*, vol. 41, no. 8, pp. 1645–1648, 2003.
- [44] A. K. Rout and A. Satapathy, "Study on mechanical and tribo-performance of rice-husk filled glass-epoxy hybrid composites," *Materials & Design*, vol. 41, pp. 131–141, 2012.
- [45] O. Amuda, A. Giwa, and I. Bello, "Removal of heavy metal from industrial wastewater using modified activated coconut shell carbon," *Biochemical Engineering Journal*, vol. 36, no. 2, pp. 174–181, 2007.
- [46] S. Maghsoodloo, B. Noroozi, A. Haghi, and G. Sorial, "Consequence of chitosan treating on the adsorption of humic acid by granular activated carbon," *Journal of Hazardous Materials*, vol. 191, no. 1-3, pp. 380–387, 2011.
- [47] M. Hasan, A. Ahmad, and B. Hameed, "Adsorption of reactive dye onto cross-linked chitosan/oil palm ash composite beads," *Chemical Engineering Journal*, vol. 136, no. 2-3, pp. 164–172, 2008.
- [48] K. Yang, L. Zhu, J. Yang, and D. Lin, "Adsorption and correlations of selected aromatic compounds on a KOH-activated carbon with large surface area," *The Science of the Total Environment*, vol. 618, pp. 1677–1684, 2018.
- [49] P. M. Sanka, M. J. Rwiza, and K. M. Mtei, "Removal of selected heavy metal ions from industrial wastewater using rice and corn husk biochar," *Water, Air, & Soil Pollution*, vol. 231, no. 5, pp. 244–313, 2020.
- [50] E. Menya, P. Olupot, H. Storz, M. Lubwama, and Y. Kiros, "Production and performance of activated carbon from rice husks for removal of natural organic matter from water: a review," *Chemical Engineering Research and Design*, vol. 129, pp. 271–296, 2018.
- [51] Y. Ma, H. Zhang, H. Yang, and Y. Zhang, "The effect of acid washing pretreatment on bio-oil production in fast pyrolysis of rice husk," *Cellulose*, vol. 26, no. 15, pp. 8465–8474, 2019.
- [52] E. Vunain, D. Kenneth, and T. Biswick, "Synthesis and characterization of low-cost activated carbon prepared from Malawian baobab fruit shells by H₃PO₄ activation for removal of Cu (II) ions: equilibrium and kinetics studies," *Applied Water Science*, vol. 7, no. 8, pp. 4301–4319, 2017.
- [53] J.-H. Lee, Y.-J. Heo, and S.-J. Park, "Effect of silica removal and steam activation on extra-porous activated carbons from rice husks for methane storage," *International Journal of Hydrogen Energy*, vol. 43, no. 49, pp. 22377–22384, 2018.
- [54] X. Zhu, Y. Liu, G. Luo, F. Qian, S. Zhang, and J. Chen, "Facile fabrication of magnetic carbon composites from hydrochar via simultaneous activation and magnetization for triclosan adsorption," *Environmental Science & Technology*, vol. 48, no. 10, pp. 5840–5848, 2014.
- [55] R.-L. Tseng, "Mesopore control of high surface area NaOH-activated carbon," *Journal of Colloid and Interface Science*, vol. 303, no. 2, pp. 494–502, 2006.
- [56] B. Xue, L. Jin, Z. Chen et al., "The template effect of silica in rice husk for efficient synthesis of the activated carbon based electrode material," *Journal of Alloys and Compounds*, vol. 789, pp. 777–784, 2019.
- [57] X. Chen, G. Chen, L. Chen et al., "Adsorption of copper and zinc by biochars produced from pyrolysis of hardwood and corn straw in aqueous solution," *Bioresource Technology*, vol. 102, no. 19, pp. 8877–8884, 2011.
- [58] M. Moyo, S. T. Lindiwe, E. Sebata, B. C. Nyamunda, and U. Guyo, "Equilibrium, kinetic, and thermodynamic studies on biosorption of Cd (II) from aqueous solution by biochar," *Research on Chemical Intermediates*, vol. 42, no. 2, pp. 1349–1362, 2016.
- [59] X. Wang, X. Li, G. Liu et al., "Mixed heavy metal removal from wastewater by using discarded mushroom-stick biochar: adsorption properties and mechanisms," *Environmental Sciences: Processes & Impacts*, vol. 21, no. 3, pp. 584–592, 2019.
- [60] S. Yuan, M. Hong, H. Li et al., "Contributions and mechanisms of components in modified biochar to adsorb cadmium in aqueous solution," *The Science of the Total Environment*, vol. 733, Article ID 139320, 2020.
- [61] G.-X. Yang and H. Jiang, "Amino modification of biochar for enhanced adsorption of copper ions from synthetic wastewater," *Water Research*, vol. 48, pp. 396–405, 2014.
- [62] Y. Xue, B. Gao, Y. Yao et al., "Hydrogen peroxide modification enhances the ability of biochar (hydrochar) produced from hydrothermal carbonization of peanut hull to remove aqueous heavy metals: batch and column tests," *Chemical Engineering Journal*, vol. 200–202, pp. 673–680, 2012.
- [63] T. Dula, K. Siraj, and S. A. Kitte, "Adsorption of hexavalent chromium from aqueous solution using chemically activated carbon prepared from locally available waste of bamboo (*Oxytenanthera abyssinica*)," *ISRN Environmental Chemistry*, vol. 2014, Article ID 438245, 9 pages, 2014.
- [64] A. Murugesan, T. Vidhyadevi, S. D. Kirupha, L. Ravikumar, and S. Sivanesan, "Removal of chromium (VI) from aqueous solution using chemically modified corncorb-activated carbon: equilibrium and kinetic studies," *Environmental Progress & Sustainable Energy*, vol. 32, no. 3, pp. 673–680, 2013.
- [65] B. Kayranli, "Adsorption of textile dyes onto iron based waterworks sludge from aqueous solution; isotherm, kinetic and thermodynamic study," *Chemical Engineering Journal*, vol. 173, no. 3, pp. 782–791, 2011.
- [66] B. Qiu, X. Tao, H. Wang, W. Li, X. Ding, and H. Chu, "Biochar as a low-cost adsorbent for aqueous heavy metal removal: a review," *Journal of Analytical and Applied Pyrolysis*, vol. 155, Article ID 105081, 2021.
- [67] A. Alfarra, E. Frackowiak, and F. Béguin, "The HSAB concept as a means to interpret the adsorption of metal ions onto activated carbons," *Applied Surface Science*, vol. 228, no. 1–4, pp. 84–92, 2004.
- [68] G. Liu, S. Gui, H. Zhou, F. Zeng, Y. Zhou, and H. Ye, "A strong adsorbent for Cu²⁺: graphene oxide modified with triethanolamine," *Dalton Transactions*, vol. 43, no. 19, pp. 6977–6980, 2014.

Research Article

Amino Acid-Doped Polyaniline Nanotubes as Efficient Adsorbent for Wastewater Treatment

Zhao Zhao, Yimin Yang, Longfei Xu, Zihan Qiu, Ziheng Wang, Yongfeng Luo, and Kun Du 

Hunan Province Key Laboratory of Materials Surface and Interface Science and Technology, College of Materials Science and Engineering, Central South University of Forestry and Technology, Shaoshan South Road, No. 498, Changsha 410004, China

Correspondence should be addressed to Kun Du; dukun@csuft.edu.cn

Received 15 February 2022; Revised 4 May 2022; Accepted 13 May 2022; Published 23 May 2022

Academic Editor: Andrea Petrella

Copyright © 2022 Zhao Zhao et al. This is an open access article distributed under the Creative Commons Attribution License, which permits unrestricted use, distribution, and reproduction in any medium, provided the original work is properly cited.

A natural amino acid-doped polyaniline nanostructure was prepared by a simple in situ chemical polymerization method in an aqueous medium. The structure and morphology of composite material were characterized by FESEM, TEM, FT-IR, and XRD. The results showed that the product possesses a large aspect ratio and a hollow tubular morphology. As-synthesized products were further applied to remove dyes and heavy metal ions from the aqueous solution, which exhibited good removal capacity toward Congo red ($955.6 \text{ mg}\cdot\text{g}^{-1}$) and Cr(VI) ($60.0 \text{ mg}\cdot\text{g}^{-1}$). The adsorption data for the former were found to be well described by the pseudo-first-order kinetic and Langmuir adsorption isotherm model. Thermodynamic studies show that the adsorption of Congo red by GluP is a spontaneous and endothermic process. Moreover, cyclic experiment results show that the polyaniline composites exhibited good recyclability. Therefore, these amino acid-doped polyaniline nanotubes can be expected to be an ideal candidate for the removal of organic dye and heavy metal ions from wastewater.

1. Introduction

With the rapid development of the global economic situation, the global problem of water pollution has become a serious challenge for human society. On the one hand, the increasingly frequent discharge of organically polluted wastewater during various human activities continues to pollute freshwater systems and terrestrial ecosystems. Organic contaminants are widespread in the environment, including pesticides, personal care products, pharmaceuticals, and organic dyes [1–5]. Generally, these emerging pollutants are harmful, bioaccumulating, and persistent and pose a potential threat to aquatic organisms and human beings. On the other hand, rapid industrialization led to a transitional release of heavy metals into the environment. They are usually toxic and carcinogenic and originate mainly from mining activities, petroleum refining, battery manufacture, smelting, and printing. Even more important is the fact that heavy metals can be accumulated in living

organisms for the long term without degradation [5]. Therefore, more and more researchers have been looking for suitable methods to obtain high-quality drinking water free from organic pollutants and heavy metals over the past few decades.

To date, several techniques have been developed for the purification of industrial wastewater, such as biological, physical, and chemical methods. Among the different treatment strategies, physical adsorption is often regarded as one of the most economical and competitive options due to its low cost, high efficiency, and ease of operation [3–5]. Different types of adsorbents, including mesoporous silica composites, metal-organic frameworks, biomass materials, polymer-based materials, and carbon materials, have been applied for pollutant removal from industrial wastewater. However, the development of green and efficient adsorbents remains an ongoing challenge considering ease of operation, cost-effectiveness, eco-friendliness, and reusability for water treatment. Among various water treatment materials,

polymer and polymer-based adsorbents have emerged as effective and promising candidates for removing different pollutants from the environment due to their advantages such as low cost, rich active sites, durability, and easy modification. Inherently conducting polymers, such as poly(phenylenevinylene) (PPV), polyaniline (PANI), polypyrrole (PPy), and polythiophene (PTH), are a special class of synthetic polymers and are extensively studied due to their tunable electrooptic properties and mechanical properties via bearing functional groups of the conjugated chains. As a representative conducting polymer, PANI has been widely explored for diverse applications, including separation, catalysis, sensing, thermoelectric generator, and corrosion protection [6–8]. Meanwhile, PANI is currently one of the most promising adsorbent materials due to its low price, easy synthesis, environmental friendliness, and unique doping/dedoping property [9]. Typically, the molecular structure of polyaniline contains large amounts of amine and imine functional groups, which enable them to interact with various organic/inorganic pollutants present in wastewater. Nonetheless, the adsorption capacity can be limited due to the poor porosity of pure PANI nanomaterials. Further preparation of polyaniline-based adsorbent materials with porous structures (e.g., nanotubes) by simple solutions is therefore particularly important for the continued promotion of efficient wastewater treatment.

Recently, Rana et al. prepared different polyaniline nanostructures with aromatic dopant acids via a facile chemical polymerization in the presence of ammonium persulfate. Results show that the symmetrical positioning of carboxyl groups plays an important role in the formation of polyaniline nanotubes [10]. Inspired by this strategy, we have prepared polyaniline nanotube composites using amino acids as dopant acids for the removal of toxic pollutants from water environment. As an acidic amino acid, glutamate (with two carboxyl groups) is a kind of desirable dopant for regulating the morphology of polyaniline. In this work, therefore, natural glutamic acid was used as a dopant for fabricating polyaniline-based adsorbent with hollow tubular morphology in an aqueous solution at a low temperature. As-synthesized GluP nanotubes were further employed to remove organic dyes (Congo red, methyl orange, indigo carmine, orange G, and crystal violet) and heavy metal ions (Cr^{6+} , Pb^{2+} , and Ni^{2+}) from the aqueous solution. The effects of adsorbent dose, contact time, pH value, and the initial dye concentration were investigated. Meanwhile, adsorption kinetic, isotherm, and thermodynamics of GluP were also studied using Congo red as a model dye molecule. Importantly, the prepared material exhibited a good cycle performance in batch experiments.

2. Experimental

2.1. Materials. Glutamic acid (Glu) and ammonium persulfate (APS) were purchased from Sigma Chemistry (Shanghai, China). Aniline, $\text{K}_2\text{Cr}_2\text{O}_7$, $\text{Pb}(\text{NO}_3)_2$, and $\text{Ni}(\text{NO}_3)_2 \cdot 6\text{H}_2\text{O}$ were obtained from Energy Chemical (Shanghai, China). Dyes used, including Congo red (CR), methyl orange (MO), indigo carmine (IC), orange G (OG),

and crystal violet (CV), were purchased from Innochem (Shanghai, China). All chemicals were used as received without further treatment. Deionized water was used for solution preparation throughout the work.

2.2. Preparation of Amino Acid-Doped Polyaniline Nanotubes.

In a typical reaction, the glutamic acid powder (0.35 mmol) was dissolved in 15 mL of water with continuous stirring at room temperature. Then, the solution of aniline (100 μL , 1.1 mmol) was added and stirred vigorously for 1 hour before being placed in a refrigerator freezer for 30 minutes. After the temperature of the mixtures was reduced to 4°C, the APS (1.1 mmol) aqueous was added dropwise without stirring, and the color of the solution slowly turned from yellow to brown. Eventually, a dark green precipitate was formed after standing for another 24 hours at 4°C. The pellet was washed with water and methanol several times to wash out the oligomers and excess APS from the reaction mixtures. Finally, the product was obtained by vacuum drying at 60°C overnight, named GluP. The same sample without adding amino acid was used as a control (PANI), and the preparation process was similar to the procedure described above.

2.3. Characterization. The morphology and structure of the products were characterized by using field emission scanning electron microscopy (FE-SEM, Zeiss Ultra 55, Germany) and Transmission Electron Microscopy (TEM, HT7800, Hitachi, Japan). X-ray powder diffraction (XRD) patterns were recorded using an XRD diffractometer (Bruker, D8 ADVANCE) at a scan rate of 4 min^{-1} and equipped with $\text{Cu K}\alpha$ radiation ($\lambda = 0.15406 \text{ nm}$) at room temperature in the 2θ range of 10–40°. The surface structure and functional groups of the samples were determined by the Fourier-transform infrared (FT-IR) spectroscopy (Shimadzu, FT-IR-8400S) with the KBr disk method.

2.4. Adsorption Investigation. Typically, the adsorption of the dyes studies was performed with the batch mode in glass vials. An equal amount of adsorbents was added to the reaction mixture with known concentrations of dyes or metal ions and gently stirred continually. Then, an aliquot of the reaction solution was taken out at an appropriate time interval and separated via centrifugation at 12000 rpm for 1 min. The concentration of dyes was monitored by a UV-Vis spectrometer according to the maximum wavelength (λ_{max} 611, 588, 478, 499, and 464 nm for IC, CV, OG, CR, and MO). The metal ion concentration was measured by inductively coupled plasma-optical emission spectroscopy (ICP-OES). The effects of experimental variables affecting adsorption, including the adsorbent dosage, pH value, and the initial dye concentration, were investigated. Besides, the recycling performance of GluP composites was also studied. For the adsorption kinetic studies, 5 mg of amino acid-doped polyaniline nanocomposites was added to 10 mL of dye solution to initiate the reaction, and the pH was fixed at neutral. The adsorption capacity, q_t , and removal efficiency,

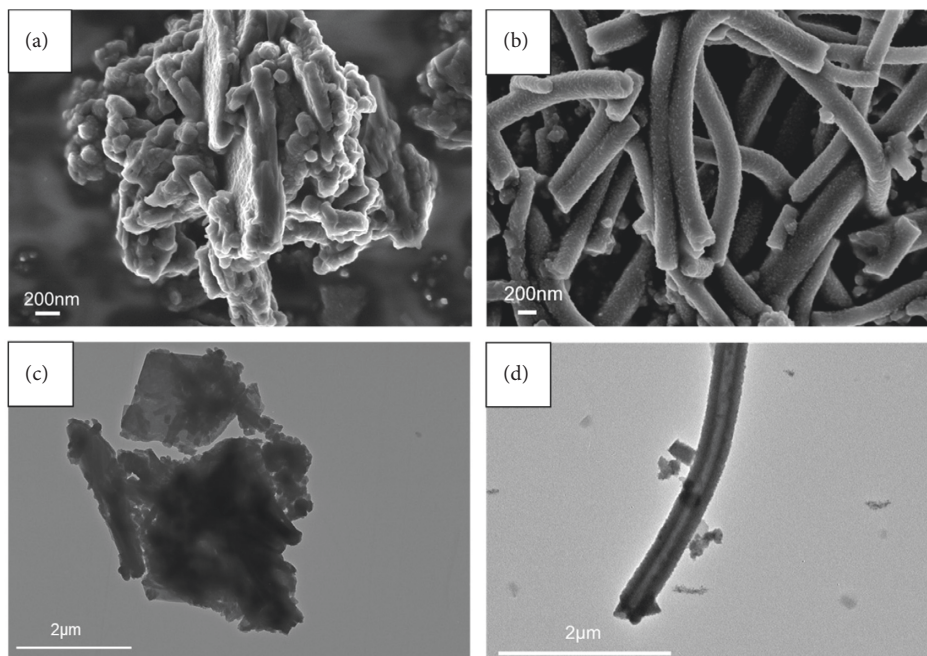


FIGURE 1: FESEM and TEM images of PANI (a, c) and GluP (b, d), respectively.

$R\%$, were calculated based on equations (1) and (2), respectively.

$$q_t = \frac{(C_0 - C_t)V}{m}, \quad (1)$$

$$R\% = \frac{(C_0 - C_t)}{C_0} \times 100, \quad (2)$$

where " C_0 " and " C_t " are the concentration (mg/L) of dye solution at the time "0" and " t ," respectively, " V " is for the total volume of reaction solution (L), and " m " is the mass of adsorbents (g) [3].

3. Results and Discussion

3.1. Characterization of PANI and GluP. GluP nano-composites were obtained by simply mixing glutamic acid with aniline monomer reaction solution under low-temperature conditions. As a comparison, undoped PANI was also prepared under the same conditions. SEM and TEM images of PANI and GluP products are shown in Figure 1.

As shown in Figures 1(a) and 1(c), the morphology of undoped polyaniline (PANI) exhibited inhomogeneous spherical particles with serious agglomeration. This phenomenon is consistent with previously reported results that polyaniline tends to aggregate during the polymerization reaction. In the presence of glutamic acid, the product of aniline oxidation was mainly composed of one-dimensional linear nanotubes with a diameter of ~ 200 nm (Figures 1(b) and 1(d)). Compared with nondoped PANI, the amino acid-doped GluP with a hollow tubular structure and a large aspect ratio may be beneficial in increasing its specific surface area, thereby affecting the adsorption performance. As can be seen, the EDS spectra showed that the polyaniline

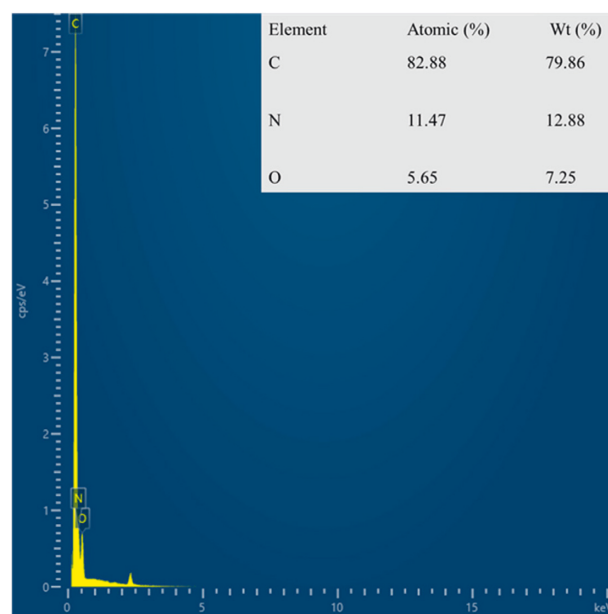


FIGURE 2: EDS spectra and element content analysis table of GluP composites.

tubes were composed of carbon, nitrogen, and oxygen elements (Figure 2), where the oxygen element (7.25%) may be derived from the carboxyl groups of doped glutamic acid.

Fourier-transform infrared (FT-IR) spectra of polyaniline-based adsorbents in the doped and undoped states are shown in Figure 3(a). As can be seen, the different adsorbents have similar adsorption band profiles in the infrared spectrum over the wavelength range of $400\text{--}4000\text{ cm}^{-1}$. The typical stretching vibration bands of polyaniline are observed at 3443 , 1581 , 1501 , 1299 , 1148 , and 823 cm^{-1} [11]. The broad band in the spectra of the samples at around 3443 cm^{-1} was attributed to the stretching

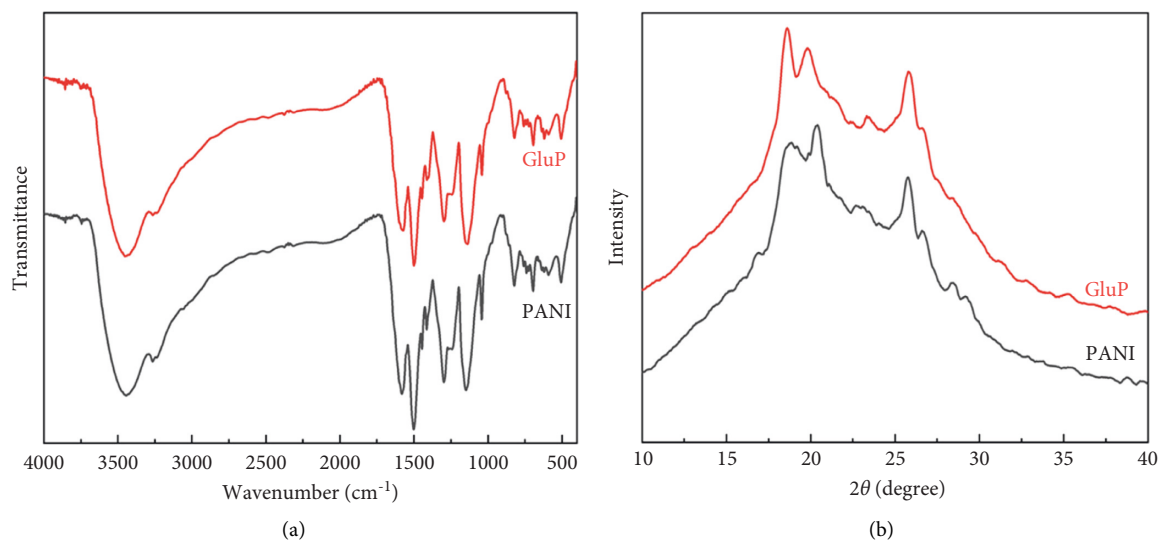


FIGURE 3: FT-IR spectra (a) and XRD patterns (b) of PANI and GluP, respectively.

vibration of N-H bond for polyaniline molecular chains. Peaks at 1581 and 1501 cm^{-1} can correspond to the stretching vibration of the C=C bond in the quinoid and benzenoid rings. The characteristic stretching bands at 1299 cm^{-1} for the C-N bond were associated with the secondary aromatic amine [10–13]. Moreover, the absorption bands at 1148 cm^{-1} and 823 cm^{-1} correspond to the C-H vibration of aromatic in-plane and aromatic out-of-plane deformation, respectively [14, 15]. Figure 3(b) shows the powder X-ray diffraction (XRD) patterns of PANI and GluP. Similarly, there is no obvious change in the XRD spectrum from each other, which indicates that the crystal structure had not been significantly altered after doping amino acids. All samples exhibited three main broad diffraction peaks at $2\theta \approx 18^\circ$, 20.4° , and 25.8° , assigned to (004), (100), and (110) planes of polyaniline. The latter two peaks correspond to the periodicity in parallel and perpendicular directions to the polymer chain of polyaniline, respectively [16, 17]. Meanwhile, the broad diffraction peak of the two samples demonstrates its poor crystallinity.

3.2. Adsorption Results. At first, Congo red (CR) was selected as a model dye molecule to explore the adsorption performance of PANI and GluP. Compared to the adsorption capacity of undoped PANI, glutamic acid-doped GluP has shown higher dye adsorption capacity as shown in Figure 4(a). According to the SEM and TEM images, this result could be explained by the morphological difference between the two types of adsorbent material. For doped GluP, the tubular structure with a large aspect ratio provides more adsorption sites for enhancing the adsorption capacity. To obtain the optimal adsorption capacity between the amount of adsorbent and dye, the concentration of adsorbent (GluP) was changed, while the dye concentration (CR) was kept constant. Results of the UV-Vis absorption spectrum after treatment with different concentrations of adsorbent are presented in Figure 4(b). It is observed that the characteristic UV-Vis absorption of the CR dyes ($\lambda_{\text{max}} = 499\text{ nm}$) in the reaction system gradually decreased and

then somewhat increased as the amount of adsorbent increased. Compared with a lower adsorbent concentration, the excess adsorption sites will not be fully utilized at a higher adsorbent dosage [18, 19]. Meanwhile, the background absorbance of samples was slightly increased beyond a certain concentration of adsorbent $0.25\text{ g}\cdot\text{L}^{-1}$. This may be caused by oligomers of polyaniline in the supernatant after centrifugation. Overall, with the increase of the dosage of GluP, the percentage removal for CR was also increased over a range of concentrations. Maximum adsorption capacities and removal efficiencies are $111.3\text{ mg}\cdot\text{g}^{-1}$ and 92.8% , respectively. And $0.25\text{ g}\cdot\text{L}^{-1}$ was chosen as the fixed dose of GluP for subsequent experiments.

Normally, industrial effluents contain a variety of toxic dyes. To further test the adsorption performance in a broad sense of GluP adsorbent, more dyes were selected for adsorption studies, namely, Congo red (CR), methyl orange (MO), indigo carmine (IC), orange yellow G (OG), and crystalline violet (CV), whose structures are shown in Figure 5.

The adsorption capacity for different dyes has been monitored with different contact times by UV-Vis spectroscopy (Figures 6(a)–6(e)). Figure 6(f) shows the instantaneous adsorption capacity with different contact times calculated by equation (1) for five model dye molecules. The results show that the adsorption efficiency is influenced by the properties of the dye molecule, including the intrinsic charge nature and chemical structure, and the adsorption capacity of anionic dyes is better than that of the cationic type. Among different dye molecules, CR has shown higher uptake efficiency. It is well known that the hydrophobic and electrostatic interactions play a significant role in dye adsorption, while Congo red is an anionic dye with two sulphonic acid groups, two naphthalene rings, and a biphenyl structure in the chemical constitution. This is probably the main reason for its high removal efficiency compared with other dye molecules. In contrast, CV is a cationic dye that has the same positive charge as the polyaniline chain (emeraldine salts). Therefore, it produces the lowest rate of uptake among all dye molecules due to the electrostatic

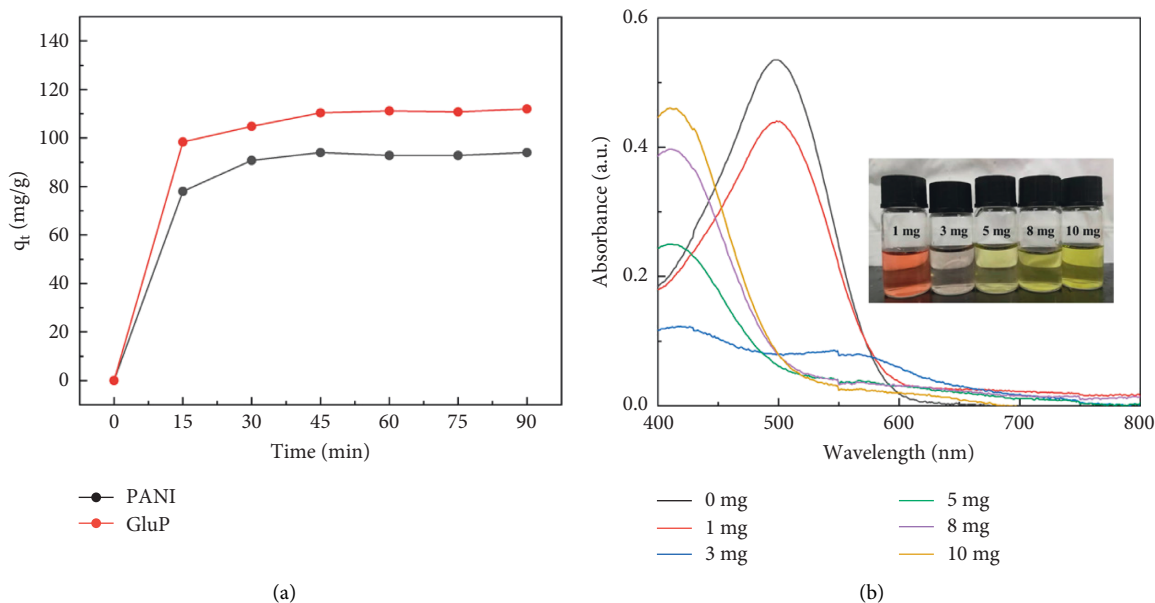


FIGURE 4: (a) Adsorption capacity of PANI and GluP at room temperature for CR ($0.25 \text{ g}\cdot\text{L}^{-1}$ adsorbent, $30 \text{ mg}\cdot\text{L}^{-1}$ dye, $\text{pH}=7$). (b) Ultraviolet-visible spectra of CR with different adsorbent doses at a fixed dye concentration for 3 h ($30 \text{ mg}\cdot\text{L}^{-1}$ dye, 25°C , $\text{pH}=7$).

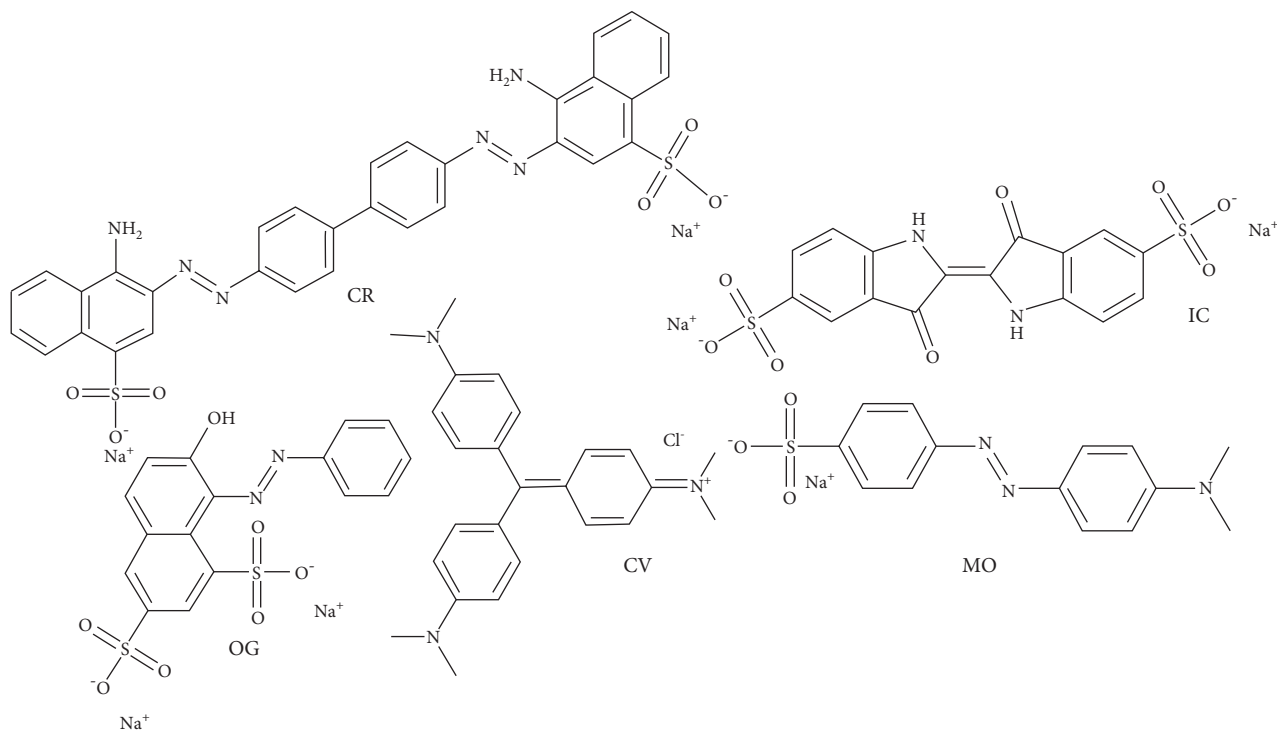


FIGURE 5: Chemical structure of different dyes (CR, MO, IC, OG, and CV).

repulsion between positive charges. Although OG, IC, and MO are anionic molecules, the MO dye has only one negative charge (sulfonic acid group) in comparison with the first two (OG and IC). At the same time, OG and IC with two sulfonic acid groups have comparable dye adsorption efficiency. On the whole, the approximate order of dye adsorption capacity is as follows: $\text{CR} > \text{OG} \geq \text{IC} > \text{MO} > \text{CV}$, and the results are summarized in Table 1.

To improve the adsorption performance of adsorbent GluP for dye CR, two important experimental parameters, including pH value and the initial dye concentration that are relevant for this assay, were also studied. The effect of solution pH on adsorption capacity was first investigated by batch adsorption experiments. During the adsorption process, the environmental pH has a direct impact on the surface charge of the adsorbent and the adsorbate [19]. As

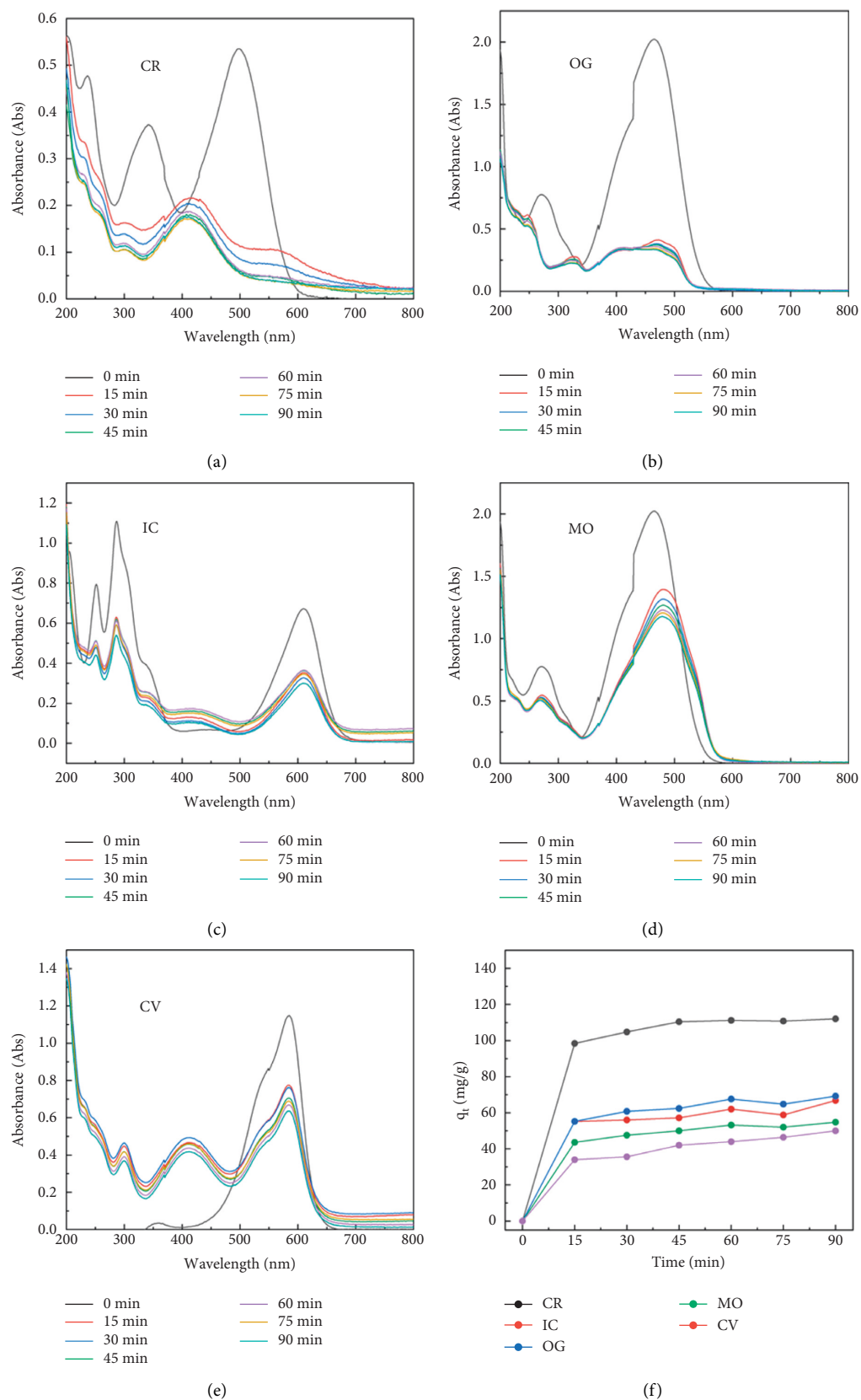


FIGURE 6: UV-Vis spectra of GluP adsorbent dispersed in aqueous solution collected at different time intervals, including (a) CR, (b) OG, (c) IC, (d) MO, and (e) CV. (f) The different adsorption capacity for five types of dye with GluP adsorbent at room temperature and pH 7 ($0.25 \text{ g}\cdot\text{L}^{-1}$ adsorbent, $30 \text{ mg}\cdot\text{L}^{-1}$ dye).

TABLE 1: Adsorption efficiency for different dyes.

Dye	λ_{\max} (nm)	Dye nature	Adsorption (mg/g)
CR	499	Anionic	112.0
OG	478	Anionic	69.2
IC	609	Anionic	66.8
MO	464	Anionic	54.8
CV	588	Cationic	50.0

shown in Figure 7(a), dye removal slightly elevated at pH values ranging from 3 to 5, followed by a rapid decrease in the pH range from 5 to 13. It is observed that the maximum adsorption capacity (about $117.0 \text{ mg}\cdot\text{g}^{-1}$) is reached under a weakly acidic medium (pH 5). With the pH switch from neutral (pH 7) to alkaline (pH 13), the adsorption capacity drops sharply to zero. This indicates that electrostatic attraction and repulsion dominate the interaction between the adsorbent and adsorbent at pH 5 and pH 13, respectively. It is well known that Congo red is a typical anionic diazo dye (pKa 4.5) with two sulfonate functional groups, while the polyaniline is positively charged when the pH value is lower than 10 as its isoelectric point is as high as 10 [20]. At lower ambient pH (pH 3), therefore, the decrease in dye adsorption is likely due to the electrostatic repulsion between adsorbate and adsorbent, both positively charged. As the pH increases, the electrostatic attraction is the main force for the adsorption of dye in the solution (pH 5). When the pH of the reaction solution exceeds the isoelectric point of GluP composites, the adsorbents become negatively charged and cause a decrease in dye adsorption capacity, especially under strongly alkaline conditions (pH 13). This also means that the dye molecules can be eluted, and the adsorbent can be regenerated at a high pH value. Besides, previous studies have also found that the zwitterionic dye molecules tend to aggregate under alkaline conditions, thereby further hindering the adsorption of dye.

Figure 7(b) plots the curve of adsorption capacity at different initial dye concentrations. It is evident that the removal efficiency increases gradually with increasing initial dye concentration in the range of $10\text{--}100 \text{ mg}\cdot\text{L}^{-1}$. When the dye concentration is further increased to $200 \text{ mg}\cdot\text{L}^{-1}$, the adsorption capacity of the adsorbent does not increase any further. The reason for this is that there are sufficient adsorption sites on the surface of the GluP adsorbent at lower initial concentrations, and as the concentration of the added dye increases, the adsorption sites are gradually saturated. That can also be explained by an increase in the adsorbate to adsorbent ratio [18]. Previous studies have found that the initial dye concentration is the main driver of mass transfer from the solution to the adsorbent [21]. With higher initial dye concentrations, the driving force for adsorption is greater, resulting in a stronger affinity of dye molecules to the adsorbent surface. At higher dye concentrations, the decrease in CR adsorption suggested that GluP may be approaching the saturation limit of adsorption [22]. On the other hand, the conductive state of polyaniline (emeraldine salt) contains a considerable quantity of amine and imine functional groups and interacts with some metal ions. Based on this consideration, GluP has been further studied for the removal of heavy metal ions (Cr^{6+} , Pb^{2+} , and Ni^{2+}) from

aqueous solutions (Figure 7(c)). It can be seen that the adsorption capacity for Cr^{6+} is $60.0 \text{ mg}\cdot\text{g}^{-1}$ with a removal efficiency of 100%. For Pb^{2+} and Ni^{2+} , the adsorption capacities are about $40 \text{ mg}\cdot\text{g}^{-1}$ with removal efficiencies of around 67% under identical conditions. This result also implies that the GluP has a good adsorption capacity for hexavalent chromium.

3.3. *Adsorption Behavior of GluP.* To evaluate the possible mechanisms of adsorption, the adsorption kinetics of CR onto GluP were fitted by the pseudo-first-order (PFO) and pseudo-second-order models (PSO), as shown in equations (3) and (4), respectively.

$$q_t = q_e(1 - e^{-k_1 t}), \quad (3)$$

$$q_t = \frac{k_2 q_e^2 t}{1 + k_2 q_e t}, \quad (4)$$

where q_t and q_e are the adsorption capacity ($\text{mg}\cdot\text{g}^{-1}$) at time t (min) and equilibrium and k_1 (min^{-1}) and k_2 ($\text{g}\cdot\text{mg}^{-1}\cdot\text{min}^{-1}$) are the rate constants of PFO and PSO, respectively. Figure 8(a) illustrates the plots of q_t versus t for PFO and PSO models. The equilibrium adsorption capacity, rate constant, and correlation coefficients are determined by corresponding kinetic models, and the results are presented in Table 2. According to the results, it is clearly demonstrated that this adsorption process fitted well with both pseudo-first-order and pseudo-second-order models, while the theoretical q_e value ($110.4 \text{ mg}\cdot\text{g}^{-1}$) calculated by the PFO model agrees better with the experimental data ($112.0 \text{ mg}\cdot\text{g}^{-1}$) compared with the PSO model ($115.4 \text{ mg}\cdot\text{g}^{-1}$). Therefore, the pseudo-first-order model is more suitable for describing the adsorption kinetic behavior of GluP on dye CR [18, 23].

The adsorption isotherms of Congo red on GluP were obtained at a constant temperature as shown in Figure 8(b). The experimental data were fitted by two well-known adsorption isotherm models, including Langmuir and Freundlich. The Langmuir model is commonly used to describe monolayer adsorption processes at homogeneous sites of the adsorbent, and the form can be represented by equation (5), while the latter describes multilayer adsorption on a heterogeneous system and can be defined by equation (6).

$$\frac{C_e}{q_e} = \frac{1}{K_L q_m} + \frac{C_e}{q_m}, \quad (5)$$

$$q_e = K_F C_e^{1/n}, \quad (6)$$

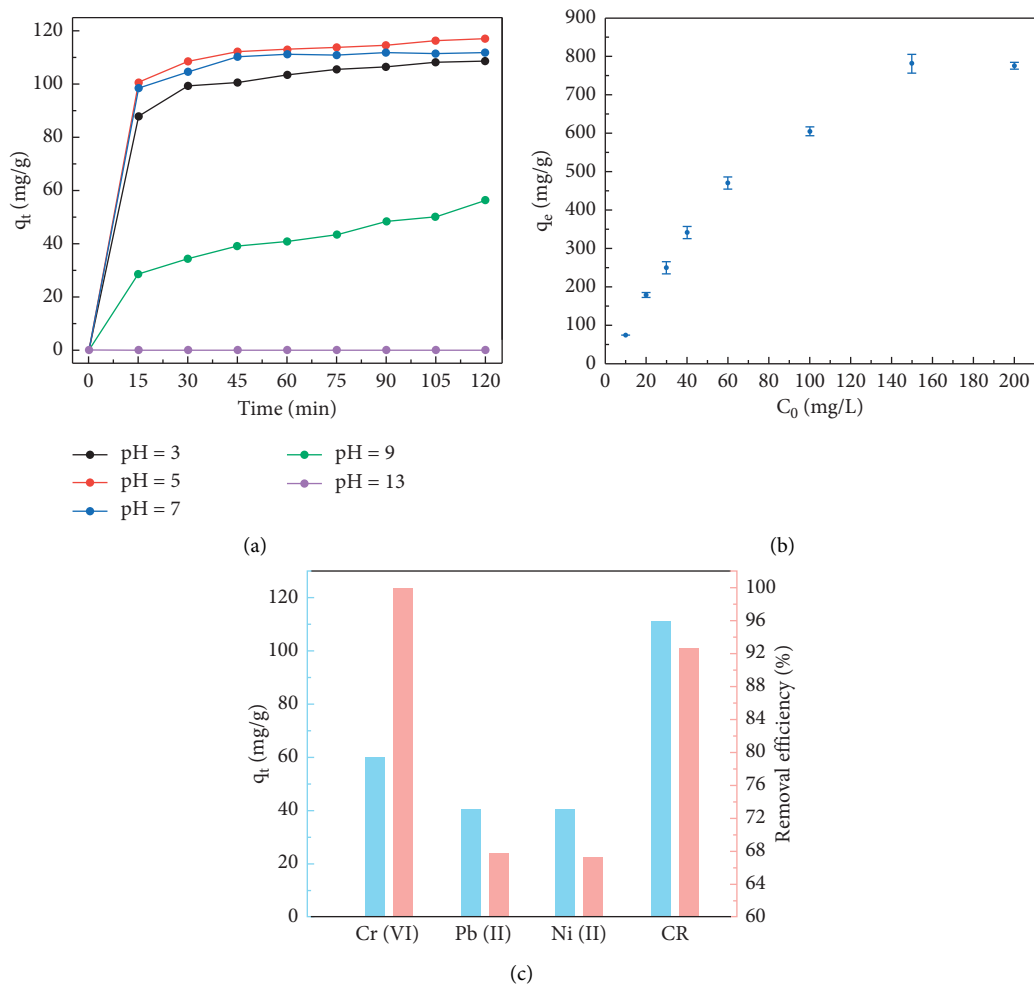


FIGURE 7: The effect of adsorption capacity for different (a) pH value ($30 \text{ mg}\cdot\text{L}^{-1}$ dye, RT), (b) initial dye concentration (RT, pH = 7, $t = 90 \text{ min}$), and (c) metal ion ($30 \text{ mg}\cdot\text{L}^{-1}$ metal ion, RT, pH = 7, $t = 2 \text{ h}$).

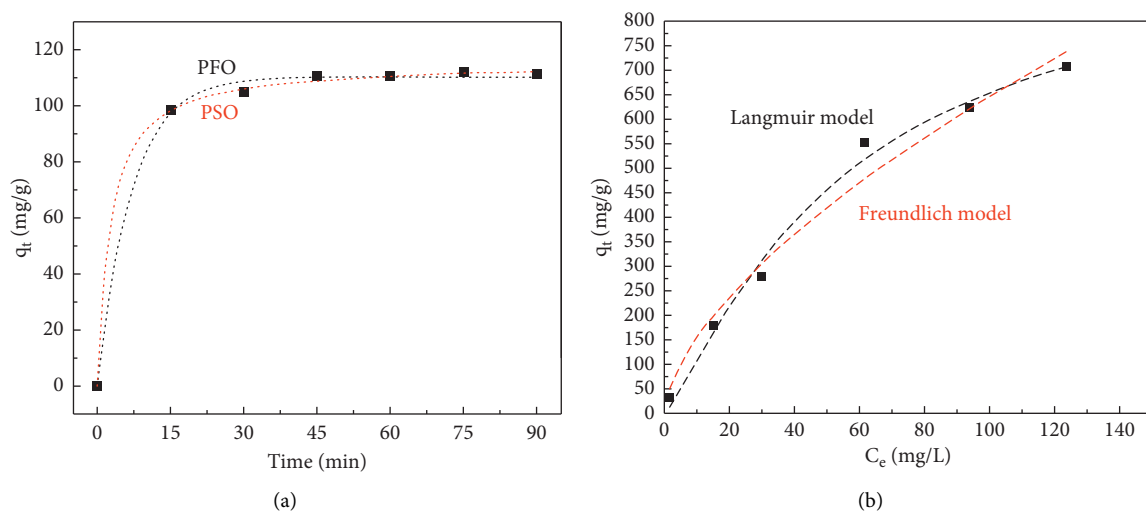


FIGURE 8: (a) Adsorption kinetics of CR onto GluP fitted by PFO and PSO models ($0.25 \text{ g}\cdot\text{L}^{-1}$ adsorbent, $30 \text{ mg}\cdot\text{L}^{-1}$ dye, pH = 7, 25°C). (b) Adsorption isotherms of CR onto GluP fitted by Langmuir and Freundlich models ($0.25 \text{ g}\cdot\text{L}^{-1}$ adsorbent, pH = 7, 25°C).

TABLE 2: Kinetic parameters for the adsorption of CR on GluP at 298 K.

Adsorbent	Pseudo-first-order model			Pseudo-second-order model		
	q_e (mg·g ⁻¹)	k_1 (min ⁻¹)	R^2	q_e (mg·g ⁻¹)	k_2 (g mg ⁻¹ ·min ⁻¹)	R^2
GluP	110.35	0.14	0.99	115.41	0.14	0.99

TABLE 3: Langmuir and Freundlich isotherm fitting parameters at 298 K.

Adsorbent	Langmuir			Freundlich		
	K_L (L·mg ⁻¹)	q_m (mg·g ⁻¹)	R^2	n	K_F (mg ^{1-(1/n)} ·L ^{1/n} ·g ⁻¹)	R^2
GluP	0.007	955.6	0.99	1.61	36.9	0.97

where C_e (mg·L⁻¹) is the equilibrium concentration of dye and q_m (mg·g⁻¹) is the maximum adsorption capacity. K_L (L·mg⁻¹) and K_F (mg^{1-(1/n)}·L^{1/n}·g⁻¹) are constants for Langmuir and Freundlich models, respectively. All corresponding parameters are calculated by these two isotherms, and the results are listed in Table 3. As we can see, the correlation coefficient (R^2) of the Langmuir model (0.99) is better than that of the Freundlich model (0.97), and the value of n is less than 2, which suggests that the adsorption behavior of CR onto the as-synthesized GluP follows the Langmuir monolayer adsorption model [18, 24]. The theoretical maximum adsorption capacity calculated by equation (5) is 955.6 mg·g⁻¹ with 0.25 g·L⁻¹ adsorbent at 298 K. Therefore, the glutamate acid-doped polyaniline is a promising adsorbent for dye (especially Congo red) wastewater treatment. As shown in Table 4, the maximum adsorption capacity of different polyaniline-based adsorbents for Congo red was compared with the values from other reported results.

Moreover, the adsorption behavior of Congo red on GluP composites at different temperatures was also investigated for a better understanding of the adsorption process and the underlying mechanisms. Thus, three sets of adsorption experiments were carried out at three different temperatures (323, 333, and 343 K). The thermal parameters, for instance, the change of Gibbs free energy (ΔG), enthalpy (ΔH), and entropy (ΔS), were calculated by fitting the data to the following thermodynamic equations (7) and (8) [3]:

$$\Delta G = -RT \ln K, \quad (7)$$

$$\ln K = -\frac{\Delta H}{RT} + \frac{\Delta S}{R}, \quad (8)$$

where R is the universal gas constant (8.314 J·mol⁻¹·K⁻¹), T is the absolute temperature in Kelvin, and K represents the thermodynamic equilibrium constant (L·mol⁻¹). The corresponding thermodynamic parameters are presented in Table 5. As can be seen, the values of ΔG (kJ·mol⁻¹) were negative (-12.54, -14.93, and -17.80 kJ/mol at 323, 333, and 343 K, resp.) and decreased with increasing temperature in all tests. These results indicated that the adsorption process was favorable and spontaneous. Meanwhile, the values of ΔH and ΔS for GluP were 74.57 kJ·mol⁻¹ and 0.27 kJ·mol⁻¹, which implies that the adsorption process for Congo red dye molecule was endothermic. This also reflects a good affinity between the adsorbent and the

TABLE 4: Comparison of the adsorption capacity of different adsorbents for Congo red.

Entry	Materials	Maximum adsorption capacity (mg/g)	References
1	PANI	250.01	[25]
2	GS/PANI/Fe ₃ O ₄	248.12	[26]
3	pTSA-pani@GO-CNT	66.66	[27]
4	PANI@TiO ₂ PANI@SiO ₂	93.71	[28]
5	PANI-GO-Fe ₃ O ₄	252.67	[29]
6	PNHM/MnO ₂ / Fe ₃ O ₄	599.49	[30]
7	PANI nanotubes	955.6	This work

TABLE 5: Thermodynamic parameters for removal of Congo red by GluP (adsorbent: 0.25 g·L⁻¹; dye: 60 mg·L⁻¹; pH = 7; and volume: 20 mL).

Adsorbent	ΔG (kJ·mol ⁻¹)			ΔH (kJ·mol ⁻¹)	ΔS (kJ·mol ⁻¹ ·K ⁻¹)
	323 K	333 K	343 K		
GluP	-12.54	-14.93	-17.80	74.57	0.27

adsorbate during adsorption. Additionally, the positive value of ΔS also represents a good affinity between adsorbent (GluP composites) and adsorbate (Congo red) [3, 30].

3.4. Adsorption Mechanisms and Recyclability Study. In general, the main driving forces for the dye adsorption process are combined intermolecular interactions, including hydrogen bonding, π - π stacking interaction, and electrostatic attraction/repulsion. Therefore, the adsorption capacity is closely related to the chemical structure and external environment of adsorbent and adsorbate. If the electrostatic interaction dominates in Congo red dye molecule adsorption process in aqueous solution, the GluP composites will exhibit a lower adsorption capacity due to electrostatic repulsion between adsorbent and adsorbate at pH 3 because the amine and imine functional groups of polyaniline and Congo red are positively charged in such an acid environment. However, this speculation does not match the experimental data since the adsorption uptake of GluP composites was maintained at a fairly high level at pH = 3 (Figure 7(a)). On the other hand, intermolecular hydrogen

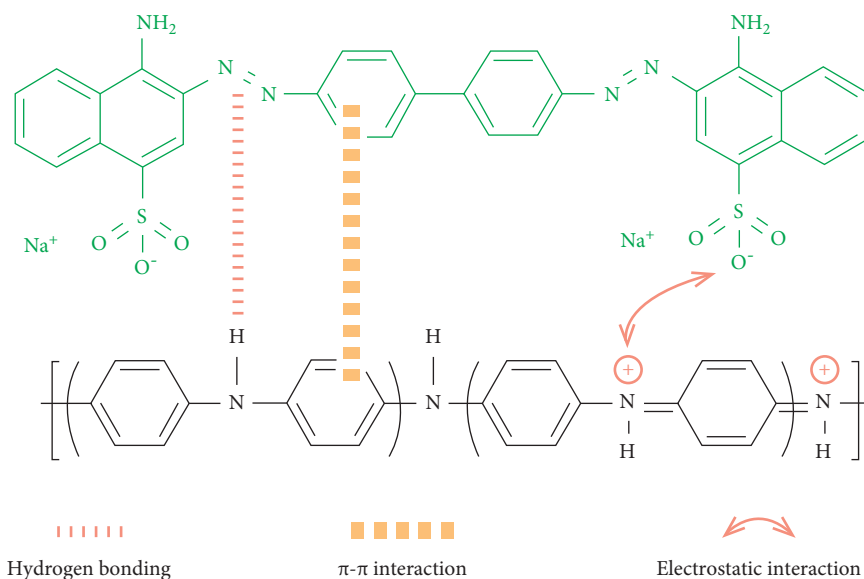


FIGURE 9: Plausible mechanism of Congo red adsorption by GluP composites.

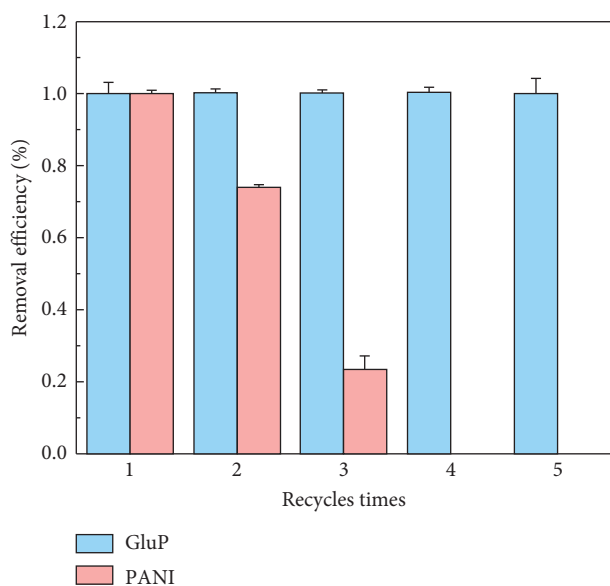


FIGURE 10: Recyclability study (0.5 g/L adsorbent, 30 mg·L⁻¹ dye, pH 7, RT, $t = 60$ min).

bonding of dye molecules usually results in multilayer adsorption [3], while the adsorption of Congo red follows the Langmuir monolayer adsorption model based on previous results (Table 3). This indicates that hydrogen bonding is not the dominant force for adsorption. According to the above analysis, the most likely driving force for Congo red is the π - π stacking interaction between benzene rings of polyaniline and dye molecules. Specifically, electrostatic attraction also plays an important role in dye adsorption, and hydrogen bonding will also be involved in dye-binding (Figure 9).

From a practical application point of view, the reusability of the adsorbent is an important indicator. After adsorption of the Congo red dyes, PANI and GluP

composites were washed appropriately with dilute NaOH solution (1 M) and regenerated by washing with HCl solution (1 M) and rinsed with deionized water. Subsequently, the two adsorbents were recovered by centrifugation and dried in the oven overnight at 60°C. Then, the next round of the same adsorption experiments was repeated several times. The cycle stability of adsorbents was monitored and analyzed by UV-Vis absorption spectrometry, as shown in Figure 10. The results show that GluP still has a very high adsorption efficiency and no significant decrease was observed after five consecutive adsorption cycles. On the contrary, the removal efficiency of pure polyaniline nanomaterials (PANI) rapidly decreases to 74% after two repeated experiments. As the number of cycles further increases, the removal efficiency rapidly drops to zero (during the fourth cycle). This demonstrates that glutamic acid-doped polyaniline nanotubes (GluP) have much better cycle stability than pure polyaniline nanomaterials (PANI) and possess more promising applications.

4. Conclusions

In conclusion, we have successfully prepared an amino acid-doped polyaniline-based adsorbent material with a hollow tubular structure. In the adsorption experiments, the adsorbent presented a good dye removal capacity, as well as better adsorption efficiency for anionic dye molecules. The maximum adsorption capacity was around 117.0 mg·g⁻¹ at pH 5. Besides, the GluP nanocomposites also have excellent adsorption capacity for metal ions, especially hexavalent chromium with an equilibrium adsorption capacity of 60.0 mg·g⁻¹. The adsorption kinetic behavior of GluP was in line with the pseudo-first-order model and Langmuir monolayer adsorption model for the dye Congo red at 298 K. In particular, the material did not significantly reduce the adsorption capacity after five reuses and showed good

recycling performance. Thus, this work not only offers a simple method to prepare polyaniline-based nanomaterials but also presents a promising adsorbent for organic dyes and heavy metal ions.

Data Availability

No data were used to support this study.

Conflicts of Interest

The authors declare that there are no conflicts of interest.

Authors' Contributions

Zhao Zhao and Yimin Yang contributed equally to this study.

Acknowledgments

This work was supported by the Scientific Research Project of Education Department of Hunan Province (no. 19C1907), Hunan Provincial Natural Science Foundation of China (no. 2021JJ41063), Hunan High-Level Talent Gathering Project Innovative Talents (no. 2019RS1061), the Research Startup Foundation of Central South University of Forestry and Technology (no. 2017YJ034), and Hunan Provincial Innovation Foundation for Postgraduate (no. CX20210866).

References

- [1] Z. Salahshoor and A. Shahbazi, "Review of the use of mesoporous silicas for removing dye from textile wastewater," *European Journal of Environmental Sciences*, vol. 4, no. 2, pp. 116–130, 2014.
- [2] N. P. Raval, P. U. Shah, and N. K. Shah, "Adsorptive amputation of hazardous azo dye congo red from wastewater: a critical review," *Environmental Science and Pollution Research*, vol. 23, no. 15, pp. 14810–14853, 2016.
- [3] J. Shen, S. Shahid, I. Amura, A. Sarihan, M. Tian, and E. A. Emanuelsson, "Enhanced adsorption of cationic and anionic dyes from aqueous solutions by polyacid doped polyaniline," *Synthetic Metals*, vol. 245, pp. 151–159, 2018.
- [4] A. K. Badawi, M. Abd Elkodous, and G. A. M. Ali, "Recent advances in dye and metal ion removal using efficient adsorbents and novel nano-based materials: an overview," *RSC Advances*, vol. 11, no. 58, pp. 36528–36553, 2021.
- [5] Y. Fei and Y. H. Hu, "Design, synthesis, and performance of adsorbents for heavy metal removal from wastewater: a review," *Journal of Materials Chemistry*, vol. 10, no. 3, pp. 1047–1085, 2022.
- [6] G. Ćirić-Marjanović, "Recent advances in polyaniline research: polymerization mechanisms, structural aspects, properties and applications," *Synthetic Metals*, vol. 177, no. 1, pp. 1–47, 2013.
- [7] T. H. Qazi, R. Rai, and A. R. Boccaccini, "Tissue engineering of electrically responsive tissues using polyaniline based polymers: a review," *Biomaterials*, vol. 35, no. 33, pp. 9068–9086, 2014.
- [8] F. Habtamu, S. Berhanu, and T. Mender, "Polyaniline supported Ag-doped ZnO nanocomposite: synthesis, characterization, and kinetics study for photocatalytic degradation of malachite green," *Journal of Chemistry*, vol. 2021, Article ID 2451836, 12 pages, 2021.
- [9] A. Samadi, M. Xie, J. Li, H. Shon, C. Zheng, and S. Zhao, "Polyaniline-based adsorbents for aqueous pollutants removal: a review," *Chemical Engineering Journal*, vol. 418, no. 15, Article ID 129425, 2021.
- [10] U. Rana, S. Mondal, J. Sannigrahi et al., "Aromatic bi-tri and tetracarboxylic acid doped polyaniline nanotubes: effect on morphologies and electrical transport properties," *Journal of Materials Chemistry C*, vol. 2, no. 17, pp. 3382–3389, 2014.
- [11] S. Bhadra, S. Chattopadhyay, N. K. Singha, and D. Khastgir, "Improvement of conductivity of electrochemically synthesized polyaniline," *Journal of Applied Polymer Science*, vol. 108, no. 1, pp. 57–64, 2008.
- [12] L. Wang, X. L. Wu, W. H. Xu, X. J. Huang, J. H. Liu, and A. W. Xu, "Stable organic-inorganic hybrid of polyaniline/ α -zirconium phosphate for efficient removal of organic pollutants in water environment," *ACS Applied Materials and Interfaces*, vol. 4, no. 5, pp. 2686–2692, 2012.
- [13] U. Rana, K. Chakrabarti, and S. Malik, "Benzene tetracarboxylic acid doped polyaniline nanostructures: morphological, spectroscopic and electrical characterization," *Journal of Materials Chemistry*, vol. 22, no. 31, pp. 15665–15671, 2012.
- [14] S. Shahabuddin, N. M. Sarih, F. H. Ismail, M. M. Shahid, and N. M. Huang, "Synthesis of chitosan grafted-polyaniline/ Co_3O_4 nanotube nanocomposite and its photocatalytic activity toward methylene blue dye degradation," *RSC Advances*, vol. 5, no. 102, pp. 83857–83867, 2015.
- [15] A. A. Farghali, M. Moussa, and M. H. Khedr, "Synthesis and characterization of novel conductive and magnetic nanocomposites," *Journal of Alloys and Compounds*, vol. 499, no. 1, pp. 98–103, 2010.
- [16] X. Du, Y. Xu, L. Xiong, Y. Bai, J. Zhu, and S. Mao, "Polyaniline with high crystallinity degree: synthesis, structure, and electrochemical properties," *Journal of Applied Polymer Science*, vol. 131, no. 19, pp. 5829–5836, 2014.
- [17] R. M. Khafagy, "Synthesis, characterization, magnetic and electrical properties of the novel conductive and magnetic polyaniline/ MgFe_2O_4 nanocomposite having the core-shell structure," *Journal of Alloys and Compounds*, vol. 509, no. 41, pp. 9849–9857, 2011.
- [18] V. Sharma, P. Rekha, and P. Mohanty, "Nanoporous hypercrosslinked polyaniline: an efficient adsorbent for the adsorptive removal of cationic and anionic dyes," *Journal of Molecular Liquids*, vol. 222, pp. 1091–1100, 2016.
- [19] J. Shen, M. F. Evangelista, G. Mkongo et al., "Efficient defluoridation of water by monetite nanorods," *Adsorption*, vol. 24, no. 2, pp. 135–145, 2018.
- [20] Q. Hu, C. Guo, D. Sun, Y. Ma, B. Qiu, and Z. Guo, "Extracellular polymeric substances induced porous polyaniline for enhanced Cr(VI) removal from wastewater," *ACS Sustainable Chemistry & Engineering*, vol. 5, no. 12, pp. 11788–11796, 2017.
- [21] M. T. Yagub, T. K. Sen, S. Afroze, and H. Ang, "Dye and its removal from aqueous solution by adsorption: a review," *Advances in Colloid and Interface Science*, vol. 209, pp. 172–184, 2014.
- [22] B. N. Patra and D. Majhi, "Removal of anionic dyes from water by potash alum doped polyaniline: investigation of kinetics and thermodynamic parameters of adsorption," *Journal of Physical Chemistry B*, vol. 119, no. 25, pp. 8154–8164, 2015.

- [23] M. H. Mohamed, A. Dolatkah, T. Aboumourad, L. Dehabadi, and L. D. Wilson, "Investigation of templated and supported polyaniline adsorbent materials," *RSC Advances*, vol. 5, no. 9, pp. 6976–6984, 2015.
- [24] J. Xiao, Y. Tan, Y. Song, Q. Zheng, W. Lv, and Z. Xie, "Environmentally friendly reduced graphene oxide as a broad-spectrum adsorbent for anionic and cationic dyes via π - π interactions," *Journal of Materials Chemistry*, vol. 4, no. 31, pp. 12126–12135, 2016.
- [25] H. Chafai, M. Laabd, S. Elbariji, M. Bazzaoui, and A. Albourine, "Study of congo red adsorption on the polyaniline and polypyrrole," *Journal of Dispersion Science and Technology*, vol. 38, no. 6, pp. 832–836, 2017.
- [26] B. Mu, J. Tang, L. Zhang, and A. Wang, "Facile fabrication of superparamagnetic graphene/polyaniline/ Fe_3O_4 nanocomposites for fast magnetic separation and efficient removal of dye," *Scientific Reports*, vol. 7, no. 1, p. 5347, 2017.
- [27] M. O. Ansari, R. Kumar, S. A. Ansari, M. Barakat, A. Alshahrie, and M. H. Cho, "Anion selective pTSA doped polyaniline@graphene oxide-multiwalled carbon nanotube composite for Cr(VI) and congo red adsorption," *Journal of Colloid and Interface Science*, vol. 496, pp. 407–415, 2017.
- [28] M. Maruthapandi, L. Eswaran, J. H. Luong, and A. Gedanken, "Sonochemical preparation of polyaniline@ TiO_2 and polyaniline@ SiO_2 for the removal of anionic and cationic dyes," *Ultrasonics Sonochemistry*, vol. 62, Article ID 104864, 2020.
- [29] C. Lv, J. Zhang, G. Li, H. Xi, M. Ge, and T. Goto, "Facile fabrication of self-assembled lamellar PANI-GO- Fe_3O_4 hybrid nanocomposites with enhanced adsorption capacities and easy recyclicity towards ionic dyes," *Colloids and Surfaces A: Physicochemical and Engineering Aspects*, vol. 585, Article ID 124147, 2020.
- [30] S. Dutta, S. K. Srivastava, B. Gupta, and A. K. Gupta, "Hollow polyaniline microsphere/ MnO_2 / Fe_3O_4 nanocomposites in adsorptive removal of toxic dyes from contaminated water," *ACS Applied Materials & Interfaces*, vol. 13, no. 45, pp. 54324–54338, 2021.

Research Article

Co-pyrolysis of Hardwood Combined with Industrial Pressed Oil Cake and Agricultural Residues for Enhanced Bio-Oil Production

P. Madhu¹, **L. Vidhya**², **S. Vinodha**³, **Shiny Wilson**⁴, **S. Sekar**⁵, **Pravin P. Patil**⁶,
S. Kaliappan⁷, and **S. Prabhakar**⁸

¹Department of Mechanical Engineering, Karpagam College of Engineering, Coimbatore, Tamilnadu 641032, India

²Department of Chemistry, Hindusthan College of Engineering and Technology, Coimbatore, Tamilnadu 641050, India

³Department of Environmental Engineering, Jayaraj Annapackiam CSI College of Engineering, Thoothukudi, Tamilnadu 628617, India

⁴Department of Chemistry, Panimalar Engineering College, Chennai, Tamilnadu 600123, India

⁵Department of Mechanical Engineering, Rajalakshmi Engineering College, Chennai, Tamilnadu 602105, India

⁶Department of Mechanical Engineering, Graphic Era Deemed to be University, Bell Road, Clement Town Dehradun, Uttarakhand 248002, India

⁷Department of Mechanical Engineering, Velammal Institute of Technology, Chennai, Tamilnadu 601204, India

⁸Department of Mechanical Engineering, Automotive Engineering Stream, Wollo University-KIOT, Ethiopia 208

Correspondence should be addressed to S. Prabhakar; prabhakar@kiot.edu.et

Received 17 March 2022; Accepted 26 April 2022; Published 12 May 2022

Academic Editor: Gonggang Liu

Copyright © 2022 P. Madhu et al. This is an open access article distributed under the Creative Commons Attribution License, which permits unrestricted use, distribution, and reproduction in any medium, provided the original work is properly cited.

Lignocellulosic biomass is the potential raw material for the production of biofuels through pyrolysis. It is an effective technique for converting biomass to biofuels. However, biofuel from agricultural residues and woody-based feedstocks shows poor fuel properties due to higher oxygen content. Co-pyrolysis is a promising process to produce high-quality bio-oil by two or more different materials. Forestry, industrial, and agricultural outcomes are the ideal co-feedstocks for improved bio-oil quality. In this study, individual and co-pyrolysis of hardwood, pressed mustard oil cake and corncob were conducted at a temperature of 500°C. Before conducting pyrolysis experiments, thermogravimetric analysis was conducted to evaluate thermal degradation behavior. Through individual pyrolysis, corncob yielded a maximum bio-oil of 43.9 wt%. On the other hand co-pyrolysis on binary blends of hardwood and corncob produced maximum bio-oil of 46.2 wt%. Compared to individual pyrolysis, the binary blend produced more bio-oil, suggesting a synergistic effect between hardwood and corncob. The decreased bio-oil yield of 40.1 wt% during co-pyrolysis of ternary blends suggests negative synergistic effects prejudiced by the volatiles available in the biomass mixture. The improved quantitative synergistic results in the co-pyrolysis process give crucial information for the development of feed-flexible, higher bio-oil production and clean operating systems. The characterization studies on bio-oil by Fourier transform-infrared spectroscopy (FTIR), gas chromatography–mass spectrometry (GC-MS), and ¹H NMR spectroscopy have shown that the bio-oil is a combination of aliphatic and oxygenated compounds. The analysis of the heating value shows that the bio-oil can be utilized as a fuel for heating applications.

1. Introduction

The rapid development of industrialization, the growth of the population, and the shortage of fossil fuels encouraged researchers to find novel alternative energy sources. According to a study conducted in 2009, the availability of coal is decreasing fast and will reach zero in 2112, and it will be

the only fossil resource after 2042 [1]. At present, numerous efforts are ongoing to identify environmentally friendly alternative energy sources. Out of many other alternative energy sources, research on biomass energy has played a significant role. More than half of the research on renewable energy technologies over the past two decades has concentrated on bioenergy (56%) and solar energy (26%) [2]. The

abundant availability of biomass throughout the world can support researchers by creating higher research opportunities. The global available biomass per year was estimated to be 220 billion tonnes [3]. The availability of total biomass resources in a country varies depending on weather conditions and agricultural activities. But compared to solar and wind, it is not a seasonable one. In many countries, biomass is widely used for generating biofuels and chemicals.

In India, biomass is considered an important energy source in view of the benefits it offers. Biomass provides for more than 32% of global primary energy consumption, and about 70% of the world's population relies on it for their energy needs. It is estimated that more than 750 million metric tonnes of waste biomass are generated per year and a surplus of 230 million metric tonnes of biomass is produced from agricultural processes [4]. Bioenergy is a strong alternative for addressing energy demand as well as emission challenges due to carbon neutrality [5]. In this context, thermochemical conversion has been considered a promising option in recent years due to its efficient usage [6]. Pyrolysis is one of the most popular thermochemical conversion processes and has attracted much attention because of the production of high value-added elements and its effective utilization [7]. Biomass is a lignocellulosic substance that is composed mainly of cellulose, hemicellulose, and lignin. In pyrolysis, at elevated temperatures, the macromolecules of the biomass will decompose in an inert atmosphere, leading to the generation of liquid oil, char, and gas [8]. Lignin is the most stable component which does not degrade at low temperature. In some cases, it decomposed when the temperature reached 700°C [9]. Cellulose and hemicellulose are the two polysaccharides which decompose between temperatures of 300 and 400°C. Pyrolysis of higher lignin biomass materials involves endothermic reactions; on the other hand, pyrolysis of lower lignin biomass materials involves an exothermic reaction [10]. Furthermore, it is evident that lignin is the primary determinant for decomposition and yield. According to Di Blasi and Branca [11], cellulose and hemicellulose are the causes of the formation of pyrolysis oil, whereas lignin promotes char and gas products. Due to increased energy density and easier transportation, pyrolysis oil has received a lot of interest among these products. The quantity of biofuel and its properties is generally influenced by feedstock characteristics and the method of pyrolysis [12]. At the same time, major parameters of the pyrolysis process, including reactor temperature, heating rate, residence time, size of the feedstock, and flow rate of the sweep gas, also influence the yield quantity as well as quality.

Co-pyrolysis is the alternative technique of using two or more different feedstocks to improve the quality of bio-oils. Several studies have focused on employing various types of feedstocks for the co-pyrolysis process and have achieved good results [13]. The interaction between the raw materials and synergistic effects is influencing the yield percentage of the bio-oil [14]. Sowmya Dhanalakshmi et al. [15] utilized palm shell and lemongrass for the co-pyrolysis process and produced 47.10 wt% of pyrolysis oil. Hope et al. [16] conducted a co-pyrolysis process by blending three different biomasses such as sugarcane bagasse, poppy capsule pulp,

and rice husk. Through individual pyrolysis, sugarcane bagasse pyrolysis yielded a maximum bio-oil of 27.4%. But co-pyrolysis of these biomass materials yielded more bio-oil than individual pyrolysis due to synergistic interactions. Wood and agricultural residues are the common feedstocks used for pyrolysis process. In many studies, wood and wood wastes are combined with many feedstocks to produce bio-fuels. Chen et al. [17] combined wood wastes with municipal sewage sludge for the production of biochar at 800°C. Echresh Zadeh et al. [18] utilized hardwood and softwood for bio-oil production. The obtained oil through this study was 30.2 wt% and 24.4 wt%. Co-pyrolysis of coal, rice straw, and wood was conducted by Krerkkaiwan et al. [13] in order to analyze the synergetic effect. During the reaction, the synergetic effect was obtained by transferring OH and H radicals. Samanya et al. [19] conducted co-pyrolysis experiments on a combination of sewage sludge, hardwood, rapeseed, and straw. In this study, the biomass fuel types had a significant impact on the co-pyrolysis process and bio-oil yield.

The goal of this research is to utilize hardwood, pressed mustard oil cake, and corncob straw for the co-pyrolysis process. These three feedstocks are obtained from forestry, industrial, and agricultural processes. To the best of our knowledge, there were no studies concentrated on the combination of woody, industrial, and agricultural wastes. The experiments are conducted on individual, binary, and ternary blends with the aid of a fixed bed reactor. The work is also aimed to find the interaction of the selected feedstock on the co-pyrolysis process and characterization of the bio-oil products.

2. Materials and Methods

2.1. Materials. The feedstocks used for this study are hardwood, pressed mustard oil cake, and corncob which belong to forestry residues, industrial by-products, and agricultural outcomes. The wooden chips are collected from a nearby saw mill; de-oiled cakes are collected from oil industries; and corncob are collected from nearby agricultural fields in Coimbatore, India. All three types of feedstocks were collected in a separate bag and stored in the laboratory. Before conducting the experiments, the samples were dried in open sunlight for more than a week. The dried samples are then milled and sieved into <0.5 mm in diameter. The sieved samples are further heated to dry for 1 hr at $\pm 100^\circ\text{C}$ to reduce moisture prior to the experiments. The tests were carried out by following ASTM standards. The CHNS analyzer (Elementar Vario EL-III) was employed to find its component analysis.

2.2. Reactor Set Up. The reactor employed for this investigation is a batch type fixed bed type. It mainly consists of a reactor, a condenser, and an oil and gas collecting system. The reactor has a 100 mm diameter and 150 mm length. The reactor is well insulated and heated by using an electrical heater. The temperature of the reactor is controlled by a PID controller and measured using K type thermocouples located at two points. The exit of the reactor is connected

to the condenser unit. The surplus of ice water (5°C) is supplied to the condenser. During experimentation, the connection was ensured with no tar deposition.

2.3. Experimental Procedure. For each experiment, 60 grams of samples was prepared and loaded into the reactor. For individual pyrolysis, 60 grams of samples was loaded directly into the reactor core. For the co-pyrolysis process, binary blends were prepared by mixing two samples at a ratio of 1: 1 (30 + 30 grams). For ternary blends, the samples were blended at a 1:1:1 ratio (20 + 20 + 20 grams). The reactor was heated to 500°C with a heating rate of 10°C and kept for 30 min to complete volatilization. A total of 7 experimental runs were conducted using individual, binary, and ternary blends under the same experimental conditions. Table 1 displays the current experimental conditions used for this study. The experiments were conducted until no vapor was visually obtained from the reactor. The condensed oil is saved in a separate beaker and weighed. The char is collected separately and weighed after the reactor is cooled to an atmospheric temperature. The mass of the gas fractions were calculated by mass difference. In order to check the repeatability of the experimental yields, the experiments were conducted three times under the same operating conditions, and the average yield value was taken into consideration.

2.4. Characterization Study and Product Analysis. The thermogravimetric study was conducted using the TGA-701 analyzer. This analysis was performed to examine the thermal behavior of the selected three biomass materials by measuring their degradation rates with respect to temperature and time. The analysis was conducted under a nitrogen environment by feeding 5 mg of sample into the furnace. The flow rate of the N_2 was maintained at 50 mL/min. In this study, the feedstocks are heated from atmospheric temperature to 600°C at the constant heating rate of 10°C/min. The data obtained from this study was also used for an extended kinetic and thermodynamic study [20]. The elemental composition of the samples and oil products was measured with the help of the Elementar Vario EL-III. The heating value of the oils is found by a Parr-6772 bomb calorimetric thermometer. The FT-IR analysis of the oil was carried out using a BRUKER TENSOR 27 FTIR spectrometer. The spectra were recorded over a range of 400–4000 cm^{-1} . For this analysis, the oil sample was diluted in KBr plate. The organic elements present in the oil were analyzed by Thermo MS DSQ II spectroscopy. For the analysis, helium gas was used as the carrier gas, and the column flow rate was fixed at 1 mL/min. The separation was done on a DB-35 column. The isothermal program of the oven was set to 50°C at the initial condition and raised to 250°C with standard increment of 5°C/min. The detailed operating condition of the GC is given in Table 2. The NIST library of mass spectra was used to identify the compounds. The 1H NMR analysis of the water free bio-oil was recorded with the help of the Bruker Ultrashield-400 and a high-performance digital FT NMR spectrometer.

TABLE 1: Experimental conditions.

Pyrolysis type	Feedstock
Individual pyrolysis	Hardwood
	Mustard oil cake
	Corncob
Co-pyrolysis	Hardwood + mustard oil cake
	Hardwood + corncob
	Mustard oil cake + corncob
	Hardwood + mustard oil cake + corncob

3. Results and Discussion

3.1. Materials Characterization. Table 3 illustrates the findings of the proximate and ultimate analysis of the selected samples, and Table 4 shows the properties of blended feedstocks. The properties in Table 4 are calculated by arithmetic mean value. From Table 3, it is observed that the weight percentage of carbon and hydrogen in corncob is high compared to the other two materials. At the same time, sulfur and nitrogen contents were identified as low when compared to hardwood and mustard oil cake. The hydrogen content of mustard oil cake is higher than hardwood and corncob. Compared to corncob and hardwood, the nitrogen content of mustard oil cake is higher. Proximate analysis is a realistic and more helpful way to determine the efficiency of any biomass material for biofuel production [21]. Volatile matter and fixed carbon are the two important indicators for pyrolysis biofuel. The higher volatile matter in the sample enhances the production of bio-oil and gas fractions. Whereas the presence of higher fixed carbon provides most biochar, it boosts the carbon conversion rate [22]. The moisture in the biomass restricts heat transfer to the core of the material and decreases the overall efficiency of the process [23]. The moisture content in mustard seed cake is identified as 10.76 wt% which is slightly more than hardwood and corncob. When the ash content of the materials was considered, it was found that mustard oil cake contained a higher ash percentage (6.9 wt%). A higher ash percentage in the sample always decreases the yield of biofuel.

3.2. Thermogravimetric Analysis

3.2.1. Thermogravimetric Analysis of Individual Biomass. The TGA and DTG analysis of three selected individual biomass and their mixtures are carried out under a nitrogen environment as shown in Figures 1 and 2. Around 5% to 8% of mass loss was obtained due to the evaporation of moisture between 30°C and 140°C. Sudden mass loss for hardwood, mustard oil cake, and corncob appeared at 380°C, 320°C and 300°C, respectively, which represents the release of volatiles. The volatiles during pyrolysis for all the biomass samples were released in three steps. The initial step is the evaporation of moisture content, whereas the second phase is the release of volatiles due to the breakdown of molecules. The major destruction of mass was occurred for mustard oil cake, hardwood, and corncob at 360, 375, and 380°C,

TABLE 2: GC-MS condition.

Instrument	GC-MS	
Make	Thermo MS DSQ II	
<i>GC condition</i>		
Column	DB-35	
Dimension	30 m × 0.25 mm × 0.25 μm	
Injection mode	Split type	
Spit ratio	10	
Injection temperature	200°C	
Flow control mode	Linear velocity	
Column flow	10 ml/min	
Carrier gas	Helium	
Column oven temperature	70°C	
<i>Column oven temperature progress</i>		
Rate	Temperature in °C	Hold time in m
—	70	5
10	250	7
<i>MS conditions</i>		
Ion source temperature	200°C	
Interface temperature	250°C	
Scan range	50–650 m/z	

TABLE 3: Material characteristics.

Parameters	Hardwood	Mustard oil cake	Corncob
Proximate analysis (wt%)			
Volatile matter	70.15	66.32	70.85
Fixed carbon	15.30	16.02	16.90
Moisture content	6.3	10.76	8.75
Ash	5.4	6.9	3.5
Ultimate analysis (wt%)			
C	46.21	41.21	40.15
H	6.4	7.20	5.95
N	2.1	6.41	1.21
S	0.3	0.9	0.2
O (by difference)	45.0	45.18	52.49

respectively. From the analysis, it was confirmed that all three biomass materials were completely pyrolyzed at 470°C. After reaching this temperature, the constant weight loss represents the burning of char particles until 650°C [24]. The unburnt char obtained at the end of the study was accounted to 22% for hardwood, 18% for mustard oil cake, and 17% for corncob. The presence of higher volatiles and lower ash in the corncob contributed to the rapid breakdown compared to the other two biomass materials. This is also the same as the outcomes of the study conducted by Munir et al. [25]. The peak at 250 to 350°C in the DTG analysis represents the decomposition of cellulose and hemicellulose. Compared to lignin, cellulose and hemicelluloses start to decompose at lower temperatures [26]. Extractives and decomposition of cellulose and hemicelluloses followed

by lignin breakdown or char formation are the common processes in biomass pyrolysis. From thermogravimetric study, it can be understood that the maximum conversion and reaction is found for all biomass materials between 250°C and 470°C. Overall, the selected materials for this study have the potential to be converted into biofuels or energy.

3.2.2. Thermogravimetric Analysis of Binary and Ternary Biomass Blends. The TGA and DTG analysis of the binary and ternary biomass blends is shown in Figures 3 and 4. Similar to the individual biomass materials, the binary and ternary blends were decomposed at temperature ranges from 150°C to 470°C. For all the blends, the maximum mass loss occurred at a temperature between 350°C and 470°C. Compared to other blends, the decomposition of the ternary blend starts late at a temperature of 370°C. The higher amount of volatile matter in the blend of hardwood and corncob contributed to the rapid breakdown compared to the other two binary and ternary blends. The char particles obtained at the end of the analysis were accounted 20% to 24% for binary blends and 16% for ternary blends. From the analysis, it was confirmed that all the blends were completely pyrolyzed at 475°C.

3.3. Product Yields

3.3.1. Individual Pyrolysis Characteristics. The product yields of hardwood, mustard oil cake, and corncob pyrolysis are shown in Figure 5. The temperature of the reactor has a substantial impact on both conversion and bio-oil production. Due to lower heat transfer phenomena, lower temperatures say below 350°C are always preferred for the production of

TABLE 4: Properties of blended feedstock.

	Volatile matter	Moisture content	Ash
Hardwood + mustard oil cake	68.23	8.53	6.15
Hardwood + corncob	70.5	7.52	4.45
Mustard oil cake + corncob	68.58	5.2	5.2
Hardwood + mustard oil cake + corncob	69.1	8.63	5.26

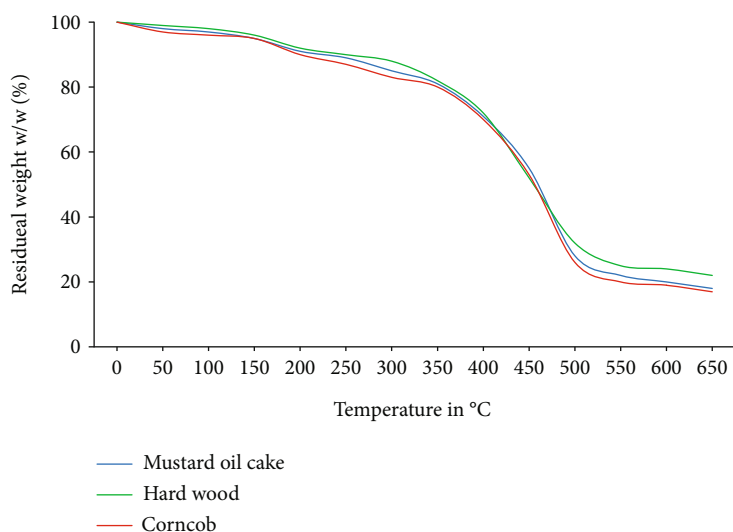


FIGURE 1: TGA analysis of individual biomass.

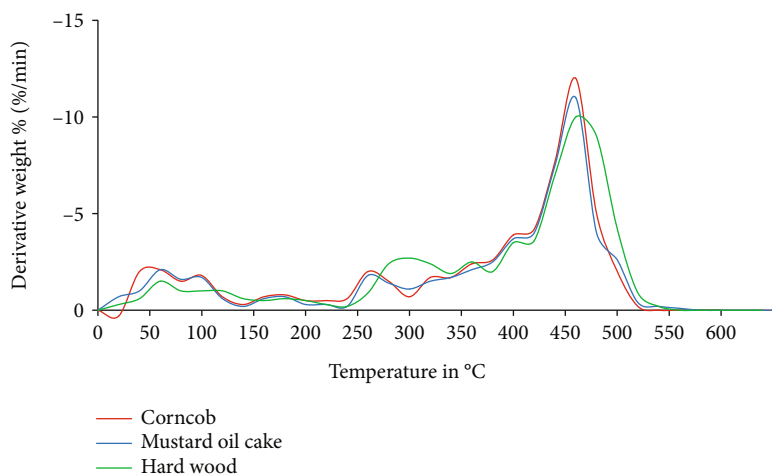


FIGURE 2: DTG analysis of individual biomass.

higher char. When the temperature exceeds 600°C, most of the reaction products are noncondensable gases. Higher gas products at higher temperatures are due to the secondary cracking of the pyrolysis vapors. Prepyrolysis is the initial stage of material degradation, which occurs between 120°C and 200°C. The removal of moisture, the bond breaking, and the formation of free radicals occur during this stage. Pyrolysis of cellulose begins below 100°C and is character-

ized by a decrease in the degree of polymerization. During heating, the hemicellulose decomposes faster than cellulose at a temperature between 200°C and 250°C compared to cellulose between 240°C and 350°C [27]. The decomposition of cellulose and hemicellulose is the main reason for the formation of the maximum bio-oil yield. Generally, more char yield can be obtained by decomposing the feed particle at a lower temperature, which happens at heteroatoms inside

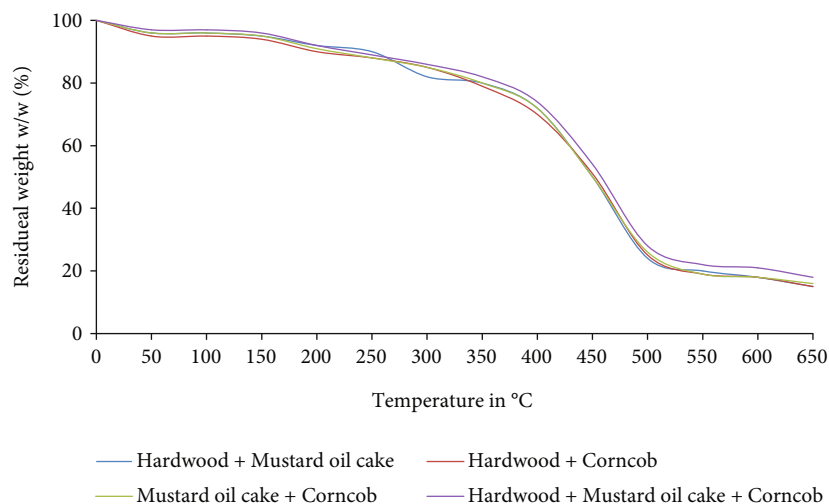


FIGURE 3: TGA analysis of mixed biomass.

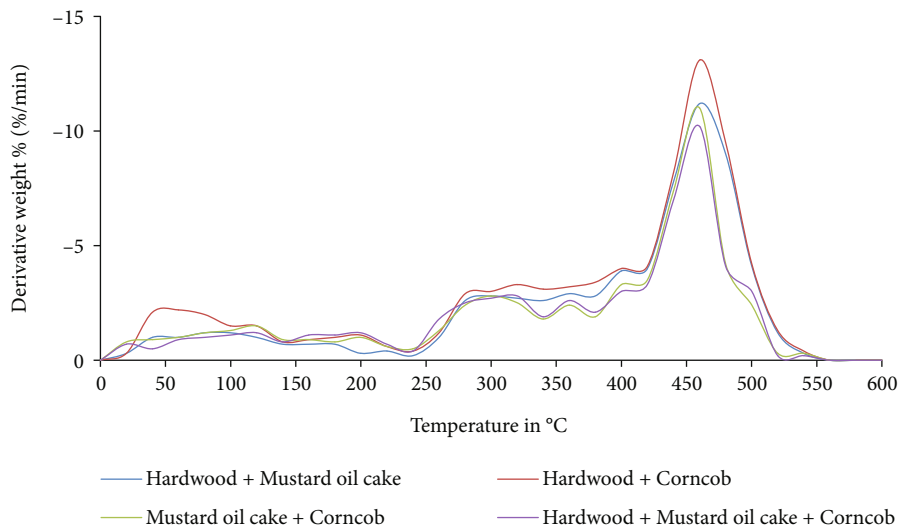


FIGURE 4: DTG analysis of mixed biomass.

the structure [28]. The extensive disintegration of biomass material at high temperatures induces high molecular dislocation and produces a variety of chemical components. According to the literature [29–31], massive conversion of biomass to bio-oil and its fragments occurs when the reaction temperature is kept between 400 and 500°C. The experiments in this phase are conducted under the same operating conditions of 500°C with a heating rate of 20°C/min. In the experiments, corncob produced a higher bio-oil of 43.9 wt%, whereas hardwood and mustard oil cake yielded 42.4 wt% and 40.5 wt%, respectively. The higher volatile matter present in the corncob may be the reason for yielding maximum bio-oil. According to Asadullah et al. [32], volatile matters are transformed into bio-oil as they condensate, and feedstock substantially improves the yield of bio-oil. The increased bio-oil production from corncob could be attributable to the presence of higher cellulose and hemicellulose. They are highly volatile and help in the formation of bio-

oil [33]. The lower bio-oil from hardwood and mustard oil cake attributed to the presence of lower volatile matters compared to corncob. In addition to that, there is a strong relationship between bio-oil production and ash in the biomass materials. Ash in the biomass is generally favored for char production [34]. Ash is a noncombustible material and remains in solid form. The higher percentage of ash in mustard oil cake produced the most of char during pyrolysis. Hardwood, mustard oil cake, and corncob produced maximum char yields of 24.2 wt%, 23.2 wt%, and 22.8 wt%, respectively. It is also confirmed that hardwood produces a maximum char of 24.2 wt% since it has higher ash content. The amount of gas produced from mustard oil cake is 36.3 wt%. The production of noncondensable gas from hardwood and corncob is almost the same.

3.3.2. *Co-pyrolysis Characteristics with Binary Blends.* Figure 6 shows the product yields during co-pyrolysis

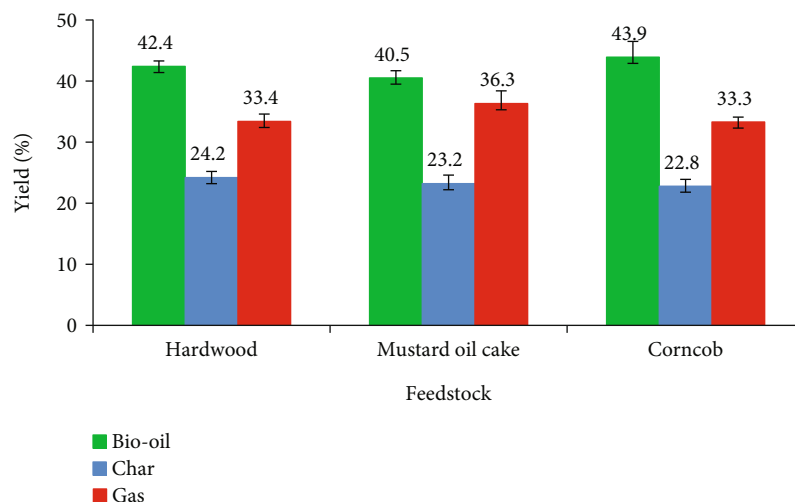


FIGURE 5: Product yield from individual pyrolysis.

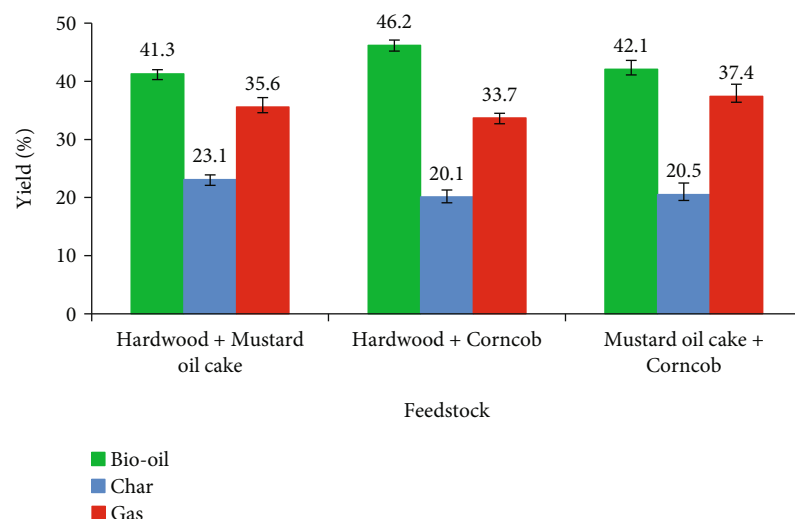


FIGURE 6: Product yield from co-pyrolysis with binary blends.

utilizing binary blends. During the co-pyrolysis process, a maximum bio-oil yield of 46.2 wt% is acquired from the combination of hardwood and corncob. For this combination, there is no synergistic effect identified for gas yields. The amount of gas produced in this combination is equal to the arithmetic mean of the gas produced from individual pyrolysis. There is a negative synergistic effect on char yield with increased bio-oil yield. When hardwood is pyrolyzed individually, it produces 42.4 wt% of bio-oil, while corncob produces 43.9 wt% of bio-oil. But the combination of these two materials yielded 46.2 wt% of bio-oil, which is more than the arithmetic mean value of bio-oils obtained from individual feedstocks. Co-pyrolysis of hardwood with mustard oil cake and corncob with mustard oil cake produced 41.3 and 46.2 wt% of bio-oil, respectively. The production of bio-oil from hardwood and corncob combined with mustard oil cake is lower due to the lower volatile content in the combined feedstocks. It is clearly identified in Table 4. The higher ash content with the combination of hardwood and

mustard oil cake produced more char products than other combinations, which is reliable from previous studies [35, 36]. During the co-pyrolysis reaction, radical interactions can have synergistic effects. It is based on the composition of the biomass material, temperature, heating rate, and hydrogen exchange [37]. Among them, blending feedstock is a crucial one that can have a substantial impact on synergistic effects, and it can be modified complicatedly [38].

3.3.3. Co-pyrolysis Characteristics with Ternary Blends. Figure 7 illustrates the product yields during co-pyrolysis utilizing a ternary blend. In this phase, the production of bio-oil is decreased compared to binary blends. There is a negative synergistic effect on bio-oil yield with increased char and gas production. When hardwood is pyrolyzed individually, it produces 42.4 wt% of bio-oil, mustard oil cake produces 40.5 wt% of bio-oil, and corncob produced 43.9 wt% of bio-oil. But the combination of these three materials yielded 40.1 wt% of bio-oil, which is lower than the

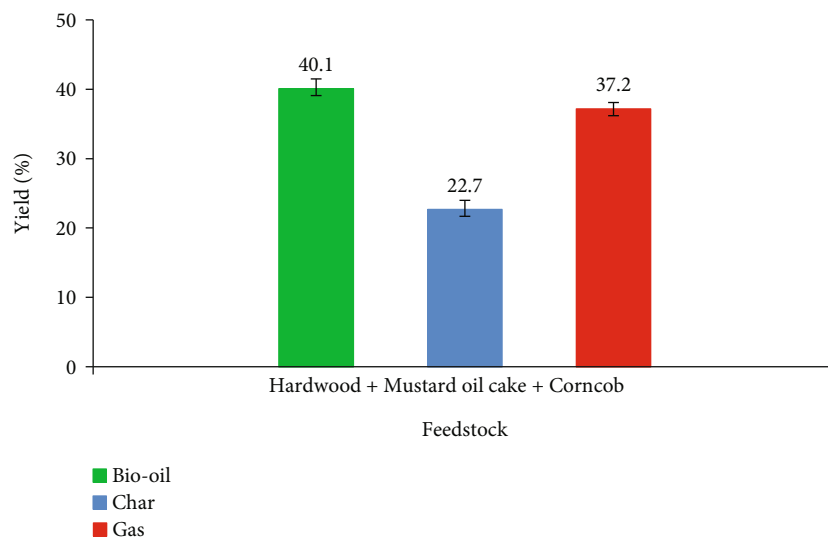


FIGURE 7: Product yield from co-pyrolysis with ternary blends.

arithmetic mean value of bio-oils obtained from individual feedstocks. According to Zhu et al. [39], the negative synergistic effects were prejudiced by the volatiles available in the biomass mixture. The mechanism of the synergistic interaction between biomass materials is unclear [40]. In ternary blends, the total availability of volatile contents is 69.1 wt% which is less than the binary mixture of hardwood and corncob, producing lower bio-oil. In this phase, positive synergy was identified in gas production. When hardwood is pyrolyzed, 33.4 wt% of gas is released, mustard oil cake produces 36.3 wt% of gas, and corncob produces 33.3 wt% of gas. But the combination of these three materials yielded 37.4 wt% of gas which is 9.04% higher than the arithmetic mean value. This may be owing to the catalytic effect of ash which promotes secondary reactions. As a result, the produced bio-oil was further degraded into gas products [41]. Previously, Gong et al. [42] and Zhang et al. [43] showed a positive synergistic effect on gas products with decreased oil and char yield during the co-pyrolysis process.

3.4. Calorific Value Analysis. Table 5 shows the results of the higher heating value of all bio-oils. The bio-oil obtained from hardwood and corncob blends shows a higher heating value of 26.50 MJ/kg. The observed higher heating value led to a synergistic effect. The lower calorific value of the bio-oil obtained from mustard oil cake is due to the presence of higher oxygen content with lower volatile content [44]. Bio-oil with heating value of more than 20 MJ/kg is recommended for use as a low-energy fuel. For agricultural biomass, which is actually good enough, the lower heating value can be improved by various chemical processes.

3.5. Chemical Analysis. The chemical characterization study to find the presence of functional groups and chemical elements was done by FTIR, GC-MS, and ^1H NMR analysis. The bio-oil acquired from co-pyrolysis of hardwood and corncob was used for this analysis since it yielded the maximum bio-oil in this study.

TABLE 5: Heating value of the bio-oils.

Source	Heating value
Hardwood	23.42
Mustard oil cake	15.30
Corncob	22.82
Hardwood + mustard oil cake	20.25
Hardwood + corncob	26.50
Mustard oil cake + corncob	19.65
Hardwood + mustard oil cake + corncob	17.10

3.5.1. FTIR Analysis. Figure 8 shows the FTIR spectra of the bio-oil. As expected, the spectra show the occurrence of alcohol, phenolic compounds, and carboxylic acid components. In the spectra, O-H stretching vibrations between 3200 cm^{-1} and 3450 cm^{-1} indicate the existence of polymeric hydroxyl compounds and alcohols. The aliphatic and aromatic C-H stretching vibrations appeared between 2800 and 3000 cm^{-1} . The carbonyl groups were also seen in the bio-oil between 1650 and 1750 cm^{-1} . Alkenes and aromatic chemicals are found in the sample between 1600 and 1650 cm^{-1} . The bending vibration of the aliphatic C-H groups also appears between 1350 and 1450 cm^{-1} . The C-O stretching and O-H bending vibrations appeared between 1200 and 1250 cm^{-1} .

3.5.2. GC-MS Analysis. Table 6 shows the presence of various chemical elements identified through GC-MS. These elements are identified with respect to retention time related to peak area. More than 35% of phenols and their derivatives are identified in this analysis. The degradation of lignin in the feedstock may be responsible for the presence of these phenolic elements. The bio-oil was found to be made up of several functional groups, including aliphatic, aromatic, ketone, ester, phenol, and fatty acids. Several processes, such

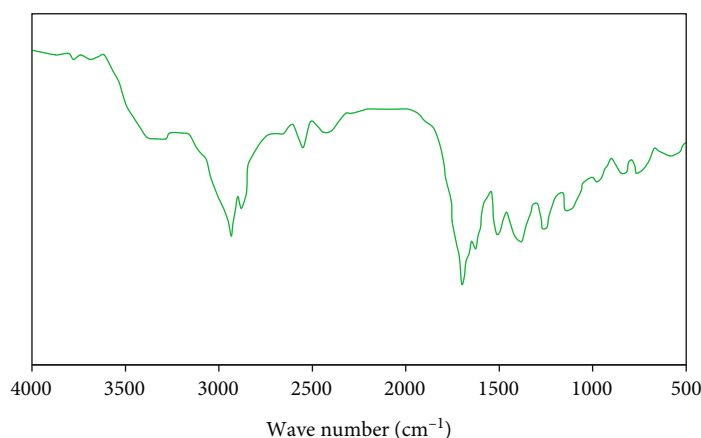


FIGURE 8: FTIR analysis of the bio-oil obtained from hardwood + corncob.

TABLE 6: GC-MS analysis of the bio-oil produced from hardwood + corncob.

RT/min	Compound name	Molecular name	% area
5.31	2-Furanmethanol	C ₅ H ₆ O ₂	2.11
6.26	2-Ethylhexyl benzoate	C ₁₅ H ₂₂ O ₂	0.96
7.83	Trans-2-furanmethanol	C ₅ H ₆ O ₂	4.52
10.25	d-Glucoheptose	C ₇ H ₁₄ O ₇	0.44
15.26	Phenol, 2,5-dimethyl-	C ₈ H ₁₀ O	11.40
17.56	Trans-propenylsyringol	C ₁₁ H ₁₄ O ₃	1.05
19.22	Benzene	C ₆ H ₆	1.74
19.99	5-Hydroxymethyl-2-furaldehyde	C ₆ H ₆ O ₃	4.30
21.11	Furfural	C ₅ H ₄ O ₂	4.63
21.52	Cyclodecasiloxane, eicosamethyl-	C ₂₀ H ₆₀ O ₁₀ Si ₁₀	2.01
22.58	Phenol, 2,6-dimethoxy-	C ₈ H ₁₀ O ₃	10.91
23.40	Methanol	CH ₃ OH	4.55
24.63	d-Mannose	C ₆ H ₁₂ O ₆	0.77
25.09	Phenol	C ₆ H ₆ O	8.22
26.24	2-(2,4,6-Trimethylphenyl)butylamine	C ₁₃ H ₂₁ N	1.70
29.78	Linalyl 2-methylpropanoate	C ₁₄ H ₂₄ O ₂	0.96
30.15	2,3,5-Trimethoxytoluene	C ₁₀ H ₁₄ O ₃	1.82
31.12	Di-(2-ethylhexyl)phthalate	C ₂₄ H ₃₈ O ₄	3.60
31.45	2-Methoxy-4-vinylphenol	C ₉ H ₁₀ O ₂	5.41
31.84	Butanoic acid	C ₂₄ H ₃₄ O ₆	1.72
32.94	Cyclopentanol	C ₅ H ₁₀ O	3.33
34.88	2H-Pyran, 2-(2 heptadecyloxy)tetrahydro-	C ₂₂ H ₄₀ O ₂	3.75
35.45	1,2-benzendiol	C ₆ H ₆ O	1.99
36.18	2-Isopropyl-2,5-dihydrofuran	C ₇ H ₁₂ O	5.36
36.41	Oleic acid	C ₁₈ H ₃₄ O ₂	3.12
37.70	4,5,6,7-Tetrahydrophthalimidine	C ₈ H ₁₁ NO	0.22
37.98	Stigmasterol	C ₂₉ H ₄₈ O	0.56
38.41	2,20-Dioxospirilloxanthin	C ₄₂ H ₅₆ O ₄	3.07
39.14	Octadecenoic acid	C ₁₈ H ₃₆ O ₂	2.04

as dehydration, decarboxylation, and decarboxylation of the biomass constituents, are responsible for the variety of chemical compounds [45, 46]. The major identified compounds are phenol 2,5-dimethyl-, phenol 2,6-dimethoxy-,

phenol 2-methoxy-4-vinylphenol, and 2-isopropyl-2,5-dihydrofuran with an area percentage of 11.40, 10.91, 8.22 5.41, and 5.36, respectively. Phenols and their derivatives are widely used in the cosmetic and food industries. Some of

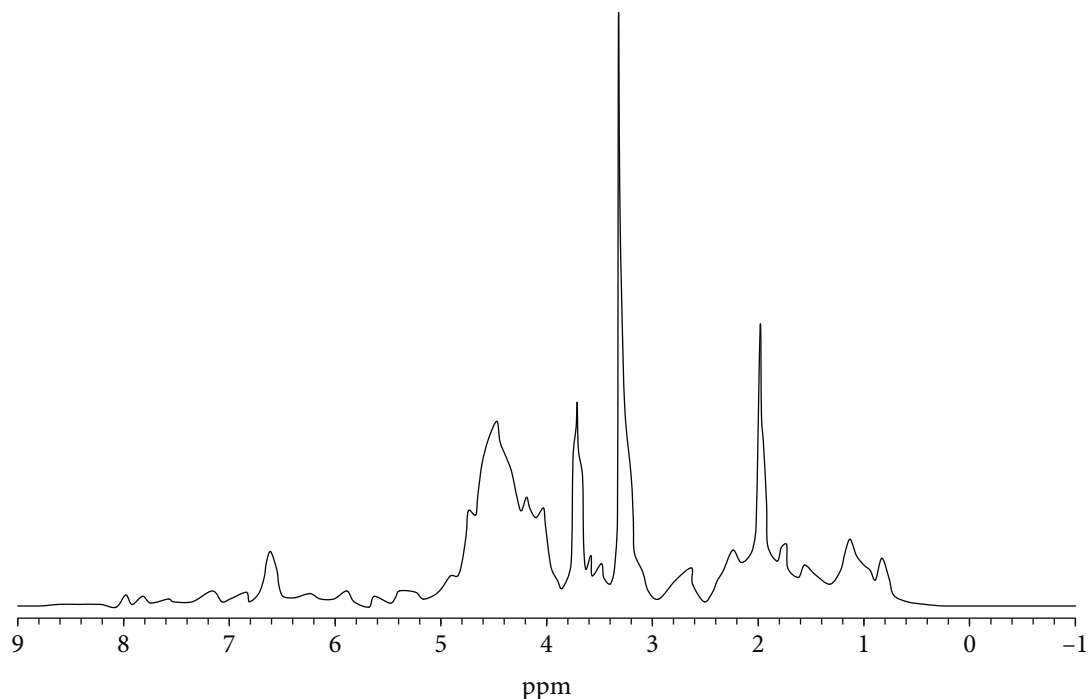


FIGURE 9: ^1H NMR of the bio-oil obtained from hardwood + corncob.

the elements identified are combustible and can be used as biodiesel for energy and power production. The obtained chemical elements are in good agreement with previously published reports on wood-based biomass pyrolysis [47, 48].

3.5.3. ^1H NMR Analysis. The structural determination of chemical compounds requires ^1H NMR studies. The ^1H NMR provides information about the proton environment. Figure 9 shows the ^1H NMR spectra of the bio-oil obtained from hardwood and corncob. The presence of alkoxy, ketone, olefinic, aromatic, and alcohol in the bio-oil is revealed by this analysis at 0.5–2.5 ppm, 3–3.6 ppm, 4.2–4.9 ppm, and 6.7–6.9 ppm. The obtained results are also consistent with Kumar et al. [49], Yorgun and Yıldız [50], and Soni and Karmee [51].

4. Conclusion

In this work, the co-pyrolysis of industrial and agricultural biomass with wood wastes was examined to evaluate the synergistic effects between the materials. Pressed mustard oil cake and corncob along with hardwood were investigated by preparing binary and ternary blends as lignocellulosic representatives for individual and co-pyrolysis processes. The co-pyrolysis of hardwood with corncob enhances the conversion efficiency during pyrolysis. The highest degree of synergy was perceived with hardwood with corncob followed by mustard oil cake and corncob. The decrement in bio-oil production with ternary blends suggested negative synergistic effects opinionated by the lower volatiles in the mixture. Co-pyrolysis is a recommended approach for sustainable energy production with improved carbon conver-

sion and volatile yield. The outcomes of the study suggested to produce bio-oil with improved quality using different lignocellulosic biomass that exhibited interaction.

Data Availability

The data used to support the findings of this study are included within the article.

Conflicts of Interest

The authors declare that there is no conflict of interest regarding the publication of this article.

References

- [1] S. Shafiee and E. Topal, "When will fossil fuel reserves be diminished?," *Energy Policy*, vol. 37, no. 1, pp. 181–189, 2009.
- [2] F. Abnisa and W. M. A. W. Daud, "A review on co-pyrolysis of biomass: an optional technique to obtain a high-grade pyrolysis oil," *Energy Conversion and Management*, vol. 87, pp. 71–85, 2014.
- [3] F. Manzano-Agugliaro, A. Alcayde, F. G. Montoya, A. Zapata-Sierra, and C. Gil, "Scientific production of renewable energies worldwide: an overview," *Renewable and Sustainable Energy Reviews*, vol. 18, pp. 134–143, 2013.
- [4] (2022), <https://mnre.gov.in/bio-energy/current-status>.
- [5] B. Hu, B. Zhang, W. L. Xie, X. Y. Jiang, J. Liu, and Q. Lu, "Recent progress in quantum chemistry modeling on the pyrolysis mechanisms of lignocellulosic biomass," *Energy & Fuels*, vol. 34, no. 9, pp. 10384–10440, 2020.
- [6] V. S. Kaushik, C. S. Dhanalakshmi, P. Madhu, and P. Tamilselvam, "Co-pyrolysis of neem wood bark and low-

- density polyethylene: influence of plastic on pyrolysis product distribution and bio-oil characterization," *Environmental Science and Pollution Research*, 2021.
- [7] P. Madhu, M. I. Neethi, and H. Kanagasabapathy, "Parametric analysis of cotton shell and Palmyra palm fruit bunch for bio oil in fixed bed pyrolysis system," *International Journal of Applied Environmental Sciences*, vol. 9, no. 5, pp. 2427–2436, 2014.
- [8] Q. Tang, Y. Chen, H. Yang et al., "Machine learning prediction of pyrolytic gas yield and compositions with feature reduction methods: effects of pyrolysis conditions and biomass characteristics," *Bioresource Technology*, vol. 339, p. 125581, 2021.
- [9] H. Yang, R. Yan, H. Chen, C. Zheng, D. H. Lee, and D. T. Liang, "In-depth investigation of biomass pyrolysis based on three major components: hemicellulose, cellulose and lignin," *Energy & Fuels*, vol. 20, no. 1, pp. 388–393, 2006.
- [10] L. Burhenne, J. Messmer, T. Aicher, and M. P. Laborie, "The effect of the biomass components lignin, cellulose and hemicellulose on TGA and fixed bed pyrolysis," *Journal of Analytical and Applied Pyrolysis*, vol. 101, pp. 177–184, 2013.
- [11] C. Di Blasi and C. Branca, "Kinetics of primary product formation from wood pyrolysis," *Industrial & Engineering Chemistry Research*, vol. 40, no. 23, pp. 5547–5556, 2001.
- [12] L. Zhao, X. Cao, O. Mašek, and A. Zimmerman, "Heterogeneity of biochar properties as a function of feedstock sources and production temperatures," *Journal of Hazardous Materials*, vol. 256–257, pp. 1–9, 2013.
- [13] S. Krerkkaiwan, C. Fushimi, A. Tsutsumi, and P. Kuchonthara, "Synergetic effect during co-pyrolysis/gasification of biomass and sub-bituminous coal," *Fuel Processing Technology*, vol. 115, pp. 11–18, 2013.
- [14] L. Leng, J. Li, X. Yuan et al., "Beneficial synergistic effect on bio-oil production from co-liquefaction of sewage sludge and lignocellulosic biomass," *Bioresource Technology*, vol. 251, pp. 49–56, 2018.
- [15] C. Sowmya Dhanalakshmi, P. Madhu, A. Karthick, and R. Vigneshkumar, "Combination of woody and grass type biomass: waste management, influence of process parameters, yield of bio-oil by pyrolysis and its chromatographic characterization," *Journal of Scientific and Industrial Research (JSIR)*, vol. 80, no. 2, pp. 172–180, 2021.
- [16] D. Y. Hopa, O. Alagöz, N. Yilmaz, M. Dilek, G. Arabacı, and T. Mutlu, "Biomass co-pyrolysis: effects of blending three different biomasses on oil yield and quality," *Waste Management & Research*, vol. 37, no. 9, pp. 925–933, 2019.
- [17] Q. Chen, H. Liu, J. Ko, H. Wu, and Q. Xu, "Structure characteristics of bio-char generated from co-pyrolysis of wooden waste and wet municipal sewage sludge," *Fuel Processing Technology*, vol. 183, pp. 48–54, 2019.
- [18] Z. Echresh Zadeh, A. Abdulkhani, and B. Saha, "Characterization of fast pyrolysis bio-oil from hardwood and softwood lignin," *Energies*, vol. 13, no. 4, p. 887, 2020.
- [19] J. Samanya, A. Hornung, A. Apfelbacher, and P. Vale, "Characteristics of the upper phase of bio-oil obtained from co-pyrolysis of sewage sludge with wood, rapeseed and straw," *Journal of Analytical and Applied Pyrolysis*, vol. 94, pp. 120–125, 2012.
- [20] S. Singh, T. Patil, S. P. Tekade, M. B. Gawande, and A. N. Sawarkar, "Studies on individual pyrolysis and co-pyrolysis of corn cob and polyethylene: thermal degradation behavior, possible synergism, kinetics, and thermodynamic analysis," *Science of the Total Environment*, vol. 783, p. 147004, 2021.
- [21] C. S. Dhanalakshmi, M. Mathew, and P. Madhu, "Biomass material selection for sustainable environment by the application of multi-objective optimization on the basis of ratio analysis (MOORA)," in *Materials, Design, and Manufacturing for Sustainable Environment*, pp. 345–354, Springer, Singapore, 2021.
- [22] W. Buss, S. Jansson, C. Wurzer, and O. Mašek, "Synergies between BECCS and biochar—maximizing carbon sequestration potential by recycling wood ash," *ACS Sustainable Chemistry & Engineering*, vol. 7, no. 4, pp. 4204–4209, 2019.
- [23] J. Dong, Y. Chi, Y. Tang et al., "Effect of operating parameters and moisture content on municipal solid waste pyrolysis and gasification," *Energy & Fuels*, vol. 30, no. 5, pp. 3994–4001, 2016.
- [24] H. H. Sait, A. Hussain, A. A. Salema, and F. N. Ani, "Pyrolysis and combustion kinetics of date palm biomass using thermogravimetric analysis," *Bioresource Technology*, vol. 118, pp. 382–389, 2012.
- [25] S. Munir, S. S. Daood, W. Nimmo, A. M. Cunliffe, and B. M. Gibbs, "Thermal analysis and devolatilization kinetics of cotton stalk, sugar cane bagasse and shea meal under nitrogen and air atmospheres," *Bioresource Technology*, vol. 100, no. 3, pp. 1413–1418, 2009.
- [26] T. Fisher, M. Hajaligol, B. Waymack, and D. Kellogg, "Pyrolysis behavior and kinetics of biomass derived materials," *Journal of Analytical and Applied Pyrolysis*, vol. 62, no. 2, pp. 331–349, 2002.
- [27] I. Kathir, K. Haribabu, A. Kumar et al., "Utilization of tea industrial waste for low-grade energy recovery: optimization of liquid oil production and its characterization," *Advances in Materials Science and Engineering*, vol. 2022, Article ID 7852046, 9 pages, 2022.
- [28] W. T. Tsai, M. K. Lee, and Y. M. Chang, "Fast pyrolysis of rice husk: product yields and compositions," *Bioresource Technology*, vol. 98, no. 1, pp. 22–28, 2007.
- [29] C. S. Dhanalakshmi and P. Madhu, "Recycling of wood bark of *Azadirachta indica* for bio-oil and chemicals by flash pyrolysis," *Indian Journal of Ecology*, vol. 46, no. 2, pp. 347–353, 2019.
- [30] C. Vibhakar, R. S. Sabeenian, S. Kaliappan et al., "Production and optimization of energy rich biofuel through co-pyrolysis by utilizing mixed agricultural residues and mixed waste plastics," *Advances in Materials Science and Engineering*, vol. 2022, Article ID 8175552, 9 pages, 2022.
- [31] Q. Sohaib, A. Muhammad, and M. Younas, "Fast pyrolysis of sugarcane bagasse: effect of pyrolysis conditions on final product distribution and properties," *Energy Sources, Part A: Recovery, Utilization, and Environmental Effects*, vol. 39, no. 2, pp. 184–190, 2017.
- [32] M. Asadullah, M. A. Rahman, M. M. Ali et al., "Jute stick pyrolysis for bio-oil production in fluidized bed reactor," *Bioresource Technology*, vol. 99, no. 1, pp. 44–50, 2008.
- [33] F. Abnisa, A. Arami-Niya, W. W. Daud, J. N. Sahu, and I. M. Noor, "Utilization of oil palm tree residues to produce bio-oil and bio-char via pyrolysis," *Energy Conversion and Management*, vol. 76, pp. 1073–1082, 2013.
- [34] I. Boumanchar, Y. Chhiti, F. E. M. H. Alaoui et al., "Effect of materials mixture on the higher heating value: case of biomass, biochar and municipal solid waste," *Waste Management*, vol. 61, pp. 78–86, 2017.

- [35] R. Zanzi, K. Sjöström, and E. Björnbom, "Rapid pyrolysis of agricultural residues at high temperature," *Biomass and Bioenergy*, vol. 23, no. 5, pp. 357–366, 2002.
- [36] S. Thangalazhy-Gopakumar, W. M. A. Al-Nadheri, D. Jegarajan, J. N. Sahu, N. M. Mubarak, and S. Nizamuddin, "Utilization of palm oil sludge through pyrolysis for bio-oil and bio-char production," *Bioresource Technology*, vol. 178, pp. 65–69, 2015.
- [37] I. Johannes, L. Tiikma, and H. Luik, "Synergy in co-pyrolysis of oil shale and pine sawdust in autoclaves," *Journal of Analytical and Applied Pyrolysis*, vol. 104, pp. 341–352, 2013.
- [38] J. Fei, J. Zhang, F. Wang, and J. Wang, "Synergistic effects on co-pyrolysis of lignite and high-sulfur swelling coal," *Journal of Analytical and Applied Pyrolysis*, vol. 95, pp. 61–67, 2012.
- [39] X. Zhu, K. Li, L. Zhang, X. Wu, and X. Zhu, "Synergistic effects on thermochemical behaviors of co-pyrolysis between bio-oil distillation residue and bituminous coal," *Energy Conversion and Management*, vol. 151, pp. 209–215, 2017.
- [40] P. I. Diaz, Z. Xie, T. Sobue et al., "Synergistic interaction between *Candida albicans* and commensal oral streptococci in a novel in vitro mucosal model," *Infection and Immunity*, vol. 80, no. 2, pp. 620–632, 2012.
- [41] B. Lin, Q. Huang, and Y. Chi, "Co-pyrolysis of oily sludge and rice husk for improving pyrolysis oil quality," *Fuel Processing Technology*, vol. 177, pp. 275–282, 2018.
- [42] Z. Gong, A. Du, Z. Wang, P. Fang, and X. Li, "Experimental study on pyrolysis characteristics of oil sludge with a tube furnace reactor," *Energy & Fuels*, vol. 31, no. 8, pp. 8102–8108, 2017.
- [43] W. Zhang, C. Yuan, J. Xu, and X. Yang, "Beneficial synergetic effect on gas production during co-pyrolysis of sewage sludge and biomass in a vacuum reactor," *Bioresource Technology*, vol. 183, pp. 255–258, 2015.
- [44] A. Demirbas, "Effects of moisture and hydrogen content on the heating value of fuels," *Energy Sources, Part A: Recovery, Utilization, and Environmental Effects*, vol. 29, no. 7, pp. 649–655, 2007.
- [45] S. Fang, Z. Yu, X. Ma et al., "Co-pyrolysis characters between combustible solid waste and paper mill sludge by TG-FTIR and Py-GC/MS," *Energy Conversion and Management*, vol. 144, pp. 114–122, 2017.
- [46] J. A. Oyebanji, O. S. I. Fayomi, O. I. Oyeniyi, P. G. Akor, and S. T. Ajayi, "Physico-chemical analysis of pyrolyzed bio-oil from *Lophira alata* (ironwood) wood," *Journal of Environmental Pollution and Management*, vol. 4, p. 101, 2022.
- [47] E. Kim, H. Gil, S. Park, and J. Park, "Bio-oil production from pyrolysis of waste sawdust with catalyst ZSM-5," *Journal of Material Cycles and Waste Management*, vol. 19, no. 1, pp. 423–431, 2017.
- [48] J. L. Chukwunke, M. C. Ewulonu, I. C. Chukwujike, and P. C. Okolie, "Physico-chemical analysis of pyrolyzed bio-oil from *swietenia macrophylla* (mahogany) wood," *Heliyon*, vol. 5, no. 6, article e01790, 2019.
- [49] P. Kumar, P. Kumar, P. V. Rao, N. V. Choudary, and G. Sriganesh, "Saw dust pyrolysis: effect of temperature and catalysts," *Fuel*, vol. 199, pp. 339–345, 2017.
- [50] S. Yorgun and D. Yildiz, "Slow pyrolysis of paulownia wood: effects of pyrolysis parameters on product yields and bio-oil characterization," *Journal of Analytical and Applied Pyrolysis*, vol. 114, pp. 68–78, 2015.
- [51] B. Soni and S. K. Karmee, "Towards a continuous pilot scale pyrolysis based biorefinery for production of biooil and bio-char from sawdust," *Fuel*, vol. 271, p. 117570, 2020.

Research Article

Optimization by Response Surface Methodology of Biodiesel Production from *Podocarpus falcatus* Oil as a Cameroonian Novel Nonedible Feedstock

Serges Bruno Lemoupi Ngomade ¹, Raoul Donald Tchuifon Tchuifon ²,
Rufis Fregue Tiegam Tagne ³, Meme Laloï Tongnang Ngueteu ¹,
Hugues Mahouli Patai ¹, George Ndifor-Angwafor Nche ¹,
and Solomon Gabche Anagho ¹

¹Research Unit of Noxious Chemistry and Environmental Engineering, Department of Chemistry, Faculty of Science, University of Dschang, Dschang, Cameroon

²Laboratory of Energy, Materials, Modeling and Method, Department of Process Engineering, National Higher Polytechnic School of Douala, University of Douala, Douala, Cameroon

³Department of Paper Sciences and Bioenergy, University Institute of Wood Technology, University of Yaoundé I, Mbalmayo, Cameroon

Correspondence should be addressed to George Ndifor-Angwafor Nche; nchegeorged4@yahoo.com and Solomon Gabche Anagho; sg_anagho@yahoo.com

Received 23 January 2022; Revised 5 March 2022; Accepted 18 March 2022; Published 4 April 2022

Academic Editor: Gonggang Liu

Copyright © 2022 Serges Bruno Lemoupi Ngomade et al. This is an open access article distributed under the Creative Commons Attribution License, which permits unrestricted use, distribution, and reproduction in any medium, provided the original work is properly cited.

The production of methyl esters (biodiesel) by the transesterification of *Podocarpus falcatus* oil (PFO) with methanol was optimized by response surface methodology (RSM) using the Box-Behnken design. The effects of parameters such as temperature, reaction time, and alcohol/oil molar ratio using yield and viscosity as responses were investigated. The optimum conditions for the production of biodiesel were as follows: temperature at 65°C, reaction time of 180 min, and molar ratio of 10:1, while the minimum viscosity was obtained for a temperature of 50°C, a reaction time of 120 min, and a molar ratio of 10:1. Physicochemical characterization by infrared spectroscopy (FT-IR) and UV visible spectroscopy showed that the free fatty acid (FFA) content of *Podocarpus* oil was 1.9%, which is less than the maximum of 2% recommended for the application of the one-step alkaline transesterification process. Also, the biodiesel obtained from the oil was seen to consist mainly of methyl esters, and that its physicochemical characteristics are within the standard set by the American Standard for Testing and Materials (ASTM).

1. Introduction

Despite its negative impact on the environment, the need for fossil fuels has increased due to population growth and rapid industrial development [1]. This situation has led to the search for alternative energy sources that could be sustainable and respectful of the environment [2]. Fossil fuels are one of the

most important energy sources, and they are widely used in various industries such as transport and thermal power plants, and their uses have caused serious pollution to the environment. Global crude oil demand in 2020 was estimated at 101.6 million barrels per day [3], while by 2040, aggregate energy demand will be around 30% higher than they were in 2010 [4], with a resultant increase in the emission of

greenhouse gases and the depletion of energy reserves. To remedy these problems, there has been the need to look for alternative energy sources.

Biodiesel, one of the main alternative fuels with low greenhouse gas emissions, is one of such alternatives. It is produced from various natural sources such as vegetable oils, animal fats, and algae [4, 5]. There are several methods for producing biodiesel from vegetable oils such as pyrolysis, dilution, microemulsion, and transesterification [6]. Among these methods, the transesterification process has been found to be more efficient and economical due to its easy implementation and relatively low cost [7]. During this process (Figure 1), three conversion reactions occur: the conversion of triglycerides to diglycerides, diglycerides to monoglycerides, and finally, the transformation of monoglycerides into glycerol. Each reaction uses one mole of alcohol in the presence of a catalyst, which could be acidic or basic, to chemically decompose the vegetable oil molecules into alkyl esters with glycerol as a by-product [8–10].

The transesterification process is governed by the control of several parameters that affect the desired product. It has become increasingly difficult and more expensive to control these parameters effectively by means of classical optimizations [11]. Current research is focusing on mathematical models obtained from experimental design to overcome this obstacle [10]. This method simultaneously studies the different factors that influence the process and their interactions with each other, while minimizing errors. The Box-Behnken (BB) design in response surface methodology (RSM) is generally used to optimize parameters influencing the transesterification reaction and using an appropriate software such as Statgraphics or STATISTICA [12].

The price of edible vegetable oils is relatively higher than that of diesel, and the use of these oils as a raw material for biodiesel production competes with food [13] and is not economical. Consequently, a solution is currently being sort through the use second generation raw materials such as inedible vegetable oils, used cooking oils, and animal fats. Thus, the use of inedible oils reduces the dependence on the use of edible vegetable oils for the production of biodiesel [14].

Podocarpus falcatus is an inedible oilseed species which belongs to the Podocarpaceae family. It grows at an altitude of 1,500–2,500 m above sea level in areas of average annual precipitation of 1,200–1,800 mm [15]. This inedible oleaginous plant is very abundant in Cameroon and can therefore be used as a raw material for the production of biodiesel. However, when we reviewed the literature, no work was reported on the production of biodiesel from *Podocarpus falcatus*. The novelty in the work is the search for the optimal conditions of the reaction of alkali-catalyzed transesterification (KOH) by response surface methodology to produce biodiesel. Another novelty is in the use of *Podocarpus falcatus* oil (PFO) as a new feedstock to produce biodiesel. The influence of process parameters such as temperature, methanol/oil molar ratio, and reaction time were investigated.

Different methods can be used to obtain PFO from its seeds, namely, the traditional extraction method, mechanical extraction, and chemical extraction [13]. Among these,

mechanical press methods are generally used to extract vegetable oils from oil plants with an oil content greater than 20% [13]. Generally, this process has the advantages of having a low production cost and the oil produced has low concentrations of free fatty acids [16]. Table 1 shows the fatty acid composition of PFO.

The challenge of our work lied in the in-depth application of the concepts of experiment methodology design, to study the parameters affecting the production of biodiesel derived from PFO, thus providing useful guidelines to promote the sustainable uses of biomass in general.

2. Material and Methods

2.1. Materials and Chemicals. All chemicals used such as methanol (99.9% purity), ethanol (98% purity), phenolphthalein, diethylether, sodium hydroxide (85% purity), and potassium hydroxide (85% purity) were purchased from Prolabo, Sion, Switzerland.

The fruits of *Podocarpus falcatus* were collected from the University of Dschang, Menoua Division in the West Region of Cameroon.

The freshly harvested fruits were stripped of their endocarps, dried in open air, and then shelled to obtain almond seeds. These almonds were further dried in the sun and then subjected to mechanical pressing extraction at the Renewable Energy Laboratory of the Faculty of Agricultural Sciences at the University of Dschang, Cameroon. About 300 g of raw materials was placed in a strong and perforated metal “cylindrical cage” and pressed by the movement of a piston. An iron tray was used in the cage to provide constant pressure through the volume of material and to speed up the oil extraction process. The compressed almonds were evacuated through a circular opening located at the bottom of the cage. The yield of the extracted oil was determined by the formula used by Carr [16].

$$\text{Yield (\%)} = \frac{\text{mass of oil extracted (g)}}{\text{mass of sample (g)}} \times 100. \quad (1)$$

Figure 2 gives the different forms of biomass used and the oil obtained.

2.2. Biodiesel Production. Biodiesel was synthesized according to the procedure reported by Hassan and Fadhil [17]. The transesterification process was performed in a 100 mL three-necked round bottom flask. 50 g of oil was used in each of the 15 experiments. For each experiment, the oil was carefully transferred to the flask and preheated on a hotplate to its reaction temperature. A solution of potassium methoxide was freshly prepared and added to the preheated oil, and the mixture was heated to reflux and stirred. After the transesterification process, the mixture underwent separation in a separating funnel for six hours. The upper phase containing the biodiesel was washed several times with hot water to remove residual impurities. After washing, the biodiesel phase was dried in an oven at a temperature of 110°C for four hours to evaporate

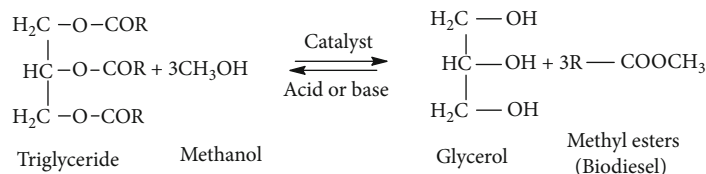


FIGURE 1: General equation of the transesterification reaction.

TABLE 1: Fatty acid composition of *Podocarpus falcatus* oil [15].

Fatty acids	Content (%)	Saturation level
Palmitic acid (16:0)	8.87	Saturated
Stearic acid (18:0)	4.45	Saturated
Oleic acid (18:1)	78.94	Monounsaturated
Linoleic acid (18:2)	4.70	Polyunsaturated
Linolenic acid (18:3)	3.04	Polyunsaturated

the traces of water and methanol. The methodology steps are illustrated in Figure 3.

The yield of the biodiesel from the esterification reaction was calculated according to the following equation:

$$\text{Yield (\%)} = \frac{\text{mass of biodiesel produced (g)}}{\text{mass of oil used (g)}} \times 100. \quad (2)$$

2.3. Experimental Design. Three-factor design was applied with a total of 15 experimental runs generated by the BB design. The parameters selected for optimization were as follows: methanol/oil molar ratio, A; reaction time (min), B; and temperature ($^{\circ}\text{C}$), C. Table 2 shows the 15 experimental runs generated. The reactions were carried out at various alcohol/oil molar ratios (6:1–10:1), reaction times (60 min–180 min), and at temperatures (50–80 $^{\circ}\text{C}$). Potassium hydroxide (KOH: 1 wt.%) was used as a catalyst for all the transesterification reactions. The parameter ranges were selected on the basis of a review of the literature [18, 19].

2.4. Statistical Analysis. The data obtained from the experiments were analysed using the STATGRAPHIC 16 software, and the response surfaces were plotted from version 8 of the STATISTICA software. The BB design reduces the number of experiments without loss of precision and more efficiently assesses complex response functions compared to other designs [20–22]. The number of experimental trials is estimated by equation (3).

$$N = k^2 + k + C_p = 3^2 + 3 + 3 = 15, \quad (3)$$

where k and C_p are the number of variables studied and the number of points replicated, respectively [23]. Table 3 presents the parameters of independent variables using the BB design.

The effect of the variables (x_1 , x_2 , and x_3) on the viscosity and the yield of the product was evaluated using a second order polynomial model given by equation (4) [24].

$$Y = a_0 + \sum_{i=1}^k a_i x_i + \sum_{i=1}^k a_{ii} x_i^2 + \sum_{i=1}^k \sum_{j=1}^k a_{ij} x_i x_j + \varepsilon, \quad (4)$$

where Y is the response obtained, a_0 is a constant, a_i is the linear effect of the input factor x_i , a_{ij} defines a linear interaction between the factors x_i and x_j , a_{ii} is the quadratic effect of the factor x_i , and ε is random error. The goodness of the fit of the model was assessed using a test of significance and analysis of variance (ANOVA).

The empirical model obtained was validated using the STATGRAPHIC 16 software as an evaluation instrument. The model is considered good when the experimental values obtained are close to those predicted by the t -test and the p value. In general, a model is validated when R^2 is greater than 75% or the p value $\leq 5\%$, with a confidence level of 95% [25].

2.5. Physicochemical Characterizations

2.5.1. Fourier Transform Infrared Spectrometry (FT-IR) Analysis. The functional groups of the extracted oil and the produced biodiesel were determined by FT-IR spectroscopy using the Thermo Scientific Nicolet iS5 FT-IR spectrometer. A few drops of each sample of biodiesel and oil were placed in the previously cleaned sample compartment and scanned using an IR spectrum of a wavelength range of 4,000–500 cm^{-1} , using the OMNIC Spectra software.

2.5.2. UV Spectroscopy Analysis. In order to study changes in electronic energy levels, π electron systems, and conjugate unsaturation within molecules present in *Podocarpus falcatus* oil and biodiesel, a Thermo Scientific UV/Vis spectrophotometer, GENESYS 10S was used. The spectra scans were 200–600 nm, with a 1 cm quartz cuvette. All samples were diluted in ethanol.

2.5.3. Physicochemical Properties of the Oil and Biodiesel Produced. The objective of this characterization was to determine the physicochemical properties of the extracted oil and the produced biodiesel in order to compare them with European (EN 14214) and American (ASTM D6751) standards. These parameters were as follows: acid number, saponification number, iodine number, cetane number, calorific value, pour point, density, and viscosity. The reproducibility of all the measurements was verified by repeating two experiments under the same conditions.



FIGURE 2: Different forms of *Podocarpus falcatus* fruit and *Podocarpus* oil: (a) fresh fruits; (b) seeds before peeling; (c) seeds after peeling; (d) *P. falcatus* oil.

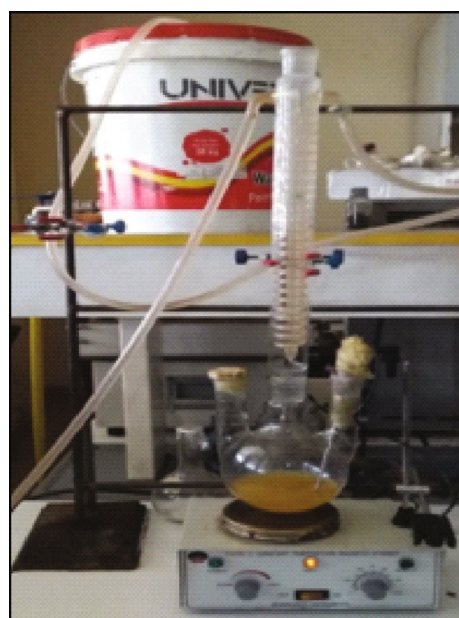
2.5.4. Determination of the Acid and the Free Fatty Acid Levels. The acid level of the oil and of the biodiesel was determined according to the protocol derived from the AFNOR NF EN ISO660 standard of 2009. Briefly, 1.5 g of sample was placed in a 250 mL Erlenmeyer flask and then supplemented with 50 mL of a 1:1 (v:v) neutralized solution of ethanol and diethyl ether. The mixture was titrated with an ethanolic solution of potassium hydroxide KOH (0.1 N) until the appearance of a persistent pink colour. The values of the acid number (I_A) and the free fatty acid number (I_{FFA}) were calculated using the formulas in equations (5) and (6):

$$I_A = \frac{N \times V \times 56.1}{m}, \quad (5)$$

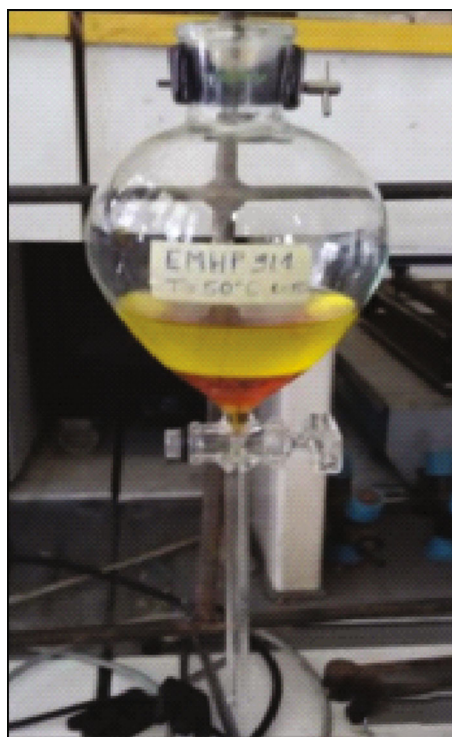
$$I_{\text{FFA}} = \frac{I_A}{1.99}. \quad (6)$$

N is the normality of the ethanolic solution of KOH in eq/L; V is the volume of the ethanolic KOH solution used for the titration in mL; m is the mass of the test sample in grams.

2.5.5. Determination of the Saponification Index. The saponification indices of the oil and the biodiesel were determined according to the protocol derived from the AFNOR NFT60-206 standard. Briefly, 1.5 g of fatty substance was placed in a flask, followed by the addition of 20 mL of alcoholic potassium hydroxide solution (0.5 N). The mixture was heated at reflux in a water bath for 45 minutes until complete saponification. After cooling, the excess KOH was titrated with a solution of hydrochloric acid, HCl (0.5 N) in the presence of phenolphthalein, until the pink colour of the solution turned colourless. A blank test was carried out beforehand under the same conditions, by titrating the ethanolic solution of KOH in the absence of fatty substances.



(a)



(b)



(c)

FIGURE 3: Steps of (a) reaction, (b) settling, and (c) washing the biodiesel.

TABLE 2: Experimental matrix and theoretical experiments and responses.

Test	Temperature (°C)	Time (min)	Molar ratio	Viscosity (mm ² /s)		Yield (%)	
	(x_1)	(x_2)	(x_3)	Y_V	Y_V^*	Y_R	Y_R^*
1	65.0	60.0	10.0	3.84	3.945	83.6	83.9725
2	65.0	120.0	8.0	4	4.12	96.1	95.2533
3	65.0	180.0	10.0	3.84	3.715	94.3	93.7875
4	65.0	180.0	6.0	4.64	4.765	87.12	86.7475
5	80.0	120.0	10.0	4.10	4.02	88.66	89.7725
6	65.0	120.0	8.0	4.08	4.12	95.40	95.2533
7	80.0	60.0	8.0	4.08	4.285	93.46	91.975
8	80.0	180.0	8.0	4.74	4.715	87.9	87.3
9	50.0	60.0	8.0	4.42	4.445	85.86	86.46
10	50.0	120.0	10.0	3.58	3.68	94.72	92.7475
11	80.0	120.0	6.0	5.54	5.54	91.22	92.1925
12	65.0	60.0	6.0	5.64	5.54	90.88	91.3925
13	50.0	120.0	6.0	4.72	4.8	92.82	91.7075
14	50.0	180.0	8.0	3.78	3.575	94.82	96.305
15	65.0	120.0	8.0	4.28	4.12	94.26	95.2533

x_1 : reaction temperature; x_2 : reaction time; x_3 : alcohol/oil molar ratio; Y_V : experimental viscosity; Y_V^* : theoretical viscosity; Y_R : experimental yield; Y_R^* : theoretical yield.

TABLE 3: Parameter of independent variables used by the BB plan for the optimization of oil transesterification of the oil *Podocarpus falcatus*.

Variables	Symbols	Level		
		-1	0	1
Temperature (°C)	A	50	65	80
Reaction time (min)	B	60	120	180
Molar ratio	C	6:1	8:1	10:1

The saponification index was calculated by formula (7):

$$I_S = \frac{V_0 - V}{m} \times N \times 56.1. \quad (7)$$

V_0 is the volume of HCl (mL) required to titrate the blank; V is the volume of HCl (mL) necessary to titrate the sample to be analysed; N is the normality of HCl (eq/L); m is the sample mass in grams for the test.

2.5.6. Determination of the Iodine Value. The AFNOR NFT60-203 standard was used to determine the iodine numbers of oil and biodiesel according to the following protocol: 1g of sample was introduced into a 250 mL Erlenmeyer flask, followed by addition of 15 mL of carbon tetrachloride and 25 mL of Wijs reagent. The mixture was stoppered, stirred, and left in the dark for one hour. Then, 20 mL of 10% potassium iodide (KI) and 150 mL of distilled water were added to the mixture, and the excess iodine was titrated with a sodium thiosulfate $\text{Na}_2\text{S}_2\text{O}_3$ solution (0.1 N) using starch solution as an indicator. Equivalence point was identified by the change in colour from a blue-violet solution to colourless. A blank test was carried out in the same way.

The iodine number was calculated by the following formula:

$$I_I = \frac{V_0 - V}{m} \times 126.9 \times N, \quad (8)$$

where V_0 is the volume of sodium thiosulfate $\text{Na}_2\text{S}_2\text{O}_3$ (0.1 N) required to titrate in the blank test, V is the volume (in mL) of sodium thiosulfate $\text{Na}_2\text{S}_2\text{O}_3$ (0.1 N) necessary to titrate the sample, m is the test sample mass (in g), and N is the normality in eq/L of $\text{Na}_2\text{S}_2\text{O}_3$.

2.6. Determination of the Cetane Number. Biodiesel cetane number (CN) was calculated by the correlation given by Krisnangkura [26] relating the iodine number (I_I) and the saponification index (I_S), as shown by equation (9):

$$\text{CN} = 46.3 + \frac{5458}{I_S} - 0.225 I_I. \quad (9)$$

2.6.1. Determination of the Calorific Value. The calorific value (P_C) of biodiesel was calculated from the model developed by Demirbas [27] using the iodine number (I_I) and the saponification number (I_S) as illustrated by equation (10):

$$P_C = 49.43 - (0.015 I_I) - (0.041 I_S). \quad (10)$$

2.6.2. Density Determination. The density of a substance is defined as the mass of that substance contained in a fixed volume, under the same well-defined temperature and pressure conditions [28]. The respective masses of the oil and biodiesel corresponding to well-defined volume were measured using a Sartorius balance. Knowledge of these masses

and volumes was used to determine the density and relative density according to equations (11) and (12):

$$\rho = \frac{m}{V}, \quad (11)$$

$$d = \frac{\rho}{\rho_e}. \quad (12)$$

m is the mass of the sample in grams (g); V is the volume of the sample in millilitres (mL); ρ is the density of the sample in grams per liter (g/L); ρ_e is the density of water (g/L).

2.6.3. Viscosity Measurement. The kinematic viscosity was studied in accordance with standard ASTM 445, using a capillary viscometer of the UBBELOHDE type, a viscometer support allowing the instrument to be kept in a vertical position, a bath equipped with a thermostat, a stopwatch to measure time, and a filter paper. For a given test temperature, the viscosity was determined by the formula given by equation (13):

$$\eta = k * t, \quad (13)$$

where k is viscometer constant, t is the liquid flow time in seconds, and η is viscosity in mm^2/s .

3. Results and Discussion

3.1. Optimization by Response Surface Methodology. Several parameters influence the transesterification reaction, the most important of which are the temperature (x_1), the reaction time (x_2), and the methanol/oils molar ratio (x_3). The regression surface equations and response curves were obtained as a function of these three parameters.

3.1.1. Regression Equation for Methyl Esters and Viscosity. In order to study the effects of the interaction between the parameters affecting the transesterification reaction on the response variables, yield, and viscosity, experiments were carried out by varying these parameters and using the BB design. The experimental results were fitted to the polynomial equations for viscosity and methyl ester (biodiesel) yield, which are presented in equations (14) and (15):

$$\begin{aligned} Y_{\text{methyl ester}} = & 11.0006 + 1.10835 * x_1 + 0.280403 * x_2 \\ & + 7.9725 * x_3 - 0.00296296 * x_1 * x_1 \\ & - 0.00403333 * x_1 * x_2 - 0.0371667 * x_1 * x_3 \\ & - 0.00102685 * x_2 * x_2 + 0.031375 * x_2 * x_3 \\ & - 0.587917 * x_3 * x_3, \end{aligned} \quad (14)$$

$$\begin{aligned} Y_{\text{viscosity}} = & 14.1944 - 0.0325185 * x_1 - 0.0419167 * x_2 \\ & - 1.39667 * x_3 + 0.000196296 * x_1 * x_1 \\ & + 0.000361111 * x_1 * x_2 - 0.0025 * x_1 * x_3 \end{aligned}$$

$$\begin{aligned} & + 0.00000671296 * x_2 * x_2 + 0.001875 * x_2 * x_3 \\ & + 0.0635417 * x_3 * x_3. \end{aligned} \quad (15)$$

In the above equations, a positive sign in front of the terms indicates a synergistic effect while a negative sign indicates an antagonistic effect. Therefore, temperature (x_1), reaction time (x_2), molar ratio (x_3), temperature-molar ratio (x_1x_3), and time-molar ratio (x_2x_3) interactions played an important role in increasing the yield, while the temperature-time (x_1x_2) interactions and the quadratic temperature-temperature (x_1x_1), time-time (x_2x_2), and molar-molar ratio (x_3x_3) effects had a negative contribution to the yield of the biodiesel. In addition, the effects of temperature-time (x_1x_2), time-molar ratio (x_2x_3) interactions, quadratic temperature-temperature (x_1x_1), and molar-molar ratio (x_3x_3) increased the viscosity. Also, the temperature (x_1), the reaction time (x_2), the molar ratio (x_3), and the temperature-molar ratio interaction (x_1x_3) promoted the decrease in viscosity.

3.1.2. Analysis of Model Variance. The validation of the model was made with the coefficient of determination R^2 , which was 0.95 for the viscosity and 0.94 for the yield, thus indicating that this model conformed with the experimental results. Linear, quadratic, or interaction effects of variables on responses were investigated using ANOVA. With regard to Table 4, it can be seen that the variables which had a more significant effect on the yield of biodiesel were the interactions between temperature and the methanol/oil ratio and between temperature and time where $p < 0.05$, followed by the quadratic terms of reaction time and molar ratio, which also had $p < 0.05$. We also note that the alcohol/oil molar ratio had a more significant effect on the viscosity ($p < 0.05$), followed by the reaction temperature and the interaction between temperature and reaction time.

3.1.3. Study of the Effects of Factors on Viscosity. The variation in the viscosity of biodiesel as a function of the interaction between reaction time and temperature is illustrated by the 3D response surface curve, coupled to the contour diagram, in Figure 4(a). This figure shows that the reaction time is a factor that changes in the opposite direction to that of the change in kinematic viscosity. When moving from low values for the reaction time to high values (60 min and 180 min), we saw that the viscosity decreased significantly from $5.54 \text{ mm}^2/\text{s}$ to $3.78 \text{ mm}^2/\text{s}$. Since transesterification is a reaction which greatly reduces the viscosity of oils, the high viscosity observed at low reaction times could be due to incomplete conversion of oil to methyl ester. Unreacted oil could thus increase the viscosity of the biodiesel [29]. Furthermore, the high viscosity observed after the optimum reaction time could be attributed to side reactions, such as saponification and esterification, since the reaction is reversible and takes place in an alkaline medium. These phenomena can lead to difficulties in separating the biodiesel layer from glycerol [30]. These observations were similar to those made by Chigozie et al. [31]. According to the American material standard test (ASTM D9751), the standard viscosity

TABLE 4: ANOVA results for biodiesel yield and viscosity.

Source	Sum of squares	Viscosity			Yield		
		Df	F-ratio	p	Sum of squares	F-ratio	p
x_1 (temperature)	0.4802	1	10.73	0.0220*	6.09005	2.33	0.1878
x_2 (reaction time)	0.0968	1	2.16	0.2012	14.9605	5.71	0.0624
x_3 (molar ratio)	3.2258	1	72.11	0.0004*	0.2312	0.09	0.7783
x_1^2	0.0072	1	0.16	0.7048	3.20493	0.63	0.4645
x_1x_2	0.4225	1	9.44	0.0277*	52.7076	20.13	0.0065*
x_1x_3	0.0225	1	0.50	0.5099	4.9729	1.90	0.2267
x_2^2	0.0022	1	4.53	0.8349	50.4567	19.27	0.0071*
x_2x_3	0.2025	1	4.53	0.0867	56.7009	21.65	0.0056*
x_3^2	0.2385	1	5.33	0.0690	20.4197	7.80	0.0383*
Total error	0.2237	5			13.0942		
$R^2 = 0.95449$		R^2 adjusted = 0.87				$R^2 = 0.94$; R^2 adjusted = 0.83	

*Significant at 95% confidence interval.

of conventional diesel is around 1.9-2.6 mm²/s. Therefore, a viscosity value outside this range does not have the properties that can be adapted to a diesel engine [32].

Figure 4(b) further shows that the methanol/oil molar ratio did not have a significant effect on viscosity. This was also confirmed by the low value of the constant observed compared to the molar ratio factor (x_3) in equation (15). This is not surprising, since after the reaction, the biodiesel was completely separated from the glycerol.

3.1.4. Study of the Effects of Methanol/Oil Molar Ratio, Reaction Time, and Temperature on the Biodiesel Yield. To investigate the interaction effects of the parameters on the reaction yield, two 3D response curves were plotted as shown in Figures 5(a) and 5(b) obtained using RSM. Figure 5(a) shows the interaction effect of reaction time and molar ratio on biodiesel yield. With respect to this figure, we noticed that high yields of 96.1% were obtained at relatively long reaction times of 120-180 min and molar ratios of 10:1 when the temperature was fixed at its average value of 50°C. This high yield of methyl ester could be due to the fact that the methanolysis of PFO is a reversible reaction and depends on the stoichiometry of the reaction. Indeed, an excess of alcohol in a molar ratio range 6:1 to 10:1 is needed to push the equilibrium in the direction of methyl ester production [33]. Moreover, for a very short reaction time (60 min), the low yields recorded could be explained by incomplete reactions. The optimal reaction time (180 min) being the longest duration could be linked to the moderate temperature, 50°C. It can be noticed that the interaction effect between reaction time and molar ratio has a positive effect on the reaction yield, as shown in equation (14). According to the results shown in Figure 5(b), the highest biodiesel yield (96.1%) was observed at the moderate reaction temperature (50°C) when the molar ratio was set at a value of 10:1. A slight reduction in yield was observed at temperature above 60°C, due to saponification reaction, which is faster than transesterification at high temperature

[34, 35]. Fadhil [32] obtained a similar result where he had an optimum production of esters from *Prunus amygdalus* seed oil at an optimum reaction temperature of 50°C.

The study of the effects of the various parameters and their reciprocal interactions led to the determination of the optimal conditions mentioned in Table 5:

3.2. Yield of Oil and Biodiesel Produced. *Podocarpus* oil was obtained with a yield of 47.8%; this may be because we used the power press. Moreover, the biodiesel produced under optimal conditions resulted in a yield of 96.1% (Figure 6). This value was very close to that predicted by the BB plan used.

3.3. Physicochemical Characteristics of Oil and Biodiesel. The physicochemical properties of biodiesel produced from PFO under optimum reaction conditions were measured according to ASTM standards. These properties were compared with those of PFO and diesel as shown in Table 6. From the results presented in this table, it can be seen that the calorific value of biodiesel produced from PFO is lower than that of diesel. This may be due to the higher oxygen content of biodiesel compared to diesel. Indeed, it has been demonstrated by Yamane et al. [36] that the presence of oxygen in the fuel improves combustion properties and emissions but lowers the calorific value. From the results presented in Table 6, it is clear that biodiesel has a lower density than PFO. This lower density of biodiesel compared to PFO is linked to the formation of methyl esters by eliminating glycerol. These results are close to those found by Tchuifon et al. [37].

Viscosity is an important parameter that affects fuel injection, lubrication, and atomization [38]. Fuels of high viscosity tend to form deposits in the engine. However, Table 6 shows that the kinematic viscosity of PFO decreased from 29.53 to 3.58 mm²/s at 40°C. This significant drop in viscosity confirms the efficiency of the transesterification reaction. Moreover, it is important to note that the high

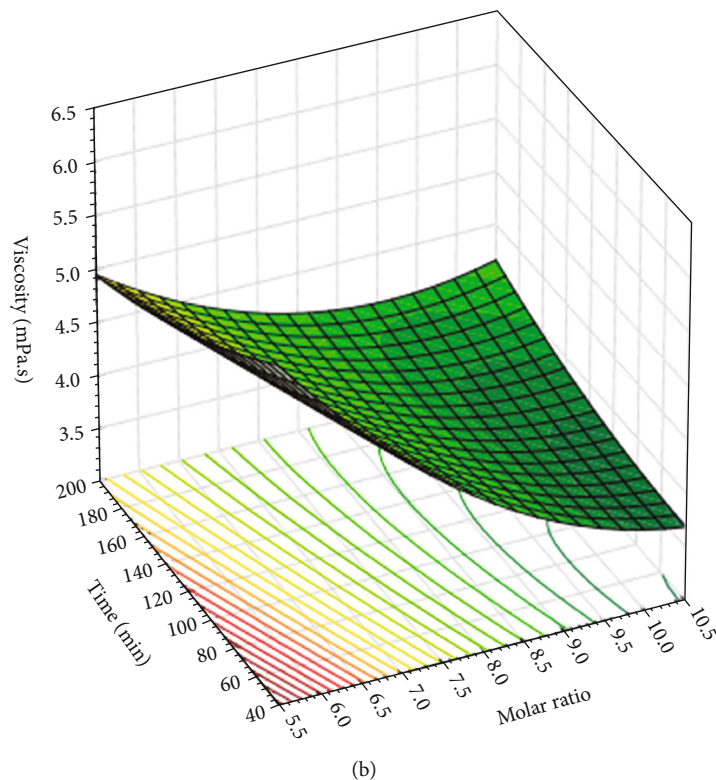
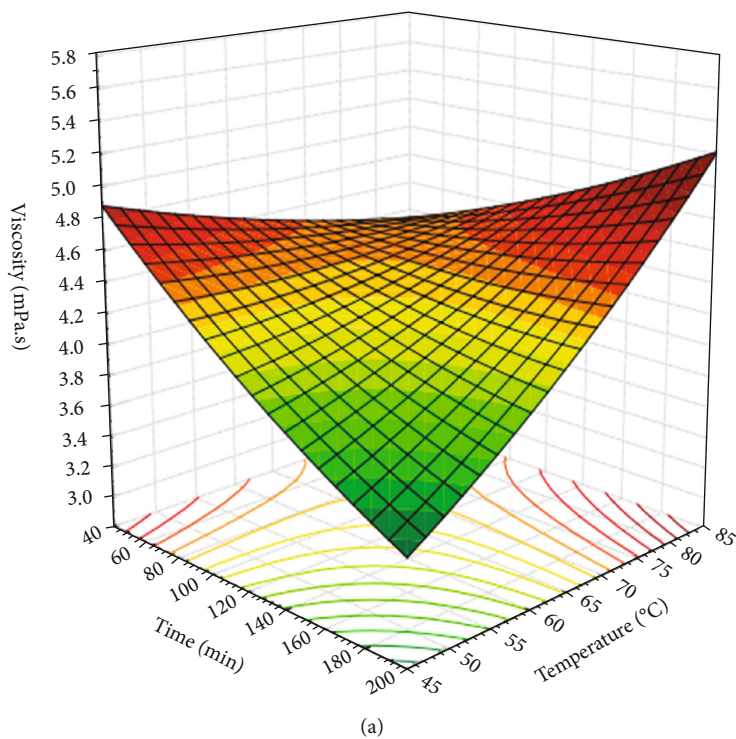
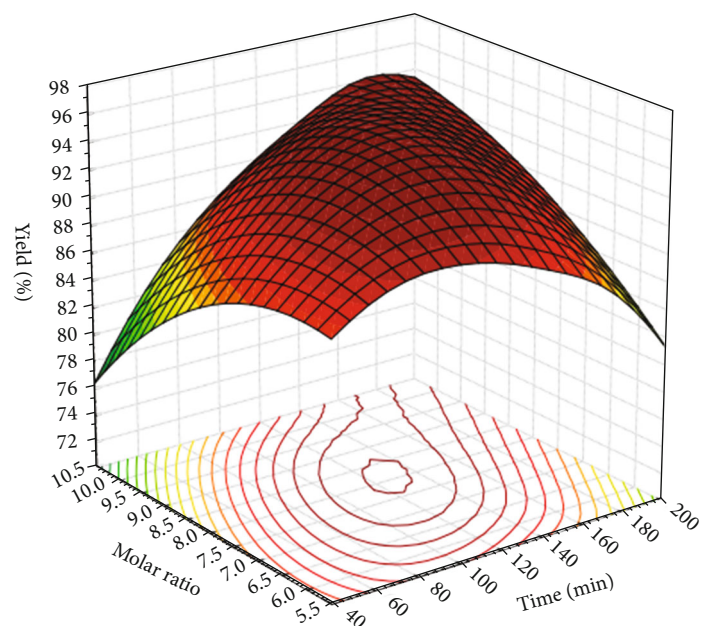


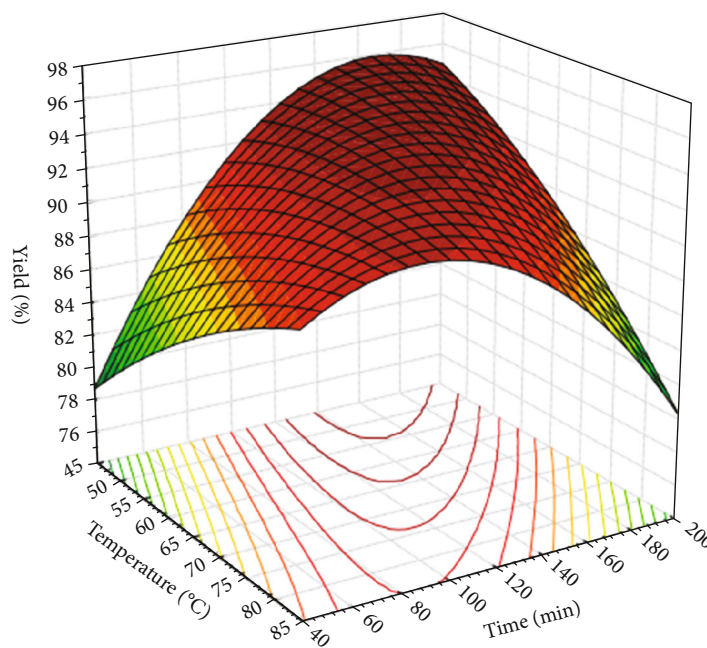
FIGURE 4: (a) Response surface contour for the effect of interaction between temperature and time on viscosity (KOH concentration: 1 wt.%). (b) Response surface contour for the effect of the interaction between time and molar ratio on viscosity (KOH concentration: 1 wt.%).

initial viscosity of this oil is due to its higher molecular weight compared to that of diesel fuel [39]. The interesting information is that the kinematic viscosity of biodiesel produced from *Podocarpus falcatus* oil is in the range 1.9-6.0 mm²/s as specified by ASTM. When a biodiesel having

a viscosity in this range is used in a diesel engine, it helps to lubricate parts of the engine [40]. Pour point analysis in the characterization of biodiesel is very important because it determines the suitability of the biofuel for large-scale storage. Pour point is the lowest temperature at which the



(a)



(b)

FIGURE 5: (a) Response surface contour for the effect of the interaction between time and molar ratio on yield (KOH concentration: 1 wt.%). (b) Response surface contour for the effect of the interaction between time and temperature on yield (KOH concentration: 1 wt.%).

TABLE 5: Optimal viscosity and yield conditions.

Parameters	Optimal values of parameters		Predicted responses	
	Viscosity	Yield	Viscosity	Yield
Temperature (°C)	79.985	50		
Reaction time (min)	60.0	180	5.4738 mm ² /s	98.738%
Molar ratio	6.00027/1	9.99997/1		

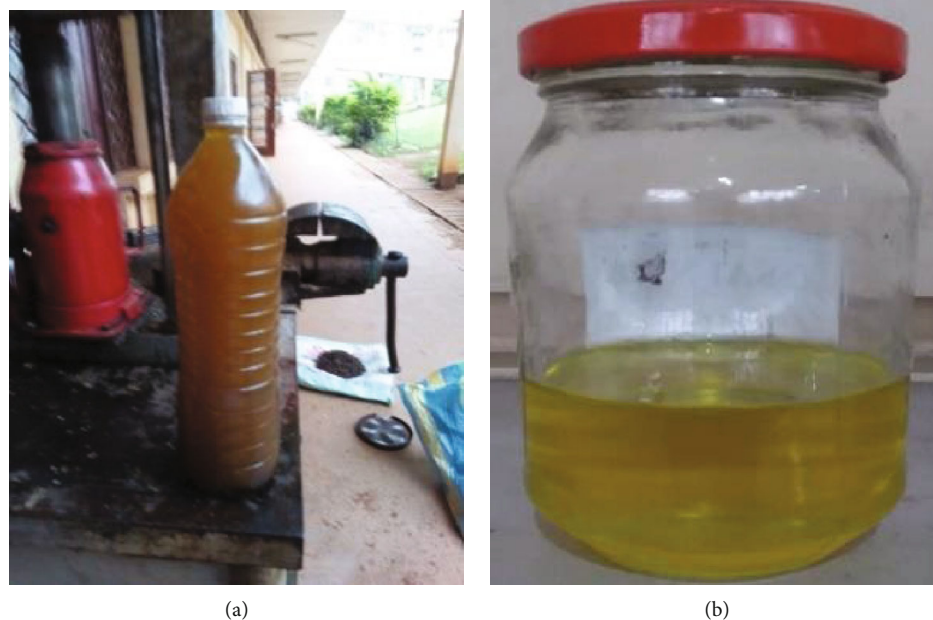


FIGURE 6: (a) *Podocarpus falcatus* oil. (b) Optimized biodiesel.

TABLE 6: Physicochemical properties of PFO and biodiesel compared to ASTM D6751.

Properties	Units	PFO	Biodiesel	Diesel	ASTM D6751
Density (at 15°C)	kg/m ³	922	872	845	880
Viscosity (40°C)	mm ² /s	29.53	3.58	2.4	1.9-6
Pour point	°C	-8.6	-15.20	-17	-15 at -16
Calorific value	MJ/kg	39.47	39.87	42.54	35
Cetane number	-	42.06	51.03	50	48-60
Acid index	mg KOH/g	1.90	0.40	-	Max. 0.5
Iodine number	g I ₂ /100 g	147.10	103.10	-	-
Saponification index	mg KOH/g	189.11	195.44	-	-

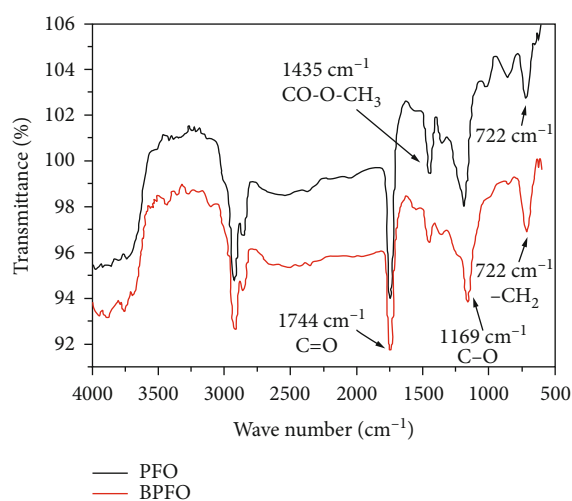


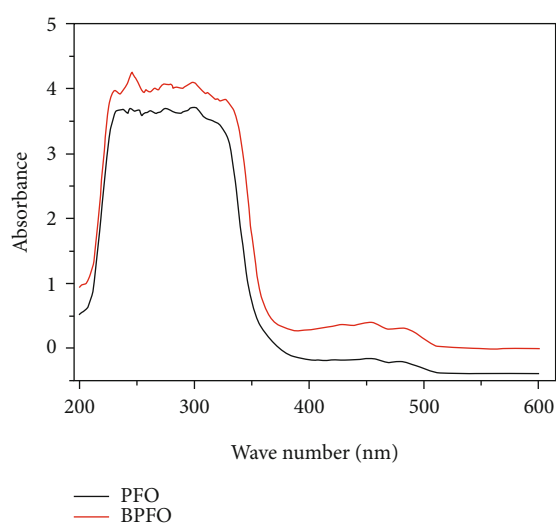
FIGURE 7: FT-IR spectra of *Podocarpus falcatus* oil (PFO) and biodiesel (BPFO).

fuel can still flow before it has gelled. This also reflects the biodiesel's ability to be used in cold climates [41]. The pour point found in this work is -15°C for the biodiesel obtained. On the other hand, the pour point value of -8.6°C obtained for *Podocarpus falcatus* oil is significantly higher than that of biodiesel. This could be due to the presence of glycerol in this oil which makes the medium more viscous and thus promotes gelation. This result is in harmony with that found by Fadhil et al. [42]. The cetane number (CN) of PFO (42.06) is lower than that of biodiesel (51.03). This variation can be attributed to the unsaturated fatty acids present in the oil. Chemical properties such as acid value, saponification value, and iodine value of PFO and biodiesel were determined and compared in Table 6. It appears that these properties are comparable with the standards of the American Society for the Testing of Materials (ASTM).

3.4. Analysis by IR-TF Spectrometry of Oil and Biodiesel. Figure 7 shows the superimposed infrared spectra of *Podocarpus falcatus* oil and the biodiesel obtained from it.

TABLE 7: Main position of characteristic bands for oil and biodiesel.

PFO		BPFO	
Absorption vibration (cm^{-1})	Functional groups	Absorption vibration (cm^{-1})	Functional groups
722	Deformation $-\text{CH}_2$	722	Tilting $-\text{CH}_2$
1362	CH_2 group deformation vibration	1362	CH_2 group deformation vibration
1744	Elongation $\text{C}=\text{O}$	1742	Elongation $\text{C}=\text{O}$
1169	Stretching $\text{C}-\text{O}$	1194	Elongation $\text{C}-\text{O}$
		1171	Elongation
		1110	$\text{C}-\text{O}-\text{O}-\text{CH}_2-\text{C}$
1435	Deformation vibration CH_2	1435	Methyl ester group ($\text{CO}-\text{O}-\text{CH}_3$)
2925	Elongation $-\text{CH}_2$	2927	Elongation $-\text{CH}_2$

FIGURE 8: Superimposed UV-VIS spectra of *Podocarpus falcatus* oil (PFO) and its biodiesel (BPFO).

The characteristic absorption peaks of *Podocarpus falcatus* oil have been shown in Figure 7 in black. The absorption peak appearing at 722 cm^{-1} corresponds to the strain vibration of $-\text{CH}_2$, and the one at $1,744\text{ cm}^{-1}$ corresponds to the stretch vibration of the $\text{C}=\text{O}$ ester group. The spectrum of biodiesel shows an absorption peak appearing at $1,435\text{ cm}^{-1}$, characteristic of a methyl ester group ($\text{CO}-\text{O}-\text{CH}_3$), and the absorption peak at $1,194\text{ cm}^{-1}$ corresponding to the ester group (CO). The reduction in the peak at $1,435\text{ cm}^{-1}$ on the biodiesel spectrum can be attributed to the departure of the glycerol molecule and the appearance of CH_3-O vibrations in the biodiesel. Additionally, the separation of $1,169\text{ cm}^{-1}$ in the oil sample to $1,194\text{ cm}^{-1}$ and $1,171\text{ cm}^{-1}$ in the biodiesel sample indicates the conversion of the oil into biodiesel. Table 7 shows the characteristic band positions of the TF-IR for *Podocarpus falcatus* oil and the *Podocarpus falcatus* oil biodiesel produced.

3.5. UV-VIS Spectrophotometric Analysis of Oil and Biodiesel. Figure 8 below shows the superimposed UV-VIS spectra of *Podocarpus falcatus* oil and its biodiesel. In this figure, we observe an intense band around 250 nm on the

spectrum of *Podocarpus falcatus* oil which is not present on the spectrum of biodiesel. This peak observed at around 250 nm is probably absorption due to the $\pi \rightarrow \pi^*$ transition of the carbonyl of the triglycerides. A second peak is also observed around 300 nm which can be attributed to the $n \rightarrow \pi^*$ transition of the carbonyl. Moreover, from these curves, we can conclude that the absence of the $\pi \rightarrow \pi^*$ carbonyl transition of the triglycerides on the black spectrum confirms the absence of glycerol in the ester mixture formed.

4. Conclusions

Oil from *Podocarpus falcatus* was used to produce biodiesel by transesterification. The oil used was extracted mechanically using a hydraulic press that gave an extraction yield of 47.8% by mass, making the oil a promising raw material for the synthesis of biodiesel. Since an analysis of the oil showed that it had an acid number of less than 2%, the biodiesel was therefore produced through a one-step transesterification process with methanol, using KOH as catalyst. The optimization of the process was achieved by applying the response surface methodology, using the Box-Benhken design. The optimum conditions to produce the highest yield of biodiesel (96.1%) were as follows: a molar ratio of 10:1, a temperature of 50°C , and a reaction time of 180 minutes. The minimum viscosity, $3.58\text{ mm}^2/\text{s}$, was obtained at a molar ratio of 10:1, temperature of 50°C , and a duration of 120 min. Physicochemical analyses of both oil and the biodiesel using IR and UV-VIS confirmed the conversion of triglycerides into methyl esters, and that the properties of the biofuel produced comply with the standard prescribed by ASTM6751. Based on the results of this study, we can conclude that *Podocarpus falcatus* oil can be used as a non-edible oil to produce good quality biodiesel under optimal conditions.

Abbreviations

ANOVA: Analysis of variance
 ASTM: American Standard for Testing Materials
 BBD: Box-Benhken design
 BPFO: Biodiesel of *Podocarpus falcatus* oil

RSM: Response surface methodology
 FFA: Free fatty acid
 FT-IR: Fourier transform infrared spectroscopy
 PFO: Podocarpus falcatus oil
 UV-VIS: Ultraviolet-visible.

Data Availability

The numerical data used to support the findings of this study have been deposited in the Mendeley repository (doi:10.17632/2n5wst4r9x.1) or <https://data.mendeley.com/datasets/2n5wst4r9x/1/>.

Conflicts of Interest

The authors declare that they have no conflicts of interest.

Acknowledgments

The authors thank the assistance offered by NGUEDAP Richard of the University of Douala for the determination of the viscosity of the samples and all the members of the Research Unit/RU-NOGEE of the University of Dschang for their various contributions in the improvement of the quality of work. The authors would like to thank everyone who supported this study.

References

- [1] I. S. Manaf, N. H. Embong, S. N. M. Khazaai et al., "A review for key challenges of the development of biodiesel industry," *Energy Conversion and Management*, vol. 185, no. 10, pp. 508–517, 2019.
- [2] M. Ashjari, M. Garmroodi, F. A. Asl et al., "Application of multi-component reaction for covalent immobilization of two lipases on aldehyde-functionalized magnetic nanoparticles; production of biodiesel from waste cooking oil," *Process Biochemistry*, vol. 90, pp. 156–167, 2020.
- [3] R. Naveenkumar and G. Baskar, "Optimization and techno-economic analysis of biodiesel production from *Calophyllum inophyllum* oil using heterogeneous nanocatalyst," *Bioresource Technology*, vol. 315, no. 1, article 123852, 2020.
- [4] T. S. Singh and T. N. Verma, "Taguchi design approach for extraction of methyl ester from waste cooking oil using synthesized CaO as heterogeneous catalyst: response surface methodology optimization," *Energy Conversion and Management*, vol. 182, pp. 383–397, 2019.
- [5] H. Hosseinzadeh-Bandbafha, M. Tabatabaei, M. Aghbashlo, M. Khanali, and A. Demirbas, "A comprehensive review on the environmental impacts of diesel/biodiesel additives," *Energy Conversion and Management*, vol. 174, pp. 579–614, 2018.
- [6] A. Srivastava and R. Prasad, "Triglycerides-based diesel fuels," *Renewable and Sustainable Energy Reviews*, vol. 4, no. 2, pp. 111–133, 2000.
- [7] A. Kumar and S. Sharma, "Potential non-edible oil resources as biodiesel feedstock: an Indian perspective," *Renewable and Sustainable Energy Reviews*, vol. 15, no. 4, pp. 1791–1800, 2011.
- [8] T. Saba, J. Estephane, B. El Khoury et al., "Biodiesel production from refined sunflower vegetable oil over KOH/ZSM5 catalysts," *Renewable Energy*, vol. 90, no. 7, pp. 301–306, 2016.
- [9] R. Sakthivel, K. Ramesh, R. Purnachandran, and P. M. Shameer, "A review on the properties, performance and emission aspects of the third generation biodiesels," *Renewable and Sustainable Energy Reviews*, vol. 82, no. 3, pp. 2970–2992, 2018.
- [10] V. Singh, F. Bux, and Y. C. Sharma, "A low cost one pot synthesis of biodiesel from waste frying oil (WFO) using a novel material, β -potassium dizirconate (β -K₂Zr₂O₅)," *Applied Energy*, vol. 172, pp. 23–33, 2016.
- [11] A. Atabani, A. Silitonga, I. A. Badruddin, T. Mahlia, H. Masjuki, and S. Mekhilef, "A comprehensive review on biodiesel as an alternative energy resource and its characteristics," *Renewable and Sustainable Energy Reviews*, vol. 16, no. 4, pp. 2070–2093, 2012.
- [12] S. T. Keera, S. M. El Sabagh, and A. R. Taman, "Castor oil biodiesel production and optimization," *Egyptian Journal of Petroleum*, vol. 27, no. 4, pp. 979–984, 2018.
- [13] L. K. Sinha, S. Haldar, and G. C. Majumdar, "Effect of operating parameters on mechanical expression of solvent-soaked soybean-grits," *Journal of Food Science and Technology*, vol. 52, no. 5, pp. 2942–2949, 2015.
- [14] A. B. Fadhil and A. I. Ahmed, "Production of mixed methyl/ethyl esters from waste fish oil through transesterification with mixed methanol/ethanol system," *Chemical Engineering Communications*, vol. 205, no. 9, pp. 1157–1166, 2018.
- [15] S. Feleke, S. Haile, A. Alemu, and S. Abebe, "Characteristics of speed kernel oil from *Podocarpus falcatus*," *Journal of Tropical Forest Science*, vol. 24, no. 4, pp. 512–516, 2012.
- [16] R. A. Carr, "Refining and degumming systems for edible fats and oils," *Journal of the American Oil Chemists' Society*, vol. 55, no. 11, pp. 765–771, 1978.
- [17] M. M. Hassan and A. B. Fadhil, "Development of an effective solid base catalyst from potassium-based chicken bone (K-CBs) composite for biodiesel production from a mixture of non-edible feedstocks," *Energy Sources, Part A: Recovery, Utilization, and Environmental Effects*, vol. 43, pp. 1–16, 2021.
- [18] G. Dwivedi and M. P. Sharma, "Impact of cold flow properties of biodiesel on engine performance," *Renewable and Sustainable Energy Reviews*, vol. 31, pp. 650–656, 2014.
- [19] J. Gupta, M. Agarwal, and A. K. Dalai, "Optimization of biodiesel production from mixture of edible and nonedible vegetable oils," *Biocatalysis and Agricultural Biotechnology*, vol. 8, no. 1, pp. 112–120, 2016.
- [20] Z. Zhang and H. Zheng, "Optimization for decolorization of azo dye acid green 20 by ultrasound and H₂O₂ using response surface methodology," *Journal of Hazardous Materials*, vol. 172, no. 2-3, pp. 1388–1393, 2009.
- [21] P. Qiu, M. Cui, K. Kang et al., "Application of Box-Behnken design with response surface methodology for modeling and optimizing ultrasonic oxidation of arsenite with H₂O₂," *Open Chemistry*, vol. 12, no. 2, pp. 164–172, 2014.
- [22] G. Yin and Y. Dang, "Optimization of extraction technology of the *Lycium barbarum* polysaccharides by Box-Behnken statistical design," *Carbohydrate Polymers*, vol. 74, no. 3, pp. 603–610, 2008.
- [23] N. Aslan and Y. Cebeci, "Application of Box-Behnken design and response surface methodology for modeling of some Turkish coals," *Fuel*, vol. 86, no. 1-2, pp. 90–97, 2007.

- [24] K. Yetilmezsoy, S. Demirel, and R. J. Vanderbei, "Response surface modeling of Pb(II) removal from aqueous solution by *Pistacia vera* L.: Box -Behnken experimental design," *Journal of Hazardous Materials*, vol. 171, no. 1-3, pp. 551-562, 2009.
- [25] F. T. T. Rufis, I. Ionel, and S. G. Anagho, "A.C. Mihaiuti Optimization of the activated carbon preparation from avocado seeds, using the response surface methodology," *Revista de Chimie*, vol. 70, no. 2, pp. 410-416, 2019.
- [26] K. Krisnangkura, "A simple method for estimation of cetane index of vegetable oil methyl esters," *Journal of the American Oil Chemists Society*, vol. 63, no. 4, pp. 552-553, 1986.
- [27] A. Demirbas, "Biodiesel fuels from vegetable oils via catalytic and non-catalytic supercritical alcohol transesterifications and other methods: a survey," *Energy Conversion and Management*, vol. 44, no. 13, pp. 2093-2109, 2003.
- [28] K. Khiari, *Contribution à l'étude des propriétés thermophysiques des biocarburants de seconde génération et leur influence sur le comportement des moteurs*, Thèse de Doctorat/PhD, Ecole des Mines de Nantes, Nantes, France, 2016.
- [29] A. N. Sarve, M. N. Varma, and S. S. Sonawane, "Response surface optimization and artificial neural network modeling of biodiesel production from crude mahua (*Madhuca indica*) oil under supercritical ethanol conditions using CO₂ as co-solvent," *RSC Advances*, vol. 5, no. 85, pp. 69702-69713, 2015.
- [30] C. Senthilkumar, C. Krishnaraj, P. Sivakumar, and A. Sircar, "Statistical optimization and kinetic study on biodiesel production from a potential non-edible bio-oil of wild radish," *Chemical Engineering Communications*, vol. 206, no. 7, pp. 909-918, 2019.
- [31] U. C. F. Chigozie, A. Nnuekwe, O. Onukwuli, S. Ofochebe, and C. Ezekannagha, "Optimal route for effective conversion of rubber seed oil to biodiesel with desired key fuel properties," *Journal of Cleaner Production*, vol. 280, article 124563, 2021.
- [32] A. B. Fadhil, "Optimization of transesterification parameters of melon seed oil," *International Journal of Green Energy*, vol. 10, no. 7, pp. 763-774, 2013.
- [33] A. B. Fadhil, "Biodiesel production from beef tallow using alkali-catalyzed transesterification," *Arabian Journal for Science and Engineering*, vol. 38, no. 1, pp. 41-47, 2013.
- [34] C. Esonye, O. D. Onukwuli, and A. U. Ofoefule, "Optimization of methyl ester production from *Prunus Amygdalus* seed oil using response surface methodology and Artificial Neural Networks," *Renewable Energy*, vol. 130, pp. 61-72, 2019.
- [35] A. A. Ayola, F. K. Hymore, M. A. Obande, and I. Udeh, "Optimization of experimental conditions for biodiesel production," *International Journal Engineering and Technology*, vol. 12, no. 6, pp. 130-133, 2012.
- [36] K. Yamane, A. Ueta, and Y. Shimamoto, "Influence of physical and chemical properties of biodiesel fuels on injection, combustion and exhaust emission characteristics in a direct injection compression ignition engine," *International Journal of Engine Research*, vol. 2, no. 4, pp. 249-261, 2001.
- [37] D. R. T. Tchuifon, S. B. L. Ngomade, G. N. Ndifor-Angwafor et al., "Production of biodiesel by transesterification reaction of waste cooking oil," *Chemical Science International Journal*, vol. 3, no. 4, 2020.
- [38] M. Ahmad, S. Rashid, M. A. Khan, M. Zafar, S. Sultana, and S. Gulzar, "Optimization of base catalyzed transesterification of peanut oil biodiesel," *African Journal of Biotechnology*, vol. 8, no. 3, pp. 441-446, 2009.
- [39] B. K. Barnwal and M. P. Sharma, "Prospects of biodiesel production from vegetable oils in India," *Renewable and Sustainable Energy Reviews*, vol. 9, no. 4, pp. 363-378, 2005.
- [40] G. B. Adebayo, O. M. Ameen, and L. T. Abass, "Physico-chemical properties of biodiesel produced from *Jatropha curcas* oil and fossil diesel," *Journal of Microbiology and Biotechnology Research*, vol. 1, no. 1, pp. 12-16, 2011.
- [41] A. B. Fadhil, O. M. Nayyef, and S. H. Sedeeq, "Valorization of mixed radish seed oil and *Prunus armeniaca* L. oil as a promising feedstock for biodiesel production: evaluation and analysis of biodiesels," *Asia-Pacific Journal of Chemical Engineering*, vol. 15, no. 1, p. 2390, 2020.
- [42] A. B. Fadhil, S. H. Sedeeq, and N. M. Al-Layla, "Transesterification of non-edible seed oil for biodiesel production: characterization and analysis of biodiesel," *Energy Sources, Part A: Recovery, Utilization, and Environmental Effects*, vol. 41, no. 7, pp. 892-901, 2019.

Research Article

Optimized Removal of Hydroquinone and Resorcinol by Activated Carbon Based on Shea Residue (*Vitellaria paradoxa*): Thermodynamics, Adsorption Mechanism, Nonlinear Kinetics, and Isotherms

Liouna Adoum Amola ¹, Theophile Kamgaing ¹, Rufis Fregue Tiegam Tagne ²,
Cyrille Donlifack Atemkeng ¹, Idris-Hermann Tiotsop Kuete ¹,
and Solomon Gabche Anagho ¹

¹Research Unit of Noxious Chemistry and Environmental Engineering, Department of Chemistry, University of Dschang, P.O. Box 67, Dschang, Cameroon

²Department of Paper Sciences and Bioenergy, University Institute of Wood Technology, University of Yaounde I, Mbalmayo, Cameroon

Correspondence should be addressed to Theophile Kamgaing; theokamgaing@yahoo.fr

Received 13 November 2021; Revised 17 December 2021; Accepted 22 December 2021; Published 17 January 2022

Academic Editor: Yuanjuan Bai

Copyright © 2022 Liouna Adoum Amola et al. This is an open access article distributed under the Creative Commons Attribution License, which permits unrestricted use, distribution, and reproduction in any medium, provided the original work is properly cited.

The present work demonstrates the adsorption of hydroquinone (HQ) and resorcinol (R) by activated carbon based on shea residue (*Vitellaria paradoxa*). The adsorbent was prepared chemically by impregnation with sulfuric acid and coded by the acronym CAK-S. The central composite design (CCD) was used to optimize the main factors that influence the adsorption of HQ or R by activated carbon such as the initial concentration, the pH of the solution, the contact time, and the mass of the carbon on the expected response, which is the adsorbed quantity of the target pollutants. The optimal conditions obtained from the statistical analysis are as follows: concentration of 158 mg/L, pH 3, time of 120 min, and mass of 50 mg for the adsorption of HQ and concentration of 180 mg/L, pH 3, time of 86 min, and mass of 118 mg for the adsorption of R. The maximum quantities of HQ and R adsorbed are 45.02 mg/g and 33.65 mg/g, respectively. The analysis of variance (ANOVA) showed a good relationship between the variables involved with the coefficients of determination $R^2 = 98.69\%$ for the adsorption of hydroquinone and $R^2 = 90.55\%$ for that of resorcinol, which means that the model is more suitable to express the adsorbed amount according to the four optimized parameters. The experimental data obtained under these optimal conditions were simulated with two and three parameter nonlinear isotherm models as well as kinetic models. The results show that Elovich kinetic model better describes the adsorption of HQ and R, indicating chemisorption with heterogeneous active sites on the surface of CAK-S. Temkin's two-parameter model shows that adsorption occurs on heterogeneous surfaces with a nonuniform adsorption energy distribution at the surface and Sips's three-parameter model confirms the heterogeneity of the surface with a localized adsorption of HQ or R by CAK-S. The thermodynamics study has shown that the adsorption is endothermic ($\Delta H^0 > 0$) and spontaneous ($\Delta G^0 < 0$).

1. Introduction

Environmental pollution remains as one of the major problems arising from technological development. Phenolic compounds and their derivatives are recognized as pollutants [1]. They are released into the environment during their

production and use. They mainly come from discharges from textile, petrochemical, petroleum refinery, rubber, dye, plastic, pharmaceutical, and cosmetic industries [2, 3]. Several phenolic derivatives such as hydroquinone (HQ) and resorcinol (R) have been recognized as being dangerous pollutants due to their potential toxicity [4]. Wastewater

laden with HQ and R is harmful to the environment in general and to the aquatic environment in particular [4, 5] because these compounds dissolve and can easily infiltrate the environment. Although the carcinogenic effects of HQ and R in humans are controversial, these compounds cause acute toxicity in several organs such as the kidneys and stomach [1] and are suspected to be endocrine disruptors. The human body exposure threshold is 0.5 mg/L [6] for HQ and 10 mg/L for R [7]. Therefore, wastewater containing these pollutants beyond these standards, respectively, must be subjected to treatment before discharge. Thus, many processes for treating water loaded with phenolic derivatives have been recommended. These include conventional physical, chemical, or biological processes such as chemical oxidation, chemical reduction, chemical precipitation, adsorption, ion exchange, solvent extraction, reversed osmosis, and aerobic and anaerobic biodegradation [8–14]. The application of some of these methods is restricted not only because of technical and economic constraints but also by the fact that some of them are not accessible to low-income developing countries. It is in this logic that, for some time, researchers have been investigating the development of less expensive methods, including adsorption on adsorbents at a lower cost [15–17]. These less expensive adsorbents can be simple biomasses or activated carbons prepared from agroindustrial residues [18–20]. Tropical Africa is full of potential valuable fruit species which are not only abundant but also available almost round the year. They tend to generate large amounts of waste residue which can be used in the preparation of activated carbons. An example of such a residue is nuts from the plant *Vitellaria paradoxa*. It is widely distributed in southern Chad.

Nowadays, the method of optimization by experimental design is increasingly appealing to researchers because it permits the extraction of maximum information with a minimum of simulation results. One of the adsorption optimization methods is the response surface methodology, which is an efficient statistical tool, making it possible to explain interactions independent of operating parameters [21–23]. The central composite design was used in this work to optimize the factors that affect the adsorption of HQ and R from solution. These factors include initial concentration, the pH of the solution, the contact time, and the mass of carbon on the response which is the adsorbed quantity of HQ or R. These experimental quantities can be simulated by kinetic or isotherm models. Nowadays, to properly describe and model the kinetic and isotherm adsorption, two methods exist: the nonlinear method and the linear method. Recent works have shown that nonlinear regression produces very satisfactory results compared to linear regression [24, 25]. Thus, for the nonlinear regression, the selection of the error functions showed a remarkable change in terms of the values of the constants linked to the models studied [26, 27]. So, nonlinear regression is the best option. The objective of this work is threefold. We propose (i) valorizing the shea residue (already calcined) of Chadian origin by examining its adsorption capacity on HQ and R in batch mode, (ii) optimizing the operating parameters of adsorption by response surface methodology, and (iii) modeling the kinetic, equilibrium, and

adsorption isotherms by the nonlinear method. We also evaluate the thermodynamic processes that accompany it. The interest of this work is the efficient removal of organic pollutants by activated carbon based on agricultural by-products for a sustainable use of local biomass.

2. Materials and Methods

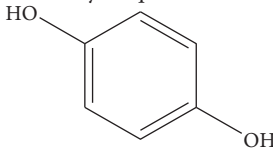
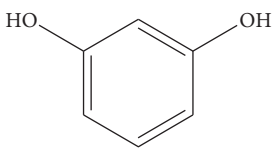
2.1. Chemicals. Hydroquinone and resorcinol are isomers with a molar mass of 110.11 g/mol. They were purchased with a purity greater than 99% from Sigma-Aldrich alongside all the other chemicals used in this work. The structures and some chemical properties of HQ and R are shown in Table 1.

2.2. Preparation of the Adsorbent. The procedure for preparing the activated carbon is that described in our previous work [28]. The shea nut shells (CNK) were collected in Baktchoro in the Division of Tandjilé-Ouest, Province of Tandjilé, Chad. Once collected, they were first washed with tap water to remove the rest of the pulp and any other form of impurities and then dried in an oven at 105°C for 24 hours to dehydrate them. They were crushed and the sizes of 0.5–2 mm were kept. A mass of 20 g of shea nut shells was impregnated with 40 mL of sulfuric acid (H₂SO₄) with concentration of 3.5 mol/L. The mixture was stirred for 24 hours to ensure reaction between the activating agent and the biomass and then filtered and dried in an oven at a temperature of 105°C for 1 hour. The impregnated materials were carbonized in a reactor (HERAEUS) at 700°C at a constant rate of 6°C/min and a residence time of 120 minutes. The carbonized material was washed to remove residual acid until it attained the pH value of the water used in washing. It was oven-dried at 105°C, crushed, and sieved to obtain particles with a diameter of less than 200 μm. The activated carbon obtained from shea nuts by impregnation with sulfuric acid was coded CAK-S.

2.3. Characterization of Activated Carbon. The use of a material in adsorption deserves broad knowledge of its physicochemical and structural properties. The activated carbon produced was characterized. These characterizations focused on energy dispersive X-ray spectrometry (EDX), scanning electron microscopy, determination of porous structure by nitrogen adsorption at 77 K by coupling the Brunauer–Emmett–Teller (BET) method to that of Barrett–Joyner–Halenda (BJH), the quantification of surface chemical functions by the Boehm method, and the pH at the point of zero charge (pHpzc). The crystalline or amorphous structure of the activated carbon was analyzed by means of X-ray diffraction. The analysis was carried out on a STOE Stage device (STOE & Co. GmbH, Darmstadt, Germany) with a Cu K α1 radiation ($\lambda = 1.54056 \text{ \AA}$, 40 kV, 30 mA).

2.4. Batch Mode Adsorption Studies. A 1000 mg/L stock solution of hydroquinone and resorcinol was prepared by dissolving 1.01 g each in 1 L of distilled water. Standards

TABLE 1: Chemical structures and some properties of hydroquinone and resorcinol.

Some chemical structures	Hydroquinone	Resorcinol
Chemical structure		
Molecular formula	C ₆ H ₄ -1,4(OH)	C ₆ H ₄ -1,3(OH)
λ _{max} (nm)	276	274
Solubility in water (25°C)	73 g/L	717 g/L
pKa	9.96	9.26

were then obtained by dilution of the stock solution. The pH of the solution was adjusted with 0.1 mol/L solution of NaOH and 0.1 mol/L solution of HCl, using a Mettler Toledo brand pH meter. Batch adsorption was performed following the central composite design matrix. A mass, m (g), of activated carbon was put in contact with 30 mL of a solution of hydroquinone or resorcinol of initial concentration, C (mg/L). The mixture obtained was placed on an agitator at a speed of 150 rpm for a contact time, t (min), at room temperature of 25°C. At equilibrium, the mixture was filtered; the filtrate obtained was analyzed by ultraviolet visible spectrophotometry (UV-Vis) at a wavelength of 276 nm and 274 nm, respectively, for hydroquinone and resorcinol. The amount adsorbed per gram of activated carbon was calculated using the following equation:

$$Q_e = \frac{C_i - C_e}{m} V, \quad (1)$$

where Q_e (mg/g) is the adsorption capacity, m (g) is the mass of activated carbon, C_i and C_e (mg/L) are the initial and equilibrium concentrations, respectively, and V (L) is the volume of the pollutant solution used.

2.5. Response Surface Methodology and Statistical Analysis of the Data. The response surface methodology is a statistical analysis tool that predicts and develops a regression model for quantitative data obtained during an experiment [22]. The model equations predict and optimize the operating conditions of the process. This makes it possible to understand the mutual dependence of the variables and to know the variables that govern the experimental system. In this work, the response surface methodology was employed to assess the interdependence of operating variables such as the initial concentration of hydroquinone or resorcinol, the pH of the solution, the contact time, and the mass of activated carbon on the adsorption process. The central composite design was used to optimize the process [22]. For four independent variables and four chosen central points, the CCD generates 28 experiments according to the following equation:

$$N = 2^k + 2k + k_c = 2^4 + 2 * 4 + 4 = 28, \quad (2)$$

where N is the total number of experiments, k is the number of factors studied, and k_c is the number of points in the center which allows measuring the reproducibility of data.

These variables were coded as such: adsorbate concentration (A : 20–180 mg/L), solution pH (B : 2–8), contact time (C : 60–120 min), and mass of activated carbon (D : 50–250 mg). The response, Y , observed is the amount of HQ or R adsorbed on CAK-S carbon. The levels of the experimental values were also coded as follows: -1 , the small value, 0 , the value in the center, and $+1$, the upper value. This unique encoding is defined from the one-to-one transformation defining the value x_i of equation (3) [29]. All coded variables are shown in Table 2.

$$x_i = \frac{L_i - L_0}{\Delta L}, \quad (3)$$

where x_i is the value of the independent variable, L_i is the value of variable i , L_0 is the value at the central point, and ΔL is the step.

The 28 experiments represent a system which translates the quadratic model (equation (4)) to study the interactions between the variables [30].

$$Y = \beta_0 + \sum_{i=1}^n \beta_i x_i + \sum_{i=1}^n \beta_{ii} x_i^2 + \sum_{i=1}^n \sum_{j=1}^n \beta_{ij} x_i x_j + \varepsilon, \quad (4)$$

where Y is the predicted response, β_0 is the constant of the quadratic equation, β_i is the linear coefficient, β_{ii} is the quadratic coefficient, β_{ij} is the coefficient of the interaction between the variables, x_i and x_j are the coded values of the factors, and ε is the uncertainty between measured and predicted values.

2.5.1. Validation of the Statistical Model. To complete the statistical analysis of the experimental data, STATGRAPHIC Plus 5.0 software was used. This software statistically evaluates according to the following criteria: (a) each factor must present a p value, that is, the value of the probability smaller than 5%, with a confidence limit of 95%, (b) the value of regression coefficient R^2 must be as close as possible to 1, which means that the experimental values and the predicted values are close to each other, (c) the t -test must be significant ($p < 0.05$), which means that the model adequately describes the experimental data, and eventually (d) the proximity between the data of the predicted points and the data of the experimental points must present a normal distribution to validate the hypothesis made by the analysis of variance (ANOVA) [22].

TABLE 2: Matrix of coded variables.

Variables	Symbols	Units	Coded variables	Variables levels		
				-1	0	+1
Concentration	C_0	(mg/L)	A	20	100	180
pH	pH	—	B	2	6	10
Time	t	(min)	C	30	75	120
Mass	m	(mg)	D	50	150	250

2.6. *Kinetic and Isothermal Adsorption Equilibrium.* To understand the mechanism that governs the binding of HQ or R on CAK-S, the experimental data were applied to nonlinear kinetic models including the pseudo-first-order model, pseudo-second-order model, Elovich kinetic model, and the intraparticle model. In addition, for the adsorption isotherm of HQ or R, the two-parameter and three-parameter nonlinear models were simulated with the experimental data (Table 3).

2.7. *Nonlinear Method and Analysis of Error Functions.* The purpose of nonlinear regression is to adjust a set of values in order to bring the experimental curves closer to the predictions. The difference between the linear and nonlinear methods is that the latter is iterative and based on an algorithm and error functions [40, 41]. Table 4 shows the mathematical expressions of the error functions used in this work.

3. Results and Discussion

3.1. *Characterization of Activated Carbon.* The detailed characterizations of CAK-S carbon have been reported in our previous work [28]. It was found that this activated carbon has a specific surface area of 490.62 m²/g, a microporous surface area of 570.56 m²/g, and a mesoporous surface area of 10.77 m²/g, as well as a pH at the zero charge point of 6.37. The X-ray diffraction of the material, which was not included in our previous work, is presented here (Figure 1). We observe in Figure 1 a broad peak around 20° for the two spectra corresponding to the amorphous structure of carbon. The spectra show that both raw and calcined shea nut shells have an amorphous structure. This amorphous structure is a preferred property of well-defined adsorbents [26].

Figure 2 shows the FTIR spectra recorded in the region of 3500 and 700 cm⁻¹. Before adsorption of pollutants HQ and R by CAK-S, a signal at 3395.41 cm⁻¹ is observed on the spectrum attributable to the O-H group of phenols and alcohols; this would be due to the presence of hydroxyl groups in the water chemisorbed [14] on CAK-S. Other peaks were observed: a peak at 2368.65 cm⁻¹ attributable to O=C=O and another at 1731.65 cm⁻¹ corresponding to the C=O group of esters and lactones. We also observed a peak at 1040.36 cm⁻¹ corresponding to the C-O group of alcohols and ethers and the same group at 1257.96 cm⁻¹ characteristic of carboxylic acids. A shift of these peaks is observed on the spectra of CAK-S after adsorption (HQ/CAK-S and R/CAK-P), which proves that

the absorption band of these two phenolic compounds was involved. The change in absorption band is much more observed on the hydroxyl, carboxylate, and C-O groups of CAK-S.

3.2. Experimental Design Using the Central Composite Design

3.2.1. *Development of Quadratic Model Equations.* The optimization process is based on a central composite design involving three main steps: (1) carrying out experiments statistically designed according to the experimental design, (2) proposing the mathematical model based on the experimental results and working out the result of the analysis of variance, and (3) predicting the response and confirming the model. The experimental results are shown in Table 5.

The empirical mathematical model (equation (4)) was used to evaluate the correlation between the experimental values and the predicted values. These quadratic model equations represent the fit between the predicted responses and the four coded variables: the initial concentration (A), the pH of the solution (B), the contact time (C), and the mass of the carbon (D). We denote by Y_{HQ} and Y_R , respectively, the responses which are the adsorbed quantities of hydroquinone and resorcinol by CAK-S.

$$Y_{HQ} = 13.2253 + 0.5210A - 1.63672B - 0.10589C - 0.06754D - 0.00154A^2 - 0.00573AB + 0.000002AC - 0.00042AD + 0.15385B^2 - 0.00254BC + 0.00007BD + 0.00091C^2 - 0.00012CD + 0.00009D^2, \quad (5)$$

$$Y_R = 7.3315 + 0.18979A - 3.19280B + 0.04996C + 0.15455D - 0.00029A^2 - 0.01179AB + 0.00002AC + 0.00001AD + 0.27958B^2 - 0.00944BC + 0.00388BD - 0.00031C^2 + 0.00015CD - 0.00076D^2. \quad (6)$$

These equations with positive and negative coefficients can be used to illustrate optimal results.

Analysis of variance (ANOVA) was used to identify the relationships between the different variables on the quantities adsorbed (Table 6). A factor is said to be significant when, at the 95% confidence interval, the probability value (p value) is less than 5% and R^2 is close to unity. With regard to the adsorption of hydroquinone onto CAK-S, the individual variables A , B , and D as well as the interactions AA , AB , and AD have a significant influence on the quantity adsorbed. For the adsorption of resorcinol, factors A , B , C , and D and the interactions AB and DD significantly influence its quantity adsorbed. By eliminating statistically insignificant terms, the quadratic models reduce to equations (7) and (8). These reductions can be translated into response surfaces in order to identify areas of interest and therefore determine optimal conditions

TABLE 3: Nonlinear forms of kinetic and isotherms models.

Models	Nonlinear forms	References
<i>Kinetic models</i>		
Pseudo-first-order	$q_t = q_e (1 - e^{-k_1 t})$	[31]
Pseudo-second-order	$q_t = k_2 q_e^2 t / (1 + k_2 q_e t)$	[32]
Elovich	$q_t = \ln(\alpha\beta) / \beta + \ln(t) / \beta$	[33]
Interparticle diffusion	$q_t = K_i a t^{1/2} + C$	[34]
<i>Two-parameter isotherms</i>		
Langmuir	$Q_e = Q_m K_L C_e / (1 + K_L C_e)$	[35]
Freundlich	$Q_e = K_F C_e^{1/n}$	[35]
Dubinin–Radushkevich	$Q_e = Q_m \exp(-K' \varepsilon^2)$, $\varepsilon = RT \ln(1 + 1/C_e)$, $E = (2K_D)^{-1/2}$	[36]
Temken	$Q_e = RT / \Delta Q \ln(A_T C_e)$	[37]
<i>Three-parameter isotherms</i>		
Redlich-Peterson	$Q_e = AC_e / (1 + BC_e^\beta)$	[38]
Sips	$Q_e = K_s C_e^\beta / (1 + a_s C_e^\beta)$	[38]
Toth	$Q_e = Q_m C_e / (K_T + C_e)^{1/n}$	[39]
Hill	$Q_e = Q_{SH} C_e^{nH} / (K_D + C_e^{nH})$	[39]
Kahn	$Q_e = Q_{max} b_K C_e / (1 + b_K C_e) a_k$	[39]

TABLE 4: Error functions and their equations.

Error function	Abbreviation	Formula	References
Residual root mean square error	RMSE	$\sqrt{(1/n - 1) \sum_{i=1}^n (q_{e,exp} - q_{e,cal})^2}$	[42]
Average relative error	ARE	$100/n \sum_{i=1}^n q_{e,exp} - q_{e,cal} / q_{e,exp}$	[43]
Sum of absolute errors	EABS	$\sum_{i=1}^n q_{e,exp,i} - q_{e,cal,i} $	[42]
Hybrid fractional error function	HYBRID	$100/n - p \sum_{i=1}^n [(q_{e,exp} - q_{e,cal}) / q_{e,exp}]$	[38]
Nonlinear chi-square test	χ^2	$\sum_{i=1}^n (q_{e,cal} - q_{e,exp})^2 / q_{e,exp}^2$	[44]
Coefficient of determination	R^2	$(q_{e,exp} - \bar{q}_{e,cal}) / \sum (q_{e,exp} - \bar{q}_{e,cal}) + (q_{e,exp} - q_{e,cal})$	[43]

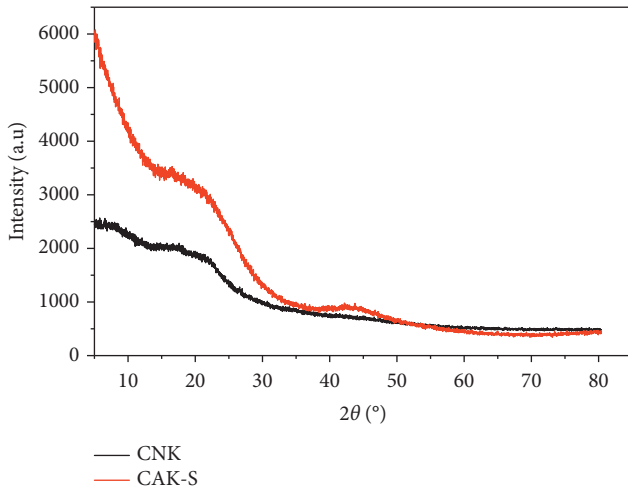


FIGURE 1: Superimposed XRD spectra of CNK shea nut shells and CAK-S activated carbon.

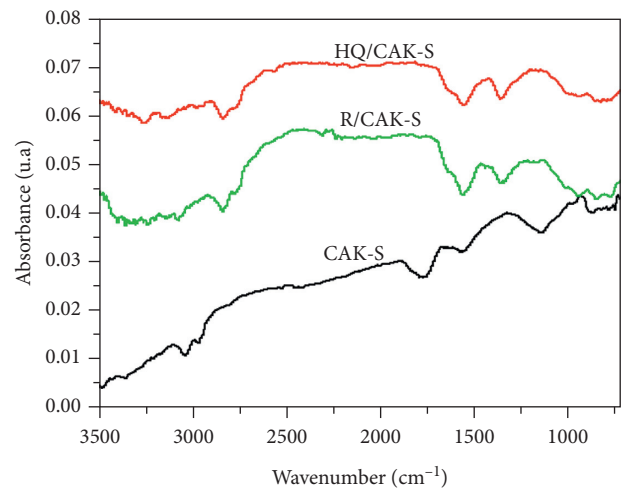


FIGURE 2: FTIR spectrum of CAK-S before and after adsorption of HQ and R.

$$Y'_{HQ} = 13.2253 + 0.5210A - 1.63672B - 0.06754 D - 0.00154A^2 - 0.00573AB - 0.00042AD, \quad (7)$$

$$Y'_R = 7.3315 + 0.18979A - 3.19280B + 0.04996C + 0.15455 D - 0.01179AB - 0.00076D^2. \quad (8)$$

3.3. *Interactions of Independent Variables.* The three-dimensional response surface curves are plotted only for the most important factor interactions. In Table 6, we see at 5% the most important interactions between concentration and pH with a probability $P = 0.0021$ and then concentration and mass with $P = 0.0000$. These interactions are shown in Figure 3. An increase in the quantity of HQ adsorbed is

TABLE 5: Matrix of coded variables associated with experimental and predicted values of adsorption of hydroquinone or resorcinol on CAK-S.

No.	Adsorption of hydroquinone (HQ) or resorcinol (R) on activated carbon CAK-S									
	Coded levels				HQ			R		
	A	B	C	D	Exp qads	Prev qads	Residu	Qads exp	Qads prev	Residu
1	0	-1	0	0	24.12	27.17	-3.05	21.27	25.64	-4.37
2	-1	0	0	0	5.37	3.42	5.34	4.21	9.55	-5.34
3	+1	-1	+1	-1	45.11	44.28	0.83	33.58	29.49	4.09
4	-1	+1	+1	+1	2.37	1.56	0.81	2.13	0.21	1.92
5	0	0	0	0	23.82	22.52	1.30	16.44	16.60	-0.16
6	0	+1	0	0	24.82	22.81	2.01	20.90	16.50	4.40
7	0	0	0	0	23.91	22.52	1.39	17.14	16.60	0.54
8	0	0	0	+1	14.38	14.39	-0.01	5.65	5.17	0.48
9	-1	-1	+1	+1	3.03	3.09	-0.06	2.67	2.08	0.59
10	+1	+1	+1	-1	36.66	35.29	1.37	2.27	6.29	-4.02
11	-1	-1	-1	-1	15.17	13.88	1.29	12.74	12.38	0.36
12	+1	+1	-1	+1	13.00	14.06	-1.06	5.11	7.84	-2.73
13	0	0	0	-1	31.48	32.48	-1.00	12.31	12.76	-0.45
14	+1	0	0	0	18.85	21.76	-2.91	25.27	19.91	5.36
15	0	0	+1	0	23.75	24.21	-0.46	10.80	14.67	-3.87
16	-1	-1	-1	+1	3.04	3.54	-0.50	2.66	0.05	2.61
17	+1	+1	+1	+1	7.58	9.47	-1.89	4.51	3.45	1.06
18	+1	-1	-1	-1	42.62	42.56	0.06	26.53	29.86	-3.33
19	-1	+1	+1	-1	12.61	13.92	-1.31	4.33	3.54	0.79
20	-1	+1	-1	+1	2.41	3.84	-1.43	2.30	4.97	-2.67
21	0	0	0	0	22.08	22.52	-0.44	16.74	16.60	0.14
22	+1	-1	-1	+1	19.46	18.75	0.71	18.65	18.03	0.62
23	+1	+1	-1	-1	34.87	35.41	0.54	14.30	13.47	0.83
24	-1	+1	-1	-1	13.80	11.73	2.07	11.53	11.08	0.45
25	0	0	0	0	23.31	22.52	0.79	16.02	16.60	-0.58
26	-1	-1	+1	-1	15.17	13.88	1.29	12.97	11.65	1.32
27	+1	-1	+1	+1	19.46	18.33	1.13	18.57	20.43	-1.86
28	0	0	-1	0	23.93	24.49	-0.56	21.14	17.24	3.90

A: initial concentration (mg/L) of hydroquinone or resorcinol, B: pH of solution, C: contact time (min), and D: mass of activated carbon (mg).

TABLE 6: Analysis of variance (ANOVA) of adsorbed quantity of hydroquinone and resorcinol by CAK-S.

Source	Df	Hydroquinone				Resorcinol			
		SS	MC	F value	p value	SS	MC	F value	p value
A	1	1509.91	1509.91	410.49	0.0000*	385.03	385.03	31.83	0.0001*
B	1	84.76	84.76	23.10	0.0003*	290.08	290.08	23.98	0.0003*
C	1	0.30	0.36	0.10	0.7577	60.97	60.97	05.04	0.0428*
D	1	1471.71	1471.71	401.17	0.0000*	188.89	18889	15.62	0.0017*
A ²	1	252.72	252.72	68.89	0.0000*	10.87	10.87	0.90	0.3604
AB	1	53.73	53.73	14.05	0.0021*	158.69	158.69	13.12	0.0031*
AC	1	0.01	0.01	0.00	0.9800	4.55	4.55	038	0.5504
AD	1	181.31	181.31	49.42	0.0000*	8.95	8.95	0.74	0.4051
B ²	1	15.63	15.63	4.26	0.0595	47.52	47.52	3.93	0.0690
BC	1	3.36	3.36	0.92	0.3555	18.51	18.51	1.53	0.2379
BD	1	0.02	0.02	0.00	0.9400	13.86	13.86	1.15	0.3040
C ²	1	8.65	8.65	2.36	0.1485	1.75	1.75	0.14	0.7101
CD	1	4.57	4.57	1.25	0.2841	27.85	27.85	2.30	0.1531
D ²	1	2.19	2.19	0.60	0.4534	157.45	157.45	13.02	0.0032*

$R^2 = 98.69\%$, adjusted $R^2 = 97.29\%$

$R^2 = 90.55\%$, adjusted $R^2 = 80.38\%$

*Significant. D: degree of freedom; SS: sum of squares; MS: mean square; adjusted R^2 : adjusted R^2 .

observed as a function of the increase in initial concentration. This is due to the increase in HQ molecules in the solution creating competition for different adsorption sites. The opposite is observed with increasing pH. In fact, the adsorption capacity of CAK-S decreases as the pH increases

(Figure 3(a)). For $\text{pH} > 6.37$ (pH_{pzc}), the carbon surface is negatively charged, and, for values of $\text{pH} > 8$, HQ in turn loses its protons and becomes a monoanion hydroquinone ($\text{HQ}(\text{OH})(\text{O})^-$) or a dianion hydroquinone ($\text{HQ}(\text{O})_2^{2-}$) [1]. The repulsion between the negatively charged CAK-S

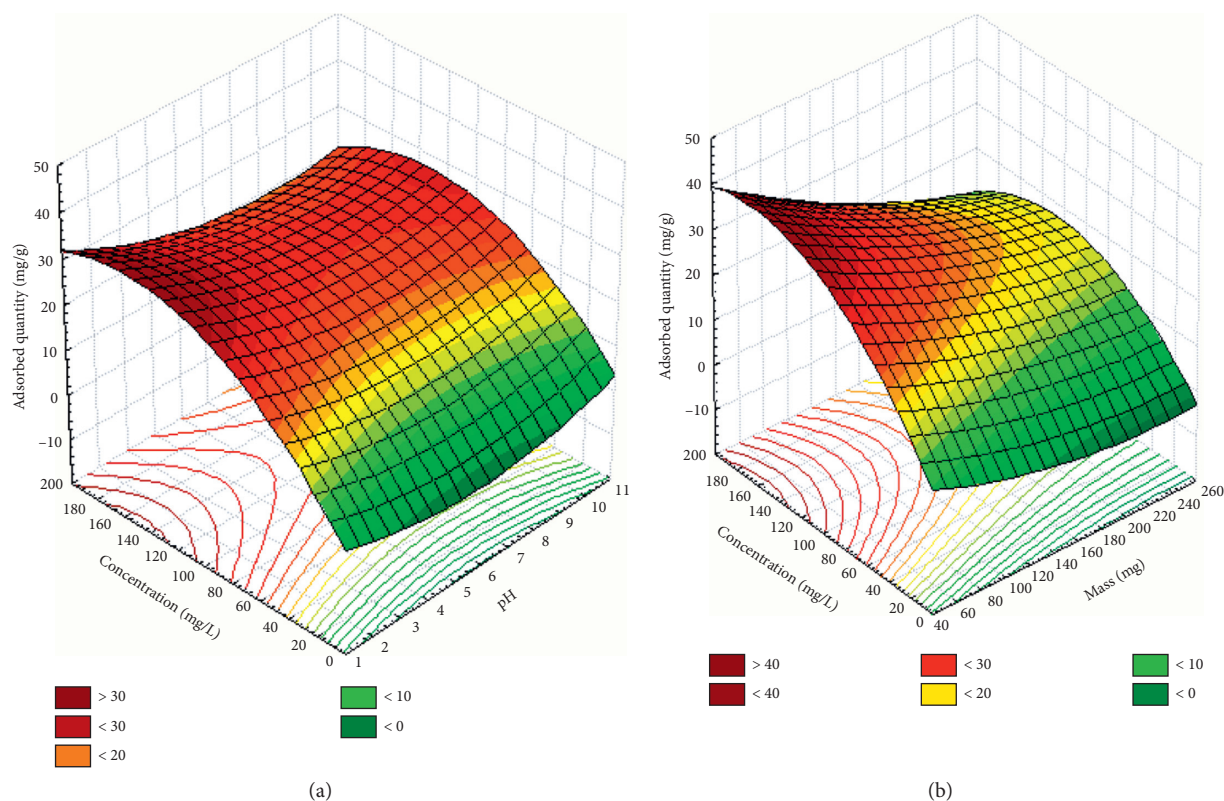


FIGURE 3: 3D surface plot of the adsorbed quantities of HQ by CAK-S as a function of (a) concentration and pH and (b) concentration and mass.

surface layer and the hydroquinone anion results in a considerable decrease in the quantity of HQ adsorbed. For this study, statistical analysis showed that the synergistic effect of concentration and the antagonistic effect of pH at high values lead to maximum adsorption at pH 3. At this pH, the surface area of CAK-S is charged with protons and HQ is stable in acidic conditions. Adsorption is maximum on the one hand by formation of hydrogen bonds with the hydroxyl groups and, on the other hand, by π - π interactions of benzene rings between HQ and CAK-S [17, 45]. In Figure 3(b), we see a decrease in the quantity of HQ adsorbed with increasing mass. This is explained by the formation of CAK-S particle clusters inducing a reduction in the total adsorption surface area and therefore a decrease in the amount of adsorbate per unit mass [46].

Regarding the adsorption of R by CAK-S, only the interaction between concentration and pH with a probability $P = 0.0031$ is significant. Figure 4 shows the 3D visualization of this interaction. It appears that the amount of R adsorbed increases as the initial concentration increases, which is also explained by a large number of R molecules in solution. The adsorbed amount of R decreases as the pH increases. This is justified by the fact that, at $\text{pH} > \text{pKa}$, a repulsion is created between the resorcinolate anions ($\text{R}(\text{OH})(\text{O})^-$ or $\text{R}(\text{O})_2^-$) and the negatively charged CAK-S surface. In the region of $\text{pH} < 6.37$ (pHpzc), the surface of CAK-S is positively charged and there is formation of hydrogen bonds and π - π attraction interactions between the molecules of R and those of the surface of CAK-S.

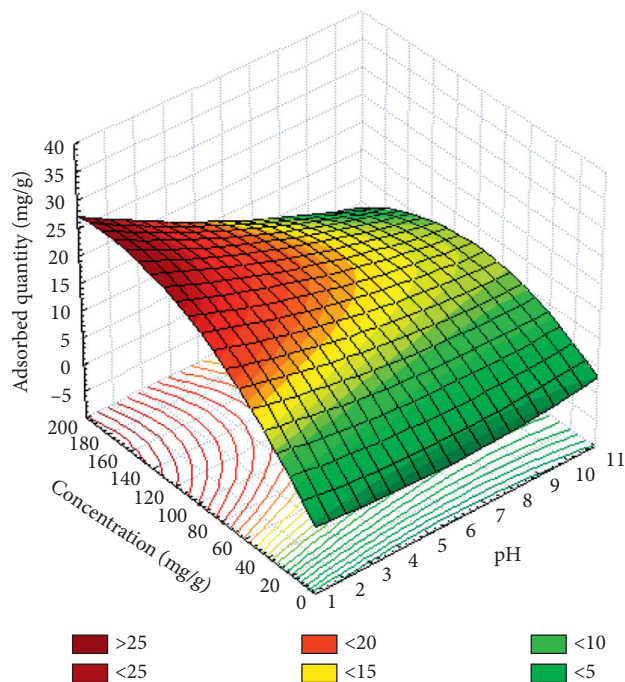


FIGURE 4: 3D surface graph of the adsorbed quantities of R by CAK-S as a function of concentration and pH.

3.4. Process Optimization and Test Validation. The optimal conditions for binding of HQ and R to CAK-S (Table 7) result from a statistical analysis of the experimental data by

TABLE 7: Validation of the experimental model of the adsorption of HQ and R by CAK-S.

Adsorbates	Operational variables		Adsorbed quantity (mg/g)		Residue
			Exp. val.	Pred. val.	
HQ	A (mg/L)	158	45.02	45.66	-0.64
	B	3			
	C (min)	120			
	D (mg)	50			
R	A (mg/L)	180	33.65	32.67	0.98
	B	3			
	C (min)	86			
	D (mg)	118			

STATGRAPHIC Plus 5.0 software. A new HQ and R adsorption experiment was repeated to confirm the best level obtained for each operating variable leading to the optimal predicted results. It emerges from this experiment that the difference between the experimental and predicted values is small, and this demonstrates the validity of the model. Therefore the experimental data are satisfactory and agree with the studied model. These results complete the analysis of variance (Table 6) which presents the high values of the correlation coefficients ($R^2 > 90$) and the adjusted correlation coefficients (adjusted $R^2 > 80$).

3.5. Nonlinear Adsorption Kinetic Studies. In order to elucidate the sorption mechanism of hydroquinone or resorcinol on CAK-S activated carbon, the contact time was varied between 5 and 160 min. The other parameters were set at their optimum values. Kinetic models such as the pseudo-first-order, pseudo-second-order, Elovich, and intraparticle diffusion models were investigated. The nonlinear plots are shown in Figures 5 and 6. Table 8 shows the calculated values of all parameters. It emerges that the nonlinear kinetic pseudo-first-order, pseudo-second-order, and Elovich models are more appropriate for the description of the adsorption of HQ and R on the CAK-S, because the coefficients of determination are closer to unity ($R^2 > 0.99$). However, the low value of χ^2 and the low values of the error functions obtained from the Elovich model show that it is the best kinetic model to describe the adsorption of HQ and R. This model suggests that the adsorption of HQ or R is primarily chemical and the active sites on the surface of CAK-S are heterogeneous [25]. This is confirmed by the values of the desorption constant $\beta < 1$ (0.198 and 0.313 mg/g.min, respectively, for HQ and R). Observation of the pseudo-first-order kinetic model (Figures 4 and 5) shows that the binding of HQ or R molecules to the surface of CAK-S occurs rapidly, thereby reaching equilibrium. For pseudo-second-order kinetics, the amounts adsorbed at equilibrium are close to experimental ones, which demonstrates the existence of majority π - π type interactions [47].

3.6. Modeling of Nonlinear Adsorption Isotherm. To model the adsorption isotherms with the experimental data, the effect of initial concentrations of HQ and R was studied in the range of 40 to 180 mg/L using optimal conditions. The equilibrium results were modeled with four two-parameter models and five

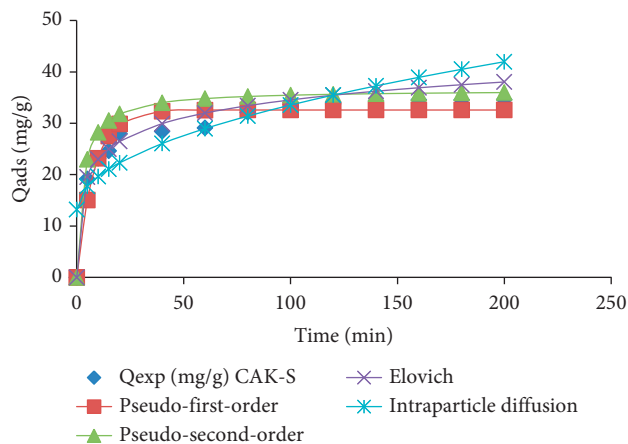


FIGURE 5: Nonlinear plot of kinetic models of HQ adsorption by CAK-S.

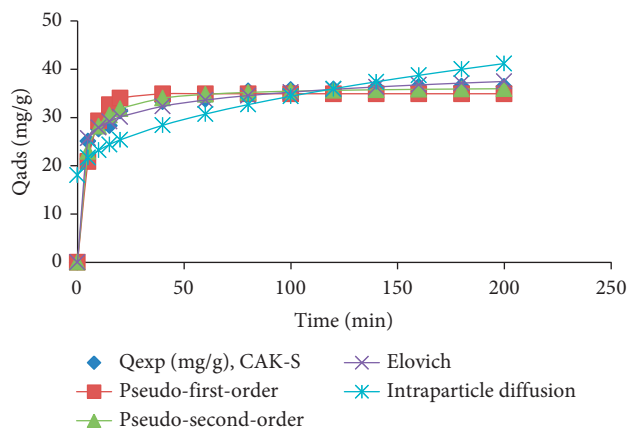


FIGURE 6: Nonlinear plot of kinetic models of R adsorption by CAK-S.

three-parameter models. Two-parameter adsorption isothermal equilibrium simulations of the two-parameter adsorption isotherms of HQ and R by CAK-S are shown in Figures 7 and 8. All calculated parameters are shown in Table 9.

It emerges from this table that the values of coefficients of determination, R^2 , are close to unity for the Langmuir, Freundlich, and Temkin models. These models can be exploited to explain the adsorption of HQ and R. Based on the high value of R^2 , low value of χ^2 , and low values of the RMSE, HYBRID, ARE, and EABS error functions, Temkin

TABLE 8: Kinetic data obtained by nonlinear fitting analysis (see equations in Table 3 and 4).

Models	Parameters	R^2	χ^2	RMSE	HYBRID	Errors		
						ARE	EABS	
<i>HQ/CAK-S</i>								
Pseudo-first-order	q_e (mg/g)	32.577	0.994	0.189	2.479	1.575	0.028	1.577
	K_1 (1/min)	0.124						
Pseudo-second-order	q_e (mg/g)	37.164	0.991	0.258	2.962	2.151	0.027	1.558
	K_2 (g/min.mg)	0.004						
Elovich	A (mg/g.min)	47.579	0.998	0.072	1.562	0.597	0.001	0.042
	B (mg/g.min)	0.198						
Intraparticle diffusion	K_{id} (mg/g.min ^{0.5})	2.036	0.979	0.658	4.732	5.488	3.5×10^{-6}	0.000
	C (mg/g)	13.182						
<i>R/CAK-S</i>								
Pseudo-first-order	q_e (mg/g)	34.930	0.996	0.143	2.269	1.191	0.017	1.057
	K_1 (1/min)	0.182						
Pseudo-second-order	q_e (mg/g)	36.503	0.998	0.030	1.045	0.253	0.003	0.187
	K_2 (g/min.mg)	0.009						
Elovich	A (mg/g.min)	2007.7	0.999	0.014	0.723	0.121	2.33×10^{-5}	0.001
	B (mg/g.min)	0.313						
Intraparticle diffusion	K_{id} (mg/g.min ^{0.5})	1.636	0.967	1.135	6.396	9.453	5.02×10^{-7}	3.04×10^{-5}
	C (mg/g)	18.048						

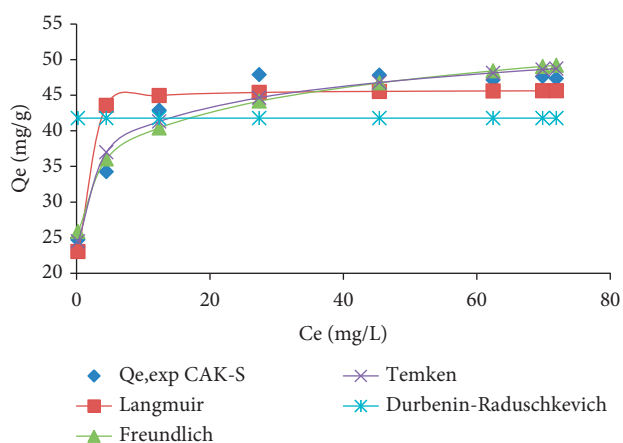


FIGURE 7: Nonlinear plot of two-parameter adsorption isotherm models of HQ by CAK-S.

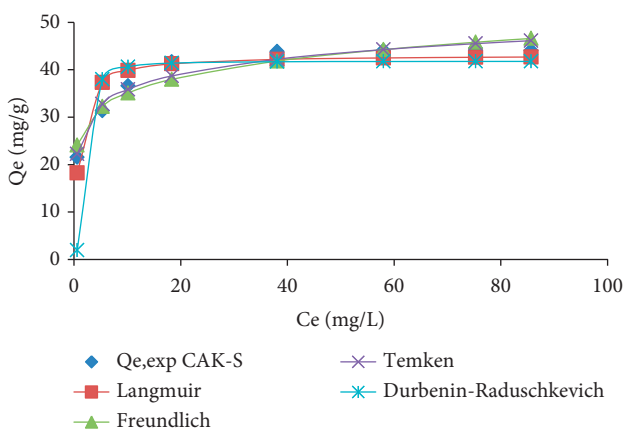


FIGURE 8: Nonlinear plot of two-parameter adsorption isotherm models of R by CAK-S.

model is found to better describe the adsorption isotherm of HQ and R by the activated carbon CAK-S. This Temkin model highlights a decrease in interactions between HQ or R molecules followed by a linear decrease in heat of adsorption with surface coverage. The adsorption energies of this model are positive (587.068 and 514.132 J/mol, respectively, for HQ and R); this is evidence of chemisorption and the process is exothermic [26]. Given the values of R^2 and those of χ^2 , the Langmuir isotherm can describe the adsorption of the two pollutants. It suggests a monolayer adsorption on the surface of the carbon, without interaction between the adsorbed molecules. By comparing the maximum adsorption capacity Q_m (Table 9), we find that hydroquinone is more adsorbed: 45.764 mg/g against 43.097 mg/g for resorcinol. Patricia et al. [3] obtained similar results. This is due to the solubility and configuration of these isomers. This is because resorcinol is more soluble than hydroquinone in water. The more soluble a substance is, the less it is adsorbed. The paraposition and metaposition of hydroxyl groups on benzene also influence adsorption. Indeed, according to the 1-4 position of hydroxy groups on benzene, hydroquinone is a symmetrical and stable molecule. This configuration allows it to easily access adsorption sites due to its greater energy stability [3]. Freundlich model's n values greater than 1 showed good affinity of the adsorbates with the material and the adsorption process occurred on heterogeneous surfaces, characterizing adsorption at localized sites [35, 48]. In short, the modeling of two-parameter isotherms leans towards the adsorption of HQ or R taking place on a heterogeneous surface with a nonuniform absorption energy distribution.

3.6.1. Three-Parameter Adsorption Isothermal Equilibrium.

The nonlinear plots of the isothermal models with three parameters studied are presented in Figures 9 and 10. Table 10 gives the values of constants related to these nonlinear regression isotherm models.

TABLE 9: Adsorption of hydroquinone and resorcinol: nonlinear fitting analysis for two-parameter isotherms (see equations in Tables 3 and 4).

Models	Parameters		R^2	χ^2	RMSE	Errors		
						HYBRID	ARE	EABS
<i>HQ/CAK-S</i>								
Langmuir	Q_m (mg/g)	45.764	0.992	0.336	4.363	5.603	0.014	0.385
	K_L (L/min)	4.424						
Freundlich	K_F (mg/L)	30.482	0.997	0.096	2.335	1.605	0.162	0.005
	n	8.930						
Temken	A_T (L/mg)	1430.831	0.998	0.074	2.054	1.243	0.0006	2.52×10^{-6}
	ΔQ (J/mol)	587.068						
Dubinin-Radushkevich	Q_m (mg/g)	41.783	0.957	1.522	9.283	25.368	5.443	0.200
	K_{id} (L/mg)	5.12×10^{-7}						
	E (kJ/mol)	= 988.21						
<i>R/CAK-S</i>								
Langmuir	Q_m (mg/g)	43.097	0.994	0.222	3.371	3.695	0.040	0.986
	K_L (L/min)	1.212						
Freundlich	K_F (mg/L)	25.795	0.997	0.116	2.436	1.929	0.283	0.011
	n	7.524						
Temken	A_T (L/mg)	166.865	0.998	0.064	1.818	1.074	0.0001	7.35×10^{-6}
	ΔQ (J/mol)	514.132						
Dubinin-Radushkevich	Q_m (mg/g)	41.783	0.964	1.522	8.835	25.372	18.758	0.762
	K_{id} (L/mg)	5.26×10^{-7}						
	E (kJ/mol)	= 974.97						

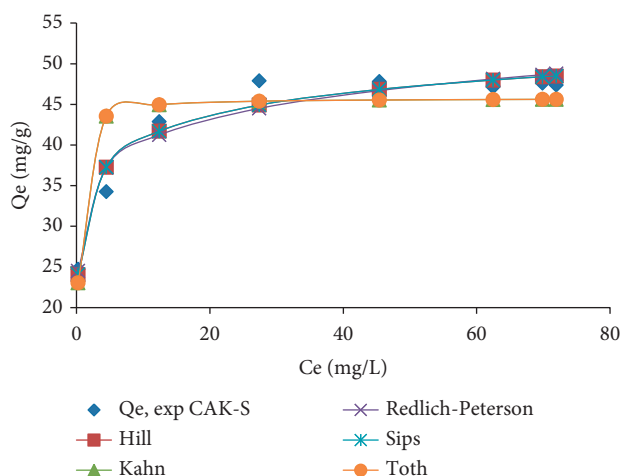


FIGURE 9: Nonlinear plot of three-parameter adsorption isotherm models of HQ by CAK-S.

We notice in Table 9 that the values of the coefficient of determination R^2 for all the isotherm models are close to unity ($R^2 > 0.99$) and the values of the corresponding error functions are low, which suggest that these models are suitable for effectively describing experimental data at equilibrium. The Sips model, having the high values of R^2 and the low values of χ^2 , shows a distribution of the molecules of HQ and of R on a heterogeneous surface of CAK-S, thus presenting energetically different adsorption sites [49]. The values of the constant n_H of the Hill model different from 1 highlight a localized adsorption [38] with formation of a bond between the molecules of HQ or R and that of carbon. The values of the β heterogeneity parameter of the Redlich-Peterson model between 0 and 1 show that the model cannot be reduced to a single-layer adsorption but

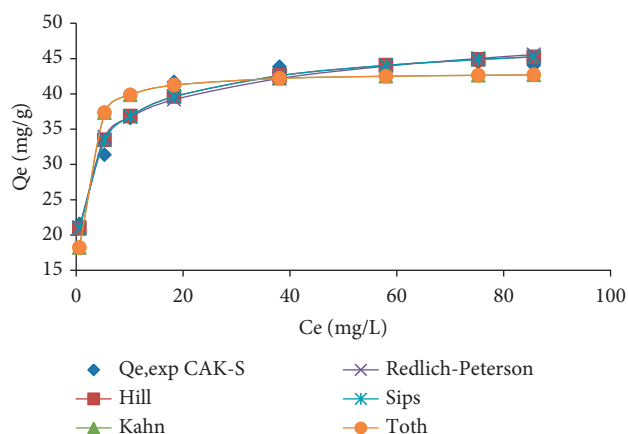


FIGURE 10: Nonlinear plot of three-parameter adsorption isotherm models of R by CAK-S.

rather to a so-called heterogeneous system. These results confirm those of the two-parameter models which suggest that the adsorption of HQ or R occurs on heterogeneous surfaces of CAK-S, with a nonuniform adsorption energy distribution.

3.7. Effect of Temperature and Thermodynamics of Adsorption.

The thermodynamic study was carried out by varying the temperature by 30, 40, 50, 60, and 70°C. The tests were carried out with 30 mL of solution and using the optimum conditions required for the adsorption of each pollutant by CAK-S. Thermodynamic parameters such as Gibbs standard free energy (ΔG^0), standard enthalpy (ΔH^0), and standard entropy (ΔS^0) are related by the two following equations [22]:

TABLE 10: Adsorption of hydroquinone and resorcinol: nonlinear fitting analysis for three-parameter isotherms (see equations in Tables 3 and 4).

Models	Parameters		R^2	χ^2	RMSE	Errors		
						HYBRID	ARE	EABS
<i>HQ/CAK-S</i>								
Hill	Q_m (mg/g)	65.611	0.998	0.068	1.967	1.368	0.002	0.045
	K_H (L/g)	0.276						
	n_H	1.150						
Kahn	Q_{max} (mg/g)	69,940	0.992	0.336	4.363	6.723	0.014	0.385
	b_K (L/g)	4.424						
	a_K	1.528						
Redlich-Peterson	A (L/g)	757.85	0.998	0.083	2.168	1.661	0.0018	0.022
	B (L/mg)	23.149						
	β	0.905						
Sips	K_S (L/g)	57.005	0.998	0.068	1.967	1.368	0.002	0.046
	a_S (L/g)	0.868						
	β_S	0.276						
Toth	Q (mg/g)	45.764	0.992	0.336	4.363	6.723	0.014	0.385
	K_e	0.832						
	N	0.120						
<i>R/CAK-S</i>								
Hill	Q_m (mg/g)	52.907	0.998	0.040	1.434	0.802	0.002	0.060
	K_H (L/g)	0.443						
	n_H	1.220						
Kahn	Q_{max} (mg/g)	92.049	0.994	0.222	3.372	4.435	0.040	0.986
	b_K (L/g)	1.212						
	a_K	2.135						
Redlich-Peterson	A (L/g)	123.84	0.998	0.058	1.372	1.177	0.001	0.032
	B (L/mg)	4.026						
	β	0.911						
Sips	K_S (L/g)	43.344	0.998	0.040	1.436	0.803	0.002	0.060
	a_S (L/g)	0.819						
	β_S	0.444						
Toth	Q (mg/g)	43.097	0.994	0.222	3.372	4.436	0.040	0.986
	K_e	0.976						
	N	0.126						

$$\Delta G^0 = -RT \ln K_d, \quad (9)$$

$$\ln K_d = \left(\frac{\Delta S^0}{R} \right) - \left(\frac{\Delta H^0}{R} \right) \frac{1}{T}. \quad (10)$$

We have that $K_d = 1000 Q_e/C_e$ is the distribution constant, Q_e (mg/g) is the adsorbed quantity of pollutant at equilibrium, C_e (mg/L) is the residual concentration of the target compound in solution, R (8.314 J/mol.K) is the constant of ideal gases, and T (K) is the absolute temperature. The results are shown in Figure 11.

Figure 11(a) shows the influence of temperature on the retention of HQ or R. It appears that the adsorbed quantity increases with increasing temperature, suggesting that the process is endothermic, and that the increase in temperature promotes the progression of adsorption. Table 11 summarizes the values of ΔG^0 , ΔH^0 , and ΔS^0 obtained from extrapolation of the linear plot $\ln K_d = f(1/T)$ (Figure 11(b)). The less negative values of ΔG^0 with increasing temperature show that the adsorption of HQ or R by CAK-S is favorable and spontaneous. Positive values of ΔH^0 indicate an endothermic nature of the adsorption process. These low positive values of enthalpy ($\Delta H^0 < 40$ kJ/mol) are

characteristics of a physisorption. Positive entropy values ΔS^0 also indicate increased randomness, including the number of species at the solid-liquid interface during sorption. Similar results were obtained during adsorption of hydroquinone in solution by granular activated carbon [1] and adsorption of hydroquinone by hydroxyethyl cellulose functionalized with magnetic/ionic liquid [49].

3.8. Mechanism Involving Hydrogen Bonding and π - π and n - π Interactions. The binding mechanism of HQ and R is discussed on the basis of surface properties of CAK-S and modeling results. In general, the surfaces of activated carbons are made of acid functions like carboxyl, hydroxyl, quinones, carbonyl, and lactone groups, as well as basic functions like pyrones and chromenes [4, 50, 51]. For the case of CAK-S, the FTIR and the Boehm titration results, supplemented by EDX/SEM [28], have shown that it has the chemical functions mentioned above. These functional groups act as nucleophilic and electrophilic sites likely to react with the hydroxyl groups and the delocalized π electron system of the benzene ring present in HQ or R. The results of the thermodynamic study show that the adsorption was mainly dominated by physisorption ($\Delta H^0 < 40$ kJ/mol).

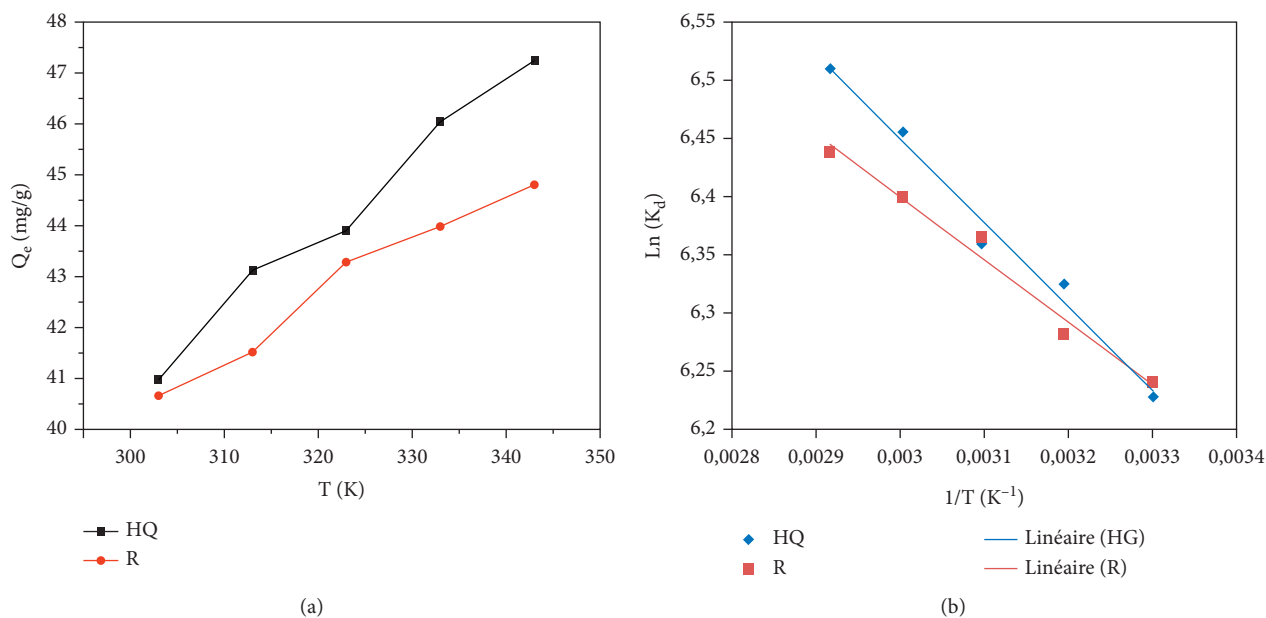


FIGURE 11: (a) Effect of temperature. (b) Linear plot $\ln(K_d)$ versus $1/T$ of the adsorption of HQ or R.

TABLE 11: Thermodynamics parameters of the adsorption of HQ and R.

Temperature (K)	HQ			R		
	ΔG^0 (kJ/mol)	ΔH^0 (kJ/mol)	ΔS^0 (J/mol.K)	ΔG^0 (kJ/mol)	ΔH^0 (kJ/mol)	ΔS^0 (J/mol.K)
303	-15.871			-15.719		
313	-16.446			-16.342		
323	-17.080	5.992	71.59	-17.079	4.447	66.54
333	-17.857			17.691		
343	-18.565			18.364		

However, Temkin model with positive adsorption energy (587.068 and 514.132 J/mol, respectively, for HQ and R) suggests chemisorption, but this was fairly minimal and was not a control mechanism. Likewise, FTIR analysis reveals shifts in the absorption bands of functional groups (hydroxyl, carboxylate, and C–O) after adsorption of HQ and R by CAK-S, but these were also small for controlling the process. For an optimal value of pH = 3 (lower than pHPzc 6.37), the carbon surface is positively charged and easily attracts electrons from HQ and R. In addition, the hydroxyl, carboxylate, and C–O functional groups on the surface of CAK-S are rich in oxygen atoms (electronegative atom), which is a good candidate for physical interactions. The main physical adsorption mechanisms involved are based on the Van der Waals forces of attraction, in particular the hydrogen bonds which are likely to play a role in absorption [52]. Based on this observation, we see that there is a co-existence of chemisorption and physisorption, with the latter being dominant during sorption of HQ or R on CAK-S. In the end, the two aromatic isomers have hydroxyl groups which largely participate in the binding onto CAK-S, consequently supported by π - π and n - π interactions as well as the formation of hydrogen and covalent bonds. It should be

noted that the attachment of these isomers to CAK-S also depends on the paraposition and metaposition of the hydroxyl groups. The HQ in hydroxide position 1–4 on benzene is symmetrical and stable and therefore is easily accessible at binding sites due to its greater energy stability, compared to R in the metaposition [3]. For this reason, we have chosen to represent only (Figure 12) the binding mechanism of hydroquinone, which has a high affinity with CAK-S activated carbon. The mechanism by which resorcinol binds to this AC is similar to that of hydroquinone.

3.9. Comparison with Other Adsorbents. The adsorption efficiency of HQ and R in aqueous solution using various adsorbents is shown in Table 12. It appears that CAK-S is shown to be a capable adsorbent that can be exploited in the removal of HQ and R of wastewater compared to other adsorbent materials. Although the operating conditions are not the same, CAK-S exhibits higher maximum removal efficiency than some adsorbents reported in previous studies. These results contribute to environmental remediation because CAK-S produced from local biomass can be exploited specifically for effective attenuation of HQ and R in aqueous media.

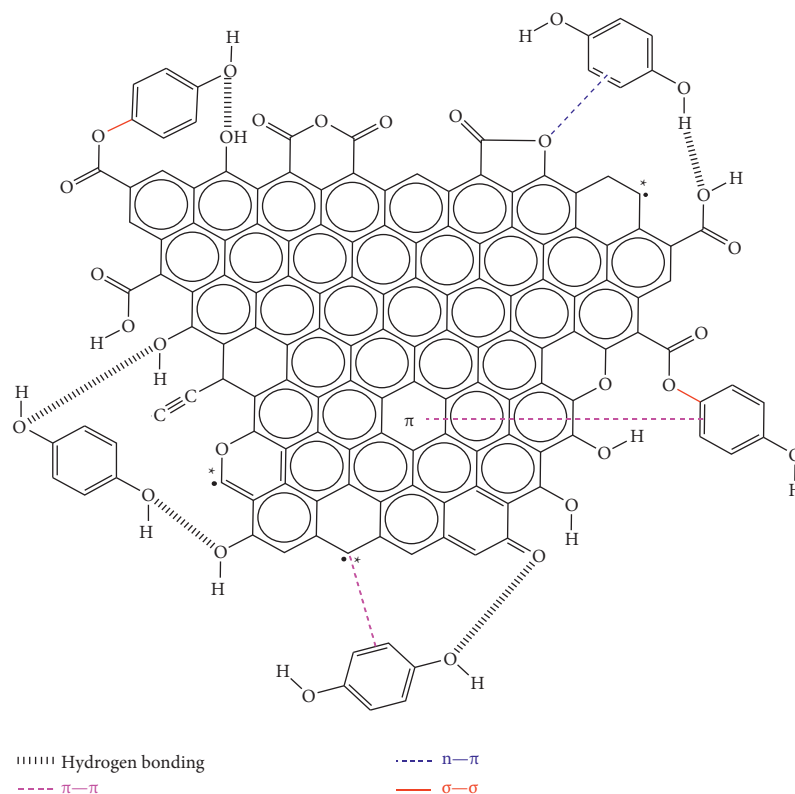


FIGURE 12: Possible interactions contributing to the mechanism of hydroquinone adsorption on CAK-S except pore filling.

TABLE 12: Comparison of CAK-S with other materials for HQ and R reduction.

Adsorbent	Condition	Adsorbed quantity	References
<i>Adsorption of hydroquinone by some adsorbents</i>			
CAK-S	C = 158 mg/L; pH = 3; t = 120 min; m = 50 mg	45.02 mg/g	Present study
Activated carbon based on monkey kola (<i>Cola lepidota</i> K. Schum) waste	C = 55.55 mg/L; pH = 6; t = 30 min; m = 100 mg	7.33 mg/g (66.57 μ mol/g)	[3]
Iron impregnated granular activated carbon	C = 100 mg/L, pH = 4, t = 14 h, m = 40 g/L	26.55 mg/g	[53]
<i>Adsorption of resorcinol by some adsorbents</i>			
CAK-S	C = 180 mg/L; pH = 3; t = 86 min; m = 118 mg	33.65 mg/g	Present study
Activated carbon based on monkey kola (<i>Cola lepidota</i> K. Schum) waste	C = 55.55 mg/L; pH = 6; t = 30 min; m = 100 mg	0.60 mg/g (5.47 μ mol/g)	[3]
OMC	C = 20 mg/L; pH = 6.5; t = 24 h; m = 0.1 g/L	34.4 mg/g	[54]

4. Conclusion

The response surface methodology was used as a simple approach to optimize the binding of HQ and R in solution on activated carbon from shea residue. The study focused on the main factors (concentration of target pollutants, pH of the solution, contact time, and mass of carbon) having an effect on the quantity adsorbed. The optimal conditions obtained from the statistical analysis were concentration of 158 mg/L, pH 3, mass of 50 mg, and time of 120 min for the HQ and a concentration of 180 mg/L, pH 3, time of 86 min, and mass of 118 mg for R. For these conditions, the maximum quantities of HQ and R adsorbed are 45.02 and 33.65 mg/g, respectively. The adsorption was better described using Elovich kinetics which suggest that the CAK-S surface is heterogeneous. Also, the Temkin two-parameter and the Sips three-parameter

isotherm models suggest a heterogeneous surface with a nonuniform adsorption distribution energy. The process was spontaneous ($-\Delta G^0$) and endothermic ($+\Delta H^0$) and resulted in increased disorder of species in solution ($+\Delta S^0$). The π - π , n - π interactions, hydrogen bonds, and pores filling were the main contributors to the mechanism of binding of HQ and R to CAK-S. This CAK-S material has shown good HQ and R removal performance, which is a very significant contribution to environmental remediation. It can be exploited specifically by environmentalists for effective mitigation of phenolic compounds from wastewater.

Data Availability

The digital data used to support the conclusions of this study have been deposited in the Mendeley repository

(<http://www.mendeley.com/reference-manager/library/recently-read>).

Conflicts of Interest

The authors declare that they have no conflicts of interest.

Acknowledgments

The authors appreciate the technical assistance of the Researchers of Material and Process Engineering Team (MPET)/RU-NOCHEE of the Department of Chemistry, Faculty of Science, University of Dschang, Cameroon. The authors also thank Dr. Tchoufon Donald and Dr. Bopda Aurelien for their contribution.

References

- [1] S. Suresh, V. C. Srivastava, and I. M. Mishra, "Adsorption of hydroquinone in aqueous solution by granulated activated carbon," *Journal of Environment Engineering*, vol. 137, pp. 1–12, 2011.
- [2] D. A. Blanco-Martínez, L. Giraldo, and J. C. Moreno-Piraján, "Effect of the pH in the adsorption and in the immersion enthalpy of monohydroxylated phenols from aqueous solutions on activated carbons," *Journal of Hazardous Materials*, vol. 169, no. 1–3, pp. 291–296, 2009.
- [3] N. N. Patricia, K. Théophile, T. T. D. Raoul, D. Giscard, B. M. M. Roger, and A. S. Gabche, "Non-linear regression, a better approach for the optimisation of hydroquinone, resorcinol and catechol adsorption by chemically activated carbon based on monkey kola (*Cola lepidota* k. schum) waste," *Chemical Science International Journal*, vol. 25, no. 1, pp. 1–18, 2018.
- [4] M. Zhang, C.-y. Ge, Y.-f. Jin et al., "Sensitive and simultaneous determination of hydroquinone and catechol in water using an anodized glassy carbon electrode with polymerized 2-(phenylazo)," *Journal of Chemistry*, vol. 2019, Article ID 2327064, 10 pages, 2019.
- [5] S. Rengaraj, S.-H. Moon, R. Sivabalan, B. Arabindoo, and V. Murugesan, "Agricultural solid waste for the removal of organics: adsorption of phenol from water and wastewater by palm seed coat activated carbon," *Waste Management*, vol. 22, no. 5, pp. 543–548, 2002.
- [6] INRS, *Base de données Fiches Toxicologiques*, INRS, Quebec City, Canada, hydroquinone edition, 2006.
- [7] INRS, *Base de données Fiches Toxicologiques*, INRS, Quebec City, Canada, Résorcinol edition, 2018.
- [8] S. E. Agarry, A. O. Durojaiye, R. O. Yusuf, M. O. Aremu, B. O. Solomon, and O. Mojeed, "Biodegradation of phenol in refinery wastewater by pure cultures of *Pseudomonas aeruginosa* NCIB 950 and *Pseudomonas fluorescens* NCIB 3756," *International Journal of Environment and Pollution*, vol. 32, no. 3, 2008.
- [9] R. Subramanyam and I. M. Mishra, "Co-degradation of resorcinol and catechol in an UASB reactor," *Bioresource Technology*, vol. 99, no. 10, pp. 4147–4157, 2008.
- [10] A. Garg, I. M. Mishra, and S. Chand, "Oxidative phenol degradation using non-noble metal based catalysts," *Clean-Soil, Air, Water*, vol. 38, no. 1, p. NA, 2010.
- [11] E. Ouabou, A. Anouar, and S. Hilali, "Élimination des polluants organiques dans la margine d'huile d'olive par filtration sur colonne d'argile et sciure de bois d'eucalyptus," *Journal of Applied Biosciences*, vol. 75, no. 1, pp. 6232–6238, 2014.
- [12] S. G. Kouassi, P. A. Grah, K. D. Bini et al., "Contribution à l'étude de quatre charbons activés à partir des coques de noix de coco," *Afrique Science*, vol. 12, no. 5, pp. 229–245, 2016.
- [13] B. Sawadogo, Y. Konaté, G. Lesage et al., "Brewery wastewater treatment using MBR coupled with nanofiltration or electro-dialysis: biomass acclimation and treatment efficiency," *Water Science and Technology*, vol. 77, no. 11, pp. 2624–2634, 2018.
- [14] B. Davoud and J. Ali, "Biosorption of Phenol using dried Rice husk biomass: kinetic and equilibrium studies," *Der Pharma Chemica*, vol. 8, no. 6, pp. 96–103, 2016.
- [15] M. J. Ahmed and S. K. Dhedan, "Equilibrium isotherms and Kinetics modeling of methylene blue adsorption on agricultural Wastes-based activated carbons," *Fluid Phase Equilibria*, vol. 317, pp. 9–14, 2012.
- [16] N. Fayoud, S. A. Younssi, S. Tahiri, and A. Albizane, "Etude cinétique et thermodynamique de l'adsorption de bleu de méthylène sur les cendres de bois (Kinetic and thermodynamic study of the adsorption of methylene blue on wood ashes)," *Journal of Materials and Environmental Sciences*, vol. 6, no. 11, pp. 3295–3306, 2015.
- [17] T. Li, Y. He, and X. Peng, "Efficient removal of tetrabromobisphenol A (TBBPA) using sewage sludge-derived biochar: adsorptive effect and mechanism," *Chemosphere*, vol. 251, Article ID 126370, 2020.
- [18] T. Robinson, G. McMullan, R. Marchant, and P. Nigam, "Remediation of dyes in textile effluent: a critical review on current treatment technologies with a proposed alternative," *Bioresource Technology*, vol. 77, no. 3, pp. 247–255, 2001.
- [19] R. Shanmugavalli, P. S. S. Shabudeen, R. Venckatesh et al., "Uptake of Pb (II) ion from aqueous solution using silk cotton hull carbon: an agricultural waste biomass," *E-Journal of Chemistry*, vol. 3, no. 4, pp. 218–229, 2006.
- [20] R. S. Alwi, R. Gopinathan, A. Bhowal, and C. Garlapati, "Adsorption characteristics of activated carbon for the reclamation of eosin Y and indigo carmine colored effluents and new isotherm model," *Molecules*, vol. 25, no. 24, pp. 6014–6015, 2020.
- [21] P. Sudamalla, P. Saravanan, and M. Matheswaran, "Optimisation of operating parameters using response surface methodology for adsorption of crystal violet by activated carbon prepared from mango kernel," *Environment Research*, vol. 22, no. 1, pp. 1–7, 2012.
- [22] S. Debnath, N. Ballav, A. Maity, and K. Pillay, "Development of a polyaniline-lignocellulose composite for optimal adsorption of Congo red," *International Journal of Biological Macromolecules*, vol. 75, pp. 199–209, 2015.
- [23] C. D. Atemkeng, G. S. Anagho, T. F. R. Tagne, A. L. Amola, A. Bopda, and T. Kamgaing, "Optimization of 4-nonylphenol adsorption on activated carbons derived from safou seeds using response surface methodology," *Carbon Trends*, vol. 4, 2021.
- [24] V. O. Shikuku, C. O. Kowenje, and F. O. Kengara, "Errors in parameters estimation using linearized adsorption isotherms: sulfadimethoxine adsorption onto kaolinite clay," *Chemical Science International Journal*, vol. 23, no. 4, pp. 1–6, 2018.
- [25] A. Bopda, T. D. R. Tchoufon, N. G. Ndi-for-Angwafor, G. Doungmo, and S. G. Anagho, "Non-linear equilibrium and kinetic study of the adsorption of 2,4-dinitrophenol from aqueous solution using activated carbon derived from olives stones and cotton cake," *African Journal of Environmental Science and Technology*, vol. 13, no. 9, pp. 365–380, 2019.

- [26] T. Kamgaing, G. Doungmo, F. M. Melatagua Tchieno, J. J. Gouoko Kouonang, and K. J. Mbadcam, "Kinetic and isotherm studies of bisphenol A adsorption onto orange albedo (*Citrus sinensis*): sorption mechanisms based on the main albedo components vitamin C, flavones glycosides and caortenoids," *Journal of Environmental Science and Health, Part A*, vol. 52, no. 8, pp. 757–769, 2017.
- [27] C. S. Ngakou, G. S. Anagho, and H. M. Ngomo, "Non-linear regression analysis for the adsorption kinetics and equilibrium isotherm of phenacetin onto activated carbons," *Current Journal of Applied Science and Technology*, vol. 36, no. 4, pp. 1–18, 2019.
- [28] L. A. Amola, T. Kamgaing, D. R. T. Tchuifon, C. D. Atemkeng, and S. G. Anagho, "Activated carbons based on shea nut shells (*vitellaria paradoxa*): optimization of preparation by chemical means using response surface methodology and physico-chemical characterization," *Journal of Materials Science and Chemical Engineering*, vol. 08, no. 08, pp. 53–72, 2020.
- [29] S. K. V. Nayarana, P. King, R. Gopinadh, and V. Sreeiakshmi, "Response surface optimization of dye removal by using waste prawn shells," *International Journal of Chemical Sciences and Applications*, vol. 2, pp. 186–193, 2011.
- [30] R. Arunachala and G. Annadurai, "Optimized response surface methodology for adsorption of dyestuff from aqueous solution," *Journal of Environmental Science and Technology*, vol. 4, no. 1, pp. 65–72, 2010.
- [31] S. Lagergren, "About the theory of so called adsorption of soluble substances," *Kungäsvenska Vetenskapsakademien- sHandlingar*, vol. 24, pp. 1–39, 1898.
- [32] Y. S. Ho and G. McKay, "Pseudo-second order model for sorption process," *Process Biochemistry*, vol. 34, no. 5, pp. 451–465, 1999.
- [33] S. H. Chien and W. R. Clayton, "Application of Elovich equation to the kinetics of phosphate release and sorption in soils," *Soil Science Society of America Journal*, vol. 44, no. 2, pp. 265–268, 1980.
- [34] W. J. Weber and J. C. Morris, "Kinetic of adsorption of carbon from solution," *Journal of the Sanitary Engineering Division*, vol. 89, no. 2, pp. 31–59, 1963.
- [35] B. Al Duri and G. McKay, "Basic dye adsorption on carbon using a solid phase diffusion model," *The Chemical Engineering Journal*, vol. 38, no. 1, pp. 23–31, 1988.
- [36] D. A. O. A. P. Olalekan, A. M. Olatunya, O. Dada, and F. "Langmuir, "Temkin and dubinin–radushkevich isotherms studies of equilibrium sorption of Zn²⁺ onto phosphoric acid modified rice husk," *IOSR Journal of Applied Chemistry*, vol. 3, no. 1, pp. 38–45, 2012.
- [37] M. I. Temkin and V. Pyzhev, "Kinetics of ammonia synthesis on promoted iron catalyst," *Acta Physicochimica*, vol. 12, pp. 327–356, 1940.
- [38] N. Ayawei, A. N. Ebelegi, and D. Wankasi, "Modelling and interpretation of adsorption isotherms," *Journal of Chemistry*, vol. 2017, Article ID 3039817, 11 pages, 2017.
- [39] S. Rangabhashiyam, N. Anu, M. S. Giri Nandagopal, and N. Selvaraju, "Relevance of isotherm models in biosorption of pollutants by agricultural byproducts," *Journal of Environmental Chemical Engineering*, vol. 2, no. 1, pp. 398–414, 2014.
- [40] M. Katell, *Méthode d'analyse de données en régression non linéaire*, pp. 7–8, Hall, Hoboken, NJ, USA, 2013.
- [41] M. A. Hossain, H. H. Ngo, and W. Guo, "Introduction of microsoft excel SOLVER function-spreadsheet method for isotherm and kinetic modeling of metals biosorption in water and wastewater," *Journal of Water Sustainability*, vol. 3, no. 4, pp. 223–237, 2013.
- [42] C. Chen, "Evaluation of equilibrium sorption isotherm equations," *The Open Chemical Engineering Journal*, vol. 7, no. 1, pp. 24–44, 2013.
- [43] K. Y. Foo and B. H. Hameed, "Insights into the modeling of adsorption isotherm systems," *Chemical Engineering Journal*, vol. 156, no. 1, pp. 2–10, 2010.
- [44] M. Can, "Studies of the kinetics for rhodium adsorption onto gallic acid derived polymer: the application of nonlinear regression analysis," *Acta Physica Polonica A*, vol. 127, no. 4, pp. 1308–1310, 2015.
- [45] X. Jing, Y. Zhu, and Z. Yong-Fa, "Elimination of bisphenol. A from water via graphene oxide adsorption," *Acta Physico-Chimica Sinica*, vol. 29, no. 04, pp. 829–836, 2013.
- [46] F. Sakr, A. Sennoui, M. Elouardi, M. Tamimi, and A. Assabbane, "Etude de l'adsorption du bleu de méthylène sur un biomatériau à base de cactus," *Journal of Materials and Environmental Sciences*, vol. 6, pp. 397–406, 2015.
- [47] H. N. Tran, Y.-F. Wang, S.-J. You, and H.-P. Chao, "Insights into the mechanism of cationic dye adsorption on activated charcoal: the importance of π - π interactions," *Process Safety and Environmental Protection*, vol. 107, pp. 168–180, 2017.
- [48] S. D. B. Maazou, H. I. Hima, M. M. Malam Alma, Z. Adamou, and I. Natatou, "Elimination du chrome par du charbon actif elabore et caracterise a partir dela coque du noyau de Balanites aegyptiaca," *International Journal of Brain and Cognitive Sciences*, vol. 11, no. 6, pp. 3050–3065, 2017.
- [49] I.-H. T. Kuete, D. R. T. Tchuifon, G. N. Ndifor-Angwafor, A. T. Kamdem, and S. G. Anagho, "Kinetic, isotherm and thermodynamic studies of the adsorption of thymol blue onto powdered activated carbons from *Garcinia cola* nut shells impregnated with H₃PO₄ and KOH: non-linear regression analysis," *Journal of Encapsulation and Adsorption Sciences*, vol. 10, no. 01, pp. 1–27, 2020.
- [50] C. Ding, Y. Li, Y. Wang et al., "Highly selective adsorption of hydroquinone by hydroxyethyl cellulose functionalized with magnetic/ionic liquid," *International Journal of Biological Macromolecules*, vol. 107, pp. 957–964, 2018.
- [51] D. Ajifack, J. Ghogomu, T. Noufame, J. Ndi, and J. Ketcha, "Adsorption of Cu (II) ions from aqueous solution onto chemically prepared activated carbon from theobroma cocoa British," *British Journal of Applied Science & Technology*, vol. 4, no. 36, pp. 5021–5044, 2014.
- [52] D. Balarak, M. Zafariyan, C. A. Igwegbe, K. K. Onyechi, and J. O. Ighalo, "Adsorption of acid blue 92 dye from aqueous solutions by single-walled carbon nanotubes: isothermal," *Environmental Processes*, vol. 8, no. 2, pp. 869–888, 2021.
- [53] A. Tyagi, S. Das, and V. C. Srivastava, "Removal of toxic hydroquinone : comparative studies on use of iron impregnated granular activated carbon as an adsorbent and catalyst," *Environmental Engineering Research*, vol. 24, no. 3, pp. 474–483, 2019.
- [54] Z. U. Ahmad, Q. Lian, M. E. Zappi, P. R. Buchireddy, and C. D. D. Gang, "Adsorptive removal of resorcinol onto surface modified ordered mesoporous carbon: kinetics and equilibrium," *Study Environmental Progress & Sustainable Energy*, vol. 12, 2018.